

**Multimodal *in vivo* biomarker-based investigation of  
Alzheimer's disease pathophysiology and drug discovery**

**Min Su (Peter) Kang**

**Integrated Program in Neuroscience (IPN)**

**McGill University, Montreal**

**August 2021**



*A thesis submitted to McGill University in partial fulfillment of the requirement of the  
degree of Doctor of Philosophy*

© Min Su Kang 2021



# 1 Table of Content

1	Table of Content .....	3
2	List of figures .....	6
3	List of tables.....	8
4	List of Abbreviations .....	9
5	Abstract .....	13
6	Résumé.....	15
7	Acknowledgements.....	17
8	Contribution to original knowledge .....	22
9	Contribution of Authors.....	23
10	Introduction.....	26
11	A comprehensive review of the relevant literature .....	29
11.1	A brief history of AD research.....	29
11.1.1	“Patient zero” .....	29
11.1.2	1901-1970s:.....	31
11.1.3	1980-2010s:.....	33
11.1.4	The A/T/(N) classification research framework: .....	39
11.2	Hypotheses.....	46
11.2.1	Amyloid cascade hypothesis .....	46
11.2.2	Tau hypothesis.....	53
11.2.3	(Neuro)Inflammation hypothesis .....	62
11.3	AD (pre)clinical trials so far .....	66
11.4	The Aims and hypotheses .....	70
12	Body of the thesis.....	72
12.1	Methodology .....	72

12.1.1	Study samples.....	72
12.1.2	Demographics.....	79
12.1.3	Positron Emission Tomography (PET) .....	81
12.1.4	Magnetic Resonance Imaging (MRI).....	85
12.1.5	Biofluids.....	88
12.2	Research findings.....	92
12.2.1	Study 1: Amyloid-beta modulates the association between neurofilament light chain and brain atrophy in Alzheimer's disease. ....	93
12.2.2	Study 2: The interaction between amyloid-beta and activated microglia drives tau propagation in Alzheimer's disease. ....	123
12.2.3	Study 3: Preclinical <i>in vivo</i> longitudinal assessment of KG207-M as a disease-modifying Alzheimer's disease therapeutic.....	160
13	A comprehensive scholarly discussion of all the findings.....	193
13.1	Validation of a new biomarker .....	193
13.2	<i>in vivo</i> biomarker-based evidence supporting disease mechanisms .....	196
13.3	<i>in vivo</i> biomarker-based evaluation of therapeutic target engagement, efficacy, and safety	199
13.4	Limitations .....	201
14	A final conclusion and summary .....	203
15	Supplementary Materials .....	205
15.1	Supplementary Figures .....	205
15.2	Supplementary Tables.....	223
16	Collaborations (Ongoing) .....	246
16.1	International .....	246
16.2	McGill University .....	246
17	Publications.....	248

17.1	First Author .....	248
17.2	Co-author .....	248
18	Presentations .....	255
18.1	Invited .....	255
18.2	Oral .....	255
18.3	Poster.....	256
19	Awards and Recognition.....	259
20	References.....	261

## 2 List of figures

Figure 1. Alois Alzheimer and Auguste Deter.....	29
Figure 2. Alzheimer’s sketches of histological staining of Auguste’s brain tissue based on Bielschowsky staining. ....	31
Figure 3. Fischer’s detailed sketches of plaques and tangles and staging of plaque pathology. ..	32
Figure 4. Hippocampal atrophy was depicted based on CT and PET in the 80s.....	36
Figure 5. Hypothetical models of dynamic biomarkers of Alzheimer’s disease pathological cascade. ....	38
Figure 6. The A/T/(N) classification system.....	40
Figure 7. Various disease models and hypotheses to test based on <i>in vivo</i> biomarkers. ....	44
Figure 8. The A/T/(N) classification system is evolving.....	45
Figure 9. The amyloid cascade hypothesis. ....	47
Figure 10. Human APP proteolytic pathways.....	48
Figure 11. Structures and different species of A $\beta$ .....	50
Figure 12. Biological effects of A $\beta$ . ....	51
Figure 13. Formation of aggregates of p-tau oligomers and NFTs.....	53
Figure 14. Different binding distributions of tau PET tracers in various tauopathies. ....	55
Figure 15. The six Braak Stages. ....	57
Figure 16. Evidence of trans-synaptic propagation of tau induced by AD-tau in non-Tg mice...	59
Figure 17. Endosomal “traffic jam” could lead to A $\beta$ production.....	61
Figure 18. The effects of reactive gliosis in Alzheimer’s disease pathophysiology.....	62
Figure 19. Disease-associated Microglia. ....	64
Figure 20. Progression of A $\beta$ pathology in McGill-R-Thy1-APP transgenic rat model. ....	76
Figure 21. A $\beta$ -induced pathophysiology in McGill-R-Thy1-APP transgenic rat model between 16-19 months old. ....	77

Figure 22. Various PET methodologies.....	83
Figure 23. A $\beta$ and neurodegeneration biomarkers and their associations in the McGill-R-Thy1-APP rat model.....	108
Figure 24. The associations between CSF NFL and DBM.....	110
Figure 25. VBM group comparisons. ....	111
Figure 26. The associations between NFL and VBM in MCI A $\beta$ - and A $\beta$ +. ....	113
Figure 27. The associations between NFL and VBM in AD and NFL effect sizes.....	115
Figure 28. Local-to-local and local-to-distal interactive effects between A $\beta$ and activated microglia on tau pathology. ....	133
Figure 29. PLS analysis using [ $^{18}\text{F}$ ]AZD4694, [ $^{11}\text{C}$ ]PBR28, and [ $^{18}\text{F}$ ]MK6240 in A $\beta$ - and AD continuum. ....	137
Figure 30. Investigating the interactive effects of A $\beta$ and activated microglia using PLS path modelling. ....	139
Figure 31. Activated microglia in the medial temporal cortex together with widespread A $\beta$ predict tau propagation in AD.....	141
Figure 32. Stepwise logistic regression ROC curves.....	144
Figure 33. The effect of A $\beta$ , activated microglia, and tau on cognition in A $\beta$ - and AD continuum. ....	146
Figure 34. <i>in vivo</i> biomarker-based study design to evaluate KG207-M target engagement, efficacy, and safety. ....	166
Figure 35. A schematic representation of KG207-M.....	176
Figure 36. Pharmacokinetic modelling of KG207-M. ....	178
Figure 37. KG207-M removes brain A $\beta$ .....	181
Figure 38. KG207-M ameliorates A $\beta$ -induced <i>in vivo</i> biomarker abnormalities. ....	184
Figure 39. No evidence of ARIA-H.....	186

### 3 List of tables

Table 1. The A/T/(N) biomarker groupings.....	41
Table 2. The A/T/(N) biomarker profiles and categories. ....	42
Table 3. A list of FDA-approved drugs for AD.....	66
Table 4. Study 1 human demographics.....	106
Table 5. Study 1 animal demographics.....	107
Table 6. Study 2 demographics.....	128
Table 7. ROI abbreviations.....	134

## 4 List of Abbreviations

ANTS	Advanced Normalization Tools
ADRDA	Alzheimer's Disease and Related Disorders Associations
ADNI	Alzheimer's Disease Neuroimaging Initiative
AA	Alzheimer's Association
AD	Alzheimer's disease
CTF $\alpha$	Amino-acid $\alpha$ -C-terminal fragment
ABP	Amyloid Binding Protein
APP	Amyloid Precursor Protein
A $\beta$	Amyloid-Beta
A/T/(N)	Amyloid-Beta/Tau/(Neurodegeneration)
ARIA-E	Amyloid-related imaging abnormalities edema
ARIA-H	Amyloid-related imaging abnormalities microhemorrhage
ANCOVA	Analysis of Covariance
ANOVA	Analysis of Variance
APOE	Apolipoprotein E
AIBL	Australian Imaging, Biomarkers and Lifestyle
AEB	Average number of enzymes per bead
BACE	Beta-site APP cleaving enzyme
BP <sub>ND</sub>	Binding potential nondisplacable Biomarkers for Identifying Neurodegenerative Disorders Early and
BIOFINDER	Reliably
BBB	Blood-brain barrier
BOLD	Blood-oxygen-level-dependent
CDRSOB	CDR sum of boxes
CNS	Central Nervous System
CSF	Cerebrospinal fluid
CDR	Clinical Dementia Rating
Co	Cobolt
CV	Coefficient of variations
CN	Cognitively Normal
CT	Computed Tomography
CBD	Corticobasal Degeneration
DMN	Default Mode Network
DBM	Deformation-based morphometry
DAM	Disease-associated microglia
kd	Dissociation constant
DVR	Distribution volume ratio
DIAN	Dominantly Inherited Alzheimer Network
EMCI	Early MCI

FDR	False Discovery Rate
FISP	Fast Imaging with Steady State Precession pulse sequence
FLASH	Fast Low Angle Shot
FOV	Field of view
[ <sup>18</sup> F]FDG	Fluorodeoxyglucose( <sup>18</sup> F)
FTD	Frontotemporal Dementia
FWHM	Full-Width at Half Maximum
GWAS	Genome-wide association studies
GoF	Goodness of Fit
HAM	Human Alzheimer's microglia
HPLC	High-performance liquid chromatography
HRRT	High-Resolution Research Tomography
p-tau	Hyperphosphorylated tau
ICA	Independent Component Analysis
IPN	Integrated Program in Neuroscience
LMCI	Late MCI
LV	Latent Variable
LOR	Line of response
LTD	Long-term Depression
LTP	Long-term Potentiation
MRI	Magnetic Resonance Imaging
MAP	Maximum A Prior
MCSA	McGill University Research Centre for Studies in Aging
MINC	Medical Imaging NetCDF
MBq	MegaBecquerel
MAPT	Microtubule-associated protein tau
MCI	Mild Cognitive Impairment
MMSE	Mini-Mental State Exam
MAO	Monoamine oxidase
MOCA	Montreal Cognitive Assessment
MNI	Montreal Neurological Institute
nM	nanoMolar
NINCDS	National Institute of Neurological and Communicative Disorders and Stroke
NIA	National Institute of Aging
NIBIB	National Institute of Biomedical Imaging and Bioengineering
NIH	National Institute of Health
NFTs	Neurofibrillary tangles
NFL	Neurofilament Light Chain
OSEM	Ordered-subsets Expectation Maximization
PFA	Paraformaldehyde
PLS	Partial Least Square

PCM-1	Pericentriolar material 1
PK	Pharmacokinetics
PBS	Phosphate-buffered saline
[ <sup>11</sup> C]PiB	Pittsburgh Compound B
PET	Positron Emission Tomography
PCC	Posterior Cingulate Cortex
PSEN1	Presenilin-1
PSEN2	Presenilin-2
PSP	Progressive Supranuclear palsy
PAM	Proportion of morphologically activated microglia
QC	Quality Control
RFT	Random Field Theory
ROI	Region of interest
rs-fMRI	Resting-state Functional Magnetic Resonance Imaging
SRTM	Simplified Reference Tissue Method
sAPP $\alpha$	Soluble $\alpha$ -APP fragment
s.e	Standard Error
SUVR	Standardized uptake value ratio
SNAP	Suspected Non-Alzheimer's Pathophysiology
FDA	The US. Food and Drug Administration
T-tau	Total tau
V <sub>T</sub>	Total volume of distribution
V <sub>T</sub> /f <sub>P</sub>	Total volume of distribution adjusted with plasma free parent ratio
Tg	Transgenic animals
TRIAD	Translational Biomarkers of Aging and Dementia
TSPO	Translocator Protein
TREM-2	Triggering receptor expressed on myeloid cells 2
TNF	Tumor necrosis factor
VBM	Voxel-based morphometry
WT	Wild type
WHO	World Health Organization
$\beta$ -CTF	$\beta$ -C-terminal fragment



## 5 Abstract

*in vivo* biomarkers of Alzheimer's disease (AD) have made remarkable progress during the past decades in detecting the pathological hallmarks of AD: aggregates of amyloid-beta ( $A\beta$ ) plaques, aggregates of hyperphosphorylated tau/neurofibrillary tangles (NFTs), and neurodegeneration. Today, such biomarkers can be quantified using advanced brain imaging techniques such as positron emission tomography (PET) as well as more readily available and accessible biofluid platforms such as in cerebrospinal fluid (CSF) and/or plasma sampling. In 2018, the US National Institute of Aging (NIA) and Alzheimer's Association (AA) has put forth a research framework, the A/T/(N) classification system –  $A\beta$ , hyperphosphorylated tau, and neurodegeneration, in which the diagnostic criteria are now exclusively based on the biological construct of AD. Although the application of the biological-based diagnostic criteria on clinical diagnosis of AD is still debated, the A/T/(N) system has provided a consensus in the AD research community. This has 1) accelerated the discoveries and validations of novel biomarkers across a multitude of platforms, 2) promoted a deeper understanding and a more accurate characterization of AD pathophysiological processes leading to cognitive impairment, 3) enabled clinical trial enrichment by precisely defining the potential therapeutic target, intervention study design, and biomarker-based evaluation of therapeutic target engagement and efficacy.

In this Ph.D. thesis, three original studies provide three novel findings using the A/T/(N) classification research framework to 1) validate a novel fluid neuronal injury biomarker, neurofilament light chain (NFL) as a new addition to the AD biomarker A/T/(N) classification, 2) support activated microglia as an important factor in AD pathophysiological processes leading to aggregation of hyperphosphorylated tau and subsequent cognitive impairment in the presence of

A $\beta$ , and 3) demonstrate a potential disease-modifying AD therapeutic and a platform, in which to facilitate new drug discovery.

## 6 Résumé

Les biomarqueurs *in vivo* de la maladie d'Alzheimer (MA) ont fait de remarquables progrès au cours des dernières décennies dans la détection des caractéristiques pathologiques de la MA: agrégats de plaques de bêta-amyloïde ( $A\beta$ ), agrégats de tau hyperphosphorylé/enchevêtrements neurofibrillaires (ENF) et neurodégénérescence. Aujourd'hui, ces biomarqueurs peuvent être quantifiés à l'aide de techniques d'imagerie cérébrale avancées, telles que la tomographie par émission de positons (TEP), ainsi qu'à l'aide de banques d'échantillons biologiques plus facilement disponibles et accessibles, telles que dans le liquide céphalorachidien (LCR) et/ou le prélèvement de plasma. En 2018, le US National Institute in Aging (NIA) et l'Alzheimer's Association (AA) ont mis de l'avant un encadrement de la recherche : le système de classification A/T/(N) —  $A\beta$ , tau hyperphosphorylé et neurodégénérescence, dans lequel les critères de diagnostic sont désormais exclusivement basés sur la construction biologique de la MA. Bien que l'application des critères diagnostiques biologiques au diagnostic clinique de la MA soit encore sujet à débat, le cadre de recherche A/T/(N) a permis de fournir un consensus au sein de la communauté de chercheurs sur la MA. Cela a permis 1) d'accélérer la découverte et la validation de nouveaux biomarqueurs sur une multitude de plateformes, 2) de favoriser une compréhension plus approfondie et une caractérisation plus précise des processus physiopathologiques de la MA conduisant à une déficience cognitive, 3) d'enrichir les essais cliniques en définissant précisément la cible thérapeutique potentielle, la conception de l'étude d'intervention et l'évaluation de l'engagement et de l'efficacité de la cible thérapeutique à l'aide de biomarqueurs.

Dans cette thèse de doctorat, trois études novatrices présentent trois nouveaux résultats utilisant le cadre de recherche A/T/(N) pour 1) valider un nouveau biomarqueur fluide de lésion

neuronale, la chaîne légère des neurofilaments (NFL), en tant que nouvel ajout à la classification A/T/(N) des biomarqueurs de la MA, 2) soutenir la microglie activée en tant que facteur important dans les processus pathophysiologiques de la MA conduisant à l'agrégation de la protéine tau hyperphosphorylée et à la déficience cognitive subséquente en présence d'A $\beta$ , et 3) démontrer une thérapie potentielle de la MA, modificatrice de la maladie, ainsi qu'une plateforme, par laquelle la découverte de nouveaux médicaments sera facilitée.

## 7 Acknowledgements

There are important people to acknowledge for their support in this Ph.D. journey. First and foremost, I would like to express my deepest gratitude towards Dr. Pedro Rosa-Neto. This journey was not possible without you. While knocking on many doors for a new chapter in my life following undergraduate graduation, you have taken a leap of faith in me to join your lab. Someone who did not have any experience in research, computer programming, extensive statistical knowledge, neuroimaging, and more. All of the crucial aspects to consider when selecting a new lab member. From a retrospective point of view now, this must have been a gamble — one that you did not need to take. You have given me an opportunity when no one else did. One chance that I have been seeking for some time. This also motivated me to help others when they were in need even if it means sacrificing my time and even sometimes my research. So, thank you, Pedro, for giving me a chance to prove myself.

Dr. Gassan Massarweh joined as my supervisor later but his supervision came at a critical point in my Ph.D. journey. I studied cell biology and anatomy during my undergraduate, but I was left with performing a blood analysis using high-performance liquid chromatography (HPLC). This is a technique that is usually performed by a chemist or an expert with extensive chemistry knowledge. When Google was my only friend helping me with the HPLC work, your words of advice and support became like a Bible to me. Gassan, you have taken your time to teach and explain a deeper understanding of chemistry and different properties to be aware of when working with the HPLC. More importantly, your trust and words of confidence in me when I had doubted myself helped me to survive in the field that I was completely new to.

Dr. Serge Gauthier and Dr. A. Claudio Cuello were my two outstanding advisory committee members. They both are world-renown researchers in AD. Their keen observations

and understanding of AD were evident from their advice in each of my advisory committee meetings. You pushed me to be a more complete scientist who understands the clinical aspects as well as the cellular and molecular aspects of the disease. Moreover, your continuous passion for AD research and better quality of life in every patient at the MCSA community has been inspirational.

Beyond my advisory committee members, I would like to also express my gratitude towards the whole MNI PET unit community. Most notably, Dr. Jean-Paul Soucy, you truly came to the rescue when our bolus and infusion project was about to be stopped due to scheduling conflicts and opened the door to continue our study at PERFORM. Dr. Stephan Blinder, you continuously support our endeavours on motion tracking and new reconstruction methodology development. We are very grateful for your expertise. Dr. Alexey Kostikov, you have also assisted me with HPLC troubleshooting and creative ways to solve the problems. Reda and Chris, your support on some of the crazy experiment designs that also pushed you out of your comfort zone cannot be forgotten. With your help, understanding, and teamwork, we are able to conduct experiments that are not possible anywhere in the world. Also, Dean, Robert, and the entire cyclotron team, your support on my HPLC endeavours and PET tracer synthesis for our projects were necessary to successfully complete some of the projects. Moreover, our generations of microPET units including Antonio Aliaga were the critical parts in the microPET to continue the work and expand new projects with different collaborators. Antonio Aliaga, you shared your knowledge of the microPET when I was alone to operate the microPET. Without you, there would not be the same microPET unit at MNI. From the Douglas Hospital side, I would like to express my gratitude to Dr. Axel Mathieu who operated MRI for our projects. MR scanning day can become very long. But our stimulating conversations were enjoyable.

From our TNL and MCSA team, there are a few names I must mention. First, I met Monica Shin during my undergraduate program at McGill University. With this connection, Monica introduced me to Pedro. Monica, you were the bridge that led to a new chapter in my life. Who could have imagined that we would become lab mates?! Sulantha Mathotaarachchi and Seqian Wang were extremely helpful with programming in Linux. I was completely new to Linux and your patience with showing the command lines as well as how to learn bash on my own helped me to get where I am. Dr. Eduardo Zimmer was the person who trained me with animal research first. Eduardo, your positive energy and passion for science was a joy to be around. It was a privilege to have worked with you! Most importantly, Arturo Aliaga Aliaga, you were my partner in crime for the entire journey. All of the countless hours that we were stuck at the animal facility collecting samples even past midnights were possible thanks to you. Your kindness and patience are admirable traits that all researchers should have! Also, I still cannot believe how we pulled off everything without speaking the same language! Last but not least, the whole TNL, MCSA, CrossRoad team, and study participants deserve a big applause. Without them, the TRIAD cohort would be possible.

When my life was consumed by the Ph.D. research, my Unicorns kept me grounded and brought balance to my life. Aaron, Zoe, Preston, Veronica, Minho, Shelly, Kevin, Esta, Alex, Vanessa, and Ryan, we have unforgettable memories that I will cherish forever. Though our journey departed once it was the time for all of you to move to Toronto, our time in Montreal was the bright sunlight in my cloudy days. Also, I give my shoutouts to my fellow McGillians, particularly Jon and Sagar. The strong bond that we set from the New Residence days is still growing. I am blessed to have you guys in my life. It means so much to know that we have each other even after 10 years since the McGill time. Though we cannot hang out and talk to each

other like we used to back in the day, just knowing that we are still on the same journey called life together gives me the strength to push forward. My oldest friend group, Old School! Our crazy storytime starts even before my university years. For attending McGill University for my undergraduate and graduate studies, I had to sacrifice some of the lifetime memories that I wished to be part of. This taught me how precious every moment I have with you all is, and I value every second that we spend together. June, Leo, Derek, BLC, Matt, Kevin, Stella, and Greg always welcome me with open arms, and our holiday gathering has now become a family tradition. Especially, June, you were my cousin first, then my closest friend, and now you are my closest brother more so than our blood siblings. I feel that you are always next to me, and your advice means the world to me even if your words may not be exactly what I want to hear. Your honesty and courage to speak from the bottom of your heart is something that I do not take for granted, and I am privileged to have.

I cannot begin to express my feelings when it comes to my family. My parents are my greatest strength, motivation, inspiration, mentors, and support. Without them, I cannot exist. Who could have known the day I left for university when I was 18 years old was the moment that I'd never live under their roof anymore? We all expected this to be a 4-year journey, but now it has been more than 10 years and continuing. Throughout all these years, you have always patiently waited for me to complete my journey and supported me from behind in any way that you could, even if you were not in the easiest circumstances. As much as it pains me to realize how much I missed out to be there for you when you needed me, I am proud to say that I have worked hard throughout the years and hope that my small accomplishments during this journey are worthy of all the sacrifices that you have made for me.

Throughout my Ph.D. journey, I have learned how difficult research can be. One must have a valid idea, conduct a controlled experiment, process, analyze, and interpret the data to see whether your expectation is true or not — not to mention all the knowledge in different aspects one must have to successfully test ideas or knowledge. Thus, I have been training to formulate innovative ideas and to control different aspects such that I can process, analyze, and interpret. This reflects general decision-making in life: trials and errors. However, I have also learned throughout my Ph.D. is that life is unpredictable. Life cannot be planned and controlled in every aspect. Sometimes, the most unpredicted and unplanned outcome can bring the greatest joy. This is you, Julie Ottoy. Like those romantic comedy movies, our story was unpredicted and started with uncertainty. But our story is real and is still being written! You have supported me throughout the darkest time and have brought love and happiness. I cannot wait to begin the next chapter of my life with you ♥

## 8 Contribution to original knowledge

In this Ph.D. thesis, three innovative studies will establish three original contributions to AD biomarker-based research.

**Study 1:** Using unprecedented multimodal biomarkers, this study validates NFL as a novel fluid neurodegenerative biomarker for the A/T/(N) classification research framework. Study 1 is titled “*Amyloid-beta modulates the association between neurofilament light chain and brain atrophy in Alzheimer’s disease*”, and is published in Molecular Psychiatry.

**Study 2:** This shows the first *in vivo* biomarker evidence of activated microglia as a driver of neurofibrillary tangles accumulation and spreading in the presence of A $\beta$ . Study 2 is titled “*The interaction between amyloid-beta and activated microglia drives tau propagation in Alzheimer’s disease*”, and is currently under review in Science Advances.

**Study 3:** The last study provides a novel biomarker pipeline for preclinical assessment of disease-modifying anti-amyloid therapeutic target engagement, efficacy, and safety based on *in vivo* biomarkers. Study 3 is titled “*Preclinical in vivo longitudinal assessment of KG207-M as a disease-modifying Alzheimer’s disease therapeutic*”, and is published in Journal of Cerebral Blood Flow & Metabolism.

These findings constitute important contributions to a growing body of biomarkers, a greater understanding of disease mechanisms, and a proof-of-concept in disease-modifying therapeutic and drug discovery.

## 9 Contribution of Authors

This Ph.D. thesis includes three original studies, and Min Su Kang (myself) led and contributed the most to all the studies. In all three studies, I conceptualized the study, developed the study design, coordinated study schedules and administration, conducted and executed all of the animal study designs, collected all the animal data, reviewed all of data quality control, processed and analyzed all of the human and animal data (unless indicated otherwise below as co-authors' contributions), interpreted, coherently articulated, and summarized original contributions to AD research, and executed the manuscript submission and review process. All of the animal data collected include blood/plasma, CSF, MRI, PET where I also operated microPET, and brain tissue collection via perfusion. All of the animal data that I processed and analyzed include structural MRI, resting-state functional MRI, susceptibility MRI, and [ $^{18}\text{F}$ ]AZD4694. Additionally, I analyzed animal CSF A $\beta$ , CSF NFL, Campbel-Switzer Silver staining, and Pearl/DAB staining. Regarding human data, I significantly contributed to the development, validation, and implementation of [ $^{18}\text{F}$ ]MK6240 SUVR methodology while I implemented the scanning protocols for [ $^{18}\text{F}$ ]AZD4694, [ $^{18}\text{F}$ ]MK6240, and [ $^{11}\text{C}$ ]PBR28. I also processed and analyzed human structural MRI and all three PET tracers. Last, I also analyzed all of the human CSF, plasma, and cognitive test data. However, without the support of the co-authors, none would have been possible, and their notable contributions are highlighted below.

### Study 1:

Dr. Pedro Rosa-Neto and Dr. Serge Gauthier also conceptualized the study, supervised the interpretation of the data, and assisted in drafting the manuscript. Monica Shin and Arturo

Aliaga assisted in animal data collection. Sulantha Mathotaarachchi assisted with statistical analysis. Dr. Axel Mathieu operated animal MRI. Dr. M. Mallar Chakravarty and Dr. Gabriel A. Devenyi assisted and provided a pipeline to process structural MRI data and assisted in drafting the manuscript. Dr. Henrik Zetterberg, Dr. Kaj Blennow, and Dr. Åsa Sandelius processed animal CSF data and assisted in drafting the manuscript. Dr. A. Claudio Cuello provided the transgenic animal model and guidance in drafting the manuscript. Dr. Gassan Massarweh assisted in drafting the manuscript.

*Study 2:*

Dr. Pedro Rosa-Neto and Dr. Julie Ottoy also conceptualized the study, aided the interpretation of the data, and drafted the manuscript. Sulantha Mathotaarachchi assisted with statistical analysis. Dr. Gleb Bezgin assisted with human data curation. Dr. Serge Gauthier, Dr. A. Claudio Cuello, Dr. Jean-Paul Soucy, Dr. Gassan Massarweh assisted in maturing the concept and drafting the manuscript. Dr. Mira Chamoun, Firoza Lussier, Jenna Stevenson, and Nesrine Rahmouni coordinated the human imaging data collection and cognitive tests and scoring.

*Study 3:*

Dr. Pedro Rosa-Neto, Dr. Serge Gauthier, Dr. Jean-Paul Soucy, Michael Waterston, Nathan Yoganathan, Dr. Kerry Rennie, Dr. Balu Chakravarthy, Dr. Danica Stanimirovic, Dr. D. Louis Collins, and Dr. Gassan Massarweh also conceptualized the study, study design, and draft of the manuscript. Dr. Julie Ottoy assisted in data analysis and drafting of the manuscript. Monica Shin, Arturo Aliaga, Kely Quispialaya assisted in animal data collection. Sulantha

Mathotaarachchi assisted with statistical analysis. Dr. Axel Mathieu operated animal MRI. Dr. M. Mallar Chakravarty provided a pipeline to process structural MRI data. Dr. Henrik Zetterberg, Dr. Kaj Blennow, and Dr. Åsa Sandelius processed animal CSF data and assisted in drafting the manuscript. Dr. A. Claudio Cuello provided the transgenic animal model and guidance in drafting the manuscript. Dr. Etienne Lessard and Dr. Arsalan Haqqani conducted the plasma pharmacokinetic modelling and assisted in drafting the manuscript. All authors reviewed in drafting the manuscript.

## 10 Introduction

Imagine one day, when you wake up, you cannot recognize your wife's or husband's face?

Imagine one day, you cannot remember which day of the week it is?

Imagine one day, you realize you don't know how to take care of your banking alone?

Imagine one day, you are diagnosed with Alzheimer's disease (AD).

AD is a debilitating progressive neurodegenerative disease that affects an individual's cognition and slowly takes away one's autonomy and oneself. In 2021, an estimated 6.2 million Americans age 65 and older are living with AD and is projected to double by 2050 with the baby boomer generation reaching age 65 and above in recent years [1]. The overall health care cost for people age 65 and older with dementia are estimated to be more than \$300 billion in 2021, while unpaid dementia caregiving is estimated to be more than \$200 billion in 2020 [1]. The impact of AD in physical, emotional, and mental health on the patients as well as caregivers throughout the disease is ineffable.

In May 2017, World Health Organization (WHO) has announced the Global action plan on the public health response to dementia 2017-2025 [2]. This plan aims to improve the quality of life of people living with dementia, their families, and caregivers while reducing the impact on communities and countries. AD contributes 60-80% of dementia cases as the most common form of dementia [1]; WHO recognizes dementia as a global health priority. In June 2021, Aducanumab (marketed as Aduhelm) is conditionally approved under the accelerated approval

pathway by the U.S. Food and Drug Administration (FDA) [3]. As the first drug to target underlying pathologic protein, Aducanumab hopes to be the catalyst in the development and advancement of preventative and disease-modifying therapeutics in AD. However, Aducanumab still needs to prove its clinical benefits. Without any effective treatments, the inevitable global war against AD will be catastrophic.

As night is the darkest before dawn, AD has been reconceptualized in its definition, stages, and diagnosis to a new clinical and research framework over the past decades. The crux of the reconceptualization of AD from a heterogeneous clinical spectrum to a biologically defined continuum has been possible by the discovery and validation of AD *in vivo* biomarkers. Since the identification of amyloid-beta ( $A\beta$ ) and hyperphosphorylated tau (p-tau) as pathogenesis hallmarks of AD, a myriad of novel AD biomarkers has been characterized and validated across multiple disciplines such as genetics, molecular biology, computational neuroimaging, and more. Also, this growing number of biomarkers has played a vital role in a deeper understanding of a complex molecular cascade of events in AD pathophysiological processes leading to cognitive impairment. As a result, numerous clinical trials have recently adapted to include biomarkers to enrich their trial populations and evaluate therapeutic target engagement and efficacy to accelerate drug discovery.

This Ph.D. thesis presents three original contributions to AD research regarding 1) validating a novel fluid neurodegenerative biomarker, 2) showing the first *in vivo* biomarker evidence of activated microglia as a driver of hyperphosphorylated tau pathology and spreading in the presence of  $A\beta$ , and 3) preclinical assessment of disease-modifying anti-amyloid therapeutic target engagement and efficacy based on *in vivo* biomarkers. These exemplify the

three important aspects in today's AD biomarker-based research to accelerate a deeper understanding and discovery in disease-modifying therapeutics.

## 11 A comprehensive review of the relevant literature

### 11.1 A brief history of AD research

#### 11.1.1 “Patient zero”

Auguste Deter was only 50 years old when her husband, Karl Deter, started to notice unusual behaviours from her. She started to lose her memory. She could not care for the housework and everyday chores anymore. Soon, she became more aggressive, paranoid, and delusional. Her symptoms progressively deteriorated to the point it was necessary to admit her to a psychiatric hospital in 1901. She was a wife and a mother but was not *herself* anymore.

Alois Alzheimer was a German psychiatrist and neuropathologist who observed Auguste Deter closely (Figure 1). With great interest in Auguste and her symptoms, Alois Alzheimer asked her several questions to examine her condition. Below is an excerpt from the recovered medical records of Dr. Alzheimer on Auguste.

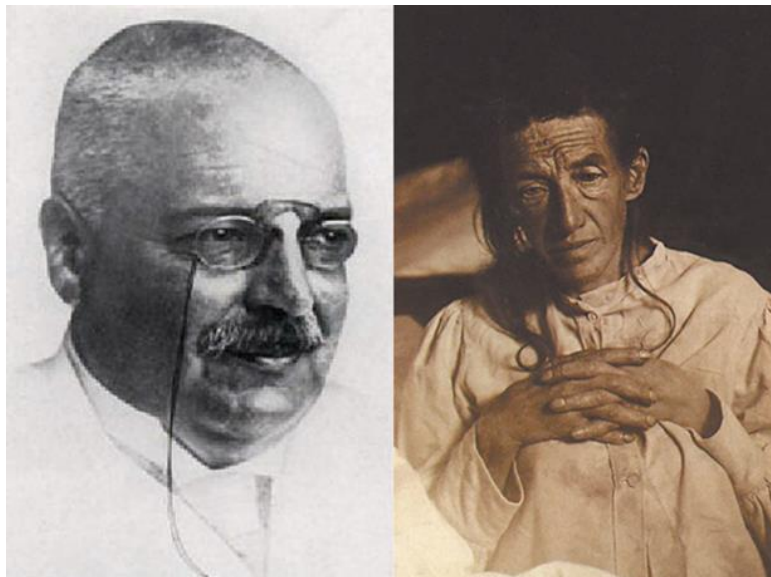


**Figure 1.** Alois Alzheimer and Auguste Deter.

Reproduced from Engelhardt et al., 2015 [4].

*Alzheimer: "What's your name?"*

*Auguste: "Auguste."*

*Alzheimer: "Family name?"*

*Auguste: "Auguste"*

*Alzheimer: "What is your husbands' name?"*

*Auguste: "I believe ... Auguste" (she hesitantly answered)*

*Alzheimer: "Are you married?"*

*Auguste: "Oh, I am so confused."*

*Alzheimer: "Where are you right now?"*

*Auguste: "Here and everywhere, here and now, you must not think badly of me."*

...

*Auguste: "I have lost myself."*

After five years at the institute, Auguste's condition became progressively worse, and she passed away on April 8<sup>th</sup>, 1906 at the age of 55. Alois Alzheimer described her symptoms to include a progressive cognitive disorder, local neurological symptoms, hallucination, delusion, and psychological social disability condition. He continued to investigate her condition by examining her brain tissue using a state-of-the-art staining technique, Bielschowsky staining, at the time. He found peculiar matters that later became the hallmarks of AD, aggregates of A $\beta$  forming plaques and aggregates of p-tau forming neurofibrillary tangles (NFTs), in her brain

(Figure 2) [4]. Furthermore, Alzheimer noted shrinking of certain brain regions. On November 3<sup>rd</sup>, 1906, Alois Alzheimer presented his findings at the Tübingen meeting of the Southwest German Psychiatrists and linked the abnormal symptoms to the abnormal matters found in the brain. Alois Alzheimer described Auguste Deter as presenile dementia, which described senile dementia before age of 65, for the first time. Shortly after, Alois Alzheimer published a landmark paper describing his findings in 1907 [4, 5]; the disease is first coined as Alzheimer's disease by Alzheimer's mentor and colleague, Dr. Emil Kraepelin, in the chapter "Presenile and senile dementia" in the 8<sup>th</sup> edition of the Handbook of Psychiatry in 1910 [4]. Since then, AD and its disease description were popularized internationally by 1911.



**Figure 2.** Alzheimer's sketches of histological staining of Auguste's brain tissue based on Bielschowsky staining.

Reproduced from Engelhardt et al., 2015 [4].

### 11.1.2 1901-1970s:

Coincidentally, Dr. Oskar Fischer, a Czech psychiatrist and neuropathologist, also noticed very similar neuropathological findings. He published his findings of neuritic plaques in more than a dozen of cases of senile dementia in 1907 [6]. His publication was complementary to Alzheimer's work by describing neuritic plaques in great detail (Figure 3). Fischer's contribution was not highlighted until the early 2000s by revisiting and uncovering the archives of Charles

University in Prague. Due to nationalist tension, the anti-Semitism of his period, and the academic competition, Oskar Fischer's significant findings were only highly recognized later.

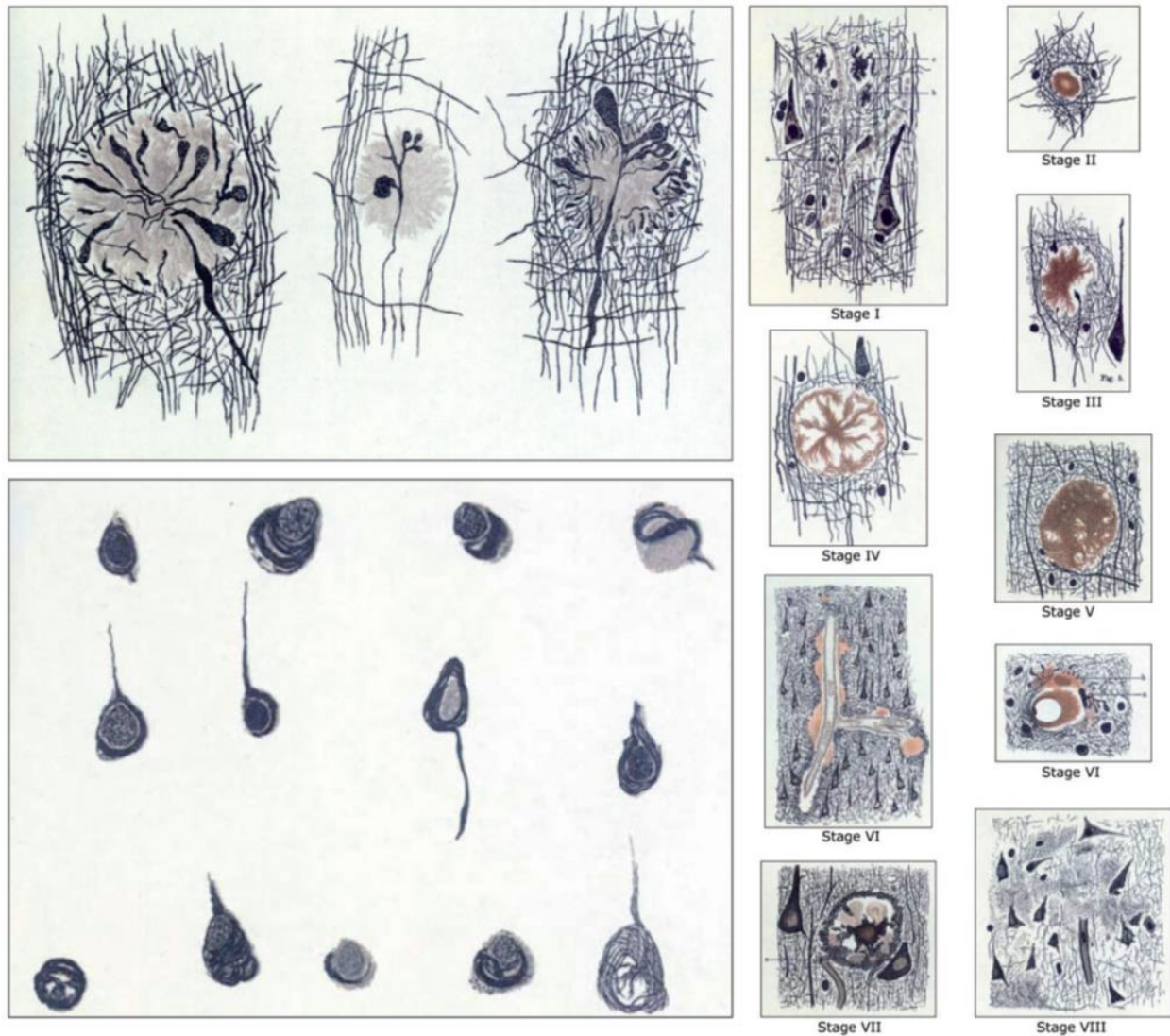


**Figure 3.** Fischer's detailed sketches of plaques and tangles and staging of plaque pathology.

Reproduced from Goedert, 2009 [6].

The initial description of AD as presenile dementia in the chapter, “Presenile and senile dementia”, distinguished it from senile dementia, which was thought to describe age-related dementia showing symptoms after the age of 65 with a vascular burden. However, continued

reports of the presence of plaques and tangles pathology in “senile dementia” at the time questioned the definition of AD as presenile dementia in the 60s to 70s [7, 8]. By the early 70s, the number of plaques and tangles was correlated with the severity of senile dementia [7, 8]; by the late 70s, substantial evidence converged to suggest that both presenile dementia and senile dementia were indistinguishable neuropathologically [9]. In 1976, Dr. Robert Katzman published a seminal paper unifying both presenile and senile dementia as AD without the age distinction and highlighted the prevalence of AD and urgency to tackle AD [9].

While early days of AD research have identified the plaques and tangles as the pathological hallmarks of AD, the popular techniques applied in the early days of research have been biochemical assays or *in vitro* in nature. As such, the early observation of selective neuronal loss in the cholinergic system has led to the birth of the cholinergic hypothesis and the first clinical trial in AD to alleviate the symptoms [10-12].

### **11.1.3 1980-2010s:**

With the growing awareness and burden of AD, the momentum of AD and dementia research was accelerated with the discovery of A $\beta$  and tau as the main component in plaques [13, 14] and tangles [15, 16] in 1984 and 1985, respectively. This was a turning point in AD research to begin investigating the underlying etiology of the disease. Subsequently, additional seminal discoveries were made. In 1987, the causative mutation for AD in amyloid precursor protein (APP) was found [17-19]. In 1991, the amyloid cascade hypothesis was published describing the mechanistic pathways in AD pathogenesis [20, 21]. Also, the invention of the first transgenic mouse model of A $\beta$  enabled investigating the amyloid cascade hypothesis in a living organism [22]. Today, the amyloid cascade hypothesis is still the most dominant hypothesis for AD. While

the A $\beta$  gained immense support for the etiology of AD, Braak and Braak published their landmark paper on the histopathological staging of AD that is the basis of the tau hypothesis as the etiology of AD [23, 24]. Moreover, evidence of glial cells in AD pathophysiology was underscored and provided a strong foundation for anti-inflammation strategies for AD that are still actively investigated today [25, 26]. In addition, the apolipoprotein E (APOE) was identified as a strong genetic risk factor for AD [27]; one allele of APOE $\epsilon$ 4 increases AD risk to three folds and two alleles of APOE $\epsilon$ 4 increase the risk eight- to 12-fold risk while APOE $\epsilon$ 2 is protective compared to having two APOE $\epsilon$ 3 [28-30]. Moreover, the significant pathological alterations in vasculature were described in AD [31] and highlighted the more common presence of mixed pathology (i.e. AD and vascular pathology) [32, 33]. Needless to say, a myriad of breakthroughs has shaped AD research as a multidisciplinary field since the 80s, and new breakthroughs are still happening today more than a century after the first case of AD.

The incipient of brain imaging techniques such as computed tomography (CT), magnetic resonance imaging (MRI), and positron emission tomography (PET) prompted a new era of research using *in vivo* methodologies; the first *in vivo* evidence of hippocampal atrophy [34, 35] and reduced brain metabolism [36] was reported in the 80s, and such changes later became a signature of AD biomarker in aiding in the differential diagnosis (Figure 4) [37-40]. The *in vivo* biomarkers of AD pathological proteins were first found in CSF in the 90s [41, 42]. The signature of AD CSF biomarker profile is reduced levels of CSF A $\beta$ <sub>42</sub> and increased levels of CSF p-tau and total tau [43, 44]. Albeit early fluid analyses suffered from the lack of standardization in the methodologies, remarkable progress was made with fluid biomarkers with improved biomarker profiling using different ratios and the ability to predict cognitive decline and conversion to AD [44, 45]. In 2004, the first PET tracer, Pittsburgh Compound B ([<sup>11</sup>C]PiB),

was used to visualize and quantify the A $\beta$  plaques in living individuals, which was only possible using a post-mortem tissue before [46]. This has accelerated the exponential growth of AD and dementia research and sparked the expansion of *in vivo* biomarkers of AD. For example, [<sup>11</sup>C]PiB was used as a reference model to create subsequent generations of A $\beta$  PET tracers and is still now considered the pillar of A $\beta$  PET tracer. In the same year, resting-state functional MRI (rs-fMRI) was used to identify and show reduced connectivity within the default mode network (DMN) as an early AD biomarker [47-49]. This highlighted the convergence and divergence of different patterns in the A $\beta$  deposition, reduced DMN connectivity, cerebral hypometabolism, and atrophy in AD and galvanized the AD research once more to begin examining the disease from network perspectives. Nevertheless, a myriad of AD biomarkers has been described since the 80s. Despite its arduous and repeated process in the validation of a novel biomarker, the discovery of new biomarkers led to a deeper understanding of a complex molecular cascade of events in AD pathophysiological processes leading to cognitive impairment.

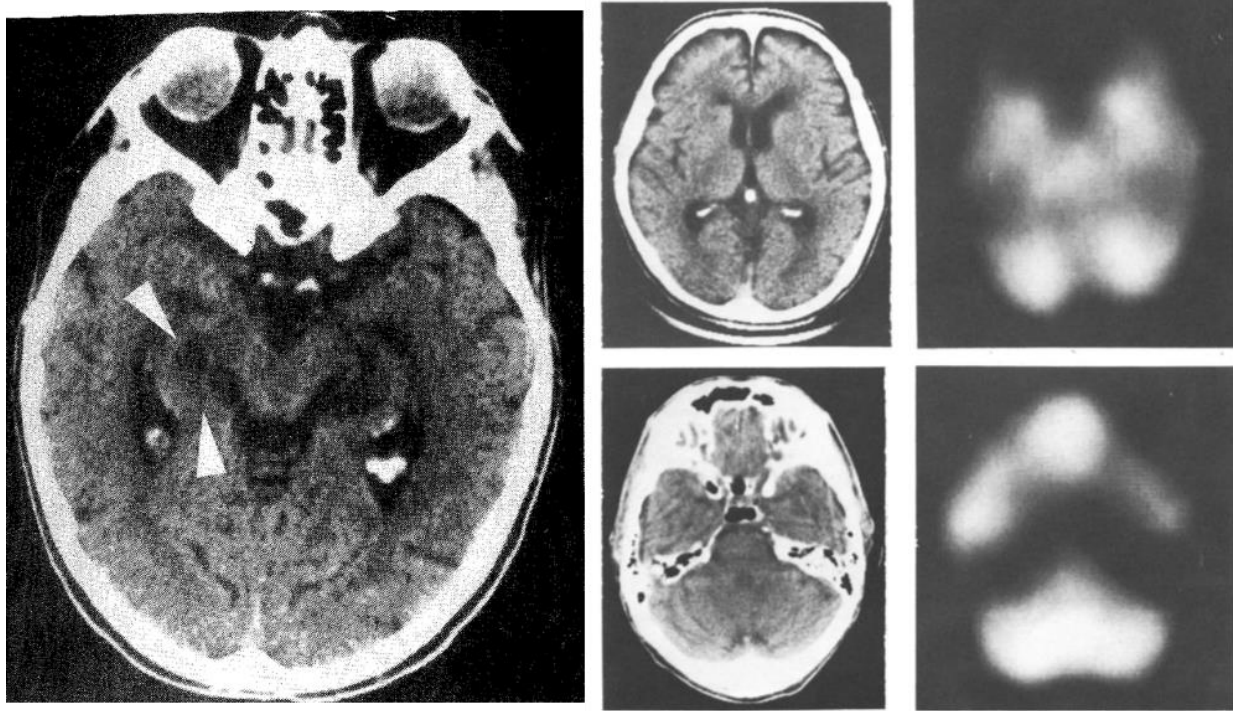


**Figure 4.** Hippocampal atrophy was depicted based on CT and PET in the 80s.

The left image is reproduced from Seab et al., 1988 [34] showing hippocampal atrophy based on CT. Right four images are reproduced from Ferris et al., 1980 [36] showing reduced hypometabolism with a reference CT image.

In 1984, the first guidelines for clinical diagnostic criteria for AD were published from the National Institute of Neurological and Communicative Disorders and Stroke (NINCDS) and Alzheimer's Disease and Related Disorders Associations (ADRDA), which is now known as Alzheimer's Association (AA) [50]. However, the first clinical diagnostic criteria of AD were relatively crude reflecting the lack of *in vivo* biomarkers and understanding of the disease. AD was described as one stage (dementia) and the diagnosis included Probably or Possible that is based only on clinical findings or Definite AD, while the Definite AD could only be supported at autopsy. In addition, no genetic causes of AD were known at the time. Due to the lack of *in vivo*

biomarkers of AD, differential diagnosis from other dementia was rather based on the exclusion criteria than inclusion criteria. For example, CT was used for exclusion purposes.

With a growing understanding of AD and biomarkers, a revised diagnostic criteria report was published in 2011 by the National Institute on Aging (NIA) and AA [51-54]. Multimodal *in vivo* biomarker-based investigations revealed distinct temporal abnormalities of different biomarkers representing various AD pathophysiology [55, 56]. For example, the hypothetical model of dynamic biomarkers of AD pathological cascade described the accumulation of A $\beta$  during a long *preclinical stage*, while the development of NFTs evolves with mild symptoms at *mild cognitive impairment (MCI) stage* just before the neurodegeneration and final *dementia stage* (Figure 5) [55]. Such temporal ordering of AD biomarkers was supported by clinical autopsy studies showing a tighter correlation between NFTs and cognitive impairment than between A $\beta$  and cognitive impairment [57, 58], but the neurodegeneration — particularly the synaptic loss — was most closely associated with cognitive impairment [59, 60]. However, it was clear that the evolution of AD pathology did not correspond to the clinical presentation. Numerous studies suggested the A $\beta$  pathology may evolve decades before the symptoms, and approximately 30% of cognitively normal elderly subjects had an abnormal level of A $\beta$  in post-mortem tissues or PET and CSF biomarkers [60-64]. Furthermore, recent characterizations of p-tau at various epitopes in CSF or plasma showed a significant increase in CN A $\beta$ <sup>+</sup> compared to CN A $\beta$ <sup>-</sup>, suggesting evidence of tauopathy even in the preclinical stage [65, 66]. As such, the distinction between the pathological vs clinical progression of AD was made. The pathological progression of AD was informed based on the biomarkers of A $\beta$ , indicative of initiating or upstream pathophysiological events, while biomarkers of neuronal injury or neurodegeneration indicate the downstream pathophysiological events that seem to be more closely linked to the

progression of clinical symptoms. The clinical progression of AD was defined as preclinical, MCI, and AD stage; the preclinical stage was based on the findings that individuals who appear to be cognitively normal but carry abnormal levels of AD pathology, particularly A $\beta$  as mentioned above; the MCI stage was established based on the realization of gradual impairments in cognitive functions before dementia; last, AD was defined as individuals who have cognitive impairment with significant interference in daily activities and a loss of autonomy. A growing number of AD biomarkers was accompanied by a wealth of knowledge in AD pathophysiology and dynamics. However, the utility of biomarkers was only complementary to the independent process of clinical diagnosis of AD based on the revised criteria [51]. While the 2011 version of diagnostic criteria was a remarkable improvement from the 1984 version, the distinction between the pathological and clinical definitions of AD led to two different entities: clinically diagnosed AD without any neuropathological evidence and AD pathologic changes.

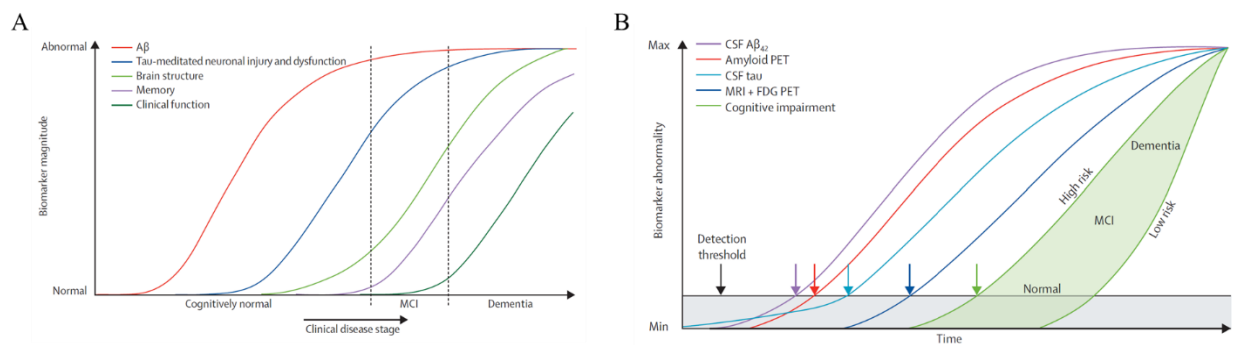


**Figure 5.** Hypothetical models of dynamic biomarkers of Alzheimer's disease pathological cascade.

A) shows the original hypothetical model of abnormal biomarkers of AD from the 2010 version. It is reproduced from Jack et al., 2010 [55]. B) shows the revised/updated hypothetical model of abnormal biomarkers of AD from the 2013 version. It is reproduced from Jack et al., 2013 [56].

#### 11.1.4 The A/T/(N) classification research framework:

Amid growing disconnection and disparity in the use of two independent definitions of AD (cognition-based clinical syndromes vs biomarker-based pathologic changes), the accumulation of data indicated a continuous progression in cognitive decline and biomarker changes in AD. This implies that AD can be conceptualized as a continuum rather than three clinically distinct entities, at least within the interventional and observational AD research. Despite the clinical utility of the three distinct categories in AD clinical progression (preclinical, MCI, and AD), a clinically defined staging cannot inform the underlying biological changes. To evaluate and discover interventions that can prevent and/or modify the course of the disease, the therapeutics must engage biologically defined targets. To this end, a biologically defined research framework of AD, the A/T/(N) classification, was introduced in 2018 to harmonize the framework across interventional and observational AD research [67, 68].

The A/T/(N) classification research framework was only possible due to the growing consensus and faithfulness of *in vivo* biomarkers as surrogate markers of biological and pathological processes in aging and AD dementia. Since 1984, tremendous efforts have been invested in validating A $\beta$  PET as a proxy of brain deposition of A $\beta$  by directly comparing the imaging and post-mortem tissues data [69, 70]. Furthermore, CSF A $\beta_{42}$  is widely accepted as a biomarker of abnormal A $\beta$  changes in the brain. This marker can be superior by using a ratio with A $\beta_{40}$  or CSF p-tau [43, 44]. Most notably, generations of different tau PET tracers, which took nearly a decade since the first A $\beta$  PET, enabled quantification and visualization of NFTs deposition longitudinally [71]. This adds CSF p-tau and tau PET as biomarkers of pathologic tau in AD [67, 72, 73]. By contrast, the neurodegeneration process that is commonly depicted by reduced hypometabolism using [ $^{18}$ F]fluorodeoxyglucose ([ $^{18}$ F]FDG) and/or structural MRI is not

specific to AD [73]. Even the classic AD signature regions have been shown to be vulnerable to neurodegeneration due to other pathologies or comorbidities rather than tau-mediated neurodegeneration [74]. Having CSF tau as part of a neuronal injury and/or neurodegeneration biomarker, the revised 2011 version would not be ideal to distinguish this [51]. As a result, the A/T/(N) classification research framework divides a list of biomarkers into pathologic markers including A for  $A\beta$ , T for tau, and (N) for neurodegeneration (Figure 6). A list of biomarkers in each biomarker group from the A/T/(N) classification in the 2018 report is summarized in Table 1. Considering (N) is not specific to AD (or you cannot separate the degree, to which the (N) biomarker changes are due to AD or other comorbidities) nor is used as a neuropathologic finding to define AD such as A/T, neurodegeneration is indicated with parenthesis.

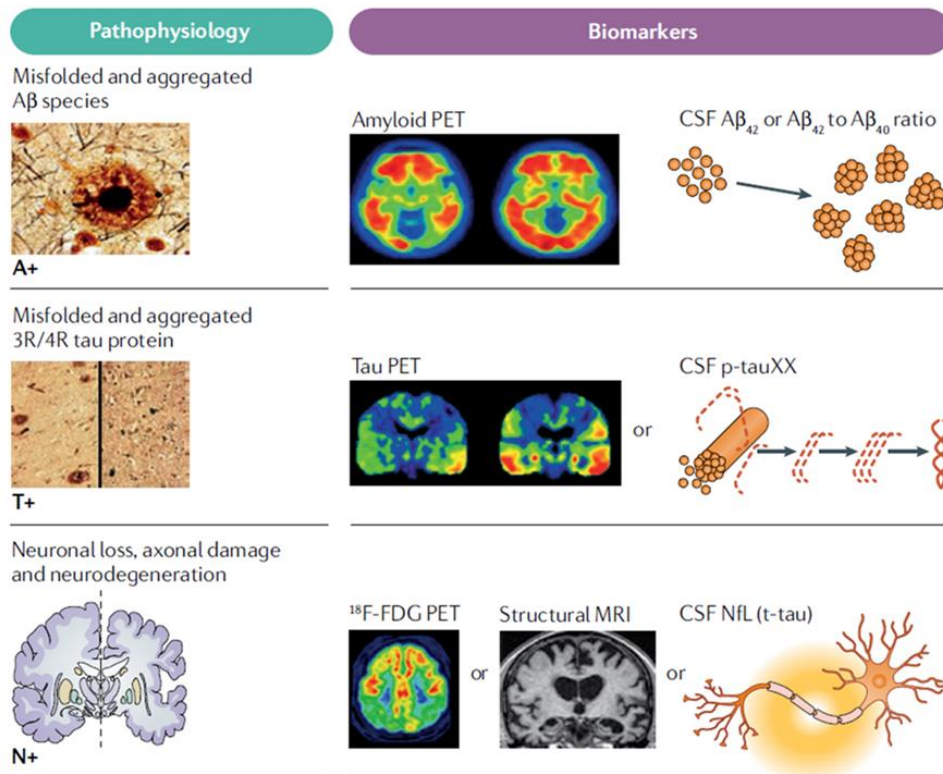


**Figure 6.** The A/T/(N) classification system.

Histopathological and *in vivo* biomarker examples of the A/T/(N) classification system. It is reproduced from Hampel et al., 2021 [68].

**Table 1.** *The A/T/(N) biomarker groupings.*

<b>A/T/(N) biomarker groups and their biomarkers</b>
A: Aggregated A $\beta$ or associated pathologic state
CSF A $\beta_{42}$ or CSF A $\beta_{42/40}$ ratio
A $\beta$ PET
T: Aggregated hyperphosphorylated tau (NFTs) or associated pathologic state
CSF p-tau
Tau PET
(N): Neuronal injury or neurodegeneration
Anatomical MRI
[ <sup>18</sup> F]FDG PET
CSF T-tau

This table is adapted from Jack et al., 2018 [67].

The A/T/(N) classification research framework is versatile; it can be applied to interventional and observational AD research. For example, the biomarker is operational here such that they can be referred to as biomarker group, biomarker profile, or biomarker category: biomarker group refers to the pathologic A $\beta$  and tau, A/T, and neuronal injury/neurodegeneration, (N); biomarker profile binarizes each of the three biomarker groups into normal or abnormal (negative or positive; -/+) to provide cutoffs in each biomarker group; biomarker category then group all the different possible combinations of biomarker profiles into three categories — A-T-(N)- is normal AD biomarkers; any combinations including A+ are AD continuum; any combinations of A- and either positivity in T or (N) or both are suspected non-Alzheimer's pathophysiology (SNAP) [75]. While biomarker profile cutoffs would enrich the screening of a clinical trial population in interventional studies, the three different biomarker categories would

provide a biological framework to investigate more heterogeneous samples in observational studies. A list of the A/T/(N) biomarker profiles and categories is summarized in Table 2.

**Table 2.** The A/T/(N) biomarker profiles and categories.

A/T/(N) biomarker profiles	A/T/(N) biomarker categories	
A-T-(N)-	Normal AD biomarker	
A+T-(N)-	Alzheimer's pathologic change	Alzheimer's continuum
A+T+(N)-	Alzheimer's disease	
A+T+(N)+	Alzheimer's disease	
A+T-(N)+	Alzheimer's and concomitant suspected non-Alzheimer's pathologic change	
A-T+(N)-	Non-Alzheimer's pathologic change	
A-T-(N)+	Non-Alzheimer's pathologic change	
A-T+(N)+	Non-Alzheimer's pathologic change	

This table is adapted from Jack et al., 2018 [67].

In addition, the A/T/(N) classification research framework is flexible. Although A $\beta$  and tau are hallmarks of AD, the real *cause* of the disease and the detailed pathophysiological steps are still unknown. As such, the A/T/(N) does not imply the order or cause of the disease but simply describes the biological definition of AD as part of the unbiased biomarker profiles.

Using this biomarker-based research framework, one can test various hypotheses of a disease model (Figure 7). In addition, it is recognized that the A/T/(N) can expand to include new biomarkers within existing groups as well as new biomarker groups. Conceptually, this framework can be discussed as A/T/X/(N) classification where X could denote other myriads of important cellular or molecular cascades of events underpinning the AD pathophysiology. If so, with sufficient evidence and validated biomarkers, this could lead to a new biomarker group, X. For example, this could be neuroinflammation or vascular pathology, which has gained more support over time as a crucial factor in AD (Figure 8). Since its publication in 2018, CSF neurofilament light chain (NFL) and CSF p-tau217 have been already added to a growing list of AD biomarkers [68].

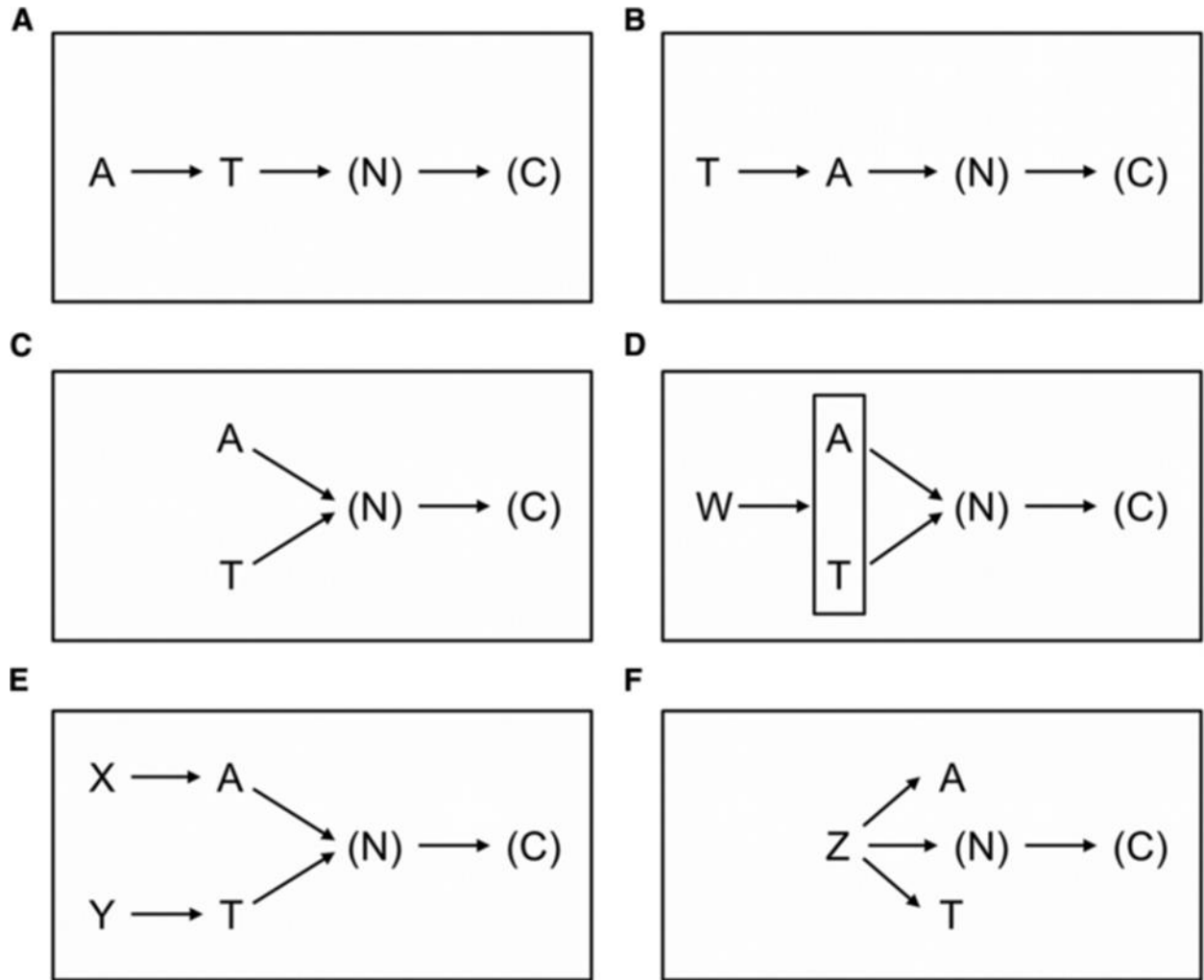


**Figure 7.** Various disease models and hypotheses to test based on in vivo biomarkers.

This is a list of various possible mechanistic pathways representing AD pathophysiology. Though the amyloid cascade hypothesis denoted in A) is most supported, several alternative models could still be true and can be tested. For example, there could be an upstream pathway denoted as W that leads to A and T or two independent upstream pathways denoted X and Y that lead to A and T, respectively. This is not a complete list of potential models but an illustration to demonstrate the alternative models can be tested using the A/T/(N) classification system. This is reproduced from Jack et al., 2018 [67].

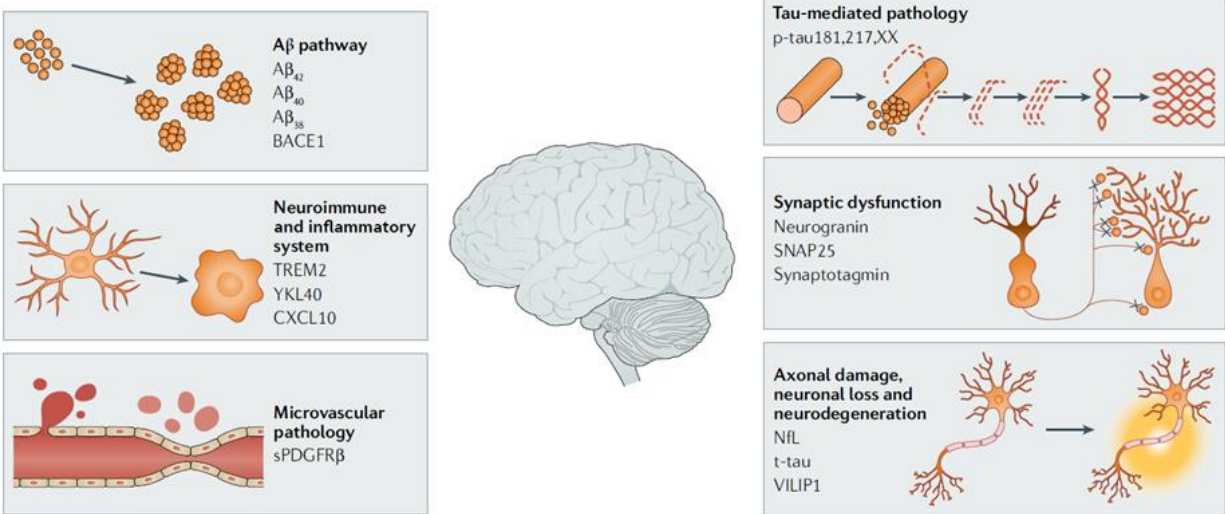


**Figure 8.** The A/T/(N) classification system is evolving.

The A/T/(N) classification system is not the complete picture of AD as it misses important aspects in AD pathophysiology such as neuroinflammation and vascular pathology. Discovery and validation of biomarkers accurately representing missing pathologic mechanisms will lead to expansion of the A/T/(N) classification system. This is reproduced from Hampel et al., 2021 [68].

Now, the *in vivo* biomarker era is here. The A/T/(N) classification system emphatically states that it is a research framework harmonizing interventional and observational AD research based on objective metrics of *in vivo* biomarkers. It is expandable for new biomarkers and applicable for new disease models. Therefore, the biomarker-based definition and research framework would create a common language and enable more accurate characterization and understanding of AD pathophysiology leading to cognitive impairment, as well as the multifactorial etiology of dementia. This will highlight new candidates for therapeutic targets and finding a cure.

## 11.2 Hypotheses

### 11.2.1 Amyloid cascade hypothesis

The Amyloid cascade hypothesis is the most dominant model of AD pathogenesis today. It posits that aggregation of A $\beta$  proteins as amyloid plaques (amyloidosis) initiates a pathological cascade of events leading to AD pathophysiology — hyperphosphorylation of tau, neurodegeneration, and subsequent cognitive impairment [76]. A multitude of disciplines in AD literature has continued to report converging evidence supporting the mechanistic pathways describing the amyloid cascade hypothesis (Figure 9) [76]. Therefore, therapeutics targeting A $\beta$  have progressed the most in AD clinical trials [77]; in June 2021, Aducanumab has been conditionally approved under the accelerated approval pathway by the FDA [3]. Although Aducanumab still needs to prove its clinical benefits, this is the first AD treatment targeting a primary aspect of underlying disease pathophysiology rather than AD symptoms alone [3].

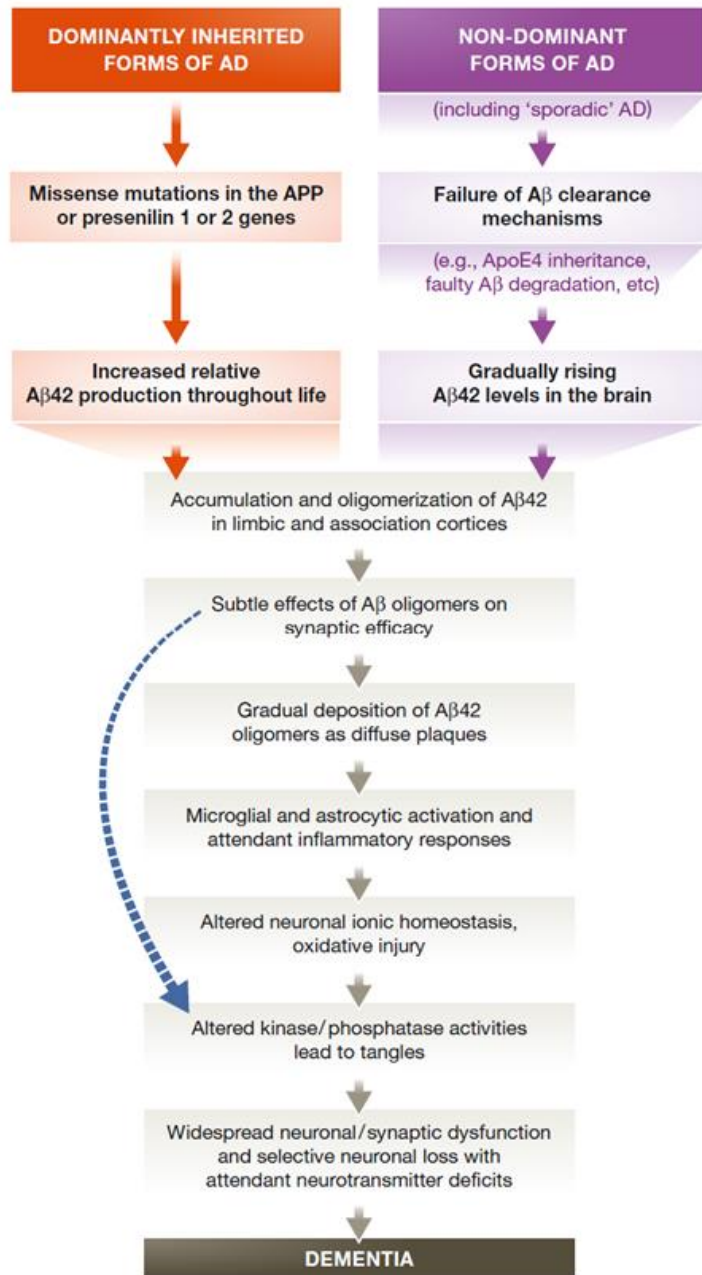


**Figure 9.** *The amyloid cascade hypothesis.*

This is a simple sequential representation of the major pathologic events and mechanisms of the amyloid cascade hypothesis. Accumulation of Aβ either by overproduction (dominantly inherited forms of AD) or failure in the clearance of Aβ (non-dominant forms of AD) leads to a subsequent cascade of pathologic events leading to AD. The blue arrow indicates that Aβ oligomers may directly insult the synapses and neurites of the neurons together with activated microglia, astrocytes, and tau oligomers.

This is reproduced from Selkoe et al., 2016 [76].

Aβ protein is produced by a proteolytic process of a transmembrane protein, amyloid precursor protein (APP), where APP can go through a non-amyloidogenic or amyloidogenic pathway (Figure 10) [78]. First, the non-amyloidogenic pathway cleaves APP protein via α-secretase, generating soluble α-APP fragment (sAPPα) and 83-amino-acid α-C-terminal

fragment, CTF $\alpha$ , (C83) [78]. Then, CTF $\alpha$  is cleaved by  $\gamma$ -secretase, producing non-toxic P3 and AICD fragments [78]. On the other hand, the amyloidogenic pathway cleaves APP protein first via  $\beta$ -secretase, also known as beta-site APP cleaving enzyme (BACE) [79], at the N-terminus, producing  $\beta$ -CTF, which is then sequentially cleaved by  $\gamma$ -secretase with 4 different subunits including Presenilin-1 (PSEN1) and Presenilin-2 (PSEN2) [78]. The final product is a monomeric A $\beta$  at various lengths producing different isoforms [78]. While normal functions of A $\beta$  are elusive and still being actively investigated, several potential roles have been suggested such as anti-microbial activity, functioning as a transcription factor, activation of kinase enzymes, and more [80-82].

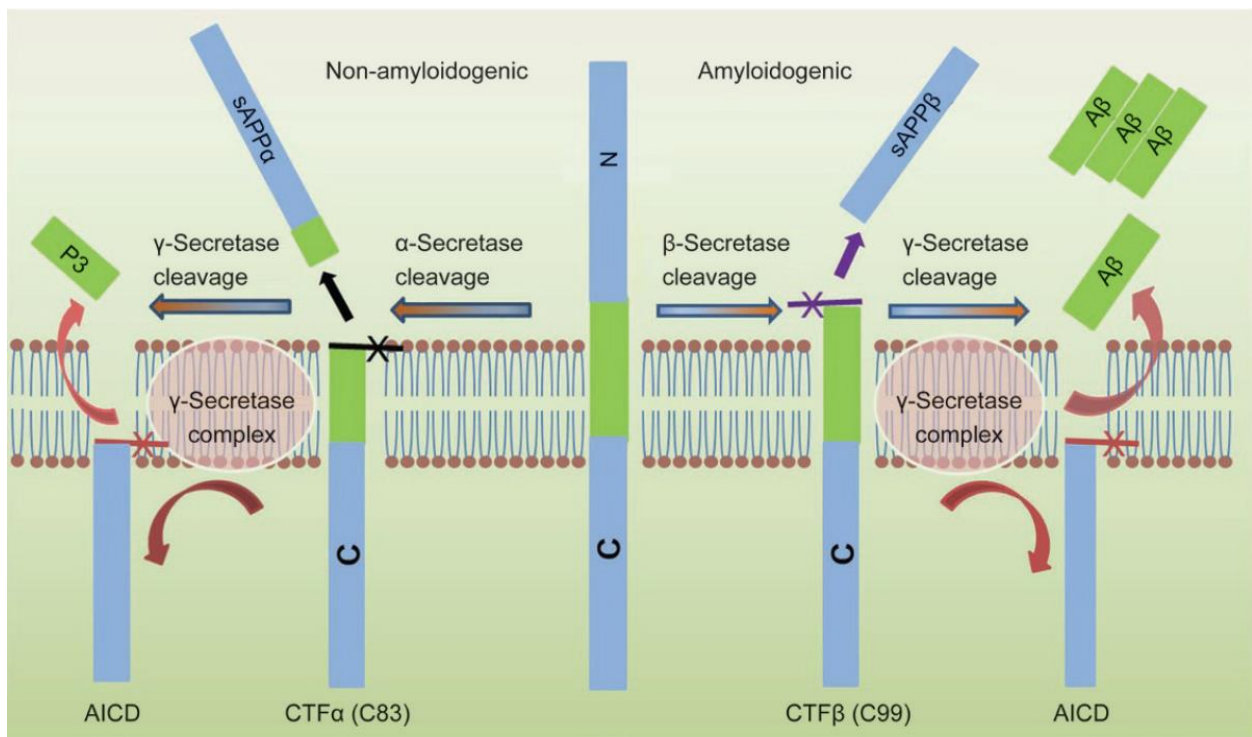


**Figure 10.** Human APP proteolytic pathways.

This is a schematic representation of different APP proteolytic pathways. The left side shows the non-amyloidogenic pathway via  $\alpha$ - and  $\gamma$ -secretase. The right side shows the amyloidogenic pathway via  $\beta$ - and  $\gamma$ -secretase. This is reproduced from Chen et al., 2017 [78].

Amongst the various isoforms of A $\beta$ , A $\beta_{42}$  is the most potent to aggregate due to its hydrophobic nature, while A $\beta_{40}$  is a more soluble variant [83]. In AD, increased concentrations of A $\beta$  peptides (due to increased production and/or decreased clearance) effectively lead to dimerization of A $\beta$  and subsequent generation of soluble oligomers, insoluble fibrils, and amyloid plaques (Figure 11) [78]. Together, A $\beta_{42}$  and A $\beta_{40}$  are the main constituents of the key characteristic of AD amyloid plaques. Being the hallmark of AD since the early days of AD research, the extracellular amyloid plaques were first considered to be the toxic culprit of AD pathophysiology. This notion quickly became a counterargument for the amyloid cascade hypothesis due to the frequent observation of amyloid plaques in ostensibly normal subjects [60, 62]. However, emerging evidence supports soluble oligomers to be the most toxic form of A $\beta$  and the importance of the relative amount of A $\beta$  species [76, 78]. By quantifying A $\beta$  oligomers using a selective biochemical assay in post-mortem brain tissues of individuals who were either non-demented or mildly demented based on Clinical Dementia Rating (CDR) with similar amyloid plaque densities, the non-demented (CDR 0) tissues showed substantially lower oligomer-to-plaque ratios than mildly demented subjects (CDR 1) [84]. It is now believed that there is a complex dynamic equilibrium reached among the different species of A $\beta$  pools: diffuse and compacted plaques form exchanging oligomers between the rest of A $\beta$  species and binding pockets in the plaques [76].

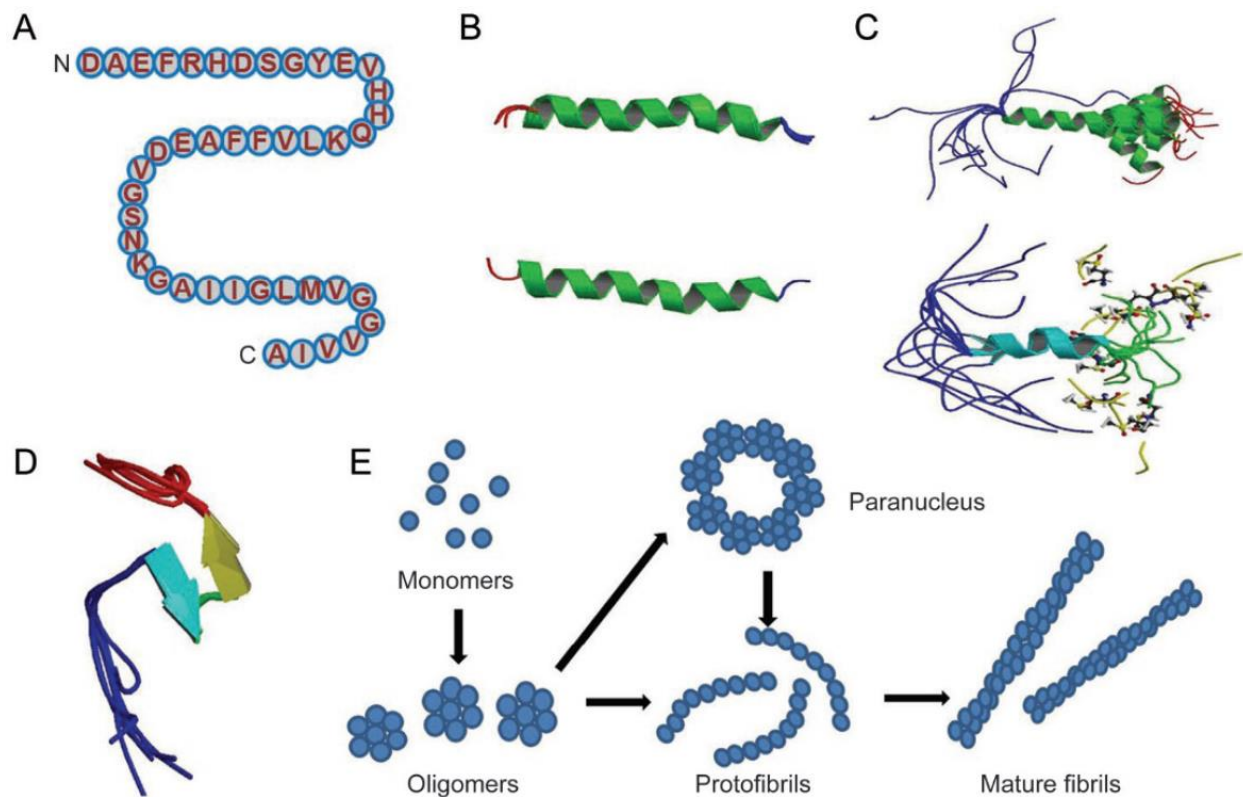


**Figure 11.** Structures and different species of Aβ.

A) shows 42 amino acid sequences of the Aβ<sub>42</sub> isoform. B) The structure of Aβ peptide (1-28), which forms predominantly an alpha-helical structure that can be converted to a beta-sheet structure. C) Solution structure of Aβ peptide (1-40). D) Aβ peptide (10-35) forms a collapse coil structure. E) Proposed sequence of Aβ monomers to higher-order oligomers, protofibrils and fibrils. This is reproduced from Chen et al., 2017 [78].

Numerous AD research studies have revealed various pathophysiological cascades of events caused by Aβ. Amongst pathological molecular interactions, notable Aβ effects include but are not limited to the disruption of long-term potentiation (LTP) and/or long-term depression (LTD) processes that are key for memory, aberrant neuronal hyper-activities, dysregulation of neurotransmitters, particularly glutamate leading to cytotoxicity (Figure 12) [78, 85]. Moreover, Aβ can elicit a cascade of neuroinflammatory reactions leading to hyperphosphorylation of tau and activation of microglia and astrocytes (Figure 12) [78, 86]. At normal physiology, activated

microglia degrade and clear A $\beta$  from the Central Nervous System (CNS) [87]. However, prolonged activation of microglia leads to a pathologic milieu, in which activated microglia are more associated with a pro-inflammatory state fueling the positive feedback to worsen the pathologic cascades of A $\beta$  [76, 87, 88]. As a result, increased p-tau starts to aggregate into NFTs, the AD hallmark that is thought to exert greater effects on neurodegeneration than A $\beta$ , and activated microglia and astrocyte transform into rather toxic phenotypes aiding in widespread neurodegeneration processes and subsequent cognitive impairment [73, 76, 87, 88].

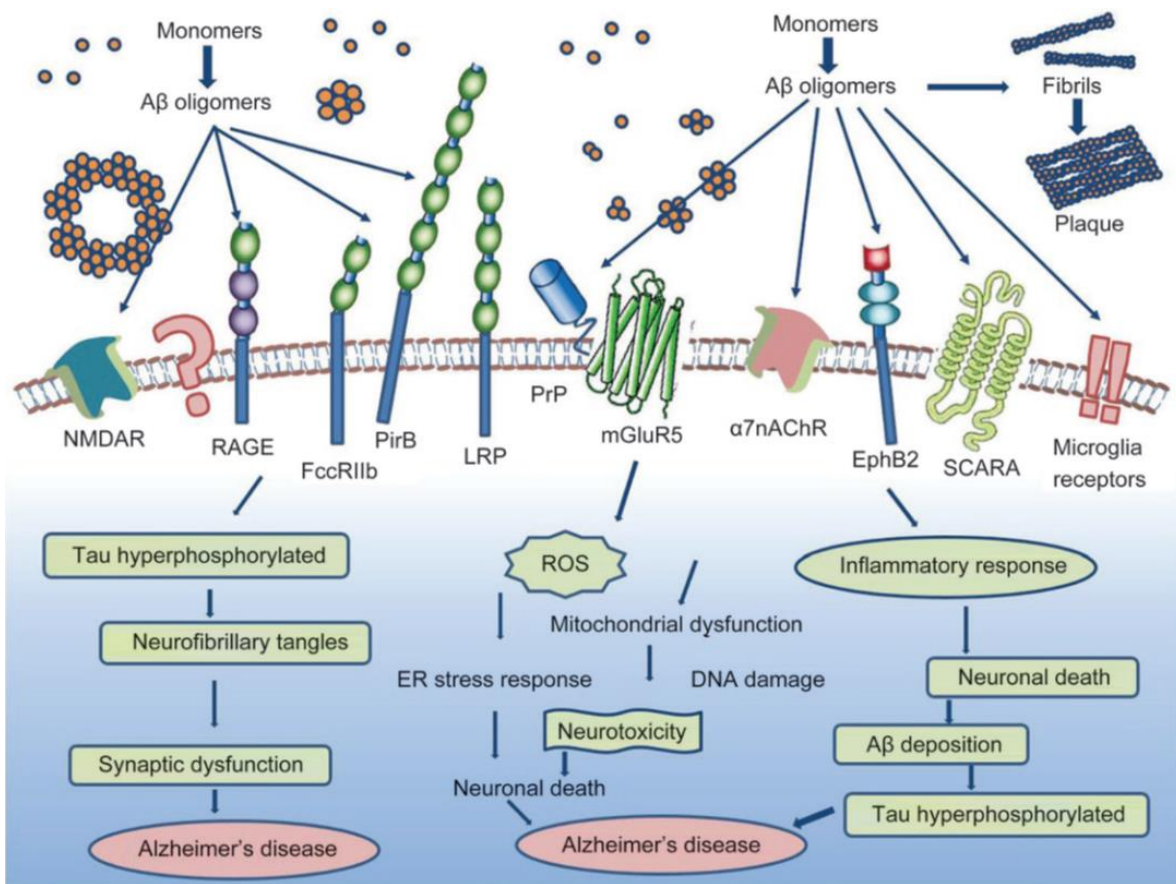


**Figure 12.** Biological effects of A $\beta$ .

This is an animated depiction of the A $\beta$  interaction on various cell surface receptors. This is not a complete list of the biological effects of A $\beta$ . This is reproduced from Chen et al., 2017 [78].

Although the complete mechanisms of all molecular pathways from A $\beta$  as the origin to AD dementia are yet to be elucidated, continuous research in AD is surely filling the missing knowledge gaps and supports the amyloid cascade hypothesis. In addition, the strongest evidence that started the hypothesis is the discovery of genetic mutations, which are involved in APP processing machinery and deterministic for AD dementia. For example, the discovery of the APP gene on chromosome 21 provided insights to individuals with Down's Syndrome, a genetic disorder with trisomy (three copies of chromosome 21), who typically develop AD neuropathology [14]. Identifying causative mutations (APP, PSEN1, and PSEN2) leading to familial AD and generating transgenic animals that recapitulate AD-like A $\beta$  pathology by inserting the same mutations testify the direct evidence of the central role of A $\beta$  in AD pathogenesis [22, 89]. However, AD cases due to these mutations account for less than 1% and about 13% of early-onset AD cases that are defined to show symptoms before age 65 [90]. While the causes of the majority of early-onset AD cases (that are not familial AD cases) are still unknown, AD research has started to identify other genetic risk factors that significantly increase the likelihood of AD, such as the APOE $\epsilon$ 4 allele [28]. On the other hand, most of the AD cases are late-onset sporadic cases that are defined by lack of familial mutations and symptom-onset after age 65 [1]. Still, the crux of the amyloid hypothesis lies in the increased amount of A $\beta$ . As such, understanding the differences between early-onset and late-onset AD and characterizing both as AD entity is an active research field; late-onset sporadic AD cases are thought to depend on reduced A $\beta$  clearance meanwhile familial early-onset AD cases are thought to have A $\beta$  overproduction to trigger A $\beta$  accumulation. This will be an important consideration in defining the AD therapeutic target cohort.

## 11.2.2 Tau hypothesis

p-tau is another hallmark of AD. Despite the lack of deterministic genetic evidence linking mutation in tau and AD, the tau hypothesis has gained significant support juxtaposing the amyloid cascade hypothesis as another potential etiology of AD.

Tau proteins arise from the microtubule-associated protein tau (MAPT) gene in human brains [91]. There are several important functions related to tau proteins. One of the important functions of tau is to stabilize microtubules in the axon and regulate microtubule-mediated axonal transport [92, 93]. However, pathologic tau is generated from increased hyperphosphorylation induced by abnormal kinase activities such as glycogen synthase kinase 3 $\beta$  (GSK3 $\beta$ ) during the post-translational modification step. Importantly, p-tau can self-assemble to NFTs of paired helical filament and straight filaments, which are involved in the pathogenesis of AD, Frontotemporal dementia (FTD), and other tauopathies [94]. Intraneuronal accumulation of p-tau and tau oligomers is thought to cause toxic effects leading to cell death and cognitive decline (Figure 13) [95-97].

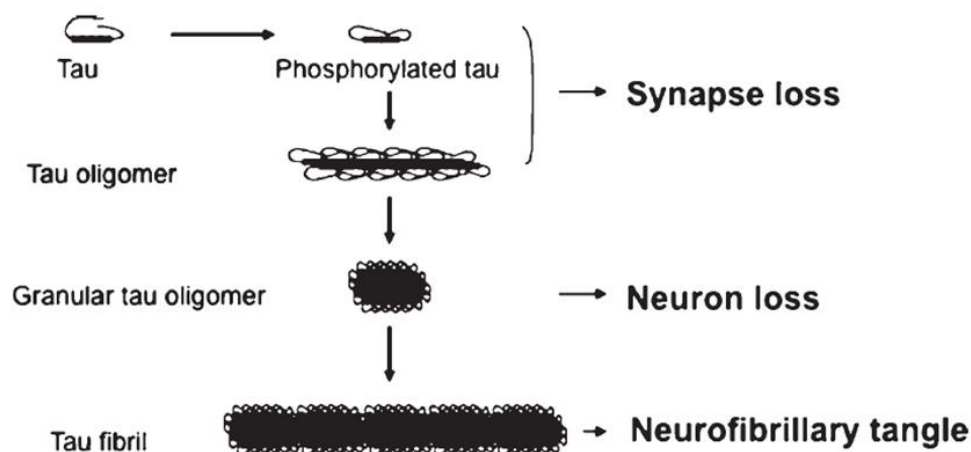


**Figure 13.** Formation of aggregates of p-tau oligomers and NFTs.

This is reproduced from Takashima, 2013 [97].

With alternative splicing, tau is produced into 6 different isoforms that can be divided into three or four repeat-regions (3R or 4R) at the C-terminal part [98]. AD NFTs are characterized by a mixture of both 3R and 4R tau isoforms with a greater portion of paired helical filaments [94, 98]. On the other hand, Pick's disease consists of 3R tau isoform with twisted filaments while Corticobasal degeneration (CBD) and Progressive Supranuclear palsy (PSP) consist of 4R tau isoform with straight filaments in general [94, 98]. This exemplifies the complexity in different tauopathies; as they are heterogeneous in their NFTs constituents, they also display heterogeneous phenotypes and spreading patterns in the brain [99]. This is an important consideration when choosing a PET tracer; different tau PET tracers seem to detect different tauopathies that depend on the isoforms. For example, [<sup>18</sup>F]AV1451 and [<sup>18</sup>F]MK6240 are two popular tau PET tracers that show a similar distribution in AD despite their differences in their tracer kinetics and off-target binding [94, 100]. When investigating other tauopathies, [<sup>18</sup>F]MK6240 does not bind to non-AD tauopathies, but [<sup>11</sup>C]PBB3 shows specific retention of 4R CBD and PSP as well as 3R Pick's disease (Figure 14) [100, 101].

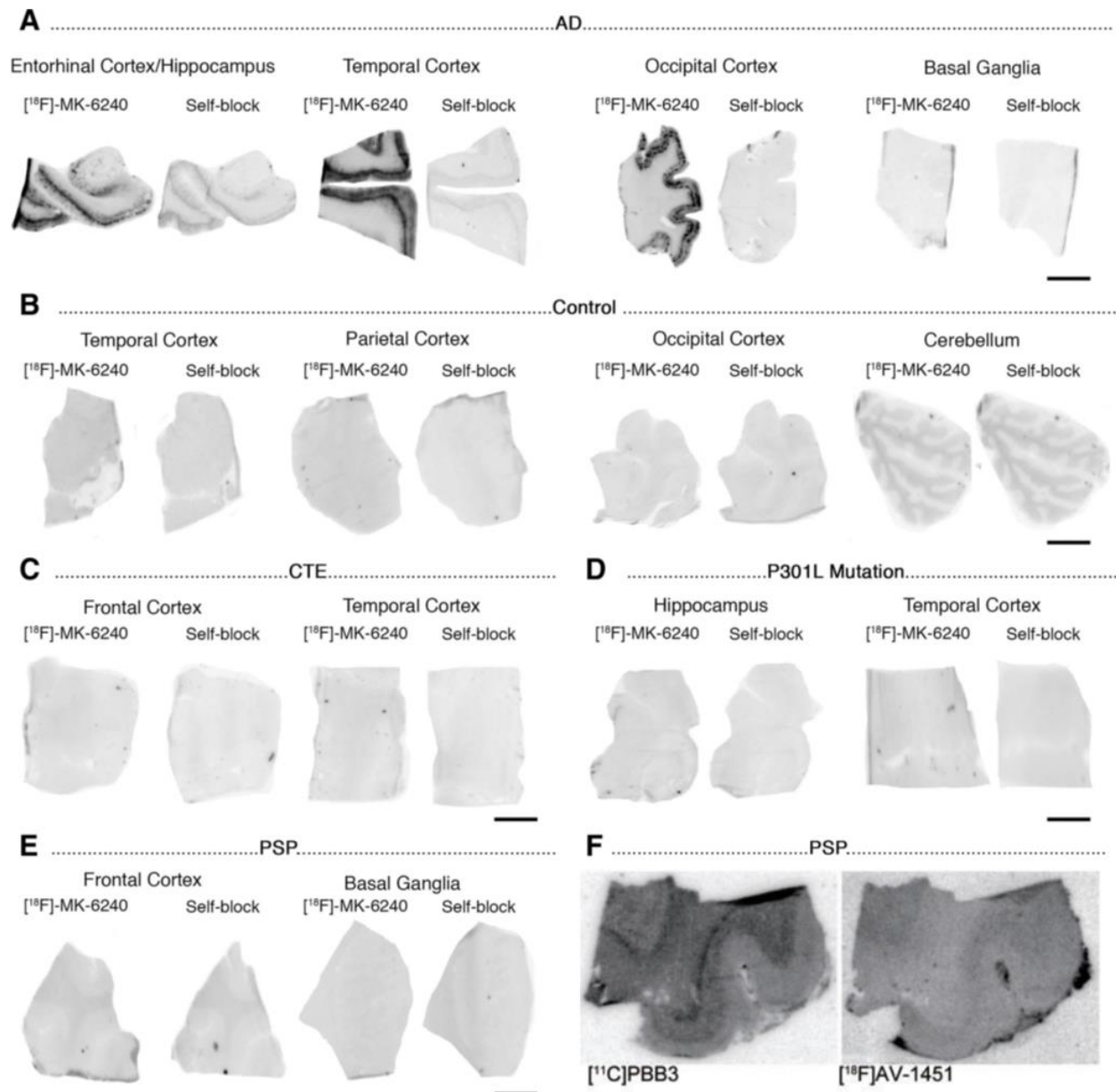


**Figure 14.** Different binding distributions of tau PET tracers in various tauopathies.

A-E) show [<sup>18</sup>F]MK6240 binding distribution in various conditions but only show significant retention in the AD tissues. F) shows a significant binding of [<sup>11</sup>C]PBB3 to PSP tissue while relatively sparse binding with [<sup>18</sup>F]AV1451. A-E) were reproduced from Agüero et al., 2019 [100] and F) was reproduced from Ono et al., 2017 [101].

While there are atypical phenotypes observed in AD (atypical AD) that seem to also depend on the heterogeneous molecular diversity in tau and tau distribution, it is believed that typical AD generally shows a stereotypical but hierarchical pattern of tau spreading called Braak staging (Figure 15) [23, 24, 102, 103]. Based on histopathological data, the earliest site of NFT deposition is observed in the transentorhinal region as Stage 1. Then, the tau tangles would *spread* to the entorhinal cortex sometimes including the hippocampus as Stage 2. Though the first two stages are limited to the focal medial temporal regions, subsequent Braak Stage 3 and Stage 4 extend over the limbic regions to include the higher-order association cortex in temporal regions. Finally, Braak Stage 5 and 6 show a significant spreading of NFT in the neocortex. With the advent of tau PET tracers, *in vivo* longitudinal validation of Braak Stages is on its way. However, conflicting findings that do not necessarily follow the Braak stages have been reported recently even though the initial publications have reported tau PET to follow the Braak stages [104-106].

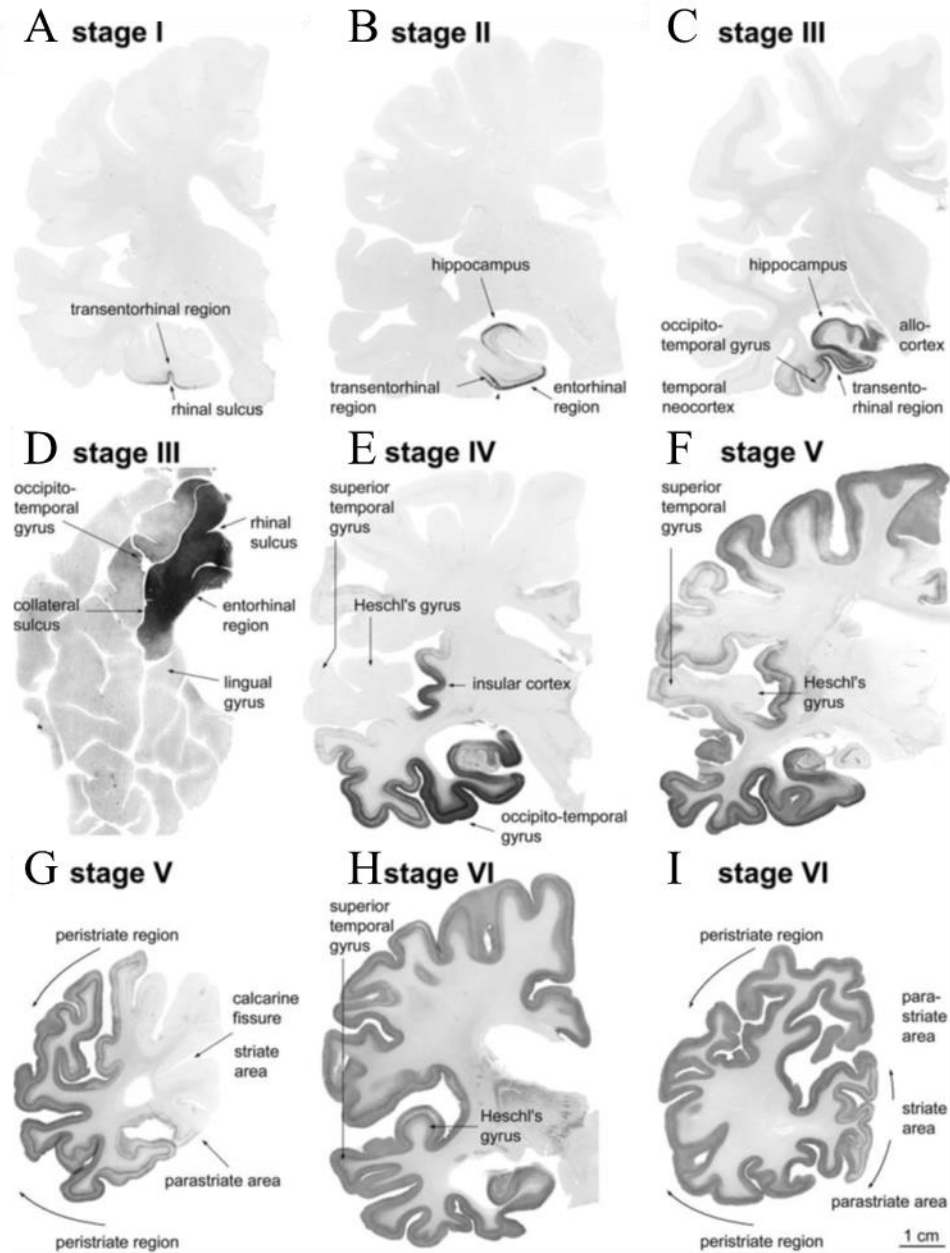


**Figure 15.** The six Braak Stages.

Histopathological staining and spreading of NFTs defining the Braak Staging. This is reproduced from Braak et al., 2006 [24].

From the observation of hierarchical spreading of NFTs, it is hypothesized that tau pathology spread along connected neurons (trans-synaptically) [107]. This is supported by compelling evidence in numerous animal studies that have demonstrated the intracranial

injections of pathological tau act as a seed and lead to widespread in the pathological tau aggregates in anatomically connected regions distant from the injection site (Figure 16) [107, 108]. Furthermore, the development of technologies in imaging biomarkers has enabled an investigation of this hypothesis using computational modelling. Surprisingly, while imaging studies support the trans-synaptic spreading model of tau, the imaging data also suggest functionally connected regions may play a significant role in tau propagation [109, 110]. This suggests there could be other important factors that also contribute significantly to tau propagation such as activated microglia [111]. Uncovering the underlying mechanisms, in which tau spread from one region to another, could highlight potential therapeutic targets for AD.

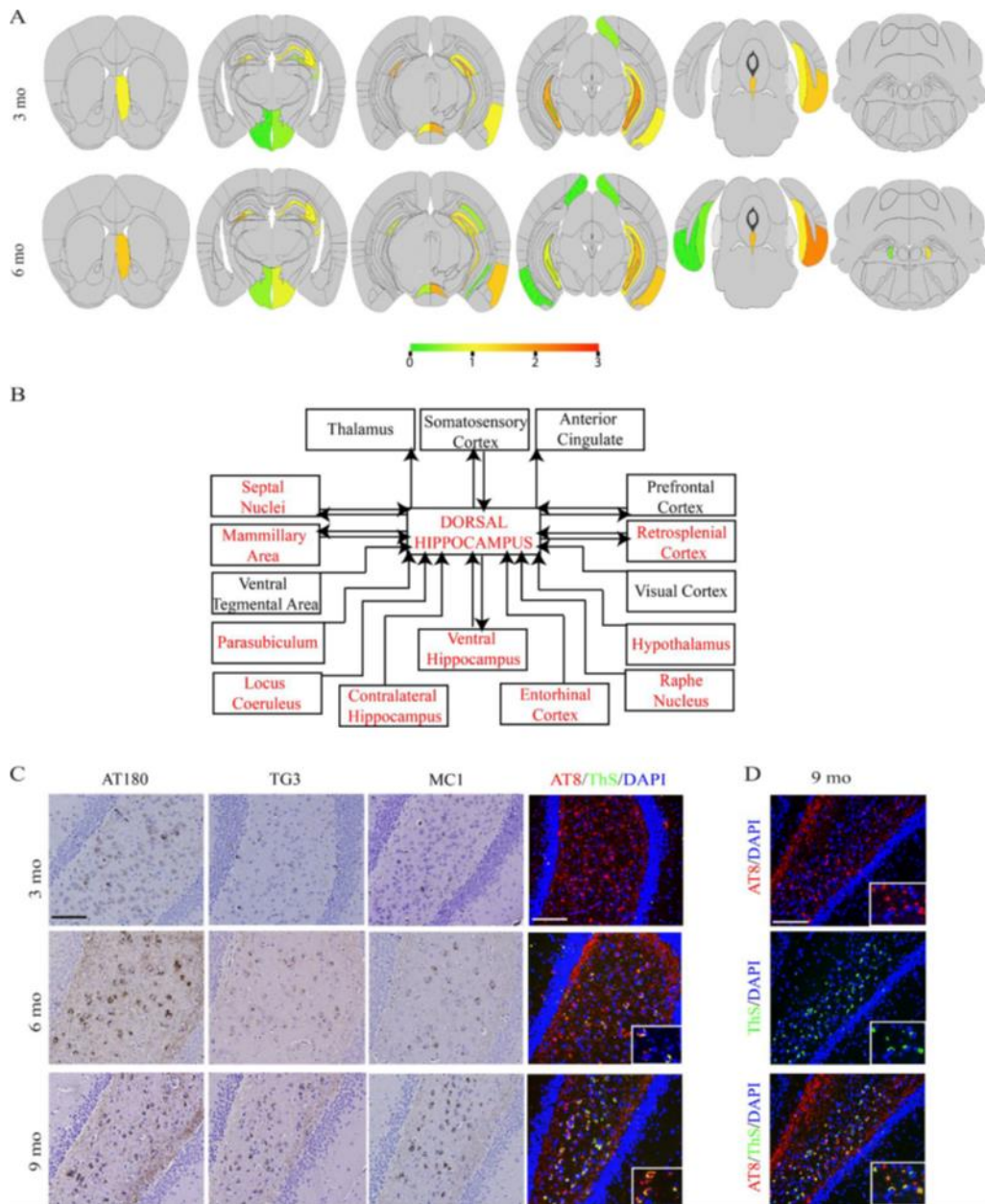


**Figure 16.** Evidence of trans-synaptic propagation of tau induced by AD-tau in non-Tg mice.

A) shows the semi quantification of pathologic tau using AT8 staining in non-Tg mouse brain following intracerebral injection of AD-tau. B) shows the connections from the Dorsal hippocampus as the primary site of injection. C) and D) show the various staining to represent maturing of tau pathology from pretangles to mature  $\beta$ -sheet rich aggregates over time. This is reproduced from Guo et al., 2016 [108].

It is well established that tau pathology is more strongly associated with neurodegeneration and cognitive impairment relative to A $\beta$  pathology in AD [60, 73]. The sequence of pathological events suggested based on the hypothetical modelling of abnormal biomarker changes in AD places tau pathology in between A $\beta$  pathology and neurodegeneration [56]. While this may fit with the amyloid cascade hypothesis, the earliest point to observe pathological tau causing AD is still very elusive. Several observational studies of post-mortem tissues suggest that the evidence of tau aggregates can be found even as early as childhood [112]. Though this may indicate that tau pathology could occur before A $\beta$  pathology, whether such earliest tau observation leads to AD is yet to be demonstrated. Despite this debate, the tau hypothesis posits that tau itself can be the initiating factor for sporadic AD [112]. Hyperphosphorylation of tau, initiated by head trauma or calcium imbalance through the aging process, could create an endosomal “traffic jam” that may lead to increased A $\beta$  production creating a vicious cycle between tau and A $\beta$  (Figure 17) [112].

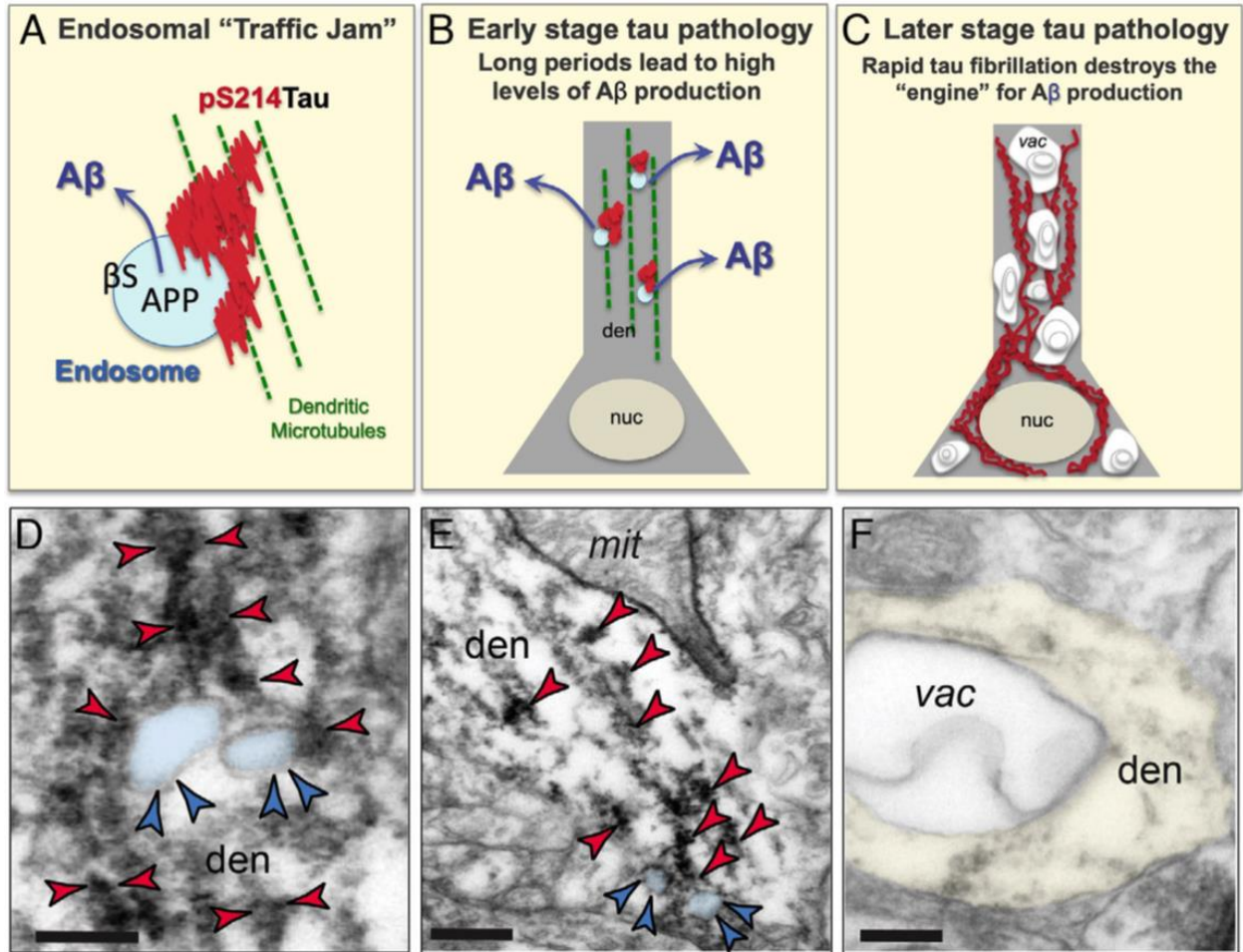


**Figure 17.** Endosomal “traffic jam” could lead to  $A\beta$  production.

A) is a schematic representation of an endosomal “traffic jam” showing an endosome containing APP and  $\beta$ -secretase trapped in aggregated pS214tau. B) is showing an early event in tauopathy where aggregated tau (red) traps the endosomes containing  $A\beta$  on the microtubule (green). C) represents late-stage tauopathy where the accumulation of fibrillar tau aggregates leads to the deterioration of neuronal organelles. The real-life examples for A-C) are represented in D-F), respectively. This is reproduced from Arnsten et al., 2021 [112].

### 11.2.3 (Neuro)Inflammation hypothesis

Inflammation or neuroinflammation (inflammation in the nervous system) is a complex and dynamic system where arrays of different cellular and molecular compartments orchestrate together to defend the host from any debris or pathogens. Some cellular components of neuroinflammation also play important roles in maintaining normal physiology in the brain such as synaptic plasticity, neurogenesis, and regulation of ions [113-117]. Unlike A $\beta$  or tau where they are defined as a family of peptides, the host defence mechanisms are diverse and walk a fine line between protection and toxic insult (Figure 18) [118]. As such, it has been challenging to find one specific therapeutic target within the neuroinflammatory system for AD clinical trials. Still, neuroinflammation is recognized to play essential roles in AD pathogenesis and promising therapeutic targets within the neuroinflammation hypothesis are discussed below.

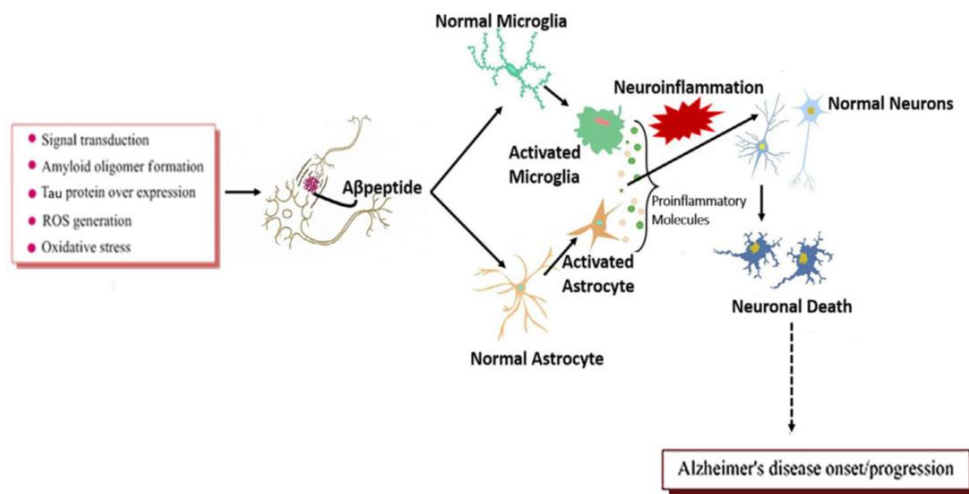


**Figure 18.** The effects of reactive gliosis in Alzheimer's disease pathophysiology.

This is reproduced from Ahmad et al., 2010 [118].

Reactive gliosis is one of the most notable neuroinflammatory features in AD since the early days. Histological studies have consistently shown that activated microglia and reactive astrocytes surround the core pathological hallmarks of AD, amyloid plaques and tau tangles [87, 119]. Recently emerging evidence in genetic and animal studies has underscored the central roles of activated microglia and reactive astrocytes again in AD risk and pathogenesis. First, microglia cells, the main immune defence line in CNS, patrol the brain for any pathogens, debris, or toxic insults [87]. In normal physiological conditions, microglia exhibit a resting phenotype and play a role in synaptogenesis, neurogenesis, and release of neurotrophic factors [88, 120-122]. However, when the homeostasis of the microenvironment is disturbed due to an injury or pathological aggregate, microglial cells shift into active phenotypes secreting pro-inflammatory cytokines, chemokines, and reactive oxidants [88, 120]. Therefore, activated microglia are sometimes described as a “dual-edge sword”, and abundant evidence is reported in the AD literature. For example, histopathological staining has captured activated microglia clearing A $\beta$  and tau in the brain supporting the protective effects [123-125]. Moreover, the triggering receptor expressed on myeloid cells 2 (TREM2), an immunoreceptor that is primarily expressed on microglia, has been identified to promote microglial survival and sustain the microglial response to A $\beta$  while APOE can interact with TREM2 to modulate microglial functions [126-128]. On the other hand, numerous genetic studies including genome-wide association studies (GWAS) have recently identified several AD risk loci to be on microglia [129-131], and various signatures of microglia related to AD have been suggested — disease-associated microglia (DAM), human Alzheimer’s microglia (HAM), or proportion of morphologically activated microglia (PAM) (Figure 19) [132-136]. In addition, a series of transgenic animal studies have demonstrated activated microglia drive tau pathology and neurodegeneration [111].

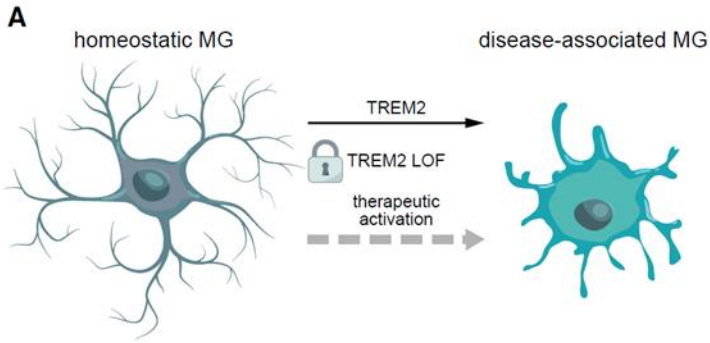


**Figure 19. Disease-associated Microglia.**

A) Homeostatic microglia surveil the environment. Upon a pathologic stimulus, a TREM2-dependent activation is induced, which switches the microglia to a disease-associated microglial phenotype. B) Loss of function (LOF) of TREM2 affects the essential signaling pathways and worsens the disease pathology. This is reproduced from Lewcock et al., 2020 [136].

**B**

	ACTIVITY	TREM2 KO/ LOF
PATHWAY BIOLOGY	pSYK	↓
	mTOR signaling	↓
	DAM transcriptional profile	↓
	microglia survival/ proliferation	↓
	lipid accumulation	↑
DISEASE BIOLOGY	Nf-L	↑
	TSPO-PET	↓
	FDG-PET	↓
	amyloid plaque pathology:	
	plaque load	variable
	clustering around plaques	↓
	barrier function	↓
	amyloid plaque seeding	↑
	diffuse plaque morphology	↑
	neuritic pathology	↑
	tau	variable

Astrocytes, the most abundant cell type in the CNS, have a similar story. While astrocytes have a multitude of important physiological functions, this cell type also reacts to A $\beta$  and tau. In cell culture, astrocytes have demonstrated the ability to travel towards A $\beta$  and degrade it [137]. The reactive process of gliosis will lead to releasing cytokines and chemokines and recruit more microglia and astrocytes and instigate more immune responses [138, 139]. However, chronic exposure to this process will lead to an overload of pro-inflammatory processes, which can trigger oxidative stress and neuronal death [118]. Notably, reactive astrocytes and activated microglia can be often found together [140]. However, their complex

relationship that depends on the vast array of different cytokines is evident: activated microglia induce reactive astrocytes A1, which show loss of neuronal survival and synaptogenesis while inducing cell death, by releasing IL-1 $\alpha$ , Tumor necrosis factor (TNF), and C1q cytokines [141]; the release of IL-3 from astrocytes, however, is able to program microglia to reduce AD pathology and cognitive decline [142].

Considering the diverse inflammatory processes that are linked to AD pathophysiology, various clinical trials targeting different aspects of inflammatory mechanisms have been tested but did not show significant benefits [77, 143]. Yet, “resilient” brains have been recently described as individuals who have rich AD pathology but uniquely avert dementia, most likely owing to suppressed neuroinflammatory process [144, 145]. Importantly, continuous growth in the understanding of inflammatory mechanisms will facilitate the discovery of more effective therapeutic targets. As exemplified based on more recent insights discussed above, a few potential therapeutic targets such as TREM2 and APOE are actively pursued in clinical trial studies [143].

While there are different notions of how neuroinflammation initiates AD pathogenesis as the disease etiology, the innate immune protection hypothesis postulates a new framework, in which the hallmarks of AD — A $\beta$  and p-tau — may have evolved as neuroprotection against a pathogen [146, 147]. Having anti-microbial effects, A $\beta$  and tau may be produced as a byproduct of the innate response to pathogenic infection in the brain to sequester and protect against the pathogen [80, 148]. Congruently, autopsy studies have shown a significant correlation between herpesviruses and amyloid plaques [149, 150]. The innate immune response against a pathogen could inadvertently lead to the accumulation of A $\beta$ , tau, and neurotoxic inflammatory response as the individual life expectancy is improved with the reduced number of deaths due to infection.

As such, A $\beta$ , tau, and even AD gene mutations may have been conserved throughout evolution as a protection against a pathogen. Therefore, if true, the innate immune protection hypothesis suggests a new model that could revolutionize the concept of AD again.

### 11.3 AD (pre)clinical trials so far

There have been enormous global efforts in the search for an effective therapy for AD. More than 2000 clinical trials have been conducted so far until 2019, and there are 126 agents currently being tested at different phases of AD clinical trials [77, 143]. From currently registered trials, more than 38,000 participants are required, and the estimated total costs for an AD drug development program are at \$5.6 billion, and the process can take 13 years from preclinical studies to approval by FDA [151]. Currently, seven drugs are approved by FDA for treating AD, of which Aducanumab is the only drug that targets the underlying biology to modify the disease progression, and hopefully, improve cognition and function in daily living (Table 3) [152]. All other drugs simply treat the symptoms by regulating the imbalance of certain neurotransmitters such as glutamate and acetylcholine (Table 3) [152]. After more than a century of research and global efforts, Aducanumab, the first of its kind to target the underlying pathologic target, has been conditionally and controversially approved only in June 2021 [3, 153, 154]. Yet, Aducanumab still needs to prove its clinical benefits.

*Table 3. A list of FDA-approved drugs for AD.*

Name (Generic/Brand)	Mechanism of action	Approved for	Side-effects
Aducanumab/Aduhelm	Pathologic A $\beta$	MCI to mild AD	ARIA, headache, and fall.
Donepezil/Aricept	Cognitive Symptoms	Mild to severe AD	Nausea, vomiting, loss of

			appetite, and increased frequency of bowel movements.
Galantamine/Razadyne	Cognitive Symptoms	Mild to severe AD	Nausea, vomiting, loss of appetite, and increased frequency of bowel movements.
Rivastigmine/Exelon	Cognitive Symptoms	Mild to severe AD or Parkinson's disease	Nausea, vomiting, loss of appetite, and increased frequency of bowel movements.
Memantine/Namenda	Cognitive Symptoms	Moderate to severe AD	Headache, constipation, confusion, and dizziness.
Memantine + Donepezil/Namzaric	Cognitive Symptoms	Moderate to severe AD	Nausea, vomiting, loss of appetite, increased frequency of bowel movements, headache, constipation, confusion, and dizziness.
Suvorexant/Belsomra	Non-cognitive Symptoms	Insomnia in people living with mild to moderate AD	Impaired alertness and motor coordination, worsening of depression or suicidal thinking, complex sleep behaviours, sleep paralysis, compromised respiratory function.

While there are numerous interesting and promising clinical trials currently ongoing, the list to review within this Ph.D. thesis is too extensive and out of scope. Akin to the above hypothesis section, this section will review and discuss the most relevant clinical trials to this Ph.D. thesis with the emphasis on the evolution of biomarker-based clinical trial study design and how the biomarker-based A/T/(N) classification research framework would be an effective strategy.

Albeit the utility of the A/T/(N) classification research framework in the clinical diagnosis of AD is still premature, the impact of the biomarker-based framework on AD clinical trials has been positive already. The most exemplary trials are the anti-amyloid immunotherapy trials. Since the first report of successful immunotherapy targeting A $\beta$  in the animal models, A $\beta$  targeted clinical trials have been conducted the most so far [77]. However, none of the anti-amyloid immunotherapy has demonstrated a statistically significant outcome on its pre-specified clinical trial endpoints [153]; even though the Aducanumab phase 3 study (EMERGE) suggested meeting the primary pre-specified clinical trial endpoint, their independent phase 3 study, ENGAGE, did not [154]. Collectively, many experts in the field did not consider that the Aducanumab met the primary endpoint. Yet, the conditional approval by the FDA on rather uncertain results caused unprecedented controversy in the regulatory decision-making.

Despite the debate, the biomarker-based study design employed by the Aducanumab studies deserves praise. The Aducanumab phase 1b clinical trial, the PRIME study, was the first study to screen the participants for the presence of an abnormal amount of A $\beta$  using A $\beta$  PET [76, 154]. Previous anti-amyloid immunotherapy studies did not screen for the presence of the very target that the drug was intended to remove; it was later revealed that a considerable study sample was amyloid-negative (30%) [76, 153]. Effectively, this would reduce the power of the

study design to evaluate the therapeutic target engagement and efficacy of the entire study. Since the PRIME study, the Aducanumab target engagement, efficacy, and safety were evaluated longitudinally based on *in vivo* biomarkers [155]. The A $\beta$  PET was used to show the direct target engagement and effect size of the A $\beta$  removal by the Aducanumab meanwhile tau and neurodegenerative biomarkers such as tau PET and CSF T-tau and p-tau were used to assess the Aducanumab efficacy [154, 155]. In the EMERGE study, removing A $\beta$  led to a significant improvement in tau pathology indicated by reduced tau PET and CSF p-tau, and there was a trend in reduced CSF T-tau [154]. This analysis was exploratory due to a low number of subjects, but it still was a remarkable proof of concept to show that tau pathology could be modified by targeting A $\beta$ . This was only possible by examining the *in vivo* biomarker changes over time. Furthermore, anti-amyloid immunotherapies tend to suffer from dose-dependent safety issues related to amyloid-related imaging abnormalities edema (ARIA-E) or microhemorrhage (ARIA-H) [156]. Having greater therapeutic effects at a higher dose, Aducanumab treatment must include safety management based on a repeated safety profile following the treatment using MRI. AD clinical trials now must screen the inclusion and exclusion criteria, evaluate therapeutic target engagement, efficacy, and safety based on *in vivo* biomarkers.

This framework is applicable across different targets in various AD pathophysiological mechanisms as well as in different species. Being able to apply the same principles, the *in vivo* biomarker-based study design for AD drug discovery and development from the preclinical stage could potentially provide richer data to predict the success in the clinical trials. Thus, it could lead to greater bench-to-bedside translation. For example, all of the anti-amyloid immunotherapy studies that had gone to phase 3 evaluated their preclinical studies based on *in vitro* biochemical assays. Consequently, the cross-sectional nature of *in vitro* observations limits the prediction in

the post-therapy A $\beta$  levels compared to its pre-dosing levels. Also, extensive assessments of therapeutic efficacy and safety are largely missing. By providing the same metrics utilized in human clinical trials, the *in vivo* biomarker-based study design at the preclinical stage can provide a direct effect size of target engagement, efficacy, and safety related to the treatment. This will increase the likelihood of translating the preclinical findings into clinical trials.

#### **11.4 The Aims and hypotheses**

It is clear that *in vivo* biomarker-based AD research framework will accelerate a deeper understanding and discovery of the disease mechanisms, potential therapeutic targets, and drug discovery. However, it is imperative to recognize that this is a long and arduous process. The *in vivo* biomarker-based AD research framework reflects the systematic approach in the scientific method, which involves formulating a hypothesis based on observations, conducting a controlled experiment to collect measurements that directly or indirectly address the research question, and deducing a conclusion refining the original question by comparing the observations and expectations/predictions. This process must be repeated, and the findings must be replicated and validated. While this procedure varies from one field to another, the *in vivo* biomarker-based AD research framework can be divided into three integral aspects: 1) a process of discovery and validation of a new *in vivo* biomarker, 2) *in vivo* biomarker-based evidence supporting a disease mechanism, and 3) evaluating therapeutic target engagement, efficacy, and safety. The three aspects are empirical and depend on one another. To achieve preventative or disease-modifying therapeutics for AD, one must have a biomarker that represents the underlying biologic and pathologic entity, which has the potential to change the course of the disease when targeted.

To this end, this Ph.D. thesis presents three original multimodal *in vivo* biomarker-based investigations of AD pathophysiology and drug discovery. This Ph.D. thesis aims to use multiparametric methods for 1) validating a novel fluid neurodegenerative biomarker, 2) showing the first *in vivo* biomarker evidence of activated microglia as a driver of tau pathology and spreading in the presence of A $\beta$ , and 3) preclinical assessment of disease-modifying anti-amyloid therapeutic target engagement, efficacy, and safety based on *in vivo* biomarkers.

This Ph.D. thesis hypothesizes that 1) NFL in CSF and plasma is a putative neuronal injury/neurodegeneration biomarker that is sensitive to track A $\beta$ -induced neuronal injury/neurodegeneration, 2) interaction between A $\beta$  and activated microglia predicts tau burden and propagation in AD, and 3) a novel anti-amyloid treatment strategy safely reduces A $\beta$  pathology in McGill-R-Thy1-APP transgenic rats. These findings constitute important contributions to a growing body of biomarkers, a greater understanding of disease mechanisms, and a proof-of-concept in disease-modifying therapeutic and drug discovery.

## **12 Body of the thesis**

### **12.1 Methodology**

This section will present all the study samples and methodologies used in the Research findings. In particular, each methodology is separated into a unique platform and will introduce and describe the underlying principles that allow the quantification of biological metrics representing a biomarker. Then, each biomarker will be described in the context of each research question and existing literature to better understand the research findings, interpretations, and discussions. As this section focuses on the concepts and context of each biomarker, the detailed technical descriptions of each methodological processing can be referred to in the Method sections in each manuscript.

#### **12.1.1 Study samples**

##### *Alzheimer's Disease Neuroimaging Initiative (ADNI):*

Alzheimer's Disease Neuroimaging Initiative (ADNI) is a longitudinal multicenter study aimed to develop clinical, imaging, genetic, and biochemical biomarkers to understand the process of healthy aging to dementia or AD. Since its birth in 2004, a total of 63 different sites across the US and Canada are involved in characterizing human participants with clinical, imaging, genetic, and biochemical biomarkers to date. The global efforts across multiple disciplines in building the ADNI cohort with standardized protocols and open data-sharing policy have been the catalyst for more than 1000 publications of novel discoveries and validations of early AD biomarkers and innovative frameworks.

The main goals of ADNI are 1) to identify biomarkers to predict and understand the pathophysiological processing leading to AD, 2) to be able to evaluate AD intervention, prevention, and treatment at the earliest stage (preclinical stage) when the intervention may be most effective, and 3) disseminate the rich, multicenter, longitudinal data to the world. As such, ADNI has been a valuable resource and used in one of the studies validating a novel neuronal injury biomarker for AD clinical trials.

The ADNI cohort consists of ages between 55-90 cognitively normal (CN), early mild cognitive impairment (EMCI), late mild cognitive impairment (LMCI), and AD participants. In addition, all participants must agree to undergo a series of screening procedures to be considered eligible as well as longitudinal neuropsychological tests, imaging procedures, blood collection for genetic testings and biomarkers, and at least one lumbar puncture for a CSF collection. However, individuals with other neurological conditions such as Parkinson's disease, Huntington's disease, etc, are excluded. Furthermore, individuals with a high burden of vascular anomalies such as lacunes and/or white matter hyperintensities, a history of substance abuse, a pacemaker or foreign object implemented in the body are excluded. A detailed description of the inclusion and exclusion criteria can be found at [www.adni-info.org](http://www.adni-info.org).

*Translational Biomarkers of Aging and Dementia (TRIAD):*

Translational Biomarkers of Aging and Dementia (TRIAD) cohort is a longitudinal *in vivo* biomarker-based characterization study of AD continuum as well as other neurodegenerative diseases. Since its launch in 2017 at the McGill University Research Centre for Studies in Aging (MCSA) centre, the TRIAD study focuses to evaluate the trajectory of

clinical, imaging, and fluid biomarkers from the preclinical stage to dementia or AD. The TRIAD cohort is growing quickly hosting more than 1000 participants in the registry. Having similar study designs and methodological protocols with ADNI, the TRIAD cohort serves as an important independent study sample representing the local community in AD research.

The TRIAD cohort aims to develop novel approaches to accurately diagnose AD at its earliest stage based on *in vivo* biomarkers. Notably, one of the largest efforts from the TRIAD cohort focuses on tracking neuroinflammation during the AD pathophysiological processes and assessing its dual effects (protective vs pathologic) on AD pathological hallmarks, A $\beta$  and p-tau, and cognitive impairment. There are more than 100 participants with a complete biomarker profile including a series of PET and MRI biomarkers, CSF and plasma fluid biomarkers, diverse batteries of neuropsychological examinations, and genetic information. Having an extensive *in vivo* biomarker profile of A $\beta$ , hyperphosphorylated tau, and neuroinflammation in imaging, fluid, and genetic platforms, the TRIAD cohort offers a unique and rare opportunity to disentangle the complex and dynamic AD pathophysiological processes leading to cognitive impairment in the preclinical stage to AD continuum.

The TRIAD cohort consists of young healthy control, CN, MCI, AD, and other neurodegenerative diseases. All participants must agree to undergo a series of screening procedures and longitudinal neuropsychological tests, imaging procedures, and blood and CSF collection. In particular, one of the most important screenings for the neuroinflammation study is the genetic screening for Translocator Protein (TSPO) rs6971 polymorphism [157]. Being the target of PET tracer for activated microglia, the rs6971 polymorphism has been shown to affect the affinity of the tracer in a dose-dependent manner. Therefore, the TRIAD cohort selects only the individuals with high-affinity binding polymorphism. However, individuals with other

neurological conditions such as Parkinson's disease, Huntington's disease, etc, are excluded. Furthermore, individuals with a high burden of vascular anomalies such as lacunes and/or white matter hyperintensities, history of substance abuse, a pacemaker or foreign object implemented in the body are excluded.

McGill-R-Thy1-APP:

McGill-R-Thy1-APP transgenic (Tg) rat model is an AD-like rat model that recapitulates the progression of AD A $\beta$  pathology [89, 158]. The McGill-R-Thy1-APP rat model is developed by introducing the human A $\beta$  precursor protein (APP) carrying Swedish double mutation (K670N and M671L) and Indiana (V717F) mutations under the murine *Thy1.2* promoter in Wistar background rat [89]. The homozygous McGill-R-Thy1-APP rats display extracellular deposits of A $\beta$  plaques as early as 6 months in the subiculum and spread throughout the cortex and hippocampus based on immunohistological staining (Figure 20). The A $\beta$  plaques progressively develop to dense and fibrillar nature that can be stained via Thioflavin-S and are associated with dystrophic neurites and neuroinflammation [89]. Consequently, the McGill-R-Thy1-APP rats show cognitive dysfunction as early as 3 months and continue to decline based on a Morris Water Maze test.

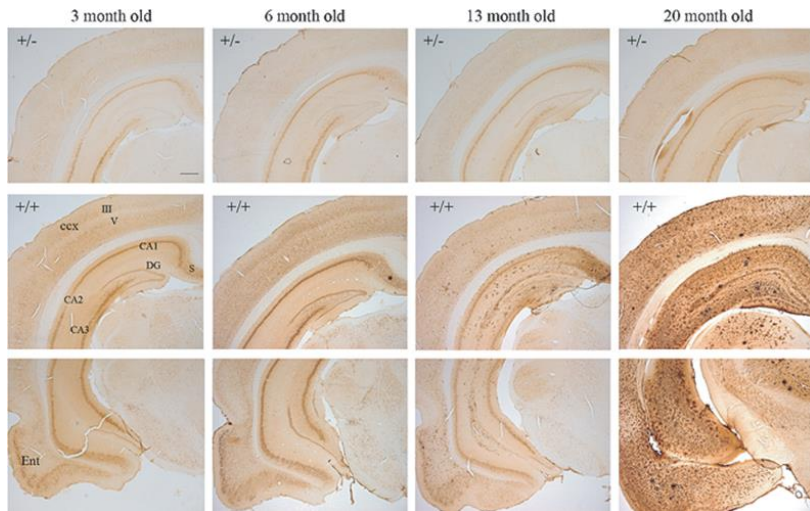


**Figure 20.** Progression of  $A\beta$  pathology in McGill-R-Thy1-APP transgenic rat model.

The top row (+/-) represents a hemizygous animal with intraneuronal  $A\beta$  pathology while the last two rows (+/+) show a homozygous animal with extracellular deposits of  $A\beta$  plaques. This is reproduced from Leon et al., 2010 [89].

Our group has extensively characterized the cascade of pathophysiological events of the McGill-R-Thy1-APP rat model induced by the human APP mutations using the same *in vivo* biomarkers used in human AD clinical trials [158]. The extracellular deposits of fibrillar  $A\beta$  plaques quantified using PET have been shown to increase significantly while CSF  $A\beta_{42}$  concentrations have been shown to decline significantly over time [158]. The statistical difference in the  $A\beta$  plaques quantification based on PET between the McGill-R-Thy1-APP rats and wild type (WT) is evident from 16-19 months of age (Figure 21) [158]. In addition, this observation is followed by substantial cerebral hypometabolism, reduced resting-state functional connectivity, neurodegeneration, and cognitive impairment (Figure 21) [158]. Interestingly, the rs-fMRI at an earlier age (9-11 months) shows an aberrant increase and mild memory dysfunction in the Tg compared to WT before the PET evidence of  $A\beta$  plaques. As such, the sequence of abnormal biomarkers observed in the McGill-R-Thy1-APP animals, in which  $A\beta$  is the pathogenesis origin, reflects the hypothetical dynamic biomarkers of the AD pathological cascade model.

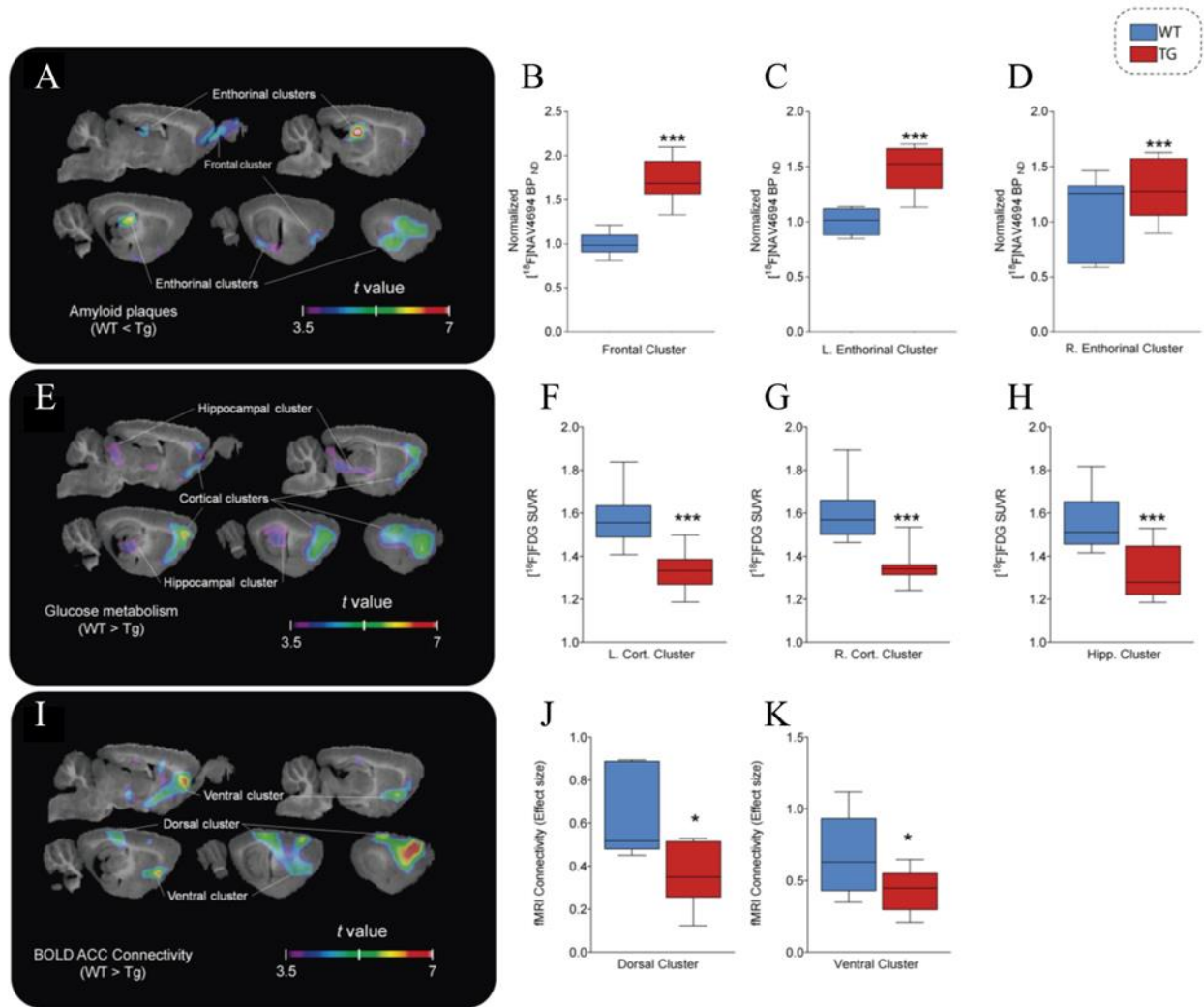


**Figure 21.**  $A\beta$ -induced pathophysiology in McGill-R-Thy1-APP transgenic rat model between 16-19 months old.

The top row shows the significant accumulation of  $A\beta$  in Tg compared to WT. The middle row shows the significant decline in the glucose metabolism in Tg compared to WT. The last row shows the significant decline in rs-fMRI cingulate-seed connectivity in Tg compared to WT. This is reproduced from Parent et al., 2017 [158].

Despite the lack of tauopathy, the McGill-R-Thy1-APP rat model provides a unique platform to bring novel insights into AD pathophysiology that is not possible in humans. For example, AD is defined by the presence of A $\beta$  plaques and NFTs. However, having A $\beta$  pathology alone, the McGill-R-Thy1-APP model recapitulates the cascade of abnormal biomarkers of AD, reflecting the similar underlying pathophysiological processes between the two species. Congruent observations have been consistently reported in the Tg murine models of AD: transgenic animals carrying a human APP mutation lead to AD-like pathologies and phenotypes, while transgenic animals carrying a human tau mutation lead to different tauopathies such as FTD [159]. This is a remarkable proof of concept in the central role of A $\beta$  in AD pathogenesis leading to a subsequent change in brain connectivity, hypometabolism, neurodegeneration, and cognitive dysfunction. On the other hand, without a clear tauopathy, the murine Tg models of A $\beta$  display only a modest/minimal level of cell death and neurodegeneration, suggesting tauopathy exerts greater effects on cell death and neurodegeneration relative to A $\beta$  [159-161]. This notion has gained immense support and validation in recent years with the advent of tau PET tracers demonstrating a greater association with neurodegeneration and cognition. Given the rich knowledge, the McGill-R-Thy1-APP Tg model has been used to validate a novel neuronal injury fluid biomarker in the context of AD as well as to evaluate an anti-amyloid therapy as a potential disease-modifying treatment for AD in this thesis.

### 12.1.2 Demographics

Studies involving human data typically include important risk factors for AD in their demographics and statistical models as covariates. Age, APOE $\epsilon$ 4, sex, and education are the more common covariates in AD research. Having an intimate relationship with AD, these risk factors can have confounding effects if they are not accounted for. Here, the importance of each risk factor is discussed in the context of AD.

#### Age:

Age is the greatest risk factor for AD and dementia [1]. The prevalence of AD is approximately 5.3% between the age of 65-74 while it reaches 13.8% between the age of 75-84 [1]. This number becomes worse above the age of 85 at 34.6% [1]. Age is significantly associated with A $\beta$ , NFTs, and neuroinflammation [162-164]. However, it is important to note that age does not necessarily cause the disease, and AD and other dementias are not part of normal aging. Therefore, understanding how healthy aging processes are similar or different relative to AD could shine novel insights into unique processes that lead to AD and other dementias.

#### APOE $\epsilon$ 4:

APOE has three different alleles,  $\epsilon$ 2,  $\epsilon$ 3, and  $\epsilon$ 4, and numerous functions including lipid transportation and metabolism. While carrying two APOE $\epsilon$ 3 alleles is the most prevalent approximately at 45.2-63.4%, carrying two APOE $\epsilon$ 2 alleles is the rarest at 0.2-0.7% [1]. However, APOE is the strongest genetic risk factor for AD currently and is significantly

involved in AD pathophysiology as it interacts with A $\beta$  and TREM2 to mediate microglial functions [1, 126]. Moreover, recent studies underscored that APOE significantly interacts with sex to worsen AD pathophysiology and showed an independent effect on the health of the blood-brain barrier (BBB) [165-167]. As such, APOE is considered a potential therapeutic target for AD.

### Sex:

Sex is also a significant risk factor for AD. Based on the prevalence of AD, there is a disproportionate number of women who are diagnosed with AD relative to men — almost two-thirds of Americans with AD are women [1]. A growing body of research on sexual dimorphism in AD shows there may be underlying biological differences resulting in a greater vulnerability in women for AD than men. In particular, sex significantly interacts with APOE such that women who carry APOE $\epsilon$ 4 have a greater risk of developing AD pathology compared to men or women who carry APOE $\epsilon$ 3 [166]. This seems to be also related to women who carry APOE $\epsilon$ 4 showing a greater tau burden in the brain [168, 169]. Thus, sex is an important variable to consider when investigating AD pathophysiology. It is worthwhile to note that sex refers to the biological presentation arising from carrying XX or XY chromosomes.

### Education:

Education is one of the modifiable risk factors in AD. Greater education attainment is associated with greater protection against AD and dementia [170]. However, it seems as though the protective effects are not from having reduced or slower progression of AD pathology.

Instead, numerous observational studies suggest that individuals with higher education attainment could endure a higher AD pathologic burden given the same clinical severity [171, 172]. This led to the notion of cognitive reserve that can be affected by external factors such as education and occupation and provide greater protection against AD pathology [171, 172]. While the pathologic definition of AD is the presence of A $\beta$  and NFTs, cognitive impairment and loss of autonomy are necessary for a clinical diagnosis of AD. As such, education would be an important variable to include when evaluating the relationship between pathology and cognition.

### **12.1.3 Positron Emission Tomography (PET)**

PET is an imaging technique that uses radioactive material known as radiotracers (PET tracers/radiopharmaceuticals/radioligands/ligands) to visualize and quantify the specific target of interest. An ideal brain PET tracer for a high-throughput study should interact with one specific target (preferably a reversible interaction) with low nonspecific interaction, be able to cross BBB, and have fast-enough kinetics with a good reference region and a [ $^{18}\text{F}$ ] radioisotope. Therefore, when an ideal PET tracer is injected as a bolus, it will be distributed throughout the body and interact with one specific target that it is designed for and emit positrons from where the target is. Then, the positrons will travel and annihilate with electrons within the local neighbourhood and generate two photons to travel at near 180 degrees as a line of response (LOR). During a scan, there are over millions of LOR events that get detected by the detector rings in a PET scanner, which can reconstruct the photon signals into a 3D image representing the amount of tracer interacting with your target. By applying a PET kinetic model that fits the properties of the tracer and/or underlying biological mechanisms (compartments), the reconstructed image can provide an accurate (absolute and/or relative) quantification in a 3D brain topography.

The gold standard PET scanning protocol requires an intricate orchestra of multidisciplinary teams beyond a simple clinical PET scanning protocol: a team of PET technicians injects the tracer, collects multiple blood samples at a precise time, and attends to a participant and materials; an anesthesiologist installs an arterial line for the arterial blood collection and monitors the health of the participant; a team of blood analysts processes and analyzes the amount of parent tracer (input function) and metabolites present in the blood samples; a PET kinetic modelling expert applies an appropriate model to the data providing a precise *absolute* quantification. As such, it is arduous to conduct an arterial PET protocol in a high throughput study even though it is considered a gold standard. On the other hand, with validation of tracer kinetics and its reference region through the gold standard protocol, PET scanning protocol can be simplified and provide a *relative* quantification that can be as robust as the absolute quantification [173]. Based on a reference region, PET images can be quantified using a dynamic scan (entire scan from 0 min until the end) or a static scan (a short window period typically 10-20 minutes). In particular, a static method deriving standardized uptake value ratio ( $SUVR = SUV_{\text{target}}/SUV_{\text{reference}}$ ) is heavily used in typical clinics or studies with a high throughput such as clinical trials. However, it is important to note a significant trade-off between quantification accuracy and practicality as you move away from the full quantification to a static SUVR protocol (Figure 22).

In this Ph.D. thesis, two studies include PET imaging using a reference region method in humans and animals. Briefly, each tracer will be presented in the context of AD biomarkers and important methodological validations required to apply a reference region method in each study.

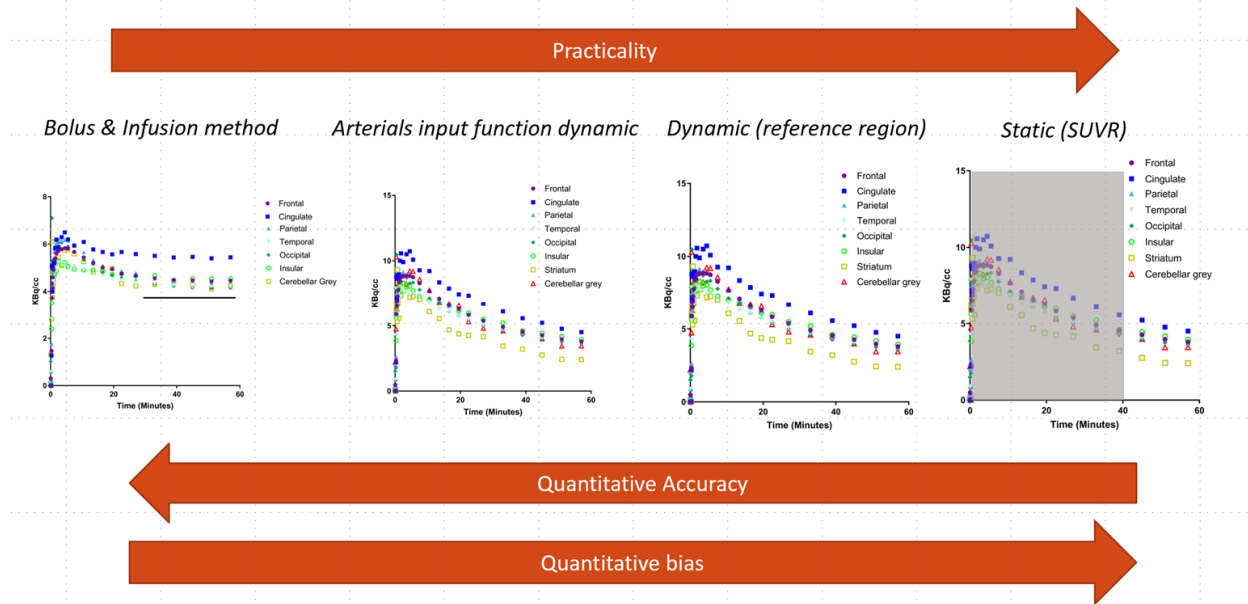


Figure 22. Various PET methodologies.

### [<sup>18</sup>F]AZD4694:

[<sup>18</sup>F]AZD4694 is an A $\beta$  PET tracer with a high affinity ( $K_d = 2.3 \pm 0.3$  nM) to A $\beta$  fibrils *in vitro* [174, 175]. Having a [<sup>18</sup>F] radioisotope, [<sup>18</sup>F]AZD4694 has a longer half-life (109.771 minutes; ~110 minutes) compared to a [<sup>11</sup>C] PET tracer (20 minutes). This is an important factor to improve the clinical applicability to be able to conduct a high throughput study with more than 100 participants. While most of A $\beta$  PET tracers with a [<sup>18</sup>F] suffer from a greater nonspecific binding in white matter, [<sup>18</sup>F]AZD4694 has a similar binding distribution with low nonspecific white matter binding and dynamic range as the gold standard A $\beta$  PET tracer, [<sup>11</sup>C]PiB [174, 176, 177]. Based on a full quantification study using arterial input data, a simplified protocol using SUVR – a static scan during the time window between 40-70 minutes post-injection with a cerebellar grey as a reference region – has been validated [177]. The significant correlation between global [<sup>18</sup>F]AZD4694 SUVR and [<sup>11</sup>C]PiB SUVR has been reported:  $r = 0.99$ ,  $p = < 0.0001$ , and slope = 0.95 [177].

### [<sup>18</sup>F]MK6240:

[<sup>18</sup>F]MK6240 is a second-generation PET tracer targeting NFTs at the subnanomolar range ( $K_d = 0.14\text{-}0.38$  nM) with minimal off-target binding to monoamine oxidase (MAO)-A and MAO-B [94]. While having a [<sup>18</sup>F] radioisotope allows conducting more PET scans from a single production, [<sup>18</sup>F]MK6240 kinetics study has reported 90-110 minutes post-injection time window to be optimal for SUVR quantification using cerebellar grey as a reference region [178]. The SUVR between 90-110 minutes post-injection has shown a significant correlation with distribution volume ratio (DVR) ( $r = 0.993$ , 95% CI 0.99-0.995) based on two-tissue compartmental modelling [178]. Interestingly, [<sup>18</sup>F]MK6240 seems to be only useful to detect AD-related tauopathy comprised of 3R/4R neurofibrillary tangles, and it does not bind to non-AD tauopathies such as PSP [100].

### [<sup>11</sup>C]PBR28:

[<sup>11</sup>C]PBR28 is a second-generation PET tracer targeting 18 kDa TSPO that is a mitochondrial outer membrane protein expressed by immune cells such as microglia [179]. As a part of the host defence system, microglia get activated to protect the brain from toxic insults and overexpress TSPO. As such, TSPO PET tracers are widely considered to reflect neuroinflammatory processes in the brain. However, there are a few important considerations regarding the [<sup>11</sup>C]PBR28 data. First, [<sup>11</sup>C]PBR28 suffers from differential binding affinities due to rs6971 polymorphism on the TSPO gene [157] even though [<sup>11</sup>C]PBR28 provides a greater signal-to-noise ratio than the first-generation TSPO PET tracer, [<sup>11</sup>C]PK11195 [179]. Second, there is no region devoid of TSPO expression in the brain. As a result, TSPO PET tracers in

general are limited to using a *pseudo*-reference region [180] or alternative data-driven techniques [181, 182] have been proposed. In particular, cerebellar grey has been suggested as a *pseudo*-reference region based on 1) the lack of difference in the volume of distribution ( $V_T$ ) along the AD clinical spectrum, 2) congruent results on regional differences in neuroinflammation based on  $V_T/f_P$  and SUVR, and 3) a positive correlation between [ $^{11}\text{C}$ ]PBR28 SUVR and CDR Sum of Boxes (CDRSOB) score, which indicates dementia severity [180]. Moreover, the variability in [ $^{11}\text{C}$ ]PBR28 SUVR quantification is reported much lower compared to the absolute quantification,  $V_T/f_P$ , providing greater statistical power in group comparisons [180]. Therefore, the TRIAD cohort only includes the high-affinity binders and acquires [ $^{11}\text{C}$ ]PBR28 SUVR between 60-90 minutes post-injection using cerebellar grey as a *pseudo*-reference region.

#### **12.1.4 Magnetic Resonance Imaging (MRI)**

MRI is one of the most widely utilized *in vivo* imaging techniques in AD research and clinics. MRI is powerful and versatile to be able to characterize and quantify a diverse array of physiological measurements at various scales at a relatively low cost. For example, MRI can provide structural measurements such as brain volume or grey matter density to assess brain atrophy, functional measurements such as blood-oxygen-level-dependent (BOLD) signals that indirectly measure the neurovascular coupling to represent a functional brain network, as well as deposits of blood or calcium based local magnetic field distortion from paramagnetic, diamagnetic, and ferromagnetic interaction. This is possible due to the underlying principle of MRI signal acquisition: by applying a varying magnetic field at various strengths and frequencies, an object or a tissue is magnetized inside of the scanner and consequently sends a radio frequency signal to be detected. Based on the compositions of the brain, physiological

properties for neuronal activities (ie. neurovascular coupling), or even blood cells, a unique set of signals is then reconstructed into a physiologically meaningful metric called a biomarker. Here, we will discuss different MRI-based biomarkers used in this thesis below.

### *Structural/Anatomical Imaging:*

Structural or anatomical MRI is most commonly used to evaluate neurodegenerative processes and brain atrophy. Following a standard structural MRI (typically, it would be a T1-weighted volumetric sequence), a 3D image of the entire brain will be represented in a volume of a given matrix. Such volumetric representations have been closely linked to neuronal counts [183] and have become valuable biomarkers to predict future AD incidents based on a unique pattern of neuronal losses in different neurodegenerative diseases [184, 185]. While there are different strategies to evaluate brain atrophy, manual hippocampal segmentation and voxel-based morphometry (VBM) have been used in this thesis.

Manual volumetric segmentation is considered a gold standard in volumetric analysis. Using brain imaging software, one can manually define a region of interest (ROI) following a specific landmark based on an atlas despite this is laborious. With increasing development in artificial intelligence, tremendous research efforts are making immense progress on machine learning strategies to automate the segmentation of ROI. Following the segmentation, the volumetric measurement of the ROI can be obtained and used for statistical analyses.

VBM is a computational technique that measures volumetric changes at every voxel without any bias from different parcellation schemes. As such, VBM is ideal to provide

comprehensive local neurodegenerative processes with topographical information revealing unique patterns of neurodegeneration signature beyond one ROI.

*Resting-state functional Imaging:*

rs-fMRI is a neuroimaging modality that has been widely used to characterize various functional networks in the brain. It can measure BOLD signals reflecting the changes in blood flow and deoxyhemoglobin due to brain activities — a process called neurovascular coupling [186]. With diverse analytical methods for BOLD signals such as hypothesis-driven seed-based connectivity or data-driven independent component analysis (ICA), rs-fMRI enables the construction of a functional network that represents an ensemble of regions driving a phenotypic outcome. For example, since the identification of the DMN, which is thought to be a large-scale brain organization that is unique to humans due to its role in conceptual processing, mind-wandering, and sustenance for consciousness, the disruption in the DMN has been identified as one of the earlier biomarkers of AD [47, 48].

*Susceptibility weighted Imaging:*

Susceptibility weighted imaging is sensitive to the materials that have different magnetic properties and their interaction leading to distortion of the local magnetic field. As such, the presence of blood products or calcium can be imaged using this MRI sequence. Although there are not as many biomarkers of AD based on the susceptibility-weighted imaging as the previously mentioned sequences, the important utility of this sequence has been highlighted recently with almost all anti-amyloid immunotherapies reporting incidences of ARIA-E and/or

ARIA-H in a dose-dependent manner [156]. This has been consistently observed at its highest dosing groups [156]. Therefore, it is important to evaluate potential ARIA-E/H following anti-amyloid therapy using susceptibility-weighted imaging.

### **12.1.5 Biofluids**

#### CSF:

CSF is a clear fluid found in the tissue that surrounds the brain and spinal cord. CSF has many functions including but not limited to protection, homeostasis, and waste clearance from the brain. Consequently, CSF offers core biomarkers of AD reflecting some of the key aspects of the disease pathophysiology such as A $\beta$ , tau, and neurodegeneration. These CSF biomarkers have been validated clinically, and a growing body of literature suggests that the CSF biomarkers are considered one of the earliest biomarkers of AD pathophysiological processes and able to complement imaging biomarkers [44, 45, 56, 187]. Importantly, CSF collection is relatively cheap and more available in clinics for real-world AD patients compared to the imaging biomarkers that require a team of experts and facilities. While brain imaging biomarkers can provide rich and accurate quantification and spatiotemporal evolution of pathological processes, CSF biomarkers offer alternative options in AD research and clinics.

#### Plasma:

Plasma is a yellowish fluid compartment in blood and carries proteins in the vascular system. While CSF is only part of the central nervous system, plasma in blood travels throughout the entire body and exchanges nutrients and waste between central and peripheral nervous

systems. Effectively, blood-based biomarkers reflecting brain proteins tend to have a greater amount of noise, degradation, and contamination from the peripheral system. Therefore, identifying sensitive and specific blood-based biomarkers of the core AD pathophysiological processes has been challenging. With great perseverance in fluid biomarker research and technological development, the late 2010s have been a blood-based biomarker boom in AD. This will not only revolutionize the clinical trial enrichment in screening at the highest throughput with a significant reduction associated with cost and invasiveness but it will also lead to greater accessibility and availability of the blood-based biomarkers in dementia clinics across the world to increase the bench-to-bedside practice.

#### CSF A $\beta$ :

Extracellular deposits of A $\beta$  can be quantified using CSF A $\beta_{42}$  concentrations [44]. The aggregation of A $\beta_{42}$  to form amyloid plaques results in reduced CSF concentrations of the protein in AD by approximately 50% [188]. Moreover, normalizing CSF A $\beta_{42}$  by A $\beta_{40}$ , which is suggested to correct for inter-subject differences in A $\beta$  production, increases diagnostic prediction of AD while the CSF A $\beta_{42/40}$  ratio shows near 100% concordance with A $\beta$  PET [189]. Interestingly, CSF p-tau/A $\beta_{42}$  discriminated PET PiB<sup>+</sup> from PiB<sup>-</sup> better than CSF A $\beta_{42/40}$  ratio [190]. In addition, those who are CSF A $\beta^+$  and PET A $\beta^-$  tend to convert to PET A $\beta^+$  more often than not within a few years [45, 191, 192]. As such, CSF A $\beta$  could track even earlier parts of A $\beta$  pathology compared to PET A $\beta$  as the PET tracers detect A $\beta$  once they form a fibrillar  $\beta$ -sheet structure [45, 191]. It is worthwhile to note that A $\beta$  PET measurements most likely represent the magnitude of A $\beta$  accumulation or pathologic load accumulated over time [67]. However, CSF A $\beta$  can be considered as a biomarker of a pathologic state within the disease stage [67].

### CSF Tau:

Progressive tauopathy in AD can also be detected in CSF. This can be reflected based on total tau (T-tau) and/or p-tau concentrations in CSF. Here, circumstantial evidence of increased CSF T-tau concentrations in neurological conditions with extensive neurodegeneration without clear amyloid and tau pathologies such as Creutzfeldt-Jakob disease, acute stroke and brain trauma support CSF T-tau as neuronal injury/neurodegeneration biomarker [67]. Therefore, CSF T-tau is thought to reflect neuronal injury and/or neurodegeneration while CSF p-tau is thought to reflect the aggregates of p-tau, NFTs [67]. Notably, there are a few different epitopes in detecting CSF p-tau (p-tau181, p-tau217, and p-tau231), and they seem to provide complementary information on AD pathophysiology [45, 193]. Recent data comparing these different epitopes have reported p-tau217 detects an abnormal increase earlier compared to the classical p-tau181, while p-tau217 and p-tau181 significantly correlate with tau PET in early Braak regions [65, 66, 162, 194]. On the other hand, CSF p-tau231 is reported to classify AD from healthy individuals with greater specificity relative to CSF p-tau181 [193]. It is important to note that both CSF T-tau and p-tau increase in AD-related tau pathophysiology [67]. However, they do not reflect tau pathology in non-AD tauopathy [67].

### NFL:

Although A $\beta$  and tau in CSF have been actively investigated since the early 2000s, accurate CSF biomarker of neuronal injury/neurodegeneration has been largely missing. However, a recent advent of NFL as a putative fluid biomarker of neuronal injury/neurodegeneration has captivated the AD biomarker field. CSF NFL is significantly

associated with neurodegenerative processes in AD and reflects the A $\beta$  and tau pathophysiological processes in AD [195-197]. NFL has emerged now as one of the newest members of A/T/(N) classification biomarker for neurodegeneration and has also transformed the fluid biomarker research as it is also identified in blood-based (plasma and serum) analytics [68]. For example, the correlation between CSF and plasma NFL is excellent, and plasma NFL shows an increased concentration 10-15 years before the expected symptom onset in familial AD [198].

## **12.2 Research findings**

So far, a brief history of AD research evolution, development of *in vivo* biomarkers of AD, and important application and utility of AD biomarkers in clinical trials searching for novel preventative and/or disease-modifying therapeutics have been covered. Here, three innovative studies will present three original contributions to AD research as part of this Ph.D. thesis.

### **12.2.1 Study 1: Amyloid-beta modulates the association between neurofilament light chain and brain atrophy in Alzheimer's disease.**

**Authors:** Min Su Kang<sup>1,2,3</sup>, Arturo Aliaga Aliaga<sup>1,2,3</sup>, Monica Shin<sup>1,2</sup>, Sulantha Mathotaarachchi<sup>1,2</sup>, Andrea L. Benedet<sup>1,2</sup>, Tharick A. Pascoal<sup>1,2</sup>, Joseph Therriault<sup>1,2</sup>, Mira Chamoun<sup>1,2</sup>, Melissa Savard<sup>1,2</sup>, Gabriel A. Devenyi<sup>2,4</sup>, Axel Mathieu<sup>2</sup>, M. Mallar Chakravarty<sup>2,4,5</sup>, Åsa Sandelius<sup>6</sup>, Kaj Blennow<sup>6,7</sup>, Henrik Zetterberg<sup>6,7,8,9</sup>, Jean-Paul Soucy<sup>3</sup>, A. Claudio Cuello<sup>10</sup>, Gassan Massarweh<sup>3</sup>, Serge Gauthier<sup>1,2,3</sup>, Pedro Rosa-Neto<sup>1,2,3,4</sup>, Alzheimer's Disease Neuroimaging Initiative\*\*

**Affiliation:** Translational Neuroimaging laboratory - McGill University Research Centre for Studying in Aging<sup>1</sup>, Cerebral Imaging Centre – Douglas Research Centre<sup>2</sup>, McConnell Brain Imaging Centre – McGill University<sup>3</sup>, Department of Psychiatry – McGill University<sup>4</sup>, Department of Biomedical Engineering – McGill University<sup>5</sup>, Department of Psychiatry and Neurochemistry, the Sahlgrenska Academy at the University of Gothenburg, Mölndal, Sweden<sup>6</sup>, Clinical Neurochemistry Laboratory, Sahlgrenska University Hospital, Mölndal, Sweden<sup>7</sup>, UK Dementia Research Institute at UCL, London, United Kingdom<sup>8</sup>, Department of Neurodegenerative Disease, UCL Institute of Neurology, Queen Square, London, United Kingdom<sup>9</sup>, Department of Pharmacology and Therapeutics– McGill University<sup>10</sup>

This study is published: Kang, M. S., Aliaga, A. A., Shin, M., Mathotaarachchi, S., Benedet, A. L., Pascoal, T. A., ... & Rosa-Neto, P. (2020). Amyloid-beta modulates the association between neurofilament light chain and brain atrophy in Alzheimer's disease. *Molecular Psychiatry*, 1-13.

## **Abstract**

Neurofilament light chain (NFL) measurement has been gaining strong support as a clinically useful neuronal injury biomarker for various neurodegenerative conditions. However, in Alzheimer's disease (AD), its reflection on regional neuronal injury in the context of amyloid pathology remains unclear. This study included 83 cognitively normal (CN), 160 mild cognitive impairment (MCI), and 73 AD subjects who were further classified based on amyloid-beta ( $A\beta$ ) status as positive or negative ( $A\beta^+$  vs  $A\beta^-$ ). In addition, 13 rats (5 wild types and 8 McGill-R-Thy1-APP transgenics (Tg)) were examined. In the clinical study, reduced precuneus/posterior cingulate cortex and hippocampal grey matter density were significantly associated with increased NFL concentrations in cerebrospinal fluid (CSF) or plasma in MCI  $A\beta^+$  and AD  $A\beta^+$ . Moreover, AD  $A\beta^+$  showed a significant association between the reduced grey matter density in the AD-vulnerable regions and increased NFL concentrations in CSF or plasma. Congruently, Tg rats recapitulated and validated the association between CSF NFL and grey matter density in the parietotemporal cortex, entorhinal cortex, and hippocampus in the presence of amyloid pathology. In conclusion, reduced grey matter density and elevated NFL concentrations in CSF and plasma are associated in AD-vulnerable regions in the presence of amyloid positivity in the AD clinical spectrum and amyloid Tg rat model. These findings further support the NFL as a neuronal injury biomarker in the research framework of AD biomarker classification and for the evaluation of therapeutic efficacy in clinical trials.

## Introduction

Alzheimer's disease (AD) is defined by the presence of amyloid and tau pathologies that lead to neuronal injury or neurodegeneration and cognitive decline. Although the exact etiology of AD is still being debated, the most widely accepted amyloid cascade hypothesis rests on amyloid-beta ( $A\beta$ ) as the initiating event leading to a cascade of AD pathophysiological processes [199]. This hypothesis has gained strong support based on the multitude of biomarker-based evidence suggesting that  $A\beta$  abnormality occurs decades before the onset of AD [56]. This evidence suggests that the  $A\beta$  pathology correlates only weakly with neuronal injury or neurodegeneration but its downstream tau pathology is more strongly associated with neurodegeneration and consequently cognitive decline [200]. As such, the new NIA-AA research framework A/T(N) focuses on measurable neuropathologic biomarkers to define and track patients along the AD continuum for staging purposes [67]. Following this framework, A (aggregated  $A\beta$ ) and T (aggregated tau) define AD and can be measured using positron emission tomography (PET) or cerebrospinal fluid (CSF) biomarkers, while N (neuronal injury or neurodegeneration) is not specific to AD but provides staging of AD pathophysiological processes and can be measured using magnetic resonance imaging (MRI), [ $^{18}\text{F}$ ]FDG-PET, and CSF total tau (T-tau) [67]. Effectively, the biomarkers of N allow predicting cognitive decline or conversion for clinical trial enrichment [201].

Recent studies suggest neurofilament light chain (NFL) as a putative biomarker for neuronal injury or neurodegeneration. NFL is a subunit of the neurofilament that plays an important role in axonal and dendritic branching and growth, and axonal integrity [202, 203]. Elevated NFL concentration in CSF has been associated not only with axonal damage but also with neuronal injury, brain atrophy and disease severity in various neurological disorders,

including AD, and in their respective animal models [204-212]. Importantly, it has already been demonstrated that CSF and plasma NFL levels are correlated to each other and are elevated in AD [213].

To maximize the utility of a novel biomarker and its proper use in AD research and therapeutic trials, it is imperative to compare it with other well-established biomarkers. In the case of the NFL, this would facilitate its incorporation among the existing biomarkers [67]. Current evidence on the influence of A $\beta$  pathology on NFL levels has been conflicting. Some previous studies suggest that NFL levels may be independent of A $\beta$  pathology as there was no statistical difference between A $\beta$ - and A $\beta$ + subjects in the clinical spectrum of sporadic AD [196, 207]. However, a recent study showed that CSF and serum NFL levels were increased in pre-symptomatic familial AD mutation carriers and the rate of increase in the serum NFL was able to discriminate the mutation carriers from non-carriers almost a decade before the expected onset of symptoms [198]. Furthermore, a recent study on the Alzheimer's Disease Neuroimaging Initiative (ADNI) cohort showed that longitudinal increases in plasma NFL levels correlate with baseline CSF indices of brain amyloidosis [197]. Moreover, it was revealed that NFL concentration was negatively associated with grey matter volumes of *a priori* defined regions of interest (ROI) that are vulnerable in AD – hippocampus, precuneus, or temporal composite regions (entorhinal, inferior temporal, middle temporal, and fusiform cortex) [198, 207, 213]. However, the empirical evidence on the NFL levels associated with reduced grey matter density at a voxel-based regional level in the context of A $\beta$  pathology is largely missing. Although NFL elevation is an indicator of the presence of neurodegenerative processes, this fluid biomarker lacks the topographical information present in [<sup>18</sup>F]FDG-PET or MRI scans [48, 185]. This is an important limitation since plasma or CSF NFL levels might reflect disease-specific grey or white

matter neurodegenerative processes or disease-independent healthy aging processes [185, 214, 215]. Understanding the topographical correlates between NFL and neuronal injury or neurodegeneration in the context of A $\beta$  pathology is crucial to interpret NFL levels as a novel fluid biomarker for neuronal injury or neurodegeneration in AD research and therapeutic trials.

In this study, we elucidate the contributing role of A $\beta$  pathology on neuronal injury reflected by NFL concentration and grey matter density maps. In addition, we illustrate voxel-based correlates between NFL and grey matter density maps in humans and the McGill-Thy1-APP transgenic (Tg) rat model [89]. This Tg model is ideal to study the effect of A $\beta$  alone as it progressively develops A $\beta$  pathology comparable to AD A $\beta$  pathology without the presence of tau pathology or minimal cell death [89, 158, 160]. The present study highlights that NFL concentration reflects neuronal injury processes in the regions that are vulnerable to AD in the presence of A $\beta$  pathology.

## **Materials & Methods**

### **Subjects**

#### **Human dataset**

Data used in the preparation of this article were obtained from the ADNI (adni.loni.usc.edu). The ADNI was launched in 2003 by the National Institute on Aging (NIA), the National Institute of Biomedical Imaging and Bioengineering (NIBIB), the Food and Drug Administration (FDA), private pharmaceutical companies and non-profit organizations, as a \$60 million, 5-year public-private partnership. ADNI is the result of the efforts of many co-investigators from a broad range of academic institutions and private corporations, and subjects

have been recruited from over 50 sites across the U.S. and Canada. For up-to-date information, see [www.adni-info.org](http://www.adni-info.org).

The criteria for cognitively normal (CN) classification are Mini-Mental State Examination (MMSE) scores between 24-30 (inclusive) without cognitive complaints or observable anomalies. The criteria for the diagnosis of mild cognitive impairment (MCI) included the presence of memory complaints, MMSE scores between 24-30 (inclusive), objective memory loss, Clinical Dementia Rating (CDR) of 0.5, preserved activities of daily living, and absence of dementia. Mild AD dementia subjects had MMSE scores between 20-26 (inclusive), CDR of 0.5 or 1.0, and fulfilled the NINCDS/ADRDA criteria for probable AD.

### **Animal dataset**

All procedures described here were performed in compliance with ethics protocols approved by McGill Animal Care Ethics Committee and following the Canadian Council on Animal Care guidelines. All rats were housed at the Douglas Mental Health University Institute animal facility on a 12/12hrs light/darkness cycle with *ad libitum* access to food and water. A starting sample of 26 animals was included in this study based on the effect size estimated from the previous study [208]. Eleven were wild-type (WT) animals and 15 were homozygous McGill-R-Thy1-APP Tg rats were randomly selected. All the animals were on Wistar's background for the study. All the animal procedures were completed blinded to the genotype.

## **Inclusion & Exclusion Criteria**

### **Humans**

ADNI inclusion and exclusion criteria can be found at ([www.adni-info.org](http://www.adni-info.org)). For our study, we included 83 CN, 160 MCI, and 73 AD individuals who have both CSF and plasma NFL, CSF A $\beta$ <sub>42</sub>, CSF phosphorylated tau (p-tau), and structural MRI data available. For plasma NFL analysis, we identified 2 CN, 8 MCI, and 4 AD subjects as outliers (2 standard deviations away from the mean) who were excluded in the analysis.

### **Animals**

All animal data points that overlap with any sign of brain tumour development or had major surgery to remove the tumour were excluded within the longitudinal data points (4 WT and 7 Tg). Last, all animals which were identified as an outlier (2 standard deviations away from the mean) were excluded (2 WT).

## **Imaging acquisition and processing**

### **Humans**

Details on the image acquisition parameters can be found here (<http://adni.loni.usc.edu/methods>). All T1-weighted MRIs were processed using an in-house processing pipeline and underwent non-uniformity correction [216], brain masking [217], normalization to the Montreal Neurological Institute (MNI) space using affine and nonlinear transformation with Advanced Normalization Tools (ANTs) registration tools [218, 219], and

segmented using 3-tissue priors in MNI space (grey matter, white matter, and CSF). Our in-house pipeline based on Medical Imaging NetCDF (MINC) toolkits ([www.bic.mni.mcgill.ca/ServicesSoftware](http://www.bic.mni.mcgill.ca/ServicesSoftware)) generated Voxel-based morphometry (VBM) images representing grey matter density maps. In brief, a log Jacobian determinant was derived based on the nonlinear vector field from the previously mentioned pipeline. Then, it was transformed into a scalar, modulated with a grey matter probability mask, and smoothed with 8mm Full-Width at Half-Maximum (FWHM). Last, three ROIs from the MNI template atlas were used to replicate the previous findings in the literature: 1) temporal composite (Temp.Comp; bilateral middle and inferior temporal gyri, fusiform and entorhinal cortices, and hippocampi), 2) Entorhinal cortices, and 3) hippocampi [197, 207, 213].

## **Animals**

All MRI images were acquired using Bruker 7T BioSpec 70/30 USR dedicated for a small animal. All rats were under 1.5% isoflurane anesthesia during the scan after a 5% anesthesia induction.

All structural images were obtained at 15 months using the Bruker standard 3D-True Fast Imaging with Steady State Precession pulse sequence (3D-TruFISP). A root-mean-square image of 8 phases acquisition was performed. Each angle acquisition was acquired in a field-of-view of 36 mm x 36 mm x 36 mm with a matrix of 180x 180x 180x of TE/TR of 2.5/5.0 ms with a flip angle of 30° and NEX of 2. The final image was an average of the 16 acquisitions with a final 250  $\mu$ m isotropic resolution and a total acquisition time of 46 minutes scan.

All images were processed using MINC toolkits ([www.bic.mni.mcgill.ca/ServicesSoftware](http://www.bic.mni.mcgill.ca/ServicesSoftware)). All individual MRI images were aligned with rigid body transformation, affine, and nonlinear transformation, and matched to generate an average population-based template based on Pydipper [220].

Non-linear vector field was used to create a log Jacobian determinant for deformation-based morphometry (DBM) representing local volume difference in each subject [220]. Considering rodent brain has white matter in limited regions, these local changes in the neocortex were considered grey matter changes. Finally, 1mm FWHM smoothing was applied. Then DBM was transformed to a scalar as VBM values for ROI analysis. Last, three ROIs based on the Paxino & Watson atlas 6<sup>th</sup> edition were used: 1) temporal composite (Temp.Comp; bilateral temporal associative cortices and hippocampi), 2) Entorhinal cortices, and 3) hippocampi.

## **Fluid collection and analysis.**

### **Human CSF**

CSF collection, processing, and storage procedures have been described previously ([www.adni-info.org](http://www.adni-info.org)). CSF A $\beta$ <sub>42</sub> and CSF p-tau concentrations were measured using the Elecsys on a cobas e 601 analyzer as described previously [221, 222]. CSF NFL concentration was measured using a commercially available enzyme-linked immunosorbent assay (NF-light; Uman Diagnostics) as described by the manufacturer. The measurements were performed by board-certified laboratory technicians, who were masked to clinical data, using one batch of reagents. Intra-batch coefficients of variation were below 10%. Amyloid positivity was classified based on

the previously established CSF p-Tau/A $\beta$ <sub>42</sub> ratio cut-off threshold (CSF p-Tau/A $\beta$ <sub>42</sub> > 0.025) [222].

### **Human Plasma NFL**

Plasma NFL collection, processing, and storage procedures have been described previously ([www.adni-info.org](http://www.adni-info.org)). In brief, plasma NFL concentration was measured using an in-house single-molecule array (Simoa) method, as described previously in detail [223]. The measurements were performed by board-certified laboratory technicians, who were masked to clinical data, using one batch of reagents. For runs in this study, the coefficient of variations (CV) for the low (11.0 ng/L) quality control (QC) sample was 6.2% for intra-assay CV and 9.0% for inter-assay CV, while the corresponding values for the high (173.0 ng/L) QC sample were 4.9% for intra-assay CV and 7.2% for inter-assay CV.

### **Animals CSF**

All animals were anesthetized with a 5% isoflurane induction for 5-8 minutes and placed in a stereotaxic apparatus. The CSF samples (100 – 150  $\mu$ L) were collected via a direct puncture through the cisterna magna at 10 to 18 months of age.

Rat CSF NFL concentration was determined using the in-house Simoa NFL assay which has been described in detail previously [212], with some modifications. Briefly, samples were diluted 100x with assay diluent and incubated for 35 minutes with paramagnetic carboxylated beads (Quanterix Corp, Boston, MA, USA) coated with a mouse anti-neurofilament light

antibody (UD1, UmanDiagnostics, Umeå, Sweden) and a biotinylated mouse anti-neurofilament light antibody (UD2, UmanDiagnostics) in a Simoa HD-1 instrument (Quanterix). The bead-conjugated immunocomplex was thoroughly washed before incubation with streptavidin-conjugated  $\beta$ -galactosidase (Quanterix). Thereafter, the bead complex was washed and resorufin  $\beta$ -D-galactopyranoside (Quanterix) was added. The immunocomplex was applied to a multi-well array designed to enable imaging of every single bead. The average number of enzymes per bead (AEB) of samples was interpolated using the calibrator curve constructed by AEB measurements on bovine NFL (UmanDiagnostics) serially diluted in assay diluent. Samples were analyzed 'blind' and in duplicate using one batch of reagents. The average repeatability coefficient of variation of a sample with a mean concentration of 18102 pg/mL was 8.5% and intermediate precision was 8.8%, and for a sample with a mean concentration of 9460 pg/mL, repeatability was 8.1% and intermediate precision was 11.5%. All samples analyzed were above the lower limit of quantification (LLoQ).

Rat CSF concentrations of  $A\beta_{42}$  and  $A\beta_{40}$  were measured using Quanterix kits according to kit instructions (Simoa  $A\beta_{42}$  2.0 211 and Simoa  $A\beta_{40}$  2.0 218, Quanterix) with a CSF dilution of 100x using the provided assay diluents. For  $A\beta_{42}$  CSF measurements, the average repeatability coefficient of variation of a sample with a mean concentration of 1650 pg/mL was 3.2% and intermediate precision was 9.2%, and for a sample with a mean concentration of 641 pg/mL, repeatability was 10.9% and intermediate precision was 16.6%. For  $A\beta_{40}$  CSF measurements, repeatability for a sample with a concentration of 5160 pg/mL was 17.2%, and intermediate precision 17.2%, and for a sample with a concentration of 3975 pg/mL repeatability and intermediate precision was 7.3% and 11.8%, respectively. For both assays, a number of samples

were below the assigned assay limit of quantification and assigned a concentration of half of the LLoQ.

## **Statistical Analysis**

The potential difference in the number of males and females in each group was tested based on a chi-square test for both humans and animals as well as APOE $\epsilon$ 4 status in humans. We also tested whether there were differences in age, education, and MMSE scores for humans based on a two-sided ANOVA. We tested if WT and Tg had any difference in age using an unpaired two-sided t-test. We log-transformed NFL in CSF and plasma, as well as CSF A $\beta$ <sub>42</sub> and p-tau.

In animals, linear mixed effect models with a random intercept were performed to measure longitudinal changes in CSF A $\beta$ <sub>42/40</sub> and CSF NFL log: 1) CSF A $\beta$ <sub>42/40</sub> ~ Age + (1|animals); 2) CSF NFL (log) ~ Age (WT or Tg) + (1|animals); 3) CSF NFL (log) ~ Age + Genotype + Age\*Genotype + (1|animals). The association between CSF NFL and CSF A $\beta$ <sub>42/40</sub> was investigated based on a linear regression model. Weight was retained as a variable only in the model showing the association between CSF NFL and CSF A $\beta$ <sub>42/40</sub> as it was shown to have a significant effect.

In animals and humans, voxel-based linear regression models were performed to detect the group contrast in DBM and VBM, respectively. Furthermore, a voxel-based linear regression was performed between DBM and CSF NFL log at 15 months for animals, and VBM and CSF or plasma NFL levels for humans: animal model: CSF NFL log ~ DBM; human model: NFL (CSF or plasma) ~ VBM + covariates in each group as well as combining all groups with adjusting for

the diagnosis. Similarly, we used those same models as the voxel-based models to replicate the previous findings using the Temp.Comp, entorhinal, and hippocampus ROIs with FDR correction for animals and humans [197, 207, 213]. In addition, we applied bootstrapping technique in the group that showed a significant association between NFL and VBM, running the standardized ROI-based models 2000 times to compare the effect size between A $\beta$ - vs A $\beta$ +. All voxel-based and ROI-based analyses and linear regression models examining the grey matter density and NFL concentrations in humans were corrected for age, sex, APOE $\epsilon$ 4 status, education, CSF p-tau (log), and the difference in dates between the NFL measurements and MRI scan. Furthermore, an additional CSF A $\beta$ <sub>42</sub>:p-tau interaction term was tested to exclude the effect of p-tau and A $\beta$ <sub>42</sub> interaction when the term was significant.

All voxel-based analyses were conducted using VoxelStats and corrected for multiple comparisons using random field theory with peak threshold at  $p = 0.05$  and cluster threshold at  $p = 0.05$  for rats and  $p = 0.005$  for humans [224]. All the statistical analyses were conducted using R 3.4.4 (<https://www.r-project.org/>).

## Results

### Demographic

Table 4 summarizes the demographic of the participants included in the study. There was no difference in age or education between groups. However, the number of males and females was different between CN A $\beta$ + vs MCI A $\beta$ - and MCI A $\beta$ - vs AD A $\beta$ +. APOE $\epsilon$ 4 status was different between groups except for CN A $\beta$ - vs MCI A $\beta$ -, CN A $\beta$ + vs MCI A $\beta$ +, and MCI A $\beta$ +

vs AD Aβ+. Furthermore, the average MMSE score was not different between CN Aβ- vs CN Aβ+ and MCI Aβ- vs MCI Aβ+, whereas all other comparisons showed significant differences.

For the animal data, there was no difference in age, sex, or weight (Table 5).

**Table 4.** Study 1 human demographics

<b>Groups</b>	<b>CN (n=83)</b>	<b>CN Aβ- (n=66)</b>	<b>CN Aβ+ (n=17)</b>	<b>MCI (n=160)</b>	<b>MCI Aβ- (n=48)</b>	<b>MCI Aβ+ (n=112)</b>	<b>AD Aβ+ (n=73)</b>
<b>Age (years)</b>	75.90 ± 5.47	75.65 ± 5.36	76.91 ± 5.95	74.61 ± 7.53	75.27 ± 7.99	74.32 ± 7.34	74.03 ± 7.64
<b>Sex (M/F)</b>	44/39	32/34	12/5	111/49	39/9 a**	72/40	42/31 c*
<b>APOEε4 carrier (%)</b>	17 (20.5%)	6 (9.1%)	11 (64.7%) a***	82 (51.3%)	9 (23.1%) b**	73 (65.2%) a***, c***	57 (78%) a***, b**, c***
<b>Education</b>	15.77 ± 2.83	15.58 ± 2.73	16.53 ± 3.16	15.72 ± 3.03	15.90 ± 3.16	15.64 ± 2.99	14.95 ± 3.25
<b>MMSE</b>	28.99 ± 1.10	29.00 ± 1.12	28.94 ± 1.03	26.96 ± 1.79	27.33 ± 1.68 a***, b**	26.79 ± 1.82 a***, b***	23.56 ± 1.74 a***, b***, c***, d***

CN, cognitively normal; MCI, mild cognitive impairment; AD, Alzheimer's Disease; Aβ-, amyloid-beta negative, Aβ+, amyloid-beta positive, MMSE, mini-mental state examination. All values are indicated as mean ± standard deviation except for sex and APOEε4. The *p*-value indicates the value assessed with analyses of variance (ANOVA) among Aβ- and Aβ+ CN, MCI, and AD for each variable except for sex and APOEε4, where a contingency chi-square test was performed with false discovery rate multiple corrections. Post-hoc Bonferroni analysis provided significant differences between groups: <sup>a</sup> from CN Aβ-; <sup>b</sup> CN Aβ+; <sup>c</sup> MCI Aβ-; <sup>d</sup> MCI Aβ+; \* = *p* < 0.05, \*\* = *p* < 0.005; \*\*\* = *p* < 0.0001.

**Table 5.** Study 1 animal demographics

<b>Groups</b>	<b>WT (n = 5)</b>	<b>Tg (n = 8)</b>
Age (months)	10 – 18	10 – 18
Sex (M/F)	3/2	6/2
Weight (g)	583.7 ± 260.2	601.2 ± 161.8

### **Longitudinal CSF biomarker changes and their association and grey matter changes in animals**

In McGill-Thy1-APP Tg rats only, a linear mixed effect analysis showed a significant longitudinal decline in CSF A $\beta_{42/40}$  from 10 months to 18 months ( $\beta = -0.01$ , standard error (s.e) = 0.0045,  $t(63) = -2.09$ ,  $p = 0.041$ ) (Figure 23). On the other hand, the longitudinal CSF NFL concentration significantly increased in both WT ( $\beta = +0.05$ , s.e = 0.012,  $t(27) = 4.06$ ,  $p = 0.0004$ ) and Tg ( $\beta = +0.04$ , s.e = 0.006,  $t(64) = 5.63$ ,  $p < 0.0001$ ) (Figure 23). When we analyzed both groups into one model by including an interaction term between the group and time, the CSF NFL concentration was progressively increased over time ( $\beta = +0.05$ , s.e = 0.01,  $t(93) = 4.38$ ,  $p < 0.0001$ ) while Tg had a significantly greater CSF NFL concentration compared to WT ( $\beta = +0.43$ , s.e = 0.2,  $t(90) = 2.14$ ,  $p = 0.035$ ) (Figure 23). However, the interaction between the genotype effect and longitudinal change in CSF NFL concentration was not significant. Similar to previous human findings, the significant inverse association between CSF NFL and CSF A $\beta_{42/40}$  was observed when adjusted for weight ( $\beta = -0.5$ , s.e = 0.2,  $t(68) = -2.40$ ,  $p = 0.02$ ) (Figure 23).

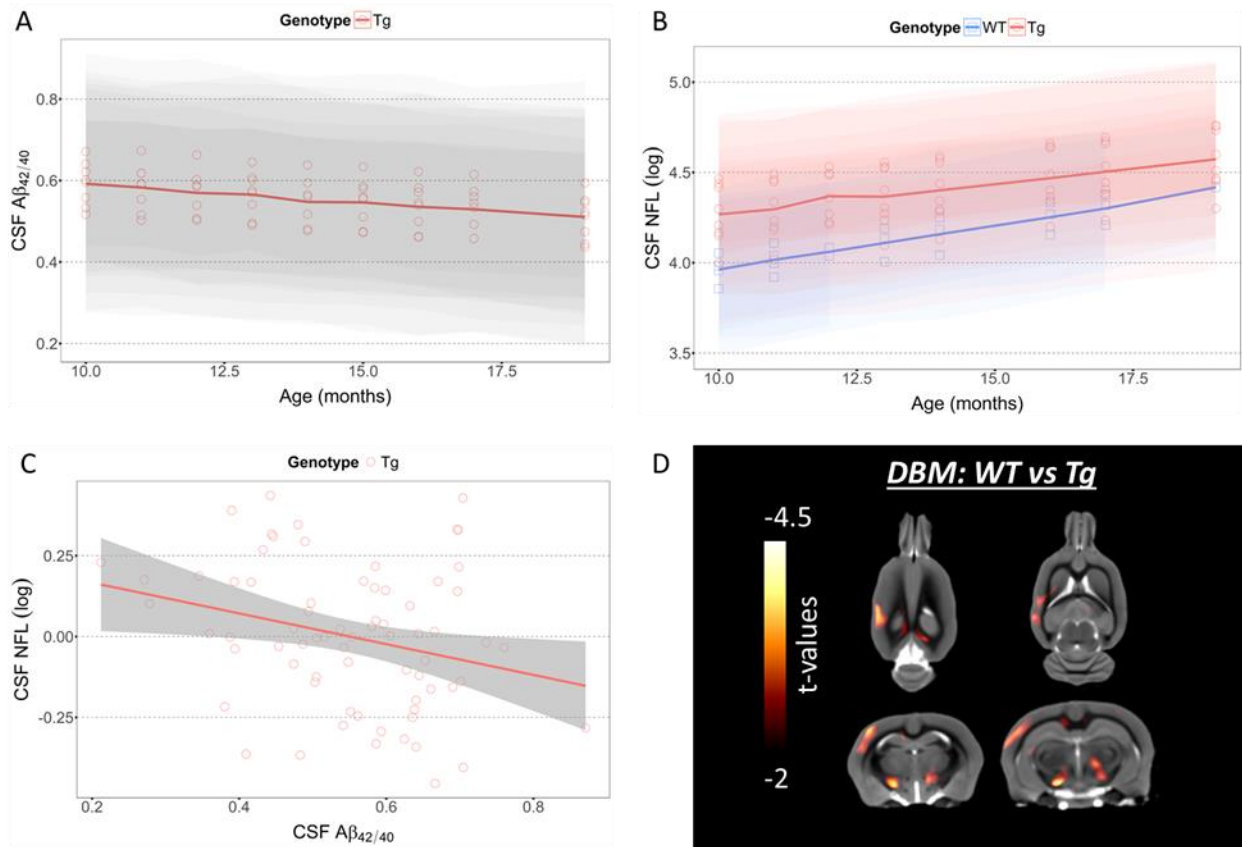


**Figure 23.**  $A\beta$  and neurodegeneration biomarkers and their associations in the McGill-R-Thy1-APP rat model.

A-B) Longitudinal analyses on CSF  $A\beta_{42/40}$  and NFL concentrations, C) an association between CSF  $A\beta_{42/40}$  and NFL concentration, and D) voxel-based group contrast between WT and Tg in DBM with the t-statistic scale. The shades in the regression lines represent 95% confidence intervals of the model.

Voxel-based group contrast in DBM at 15 months showed significant reduction in parietotemporal cortex ( $t(11) = 3.2$ ,  $p = 0.008$ ), bilateral dorsal hippocampi ( $t(11) = 2.3$ ,  $p = 0.042$ ), and striatum in Tg compared to WT with the greatest contrast seen in thalamus ( $t(11) = 5$ ,  $p = 0.0004$ ) (Figure 23, Supplementary Figure 1, and Supplementary Table 1).

### **CSF NFL and DBM association is modulated by amyloid in AD-vulnerable regions in Tg**

Increased CSF NFL concentration was significantly associated with reduced DBM only in Tg, encompassing the parietotemporal cortex, hippocampus, striatum, thalamus, and cerebellum in the voxel-based analysis. The greatest effect was observed in the parietotemporal cortex ( $t(6) = 13$ ,  $p = 0.0001$ ) and hippocampus ( $t(6) = 8$ ,  $p = 0.0002$ ) (Figure 24, Supplementary Figure 2, and Supplementary Table 2). The ROI-based linear regression analyses revealed significant negative associations between CSF NFL concentration and the Temp.Comp VBM ( $\beta = -4.09$ ,  $s.e = 1.29$ ,  $t(6) = -3.18$ ,  $p = 0.037$ ), entorhinal cortex ( $\beta = -3.50$ ,  $s.e = 1.17$ ,  $t(6) = -2.99$ ,  $p = 0.037$ ), and hippocampus VBM ( $\beta = -3.90$ ,  $s.e = 1.58$ ,  $t(6) = -2.47$ ,  $p = 0.048$ ) only in Tg while WT showed no association. (Figure 24).

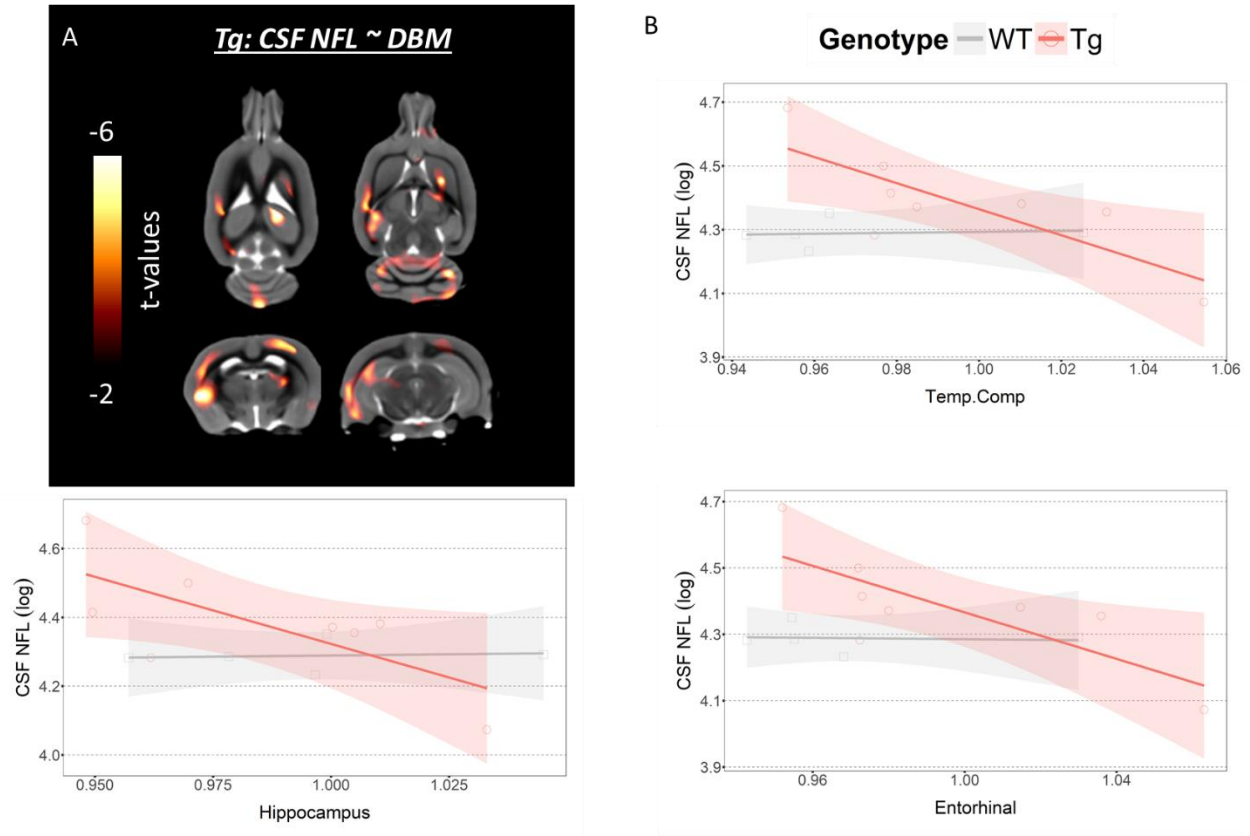


**Figure 24.** The associations between CSF NFL and DBM.

The association between CSF NFL concentration and DBM at 15 months of age in Tg with the t-statistic scale. B) The association between CSF NFL concentration and ROIs from Temp.Comp, entorhinal, and hippocampus VBM in WT and Tg. The shades in the regression lines represent 95% confidence intervals of the model.

### **VBM is reduced in AD-vulnerable regions in humans**

A voxel-based group contrast on VBM between CN and MCI revealed a significant reduction in the hippocampus, precuneus/posterior cingulate cortex (PCC), medial frontal cortex, and lateral temporal cortex (Figure 25, Supplementary Figure 3, and Supplementary Table 3). The greater difference was seen in CN and AD contrast where the clusters extended to the orbital frontal cortex, basal lateral temporal cortex (including entorhinal cortex), as well as the parahippocampal gyrus (Figure 25, Supplementary Figure 4, and Supplementary Table 4). When

we compared MCI and AD, the latter showed a significant VBM reduction in precuneus/PCC, medial frontal cortex, basal lateral temporal cortex, inferior parietal cortex, and hippocampus (Figure 25, Supplementary Figure 5, and Supplementary Table 5.). Within the same clinical diagnostic group, CN and MCI showed a difference where CN  $A\beta+$  had a greater VBM reduction in the medial frontal cortex and MCI  $A\beta+$  had greater VBM reduction in the medial frontal cortex, lateral temporal cortex, and right hippocampus compared to the counter  $A\beta-$  group, respectively (Figure 25, Supplementary Figure 6-7, and Supplementary Table 6-7).

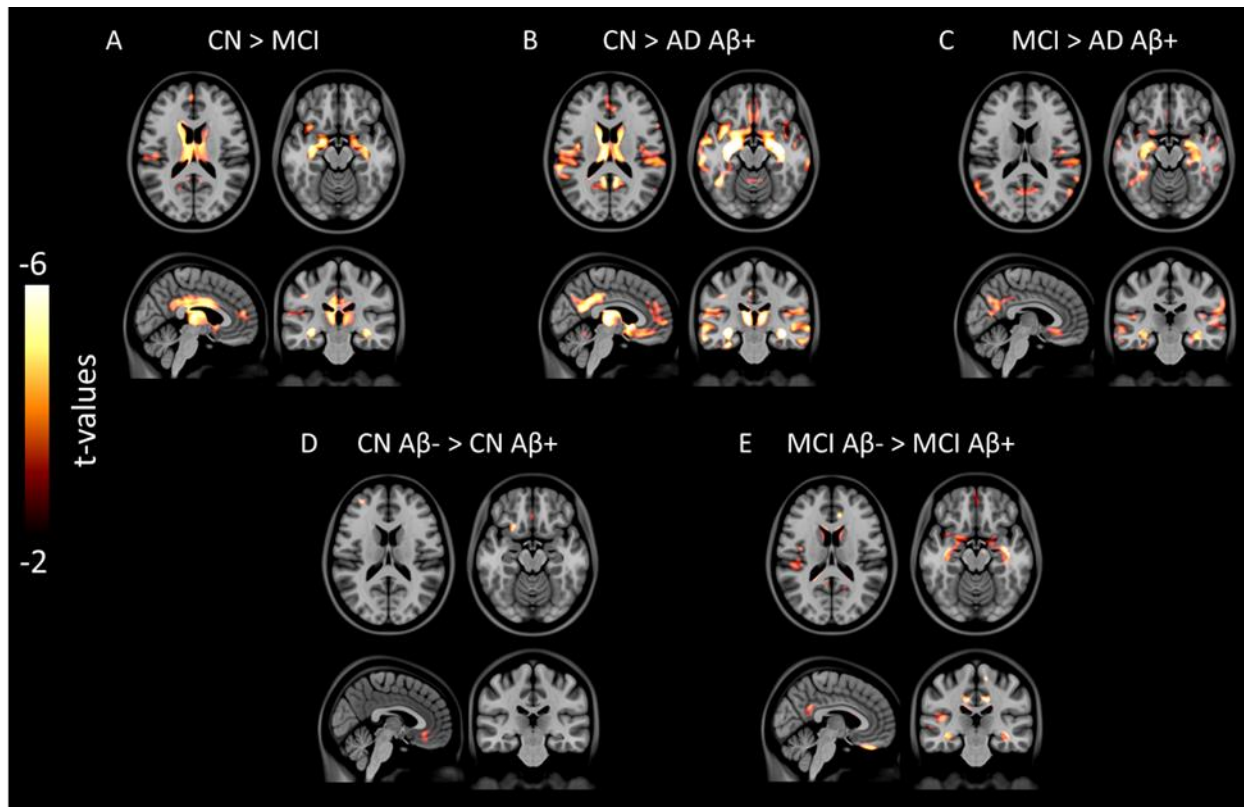


*Figure 25. VBM group comparisons.*

Significant group contrast maps showing the difference in the VBM between A) CN and MCI, B) CN and AD  $A\beta+$ , C) MCI and AD  $A\beta+$ , and D) CN  $A\beta-$  and  $A\beta+$  E) MCI  $A\beta-$  and MCI  $A\beta+$ . All of the result images are represented on the same t-statistic scale.

## **The NFL concentration and VBM association is modulated by amyloid in AD-vulnerable regions in humans**

In MCI A $\beta$ <sup>+</sup> cases, increased CSF NFL concentration was significantly associated with reduced VBM in the orbitofrontal cortex, lateral temporal cortex, precuneus/PCC, hippocampus and thalamus based on the voxel-based analysis (Figure 26, Supplementary Figure 8, and Supplementary Table 8). Also, increased plasma NFL concentration was significantly associated with reduced VBM in the lateral temporal cortex and right hippocampus ( $t(99) = -3.3$ ,  $p = 0.0034$ ) in MCI A $\beta$ <sup>+</sup> (Figure 26, Supplementary Figure 9, and Supplementary Table 9). The ROI-based linear regression analyses revealed significant negative associations between CSF NFL concentration and the Temp.Comp VBM ( $\beta = -0.93$ ,  $s.e = 0.39$ ,  $t(104) = -2.38$ ,  $p = 0.018$ ), entorhinal cortex VBM ( $\beta = -0.85$ ,  $s.e = 0.32$ ,  $t(104) = -2.51$ ,  $p = 0.015$ ), and both CSF and Plasma NFL were associated with hippocampus VBM ( $\beta = -0.90$ ,  $s.e = 0.20$ ,  $t(104) = -4.59$ ,  $p < 0.0001$ ;  $\beta = -0.70$ ,  $s.e = 0.24$ ,  $t(99) = -3.03$ ,  $p < 0.013$ , respectively) in MCI A $\beta$ <sup>+</sup> (Figure 26). In the MCI A $\beta$ <sup>+</sup>, only the plasma NFL and ROI-VBM analyses showed a significant CSF A $\beta$ <sub>42</sub>:p-tau interaction. Even when this term was included the results stayed the same.

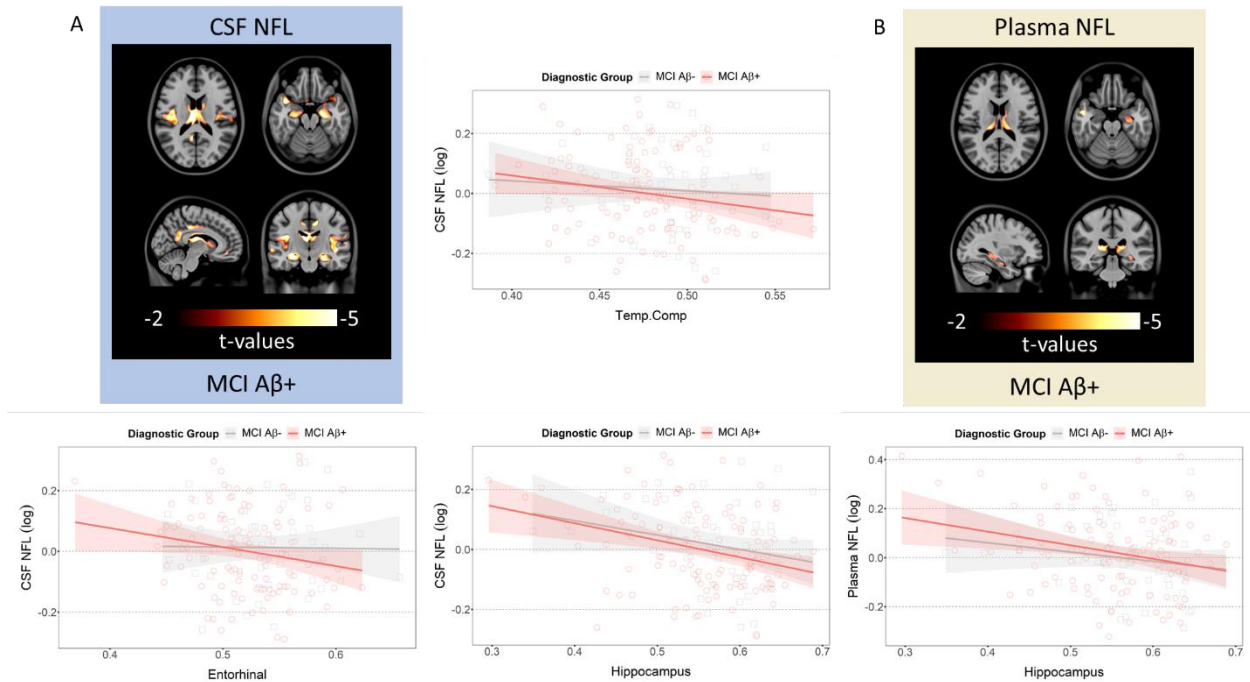


**Figure 26.** The associations between NFL and VBM in MCI A $\beta$ - and A $\beta$ +

A) Voxel-based maps showing significant associations between CSF NFL concentration and VBM in MCI A $\beta$ + and ROI-based analyses in MCI A $\beta$ - (in grey) and MCI A $\beta$ + (in red) showing the association between CSF NFL and Temp.Comp, Entorhinal cortex, or hippocampus. B) Voxel-based maps showing significant associations between plasma NFL concentration and VBM in MCI A $\beta$ + and ROI-based analyses in MCI A $\beta$ - (in grey) and MCI A $\beta$ + (in red) showing the association between plasma NFL and hippocampus.

In AD A $\beta$ +, both CSF and plasma NFL levels were significantly associated with VBM results in dorsal lateral frontal cortex, lateral temporal cortex, precuneus/PCC, medial frontal cortex, angular gyrus, hippocampus, and cerebellar grey in the voxel-based analyses (Figure 27, Supplementary Figure 10-11, and Supplementary Table 10-11). Moreover, CSF NFL levels were significantly associated with occipital gyrus VBM measurements in AD A $\beta$ + (Figure 27). The ROI-based linear regression analyses revealed significant negative associations between CSF and the Temp.Comp VBM ( $\beta = -1.15$ , s.e = 0.44,  $t(65) = -2.69$ ,  $p = 0.016$ ) and hippocampus VBM ( $\beta$

= -0.82, s.e = 0.20,  $t(65) = -3.99$ ,  $p < 0.0001$ ) while plasma NFL and VBM in the Temp.Comp and hippocampus ROIs showed a small trend ( $t(61) = -1.88$ ,  $t(61) = -1.81$ , respectively,  $p = 0.15$ ).

Although CN A $\beta$ <sup>-</sup> and A $\beta$ <sup>+</sup> and MCI A $\beta$ <sup>-</sup> groups showed a significant association between NFL and VBM, the RFT-survived clusters were small. CN A $\beta$ <sup>-</sup> showed a negative association between CSF NFL and lateral front-orbital cortex while CN A $\beta$ <sup>+</sup> showed in the cingulate cortex (Supplementary Figure 12-13 and Supplementary Table 12-13). MCI A $\beta$ <sup>-</sup> group showed a negative association between plasma NFL and VBM in the insular cortex only (Supplementary Figure 14 and Supplementary Table 14). When combining all the groups and adjusting for the diagnosis, only the A $\beta$ <sup>+</sup> group showed a negative association between CSF or plasma NFL and precuneus/PCC, basolateral temporal cortex, medial frontal cortex, and striatum (Supplementary Figure 15-16 and Supplementary Table 15-16).

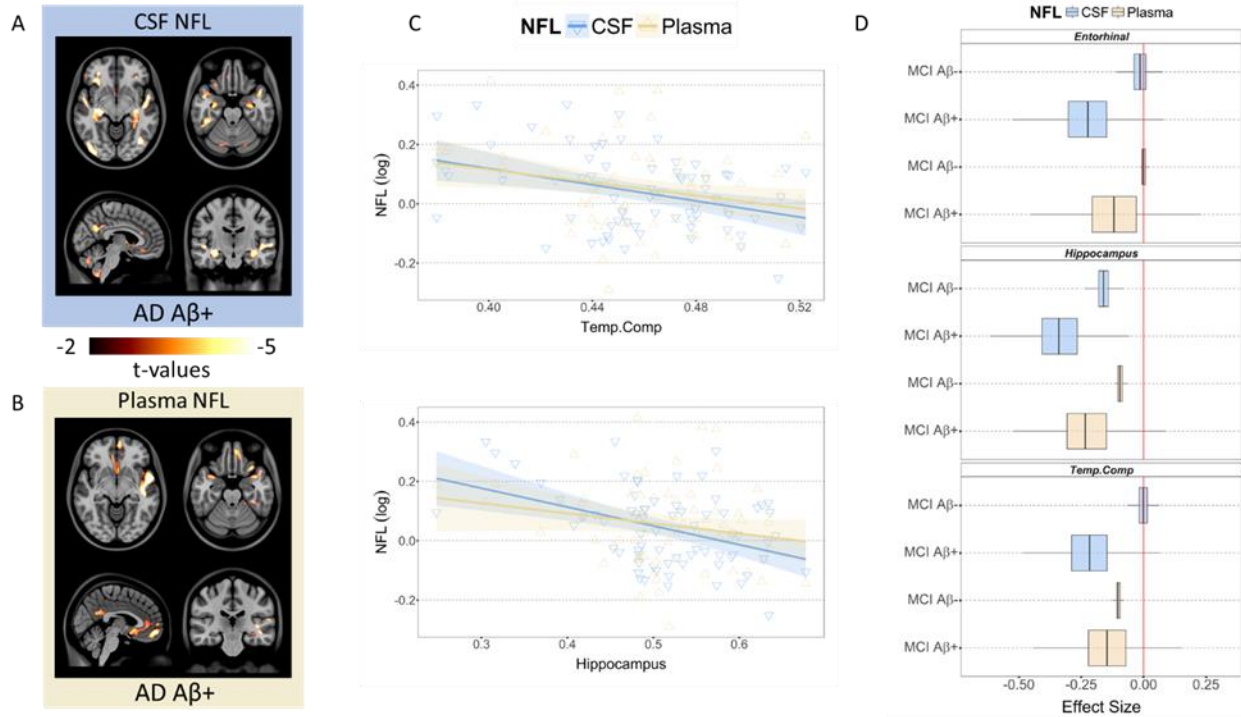


**Figure 27.** The associations between NFL and VBM in AD and NFL effect sizes.

Voxel-based maps showing significant associations between A) CSF NFL concentration and VBM, B) plasma NFL concentration and VBM, and C) the association between CSF NFL (blue) or plasma NFL (yellow) and Temp.Comp or hippocampus ROIs in AD A $\beta$ +. The shades represent a 95% confidence interval of the regression models. D) Bootstrap analysis showing the difference in the effect sizes between MCI A $\beta$ + and A $\beta$ - in CSF or plasma NFL association with VBM.

### Greater effect sizes in A $\beta$ + groups and CSF-NFL

To compare the effect size of the association between CSF or plasma NFL and VBM in A $\beta$ - and A $\beta$ +, we applied bootstrapping to run the standardized ROI-based models 2000 times while matching the number of subjects between MCI A $\beta$ - and A $\beta$ +. We selected the MCI group to compare because MCI A $\beta$ + showed significant results from the ROI analyses. In all three ROIs, MCI A $\beta$ + showed greater effect size in both CSF and plasma NFL and VBM associations compared to MCI A $\beta$ - (Figure 27). This corresponds with our animal results where only the Tg

group showed significant associations between CSF NFL and VBM in the homologous ROIs (Figure 24). In addition, we applied bootstrapping to run standardized ROI-based models 2000 times in MCI A $\beta$ <sup>+</sup> and AD A $\beta$ <sup>+</sup>. This revealed the association between CSF NFL and VBM had greater effect sizes in most of the regions compared to the association between plasma NFL and VBM (Supplementary Figure 17).

## Discussion

In this present study, we found an unbiased voxel-based association between NFL concentrations and grey matter density maps in A $\beta$  pathology in humans and animals. NFL has been reported to be a novel neuronal injury or neurodegeneration biomarker but previous studies have only focused on the association between NFL concentrations and *a priori* ROIs volume over regions typically affected by AD [198, 207, 213]. Assessing the association between NFL concentrations and grey matter changes over the brain allowed us to probe whether the levels of NFL are driven by AD-vulnerable regional neuronal injury or age-related neurodegeneration. Based on our empirical evidence from human and Tg animal model analyses, the A $\beta$  was sufficient to elevate NFL levels and reduce grey matter density and they were associated in AD-vulnerable regions in the presence of A $\beta$  pathology.

Considering that the level of NFL is influenced by other pathophysiological processes (ie. tau pathology, neuroinflammation) that also are invariably present in clinically manifested AD, it is difficult to fully dissect the degree of contribution from A $\beta$  alone on NFL concentration [196, 204, 206, 225]. Therefore, in this study, we investigated Tg rats with the McGill-R-Thy1-APP model in parallel with the human analyses, using the same methodological approach. Previously,

this rat model was shown to have minimal cell death at 18 months of age, reduction in hippocampal volume, and loss of resting-state cingulate connectivity at 16-19 months of age in the presence of A $\beta$  pathology but without tau pathology [89, 158, 160]. This most likely reflects the synaptic dysfunction, neuronal injury, and network dysfunction caused by A $\beta$  rather than cell death [76, 158, 160]. Here, our results revealed significant DBM results in the neocortex at 15 months of age and increased CSF NFL concentration in Tg as compared to WT. Therefore, this study strongly supports the notion that the A $\beta$  pathology alone is sufficient to induce neuronal injury with minimal cell death. Association between the A $\beta$ -induced CSF NFL concentrations increase and the DBM measurements reduction was evident in the neocortex and hippocampus where the A $\beta$  pathology is prominent in this animal model. This strongly supports our findings that NFL reflects neuronal injury in AD-related regions in the presence of A $\beta$  pathology.

In addition, our novel findings from the first longitudinal animal CSF analyses revealed that the CSF NFL concentration significantly increased during the healthy aging process as indicated by the results in WT. Also, the CSF A $\beta_{42/40}$  significantly decreased while CSF NFL concentration was significantly increased in Tg animals, showing the inverse relationship between the two biomarkers, thereby replicating the human finding [207]. Considering that the McGill-R-Thy1-APP Tg rat model displays only A $\beta$  pathology without tau pathology, we demonstrated a modest but significant A $\beta$  effect on CSF NFL concentration in Tg compared to WT without the potential effect of tau pathology. Importantly, there was no significant interaction effect between genotype and age. This Tg model has been reported to start accumulating A $\beta$  plaques between the age of 6 to 9 months; the soluble forms of A $\beta$  oligomers dominate prior to this point [89, 158, 226]. Here, we showed that CSF NFL concentration was already elevated before 10 months and remained high throughout the time over which we

collected our samples. This most likely represents the neurotoxic events induced by soluble A $\beta$  oligomers, which in turn increase CSF NFL concentration during the early stage of the pathology in this animal model [76]. Therefore, our study suggests that the association between A $\beta$  and CSF NFL level is established at an early stage of the pathology. Interestingly, it has been reported that there is a significant interaction between age and genotype on CSF NFL concentration in an APPPS1 mice model [208]. The discrepancy with our results could be due to much more aggressive A $\beta$  pathology accumulation in the APPPS1 mice model as compared to the McGill-R-Thy1-APP rat model, in which the A $\beta$  pathology develops at an equivalent rate as seen in the humans in the McGill-R-Thy1-APP rat model [158]. Our longitudinal findings are in agreement with the other recently published longitudinal NFL measurements findings indicating that the rate of serum NFL change increases during the pre-clinical phase of the disease but plateaus before symptoms onset in familial AD and that CSF NFL levels over time follow a U-shaped curve in sporadic AD [198, 227]. Nonetheless, the animal models of A $\beta$  pathology concurringly argue that A $\beta$  pathology leads to the increased CSF NFL concentration.

Neuronal injury or neurodegeneration is not an AD-specific process. Besides AD, increased levels of NFL are also reported in other neurodegenerative conditions such as frontotemporal dementia, progressive supranuclear palsy, and Creutzfeldt-Jakob disease [205, 206, 209, 228, 229]. However, an increasing number of large-scale network analyses have shown a disease-specific vulnerability in an ensemble of regions for each of them [185, 214]. Thus, it is imperative to study if an increased level of a fluid biomarker reflecting neuronal injury or neurodegeneration is linked to anomalies within the network affected by a given disease. Recent evidence based on the association between NFL levels and VBM measurements was in agreement with other studies using *a priori* defined ROIs in frontotemporal lobar degeneration

and Huntington's disease, showing that increased NFL concentration was associated with reduced frontal cortex and striatum VBM measurements, respectively. This supports the hypothesis that indeed increased NFL concentrations in those diseases follow neuronal injury in their specific network [206, 209]. To the best of our knowledge, our study is the first to describe voxel-based associations between the NFL levels and VBM measurements in regions targeted specifically by AD. We show that the elevated NFL concentration is associated with reduced VBM measurements in the presence of A $\beta$  pathology in the precuneus/PCC, medial frontal cortex, lateral temporal cortex, inferior parietal cortex, and hippocampus, which are all considered to be AD-vulnerable regions. It is important to note that these cortical regions also form the default mode network on which AD pathological, functional, and structural abnormalities converge, leading to network failure [48, 185, 230-232]. We dichotomized A $\beta$  pathology based on the previously used cut-off points and included covariates, such as CSF p-tau and/or CSF A $\beta$ <sub>42</sub>:p-Tau interaction that could potentially confound the association between NFL levels and grey matter density maps, and yet, we found correlations only in the A $\beta$  positive groups and in the AD-vulnerable regions [222]. The reason why these regions are vulnerable to AD still remains poorly understood.

There are some important limitations to this study. Due to the modest effect size in the association between NFL concentration and grey matter density maps, the available number of individuals who have both CSF and plasma NFL concentration and MRI data in the ADNI database is overall low, which limited the statistical power of our study. Perhaps this weakness could explain why we observed a minimal association in CN A $\beta$ <sup>+</sup>. Future studies with a greater number of participants and longitudinal data would be of interest. Another possible reason for the minimal association in CN A $\beta$ <sup>+</sup> maybe because some cognitively normal elderly individuals

with high A $\beta$  pathology might actually have minimal levels of toxic soluble A $\beta$  oligomers [84]. Indeed, our animal results suggest that the increase in CSF NFL concentration occurs most likely due to the presence of soluble A $\beta$  oligomers as opposed to that of plaques [76, 226]. In addition, we corrected the analysis for CSF p-tau levels and/or CSF A $\beta$  and p-tau interaction to exclude a potential effect of tau pathology on the association between NFL levels and grey matter density maps. However, it would be interesting to include tau-PET imaging data in a future study as it would allow controlling for the different tau loads in different brain regions. Regarding our animal data, although the number of animals in WT and Tg cohorts was not significantly different initially, some of the WT animals developed pituitary tumours during the course of the study. An exploratory analysis revealed that this condition to be a confounding factor due to the significantly increased CSF NFL concentration in the animals that developed those pituitary tumours as compared to the healthy animals (data not included). Therefore, they were excluded from the group comparison analysis.

In summary, our evidence supports that elevated NFL levels in AD result from A $\beta$ -induced neuronal injury in AD-vulnerable regions. NFL is a sensitive biomarker capable of detecting the modest levels of neuronal injury linked to the healthy aging process or pure A $\beta$  pathology. As such, our study supports the hypothesis that NFL is a novel biomarker of neuronal injury and neurodegeneration that may be utilized within the A/T/(N) classification scheme and for the evaluation of therapeutic efficacy in clinical trials.

## **Acknowledgements**

The authors would like to send gratitude to Eve-Marie Charbonneau and her animal facility team for their technical support with animal care. This work was supported by the Canadian Institutes of Health Research (CIHR; FRN, 152985, PR-N), the Alzheimer's Association (NIRP-12-259245, PR-N), Fonds de Recherche du Québec – Santé (FRQS; Chercheur Boursier, PR-N). ACC acknowledges support from the Canadian Institutes for Health Research (CIHR grant-2016PJT-364544). KB holds the Torsten Söderberg Professorship in Medicine at the Royal Swedish Academy of Sciences and is supported by the Swedish Research Council (#2017-00915), the Swedish Alzheimer Foundation (#AF-742881), Hjärnfonden, Sweden (#FO2017-0243), and a grant (#ALFGBG-715986) from the Swedish state under the agreement between the Swedish government and the County Councils, the ALF-agreement. HZ is a Wallenberg Academy Fellow supported by grants from the Swedish Research Council (#2018-02532), the European Research Council (#681712), Swedish State Support for Clinical Research (#ALFGBG-720931) and the UK Dementia Research Institute at UCL. Data collection and sharing for this project were funded by the Alzheimer's Disease Neuroimaging Initiative (ADNI) (National Institutes of Health Grant U01 AG024904) and DOD ADNI (Department of Defense award number W81XWH-12-2-0012). ADNI is funded by the National Institute on Aging, the National Institute of Biomedical Imaging and Bioengineering, and through generous contributions from the following: AbbVie, Alzheimer's Association; Alzheimer's Drug Discovery Foundation; Araclon Biotech; BioClinica, Inc.; Biogen; Bristol-Myers Squibb Company; CereSpir, Inc.; Cogstate; Eisai Inc.; Elan Pharmaceuticals, Inc.; Eli Lilly and Company; EuroImmun; F. Hoffmann-La Roche Ltd and its affiliated company Genentech, Inc.; Fujirebio; GE Healthcare; IXICO Ltd.; Janssen Alzheimer Immunotherapy Research &

Development, LLC.; Johnson & Johnson Pharmaceutical Research & Development LLC.; Lumosity; Lundbeck; Merck & Co., Inc.; Meso Scale Diagnostics, LLC.; NeuroRx Research; Neurotrack Technologies; Novartis Pharmaceuticals Corporation; Pfizer Inc.; Piramal Imaging; Servier; Takeda Pharmaceutical Company; and Transition Therapeutics. The Canadian Institutes of Health Research is providing funds to support ADNI clinical sites in Canada. Private sector contributions are facilitated by the Foundation for the National Institutes of Health ([www.fnih.org](http://www.fnih.org)). The grantee organization is the Northern California Institute for Research and Education, and the study is coordinated by the Alzheimer's Therapeutic Research Institute at the University of Southern California. ADNI data are disseminated by the Laboratory for Neuro Imaging at the University of Southern California.

### **Conflict of Interests**

KB has served as a consultant or at advisory boards for Alector, Biogen, CogRx, Lilly, MagQu, Novartis and Roche Diagnostics, and is a co-founder of Brain Biomarker Solutions in Gothenburg AB, a GU Venture-based platform company at the University of Gothenburg.

HZ has served at scientific advisory boards of Roche Diagnostics, Wave, Samumed and CogRx, has given lectures in symposia sponsored by Biogen and Alzecure, and is a co-founder of Brain Biomarker Solutions in Gothenburg AB, a GU Ventures-based platform company at the University of Gothenburg.

## **12.2.2 Study 2: The interaction between amyloid-beta and activated microglia drives tau propagation in Alzheimer's disease.**

**Authors:** Min Su Kang<sup>1,2,3</sup>, Julie Ottoy<sup>1</sup>, Gleb Bezgin<sup>1,2</sup>, Sulantha Mathotaarachchi<sup>1,2</sup>, Melissa Savard<sup>1,2</sup>, Mira Chamoun<sup>1,2</sup>, Tharick A. Pascoal<sup>1,2</sup>, Joseph Therriault<sup>1,2</sup>, Firoza Lussier<sup>1,2</sup>, Jenna Stevenson<sup>1,2</sup>, Nesrine Rahmouni<sup>1,2</sup>, Jean-Paul Soucy<sup>3</sup>, A. Claudio Cuello<sup>4,5</sup>, Gassan Massarweh<sup>3</sup>, Serge Gauthier<sup>1,2</sup>, Pedro Rosa-Neto<sup>1,2,3,\*</sup>

**Affiliation:** Translational Neuroimaging laboratory - McGill University Research Centre for Studying in Aging<sup>1</sup>, Cerebral Imaging Centre – Douglas Research Centre<sup>2</sup>, McConnell Brain Imaging Centre – McGill University<sup>3</sup>, Department of Pharmacology and Therapeutics – McGill University<sup>4</sup>, Department of Pharmacology – Oxford University<sup>5</sup>

Submitted to Science Advances.

## Abstract

Amid evidence supporting tau propagation via connected neurons, a new framework from genetic and preclinical studies has demonstrated activated microglia as a driver of tau pathology in Alzheimer's disease (AD). Here, we investigated the new framework in living individuals within A/T/(N) classification (amyloid-beta negative ( $A\beta$ -Tau-) and AD continuum ( $A\beta$ +Tau-/++)) using *in vivo* positron emission tomography. We found that the interactive effect between  $A\beta$  and activated microglia predicted tau burden at a local-to-local and local-to-distal level. Multivariate analyses revealed activated microglia in the medial inferior temporal cortex and global  $A\beta$  predicted tau propagation throughout Braak stages 1-4, leading to cognitive decline in the AD continuum group. In contrast, activated microglia showed relatively balanced and neuroprotective effects on tau and cognition, respectively, in the  $A\beta$ - group. This study highlights the multidimensional roles of activated microglia that are modulated by  $A\beta$ , leading to tau propagation and cognitive decline. Future clinical trials targeting activated microglia should consider  $A\beta$  load and may provide greater benefit as a combination therapy.

## Introduction

Microglia are the most abundant cells (10-15%) and respond first as part of the innate immune system in the central nervous system [233, 234]. In physiological conditions, microglia exhibit a resting phenotype and play a role in synaptogenesis, neurogenesis, and release of neurotrophic factors [88, 120-122]. However, when the homeostasis of the microenvironment is disturbed due to an injury or pathological aggregate, microglial cells shift into active phenotypes secreting pro-inflammatory cytokines, chemokines, and reactive oxidants [88, 120]. Although acute inflammatory responses provide numerous benefits, the chronic release of pro-inflammatory signals by activated microglia has shown detrimental effects and further exacerbated the neuronal injury in Alzheimer's disease (AD) [88]. Indeed, numerous genome-wide association studies (GWAS) have identified several genetic risk loci for AD to be in microglia [129-131]. Also, it has been reported that activated microglia have both protective and deleterious effects on AD pathology, disease progression, and cognition [87, 235, 236].

Recent animal model studies have highlighted that the presence of activated microglia is necessary for tau deposition and tau-mediated neurodegeneration [111, 237]. Moreover, the 3D human triculture system provided empirical evidence showing microglia to play a bridge between the A $\beta$  and tau pathologies [86]. With advancing technologies in the cell culture system and transgenic animal models, we are now accumulating more evidence to support activated microglia as a key element in tau seeding and propagation. Although the animal model and the cell culture studies have recapitulated the human AD pathophysiology, it is imperative to translate and replicate the findings using *in vivo* biomarkers in living individuals.

With the advent of second-generation positron emission tomography (PET) tracers with higher specificity and sensitivity targeting activated microglia, amyloid-beta (A $\beta$ ) plaques, and

neurofibrillary tangles, *in vivo* studies have recently demonstrated the association among the three AD pathological hallmarks. In addition, activated microglia have been shown a bi-phasic trajectory during the clinical progression of AD, in which the first peak is associated with a protective effect in the preclinical/prodromal AD stage whereas the second peak is associated with a deleterious effect in the AD stage, suggesting different microglial roles during the disease progression [235, 236, 238]. However, the direct interrogation of different phenotypes and modulated effect of activated microglia based on the pathologic definition of AD — A/T/(N) classification — within the A $\beta$  cascade hypothesis framework is elusive.

Here, we show activated microglia ([<sup>11</sup>C]PBR28) are increased in the AD continuum (A $\beta$ +Tau-/+) group, defined by the abnormal amount of pathological A $\beta$  ([<sup>18</sup>F]AZD4694; A $\beta$ +) or A $\beta$ + and tau ([<sup>18</sup>F]MK6240; tau+), compared to individuals without any evidence of AD pathologies (A $\beta$ -Tau-), A $\beta$ - group, using *in vivo* PET imaging. Importantly, the interactive effect between regional A $\beta$  and activated microglia predicts a greater tau burden in the AD continuum rather than in the A $\beta$ - group. We show that the local-to-local interaction between A $\beta$  and activated microglia provides positive interactive effects while local-to-distal interaction provides both positive and negative effects on the tau burden. Notably, activated microglia in the inferior medial temporal cortex together with widespread A $\beta$  play a pivotal role in predicting the tau propagation in AD vulnerable regions over one year. Considering the multidimensionality of AD pathophysiology, we substantiate further through a multivariate analysis to find disparate positive and negative effects of activated microglia on tau pathology that is modulated by A $\beta$  — a significant contribution of the interactive effect between activated microglia in the medial inferior temporal cortex and widespread A $\beta$  on tau propagation beyond Braak region 1-2 to Braak 4 over one year. Effectively, we show *in vivo* evidence to support the A $\beta$  cascade

hypothesis ( $A\beta \rightarrow$  activated microglia  $\rightarrow$  phosphorylated tau  $\rightarrow$  cognitive decline/(neurodegeneration)) pathway rather than the “tau-first” pathway. Furthermore, a stepwise logistic regression analysis demonstrates a significant contribution of activated microglia in addition to the  $A\beta$ , age, sex, education, and APOE $\epsilon$ 4 status in predicting tau positivity, supporting the importance of activated microglia on tau burden. Consequently, the regional tau burden shows the greatest deleterious effects on different cognitive tests in the AD continuum. On the other hand, activated microglia show protective effects on cognition in the  $A\beta$ -. Together, our data support the multidimensional processes, in which the neuroprotective effect of activated microglia is modulated by  $A\beta$ , leading to tau propagation and subsequent cognitive decline in AD.

## **Results**

### **Demographics**

Two independent and blinded neurologists at our memory clinic visually assessed the presence of abnormal pathological  $A\beta$  and/or tau in a total of 120 individuals. The visual reading was corroborated by performing a receiver operating characteristic analysis using global  $A\beta$  and Braak region 3-4 tau PET standardized uptake value ratio (SUVR) comparing the visually  $A\beta$ - ( $A\beta$ -Tau-) subjects younger than 55 years old ( $N = 17$ ) to the clinical AD subjects who were visually  $A\beta$ + ( $N = 14$ ). This provided the  $A\beta$  and tau threshold at 1.58 and 1.22 SUVR, respectively. There was only a net change of 2 subjects to the AD continuum. Therefore, we present our data based on the visual reading scheme here. There was a significant difference in age between the  $A\beta$ - ( $N = 72$ ) and AD continuum ( $N = 48$ ) due to the inclusion of younger

subjects (age < 55 years,  $t(82.6) = -5.15$ ,  $P < 0.001$ ) in the A $\beta$ -. Also, there was a significant difference in the number of APOE $\epsilon$ 4 carriers between the groups ( $\chi^2(1) = 12.78$ ,  $P = 0.0003$ ). There was no significant difference in the education attainment or ratio between males and females. A subset of the subjects completed the cognitive assessments where the AD continuum performed significantly worse compared to the A $\beta$ - in mini-mental state examination (MMSE,  $F(1) = 30.56$ ,  $P < 0.0001$ ), Clinical Dementia Rating Scale Sum of Boxes (CDRSOB,  $F(1) = 11.87$ ,  $P < 0.001$ ), Montreal Cognitive Assessment (MOCA,  $F(1) = 28.03$ ,  $P < 0.001$ ), adjusted for age, sex, APOE $\epsilon$ 4 status, and education. The summary of the full demographic analysis is shown in Table 6. In all of the subsequent analyses below, we included age, sex, APOE $\epsilon$ 4 status, and education as covariates, and all of the continuous independent variables were scaled and mean centred at 0.

**Table 6.** Study 2 demographics

<b>Groups</b>	<b>A<math>\beta</math>- (A-T-)</b> (N = 72)	<b>AD continuum (A+T-/+) </b> (N = 48)
<b>Diagnosis</b>	60 CNs, 12 MCIs	16 CNs, 18 MCIs, 14 ADs
<b>Age (years)</b>	60.26 $\pm$ 21.62	73.91 $\pm$ 5.13**
<b>Sex (M/F)</b>	23/49	17/31
<b>APOE<math>\epsilon</math>4 carrier (%)</b>	15 (20.8)	26 (54.2)**
<b>Education (years)</b>	15.61 $\pm$ 3.69	14.65 $\pm$ 3.12
<b>Global [<sup>18</sup>F]AZD4694 SUVR</b>	1.25 $\pm$ 0.12	2.19 $\pm$ 0.36***
<b>Braak 1-2 [<sup>18</sup>F]MK6240 SUVR</b>	0.87 $\pm$ 0.13	1.45 $\pm$ 0.44***

<b>Braak 3-4 [<sup>18</sup>F]MK6240 SUVR</b>	1.04 ± 0.09	1.62 ± 0.76***
<b>Braak 5-6 [<sup>18</sup>F]MK6240 SUVR</b>	1.13 ± 0.15	1.44 ± 0.57***
<b>MMSE</b>	N = 71; 29.17 ± 1.18	N = 48; 29.05 ± 2.74***
<b>CDRSOB</b>	N = 46; 0.28 ± 0.66	N = 37; 1.65 ± 2.62**
<b>MOCA</b>	N = 63; 27.84 ± 2.04	N = 37; 23.49 ± 5.96**

---

CN, cognitively normal; MCI, mild cognitive impairment; AD, Alzheimer's Disease; MMSE, mini-mental state examination; CDRSOB, clinical dementia rating scale sum of boxes; MOCA, Montreal Cognitive assessment; PCC, posterior cingulate cortex. All values are indicated as mean ± standard deviation except for sex and APOEε4. The p-value indicates the value from the unpaired two-tail t-test between Aβ- and AD continuum for age and education. Sex and APOEε4 were assessed based on a contingency chi-square test. All of the [<sup>18</sup>F]AZD4694 and [<sup>18</sup>F]MK6240 SUVRs and cognitive tests were assessed based on a multiple linear regression using the group contrast and covariates (age, sex, education, and APOEε4); \* = P < 0.05, \*\* = P < 0.01; \*\*\* = P < 0.0001.

### **Regional difference in activated microglia between Aβ- and AD continuum.**

To assess the difference between the Aβ- and AD continuum in activated microglia, we quantified [<sup>11</sup>C]PBR28 SUVR in 25 regions of interest (ROIs; global meta ROI, 24 grey matter ROIs in the neocortex from the LPBA40 atlas ([http://www.ion.usc.edu/atlas/Atlas\\_Detail.php?atlas\\_id=12](http://www.ion.usc.edu/atlas/Atlas_Detail.php?atlas_id=12)) with cerebellar grey as a reference region. Based on a two-way interaction ANCOVA, we found a significant increase in activated microglia in the posterior cingulate cortex (PCC), middle and inferior temporal cortex, fusiform gyrus, gyrus rectus, and middle and lateral orbital frontal cortex in the AD continuum compared to the Aβ- following False discovery rate (FDR) multiple comparisons correction (P < 0.05) based on the number of ROIs tested. Interestingly, we found a significant decrease in

activated microglia in the superior parietal gyrus, angular gyrus, superior temporal gyrus, superior occipital gyrus, and cuneus ( $P < 0.05$ ) following FDR correction.

### **Activated microglia are associated with A $\beta$ or tau in A $\beta$ - and AD continuum.**

Using a multiple linear regression model, we investigated the association between the three AD hallmarks of interests in this study: A $\beta$  quantified by [ $^{18}\text{F}$ ]AZD4694 SUVR using cerebellar grey as a reference region and tau quantified by [ $^{18}\text{F}$ ]MK6240 SUVR using inferior cerebellar grey as a reference region, and activated microglia. Based on the previous PET imaging studies, we expected significant associations among the 3 AD hallmarks. Thus, in this study, we investigated the association between two PET biomarkers while correcting for the remaining PET biomarker. In the A $\beta$ -, we found a significant positive association between A $\beta$  and activated microglia in the global ROI, supramarginal gyrus, angular gyrus, superior parietal gyrus, precuneus, anterior cingulate cortex (ACC), middle temporal gyrus, cuneus, superior and middle occipital gyrus, and frontal cortex ( $P < 0.05$ ). Also, there was a significant positive association between tau and activated microglia in the supramarginal gyrus, angular gyrus, superior parietal gyrus, superior and middle occipital gyrus ( $P < 0.05$ ). However, there was no association between A $\beta$  and tau in the A $\beta$ -. In the AD continuum, we found a significant positive association between A $\beta$  and activated microglia in the superior parietal gyrus and superior occipital gyrus as well as tau and activated microglia in the inferior temporal gyrus ( $P < 0.05$ ). Furthermore, there was a significant association between A $\beta$  and tau in the precuneus, PCC, fusiform gyrus, middle and inferior temporal gyrus, superior parietal gyrus, insular cortex, inferior occipital gyrus, and middle orbitofrontal gyrus ( $P < 0.05$ ). All of the analyses mentioned here were adjusted for multiple comparisons correction using FDR.

## **Local-to-local and local-to-distal interactive effects between A $\beta$ and activated microglia on tau.**

Following the independent association between activated microglia and A $\beta$  or tau, we investigated whether there was a significant interactive effect between A $\beta$  and activated microglia on tau by performing a voxel-based regression model. We found only a positive interactive effect on tau that is mainly driven by the AD continuum after Random Field Theory (RFT) for the multiple comparisons correction. The significant local-to-local (voxel-to-voxel) interactive effect was present in the precuneus, PCC, medial frontal cortex, superior parietal cortex, and basolateral temporal cortex (Figure 28). Then, we investigated the local-to-distal interactive effects between A $\beta$  and activated microglia on tau. To do so, we included additional ROIs that are relevant in AD and tau propagation such as Braak regions, leading to a total of 35 ROIs (Table 7). This allowed us to investigate all the possible combinations of the regional A $\beta$  and activated microglia interactions representing the A $\beta$  and activated microglia interaction network on tau (42,875 possible combinations) including the covariates. Following the FDR correction, we found both significant positive and negative interactive effects between A $\beta$  and activated microglia on tau burden (Figure 28). Interestingly, the regions where a substantial amount of hyperphosphorylated tau aggregates were known to deposit had a greater number of positive interactive outcomes such as Braak stage 1 and 4, Precuneus, PCC, middle and inferior temporal cortex (including the hippocampus and parahippocampal gyrus), and frontal cortex (Figure 28). On the other hand, the opposite was also seen with the negative interactions at Braak stage 6 and the Occipital cortex (Figure 28). In addition, most of the regional A $\beta$  contributed to the positive interactive effects: these are Precuneus/PCC, orbitofrontal cortex, temporal cortex, insular cortex, Braak stage 4 and 5, and Int region, which was defined as the voxel-based

interaction network in Figure 28A, while superior parietal gyrus and middle and inferior occipital gyrus contributed to the negative interactive effects (Figure 28). On the other hand, activated microglia in the Int ROI, ACC, PCC, and inferior medial temporal regions (Braak 1, parahippocampus gyrus, fusiform gyrus, and inferior temporal gyrus) contributed to the positive interactive effects, while supramarginal gyrus, superior parietal gyrus, and superior occipital gyrus contributed to the negative interactive effects (Figure 28).

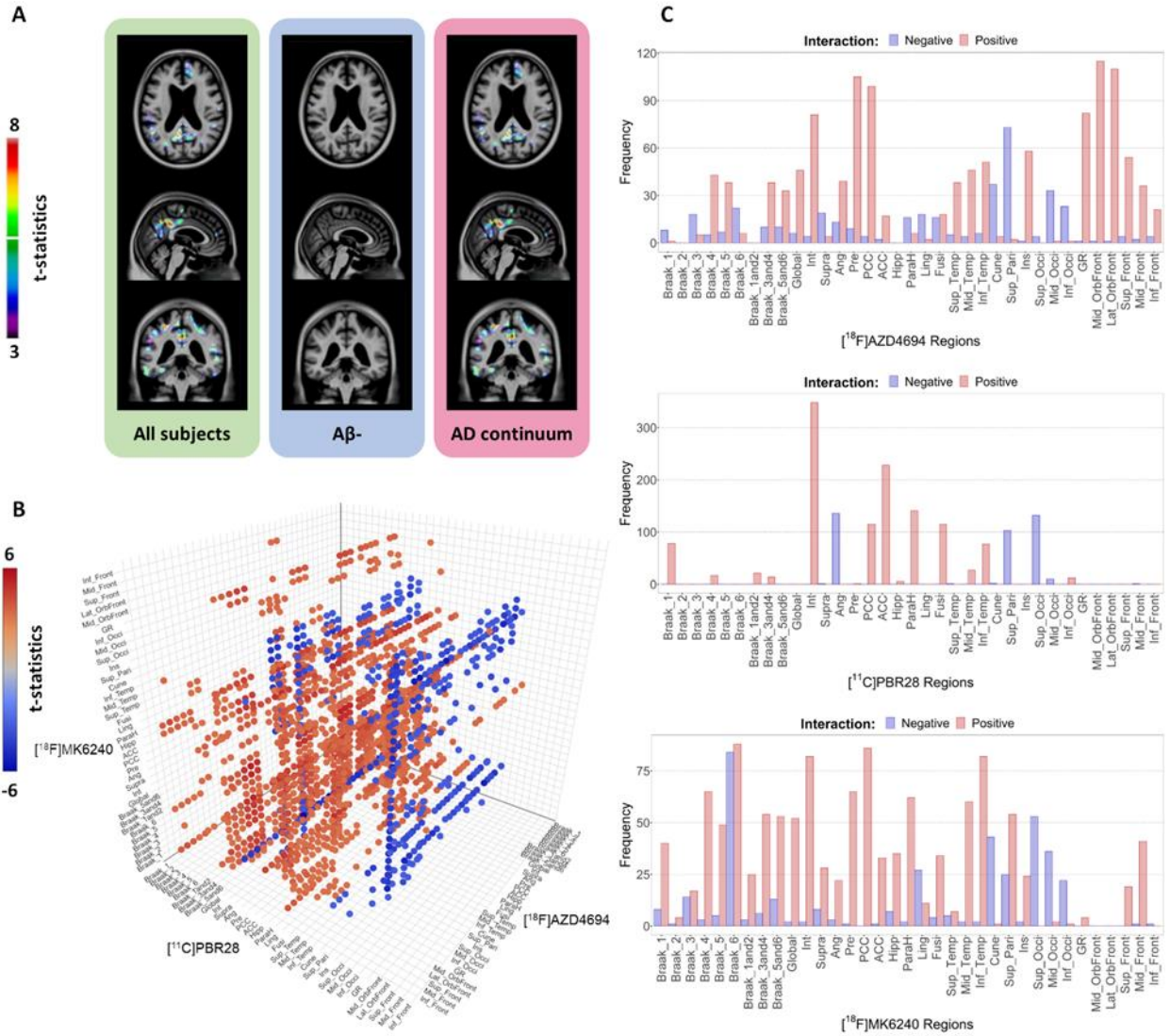


**Figure 28.** Local-to-local and local-to-distal interactive effects between Aβ and activated microglia on tau pathology.

A) The voxel-based images represent the local-to-local (voxel-to-voxel) interactive effect between  $[^{18}\text{F}]\text{AZD4694}$  and  $[^{11}\text{C}]\text{PBR28}$  on  $[^{18}\text{F}]\text{MK6240}$ , including age, sex, education, and APOE $\epsilon$ 4, and corrected for multiple comparisons using RFT based on all subjects (N = 120), Aβ- (N = 72), and AD continuum (N = 48). The resulting regions include precuneus, PCC, basal temporal cortex, superior parietal cortex, and medial frontal cortex, which are AD vulnerable regions. B) The image depicts 42,875 possible combinations of regions interrogating the local-to-distal interactive effects. The red circles depict statistically significant positive interactive effects while blue circles depict significant negative interactive effects. These results are corrected for multiple comparisons using FDR. C) The histogram representation of the frequency, in which interactive effects are significant from 42,875 models in each PET biomarker.

*Table 7. ROI abbreviations*

<b>Regions</b>	<b>Abbreviations</b>
Braak region 1	Braak_1
Braak region 2	Braak_2
Braak region 3	Braak_3
Braak region 4	Braak_4
Braak region 5	Braak_5
Braak region 6	Braak_6
Braak region 1 & 2	Braak_1and2
Braak region 3 & 4	Braak_3and4
Braak region 5 & 6	Braak_5and6
Global	Global
Interaction ROI	Int
supramarginal_gyrus	Supra
angular_gyrus	Ang
precuneus	Pre
posterior_cingulate	PCC
anterior_cingulate_gyrus	ACC
hippocampus	Hipp
parahippocampal_gyrus	ParaH

lingual_gyrus	Ling
fusiform_gyrus	Fusi
superior_temporal_gyrus	Sup_Temp
middle_temporal_gyrus	Mid_Temp
inferior_temporal_gyrus	Inf_Temp
cuneus	Cune
superior_parietal_gyrus	Sup_Pari
insular_cortex	Ins
superior_occipital_gyrus	Sup_Occi
middle_occipital_gyrus	Mid_Occi
inferior_occipital_gyrus	Inf_Occi
gyrus_rectus	GR
middle_orbitofrontal_gyrus	Mid_orbitoFront
lateral_orbitofrontal_gyrus	Lat_OrbFront
superior_frontal_gyrus	Sup_Front
middle_frontal_gyrus	Mid_Front
inferior_frontal_gyrus	Inf_Front

---

## **Amyloid, tau, and neuroinflammation covariance differ between A $\beta$ - compared to AD continuum.**

Considering the multidimensionality reported in the current finding, we applied a partial least square (PLS) analysis with 2000 bootstrap and permutation tests, contrasting the A $\beta$ - and AD continuum groups. We found two significant latent variable (LV) patterns (LV1:  $P = 0.0005$ ,  $R^2 = 0.704$ ; LV2:  $P = 0.0015$ ,  $R^2 = 0.18$ ) that differentially relate to the regional tau burden (Figure 29). This is indicated by the opposing direction in the correlation among the regions and/or disparate significance in the regional contribution to the covariance. The AD continuum mainly contributed to the LV1 showing a positive association between the regional tau burden and activated microglia in the Int ROI, PCC, middle and inferior temporal gyrus, medial temporal regions (Braak 1, 3, and 4, parahippocampal gyrus, and fusiform gyrus), and most of the regional A $\beta$  (Figure 29A). In the LV2, only APOE $\epsilon$ 4 had a significant association with tau in the AD continuum (Figure 29B). The A $\beta$ - mainly contributed to the LV2. Here, the covariance between the regional activated microglia and tau burden revealed bi-directional covariance that depended on the region. This represents both the positive and negative association between the activated microglia and hyperphosphorylated tau, which may represent the homeostatic balance between the protective and deleterious roles of microglia (Figure 29).

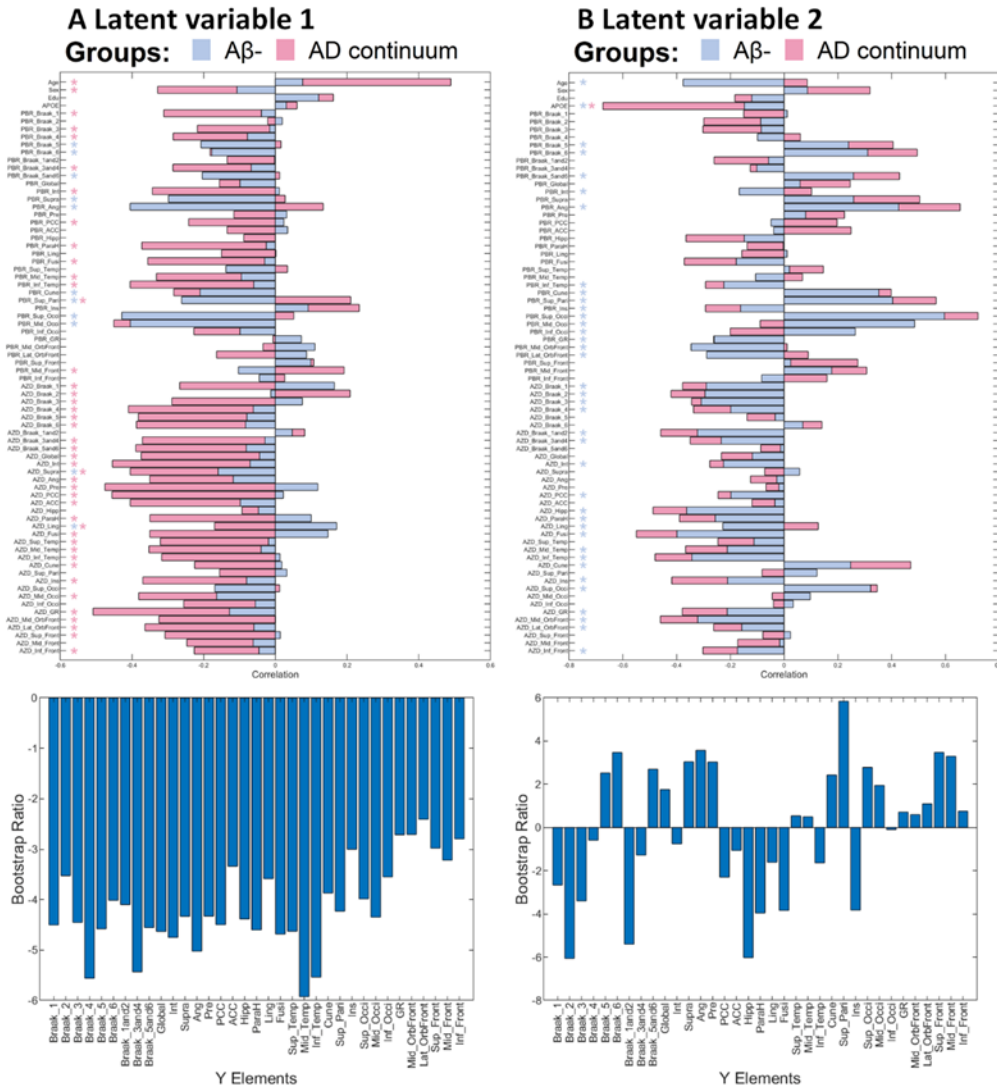


**Figure 29.** PLS analysis using  $[^{18}\text{F}]\text{AZD4694}$ ,  $[^{11}\text{C}]\text{PBR28}$ , and  $[^{18}\text{F}]\text{MK6240}$  in A $\beta$ - and AD continuum.

A group contrast between the A $\beta$ - and AD continuum based on a PLS analysis is shown in this figure. A) The salience regional tau were significantly correlated (positive correlation) with almost all  $[^{18}\text{F}]\text{AZD4694}$  and  $[^{11}\text{C}]\text{PBR28}$  regions in the latent variable 1 ( $P = 0.0005$ ,  $R^2 = 0.704$ ). This is depicted by having both a negative bootstrap ratio and a correlation of the latent variables. B) The region tau saliences show early tau pathology regions to have a negative bootstrap ratio and late tau pathology regions to have a positive bootstrap ratio. Most of the  $[^{18}\text{F}]\text{AZD4694}$  regions show a significant positive correlation with early Braak regions as indicated by both negative bootstrap ratio and correlation whereas  $[^{11}\text{C}]\text{PBR28}$  show bi-directional correlations that depend on the region in the latent variable 2 ( $P = 0.0015$ ,  $R^2 = 0.18$ ).

## **The effect of activated microglia is modulated in the AD continuum.**

Insofar, we identified two effects or phenotypes (“positive effect” or “negative effect”) of activated microglia associated with tau. To evaluate if the interactive effects fit within the A $\beta$  cascade hypothesis framework (A $\beta$   $\rightarrow$  activated microglia  $\rightarrow$  phosphorylated tau), we performed a series of PLS path analyses including both positive and negative effects of activated microglia and interactive terms in the model with 2000 bootstrap tests. Then, the difference in the PLS path effects between the A $\beta$ - and AD continuum was evaluated with 2000 permutation tests. The PLS path analyses revealed that the A $\beta$  imposed the greatest positive effect on tau (Figure 30). In addition, we demonstrated two types of activated microglia effects, similar to the distinctive microglial GWAS phenotypic profiles, associated with tau: there was a significant protective (negative effect of activated microglia on tau indicated by “PBR\_protect”) and adverse (positive effect of activated microglia on tau indicated by “PBR\_adverse”) effects of activated microglia on tau (Figure 30A). Congruently, there were significant protective and adverse interactive effects between activated microglia and A $\beta$  on tau as well (Figure 30A). Furthermore, there was a significant difference between the A $\beta$ - and AD continuum in the following path coefficients: A $\beta$  effect on tau ( $P = 0.035$ ), PBR\_protect effect on tau ( $P = 0.016$ ), PBR\_adverse effect on tau ( $P < 0.001$ ), and positive interactive effect on tau ( $P = 0.029$ ). It’s important to note that the A $\beta$ - demonstrated only negative interactive effects (negative path coefficients) whereas the AD continuum showed both positive and negative interactive effects on tau (Figure 30B). Moreover, activated microglia showed only positive effects on tau in the AD continuum, while activated microglia showed both positive and negative effects on tau in the A $\beta$ - (Figure 30). Effectively, the A $\beta$ - demonstrated only the protective interactive effects between A $\beta$  and activated microglia

on tau, while the AD continuum reinforced the adverse effects from activated microglia on tau (Figure 30B).

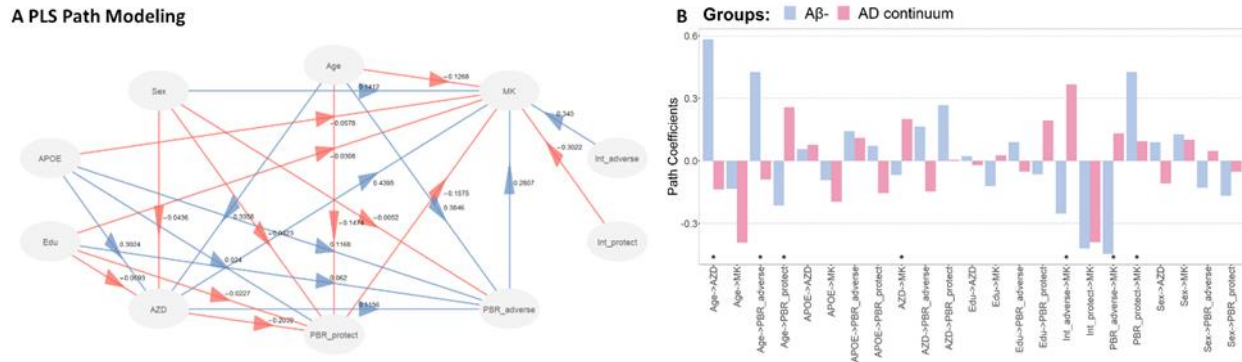


**Figure 30.** Investigating the interactive effects of  $A\beta$  and activated microglia using PLS path modelling.

A) Based on the cohort, PLS path modelling with 2000 bootstrap supports the  $A\beta$  cascade hypothesis framework. Blue arrows depict positive path coefficients while red arrows depict negative path coefficients. B) Group contrast between  $A\beta$ - (blue) and AD continuum (pink) in the PLS path modelling with 2000 permutation tests is shown here. There is a significant difference in the effect of Age on [ $^{18}\text{F}$ ]AZD4694 ( $P < 0.001$ ), Age on PBR\_protect ( $P = 0.034$ ), Age on PBR\_adverse ( $P = 0.001$ ), [ $^{18}\text{F}$ ]AZD4694 on [ $^{18}\text{F}$ ]MK6240 ( $P = 0.035$ ), PBR\_adverse on [ $^{18}\text{F}$ ]MK6240 ( $P < 0.001$ ), PBR\_protect on [ $^{18}\text{F}$ ]MK6240 ( $P = 0.016$ ), and Int\_adverse on [ $^{18}\text{F}$ ]MK6240 ( $P = 0.029$ ).

### Activated microglia in the medial temporal cortex together with widespread $A\beta$ drive the one-year tau propagation to AD vulnerable regions.

A subset of the subjects received one-year follow-up [ $^{18}\text{F}$ ]MK6240 scan ( $A\beta$ -  $N = 24$ ; AD continuum  $N = 12$ ). Based on a linear mixed-effect model with the covariates,  $A\beta$ - did not show any changes in tau burden over one year. However, the AD continuum showed a significant increase in tau burden in all anatomical ROIs except in the cuneus, superior parietal cortex, and occipital cortex after FDR correction based on the number of ROIs tested. We investigated how the  $A\beta$  and activated microglia were associated with a one-year change

(defined as a follow-up – baseline) in the tau burden representing the tau propagations (delta tau). Here, we conducted the regional interaction between A $\beta$  and activated microglia as the A $\beta$  and activated microglia interaction network on one-year delta tau (42,875 possible combinations). We found only the significant positive interaction following FDR correction, which had a predominant contribution by activated microglia in the medial temporal cortex together with widespread A $\beta$  regions (Figure 31A-B). A significant interactive effect was present in PCC, basal temporal cortex, insular cortex, and frontal cortex in predicting delta tau (Figure 31). To contrast the extensive coverage by the interactive effect of activated microglia in the medial temporal cortex and widespread A $\beta$  relative to other regional activated microglia, we performed voxel-based interactive analyses in the following regions: global A $\beta$ \*activated microglia in the medial temporal cortex (parahippocampal gyrus and hippocampus), lateral temporal cortex (middle and inferior temporal cortex), middle orbitofrontal cortex, or functional hub (Precuneus and PCC). These regions were selected because they demonstrated significant interactions or were reported to be the early A $\beta$  accumulation region (Figure 31C). The interaction between activated microglia in the medial temporal cortex and global A $\beta$  predicted tau propagation in the precuneus, PCC, medial orbitofrontal cortex, supramarginal gyrus, angular gyrus, and inferior temporal cortex (parahippocampal gyrus, fusiform gyrus, middle and inferior temporal gyrus), covering 107,254 mm<sup>3</sup> volume resembling Braak stage 4 (Figure 31C). However, the interaction between global A $\beta$  and activated microglia in the lateral temporal cortex or middle orbitofrontal cortex predicted tau propagation in the gyrus rectus and parahippocampal gyrus, and each model represented only 7,487 mm<sup>3</sup> and 14,683 mm<sup>3</sup>, respectively (Figure 31C). The interaction between the global A $\beta$  and activated microglia in the functional hub did not survive multiple comparisons correction (Figure 31C).

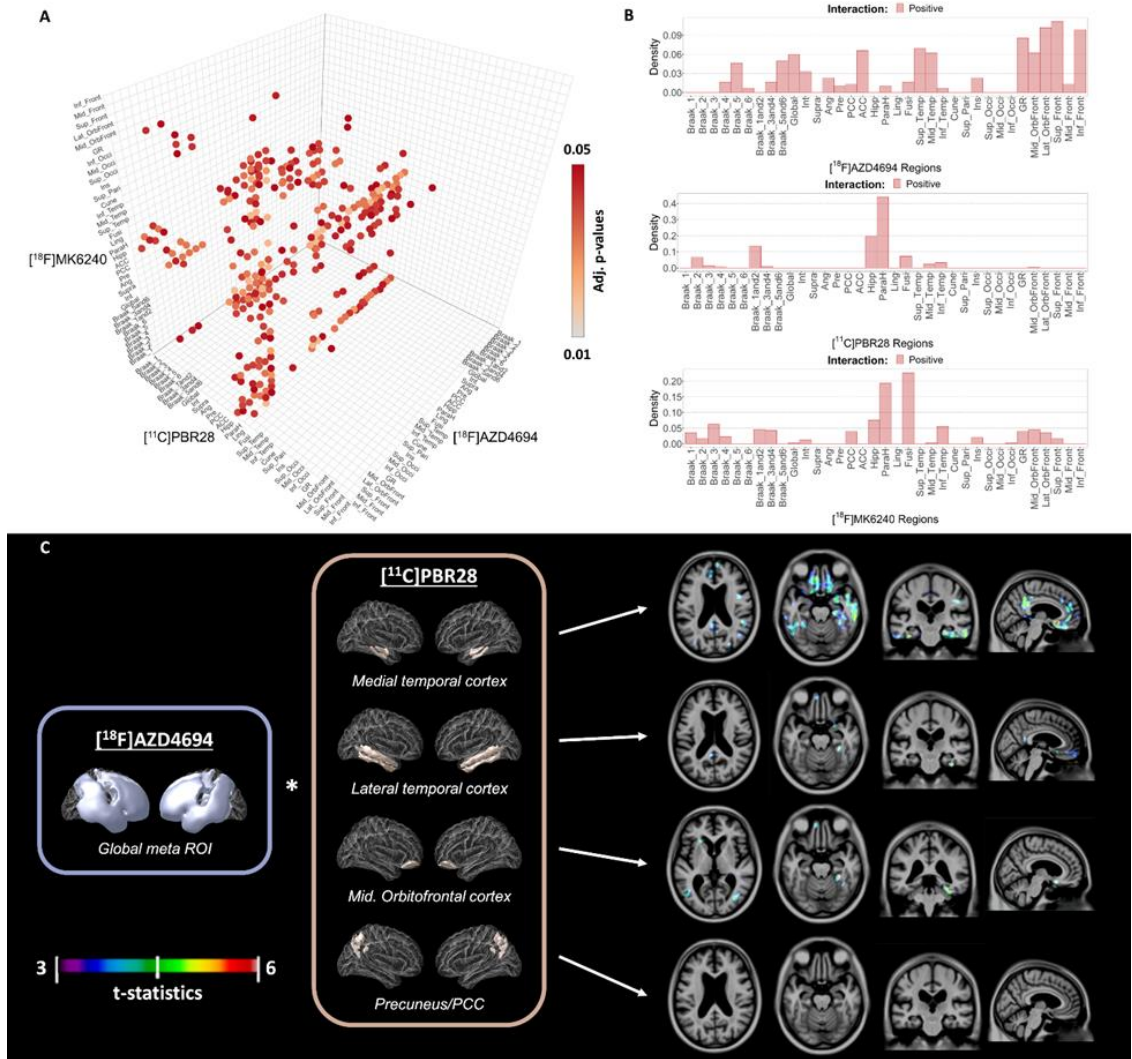


**Figure 31.** Activated microglia in the medial temporal cortex together with widespread  $A\beta$  predict tau propagation in AD.

A) The image depicts 42,875 possible combinations of regions interrogating the local-to-distal interactive effects between  $[^{18}\text{F}]\text{AZD4694}$  and  $[^{11}\text{C}]\text{PBR28}$  on a one-year delta  $[^{18}\text{F}]\text{MK6240}$  in a subset of our cohort (24  $A\beta$ - and 12 AD continuum) with FDR correction. The surviving results show only positive interactive effects. Therefore, the red circle depicts the FDR adjusted p-values. B) The histogram in density representation of the interactive effects from 42,875 models in each PET biomarker.  $[^{18}\text{F}]\text{AZD4694}$  showed significant interactive effects in widespread regions whereas  $[^{11}\text{C}]\text{PBR28}$  regions are focal to the inferior medial temporal cortex. C) The voxel-based interactive effects between global  $[^{18}\text{F}]\text{AZD4694}$  and medial temporal cortex, lateral temporal cortex, middle orbitofrontal cortex, or Precuneus/PCC  $[^{11}\text{C}]\text{PBR28}$  on one-year delta  $[^{18}\text{F}]\text{MK6240}$  including age, sex, education, and  $\text{APOE}\epsilon 4$  and corrected for multiple comparisons using RFT are displayed.

## **The effect of activated microglia in the parahippocampal gyrus is modulated in AD pathology.**

We performed the PLS analysis to investigate the covariance in the A $\beta$ , activated microglia, and one-year delta tau with 2000 bootstrap and permutation tests. This revealed one significant latent variable pattern ( $P = 0.005$ ,  $R^2 = 0.76$ ) where the majority of the positive covariance between A $\beta$  and one-year delta tau was present from the AD continuum group. Moreover, the majority of the negative covariance between activated microglia and one-year delta tau was present from the A $\beta$ - group. Notably, the parahippocampal gyrus showed a juxtaposing covariance pattern between the A $\beta$ - and AD continuum. This was confirmed in the PLS path analysis with 2000 bootstrap tests that the significant interaction between activated microglia in the parahippocampal gyrus and widespread A $\beta$  predicted the tau propagation in AD, corroborating the regression analyses. Furthermore, we did not find the negative effects of microglia in the one-year delta tau. Due to the limited power of the longitudinal tau data, we tested the difference in the PLS path coefficients between the A $\beta$ - and AD continuum by using a simpler PLS path model excluding the 4 covariates. With 400 permutation tests, we found a significant difference in the A $\beta$  effect on delta tau and activated microglia ( $P < 0.05$ ).

### **Supporting A $\beta$ cascade hypothesis rather than tau-first hypothesis.**

To assess the directionality of the effects, we tested the interactive effect between activated microglia and tau on A $\beta$ . Based on our voxel-based and ROI regression models, we found no significant interactive effects at local-to-local or local-to-distal in both groups. Using PLS path analysis, we tested the “tau-first” pathway model (hyperphosphorylated tau  $\rightarrow$

activated microglia  $\rightarrow$  A $\beta$ ). Here, the variance explained in the endogenous variables as well as the goodness of fit (GoF) by the A $\beta$  cascade hypothesis model was superior (the variance explained in the final endogenous variable (tau) was 63%; GoF was 39%) compared to the “tau-first” pathway (the variance explained in the final endogenous variable (A $\beta$ ) was 55%; GoF was 36%).

### **Activated microglia contribute to predicting tau positivity beyond A $\beta$ in AD.**

To further substantiate the predictive effects of activated microglia in the medial temporal cortex on tau, we conducted a stepwise logistic regression analysis following three steps: 1) the covariates (age, sex, APOE $\epsilon$ 4 status, and education), 2) covariates + global A $\beta$ , and 3) covariates + global A $\beta$  + activated microglia. This procedure was conducted using the 35 ROIs from activated microglia. Following a likelihood ratio test between each subsequent step, we found that the covariates + global A $\beta$  model performed significantly better than the covariates model ( $\chi^2(1) = 72.64$ ,  $P < 0.0001$ ), while the addition of activated microglia was significant compared to the model including global A $\beta$  in 13 different ROIs following FDR correction. To illustrate the models, the stepwise logistic regression ROC curves including 4 different ROIs are shown in Figure 32. Importantly, the majority of the 13 regions are found in the inferior medial and lateral temporal cortex, suggesting activated microglia in the inferior temporal cortex significantly contribute to predicting tau positivity.

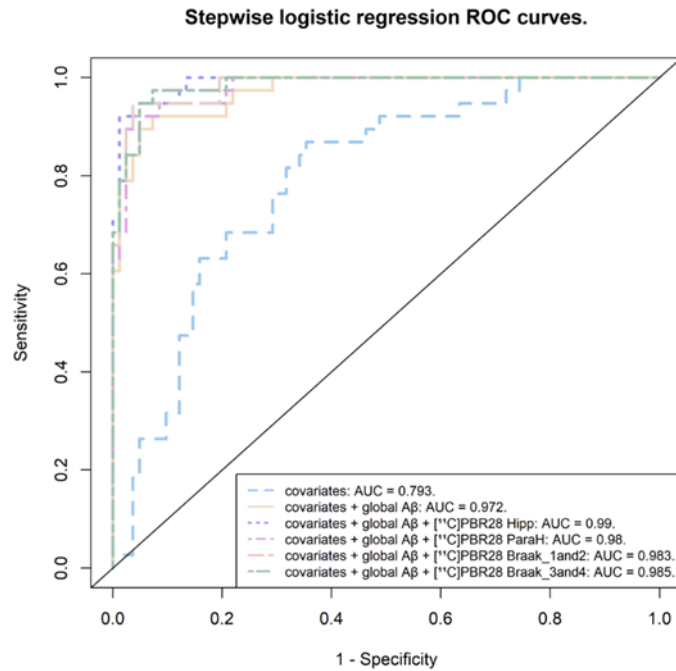


**Figure 32.** Stepwise logistic regression ROC curves.

A stepwise logistic regression analysis was performed to generate a ROC curve for each step. The first step includes the four covariates (age, sex, APOE $\epsilon$ 4 status, and education), the second step includes the four covariates and global A $\beta$ , and the last step includes the four covariates, global A $\beta$ , and activated microglia in 35 different regions. Based on a likelihood ratio test, the second step is significantly better than the first step, and the third step is significantly better than the second in 13 different ROIs. This suggests that global A $\beta$  significantly contributed to predicting tau in addition to the four covariates, while activated microglia from the 13 different ROIs significantly contributed to predicting tau in addition to the four covariates and global A $\beta$ . Here, we include the first, second, and 4 different third steps for the illustration purpose.

### **AD pathophysiology on cognition.**

Last, we examined the effects of A $\beta$ , activated microglia, and tau on cognitive measures represented by MMSE (A $\beta$ - N = 71; AD continuum N= 48), CDRSOB (A $\beta$ - N = 46; AD continuum N= 37), and MOCA (A $\beta$ - N = 63; AD continuum N= 37) by performing a multiple linear regression model based on the 42,875 possible combinations of the regions, including the two remaining PET variables as additional covariates. Then, we calculated the average standardized effects of A $\beta$ , activated microglia, or tau following the FDR correction in each region. Thus, the mean standardized effect represents the cumulative average effect of one AD hallmark in each region on cognition after adjusting for the remaining two PET biomarkers and covariates. We found the activated microglia in the fusiform gyrus, insular cortex, and Braak 1 and 2 regions provided protective effects on CDRSOB, while A $\beta$  and tau did not show any effects in A $\beta$ - (Figure 33A). However, in the AD continuum, we found that tau alone imposed deleterious effects on all cognitive measures; all of the regional tau burdens had significantly deleterious cumulative effects (Figure 33B-D). However, the A $\beta$  and activated microglia effects did not survive the multiple comparisons test.

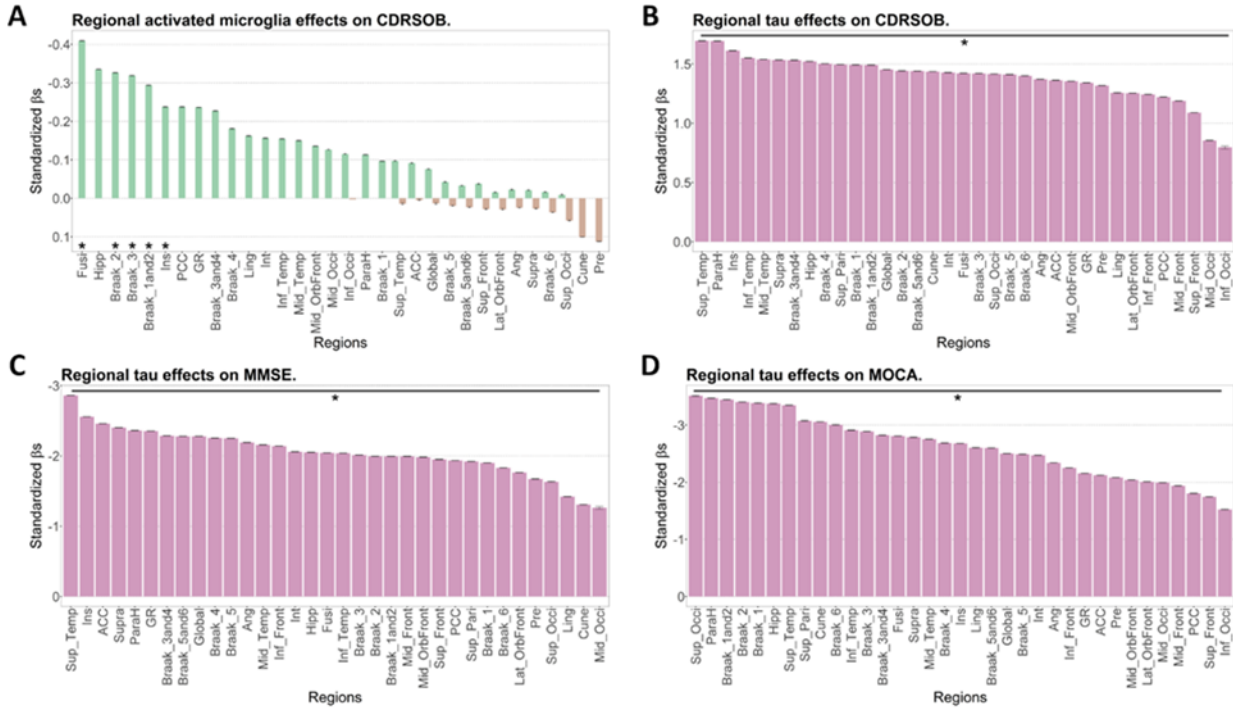


**Figure 33.** The effect of  $A\beta$ , activated microglia, and tau on cognition in  $A\beta$ - and AD continuum.

A total of 42,875 combinations of multiple linear regressions are conducted to interrogate the main effect of [ $^{18}\text{F}$ ]AZD4694, [ $^{11}\text{C}$ ]PBR28 or [ $^{18}\text{F}$ ]MK6240 on cognitive tests. As such, each bar represents a cumulative mean standardized effect of one PET biomarker in each region adjusted for the remaining two PET biomarkers in the 35 regions, age, sex, education, and APOE $\epsilon$ 4. A) The green bar represents negative effects while the brown bar represents positive effects of [ $^{11}\text{C}$ ]PBR28 on CDRSOB in each region in the  $A\beta$ -. The asterisk mark represents a significant result following the FDR correction. B-D) The pink bars represent the cumulative mean standardized effects of [ $^{18}\text{F}$ ]MK6240 on CDRSOB, MMSE, and MOCA in the AD continuum. All of the regional [ $^{18}\text{F}$ ]MK6240 effects on the cognitive tests stay significant following the FDR correction in the AD continuum. The error bar represents the standard error in the cumulative mean of the standardized effects.

## Discussion

This study highlights the effect of activated microglia is modulated in the AD continuum ( $A\beta$ +Tau- or  $A\beta$ +Tau+) compared to the  $A\beta$ - ( $A\beta$ -/Tau-) and interact with widespread  $A\beta$  to

predict tau pathology using *in vivo* PET imaging. Notably, the local-to-local and local-to-distal interactive effects that modulated the protective or adverse influence of activated microglia on tau depended on the region. Furthermore, our multivariate approach substantiated the disparate positive and negative effects of activated microglia on tau pathology that is modulated in the AD continuum. Investigating one-year propagation of tau, we showed significant interactive effects between activated microglia in the medial temporal cortex and widespread A $\beta$  on delta tau in AD vulnerable regions encompassing Braak stage 4. In particular, the stepwise logistic regression analysis demonstrated the significant role of activated microglia in the inferior temporal cortex in predicting tau positivity. As such, our data were best described within the A $\beta$  cascade hypothesis framework. Consequently, the tau pathology demonstrated the greatest deleterious effects on cognition in the AD continuum, while activated microglia showed a protective effect in the A $\beta$ -.

Microglia are the first line of defence in the brain, and they are under a tight homeostatic balance between scavenging and promoting repair and recovery. However, A $\beta$ , tau, and damaged synapses signal to activate and recruit microglia in AD. Then, activated microglia clear the pathologic aggregates and injured synapses via phagocytosis and begin the remodelling processes [239-242]. However, beyond the phagocytosis and recovery of the synapses as a protective immune response, a multitude of studies has provided strong evidence that activated microglia have detrimental effects. Recent reports from histopathological or single-cell transcriptomic studies have identified different activated microglial phenotypes — ie. Disease-associated microglia (DAM), MGnD, human Alzheimer's microglia (HAM), or proportion of morphologically activated microglia (PAM) — in AD apart from healthy ageing [132-134, 243]. These microglia showed distinctive transcriptomic profiles and endophenotypes, which demonstrate enhanced immune-inflammatory pathways, and were associated with pathological

A $\beta$  and tau [134, 244]. In addition, GWAS studies corroborated by showing different genetic loci related to AD risk genes to be implicated in immunity, lipid metabolism, tau binding proteins, and amyloid precursor protein metabolism [129, 130]. Here, we investigated the disease-related activated microglia effects in AD using *in vivo* PET imaging. Congruently, we report a significant association between activated microglia and A $\beta$  or tau and demonstrate the interactive effect of activated microglia in the AD continuum, suggesting there are different phenotypes of activated microglia in AD compared to A $\beta$ -. In particular, we show an overall balance in the association (having both positive and negative effects) between activated microglia and tau in the A $\beta$ -. However, this effect became positive in part due to A $\beta$  in the AD continuum. Furthermore, the regional association between activated microglia and tau encompassed bi-directional effects in the A $\beta$ -, while the AD continuum showed mainly the exacerbating profile of microglia on tau pathology.

Recent transgenic tau mouse model studies provided empirical evidence underscoring the mechanistic role of activated microglia in driving tau pathology and neurodegeneration. By depleting microglia, there was a significant reduction in tau pathology as well as protection from TREM2- or APOE-related neurodegeneration [111, 133, 237]. Concurrently, our study substantiates the notion that disease-related activated microglia drive the tau pathology. In contrast to the A $\beta$ -, the AD continuum mainly showed a positive effect of activated microglia on tau pathology. Specifically, A $\beta$  moderated the activated microglia, like a switch, to be more like a disease-related effect than a balanced homeostatic effect. Thus, the interaction between widespread A $\beta$  and activated microglia in the medial temporal cortex predicted tau propagation into associative cortices. Moreover, activated microglia in the inferior temporal cortex significantly contributed to predicting tau positivity in addition to A $\beta$ . Although the transgenic

tau mouse model used in the previous studies does not display A $\beta$  pathology, AD-related phenotype in activated microglia is not solely caused by tau pathology alone. Myriad of genetic evidence reports diverse disease-related microglial phenotypes suggesting the ensemble of pathologic milieu would determine the disease-related microglial phenotypes rather than just one pathology [129-131]. In addition, A $\beta$  and activated microglia interact via the cell surface receptors (ie. TREM2) on the neurons or glial cells [87, 245, 246]. The interactive effects between the A $\beta$  and activated microglia on tau could potentially be capturing the exponential growth of the intracellular signalling cascade to trigger greater hyperphosphorylated tau deposition.

Interestingly, the positive/negative interactive effects between global A $\beta$  and activated microglia on tau pathology depended on the region. Remarkably, the regions that are known to deposit a great amount of tau early such as Braak stage 1-4 regions (medial temporal cortex, PCC, ACC, fusiform gyrus, parahippocampal gyrus, inferior occipital gyrus, middle and inferior temporal gyrus), showed overall positive cumulative net interactive effects. On the other hand, the regions such as occipital regions that are known to have sparse tau deposits showed greater negative interactive effects. Similarly, our multivariate analyses corroborated the positive and negative association between microglia and tau demonstrating the regional dependency. Regarding the one-year change in tau burden, the significant positive interactive effects between activated microglia in the medial temporal cortex and global A $\beta$  were observed in Braak stage 1-4. This regional dependency in our study adds to the growing body of evidence from the histopathology, animal, and computational studies establishing the regional vulnerability related to tau deposition patterns [24, 185, 247]. Although the exact mechanism underpinning the regional vulnerability is still elusive, histopathological staining of post-mortem studies has

defined the regional progression as Braak stages, which have been recapitulated using *in vivo* PET tau imaging [24, 247]. Furthermore, recent animal model and cell culture studies have provided empirical evidence to support the tau propagation hypothesis, which posits cell-to-cell transmission of pathological tau-like prion disease from seeding to spreading via synaptic contacts or activity between the cells [248-251]. Therefore, anatomically and functionally connected brain architecture has been reported to predispose the regional vulnerability to tau pathology [109, 110, 248]. Here, microglia may play a direct role as well. At the synapse, microglia are shown to release pathologic tau via exosome and inhibiting the exosome significantly reduced the tau propagation [252]. Throughout the homeostatic maintenance of synaptic integrity, function, and turn-over, microglia may inadvertently aid in tau propagation.

Alternatively, the regional heterogeneity of microglia may play a role in regional vulnerability. Recent studies have reported a profound influence of microenvironment and origin of microglia to alter the transcriptomic that can be switched to the pro-inflammatory profile [87, 253, 254]. In addition to the transcriptomic profile, microglial epigenetic alteration based on the regional demand determines the microglial clearance activity [255]. For example, having a higher neuronal attrition rate in the cerebellum compared to the striatum, the PRC2 in microglia controlled the gene expressions supporting the clearance activity via epigenetic alterations. However, the aberrant activation of clearance in PRC2-deficient microglia displayed altered neuronal spines that resembled the AD pathology induced by microglial activation in the AD mouse model [255]. As the regions that show early tau deposition are intimately related to the neurogenic region such as in the dentate gyrus, microglial function during the neurogenesis may contribute to promoting tau propagation by spilling exosomes [252, 256]. Therefore, the

spatiotemporal dynamics in the microglial phenotypes are evident and may contribute to the regional tau predisposition.

While *in vivo* imaging studies in humans are computational and data-driven, our imaging platform provided rich longitudinal data to investigate which direction of effects is deemed most probable. Here, our data support the A $\beta$  cascade hypothesis, revealing the direct and indirect effects of A $\beta$  and activated microglia on tau. Moreover, the PLS path analysis provided a superior model fit following the A $\beta$  cascade hypothesis model compared to the “tau-first” model. Although the simplified PLS path analysis model included only the main effect of A $\beta$ , activated microglia, and their interactive effect, this model explained 63.1% of the variance on the one-year change in tau. Importantly, even with limited power on our current longitudinal data, our findings are substantiated through complementing statistical methods, including multivariate approaches, and the FDR multiple comparisons correction. This testifies the staggering interactive effects between activated microglia and amyloid-beta on tau. Together with the 3D cell culture and transgenic animal findings, the collective data provide circumstantial evidence for activated microglia as a driver of tau pathology in AD. A potential mechanistic pathway, in which activated microglia promote tau pathology through NLRP3 inflammasome, exosome release, APOE, TREM2, pro-inflammatory signals, is a novel therapeutic target in AD [86, 111, 126, 136, 257-260]. Important to note, our data provided the same amount of variance explained when we tested A $\beta$   $\rightarrow$  activated microglia  $\rightarrow$  tau or activated microglia  $\rightarrow$  A $\beta$   $\rightarrow$  tau. This could be related to activated microglia promoting A $\beta$  pathology through ASC specks, NLRP3, or APOE [261, 262]. In addition, our data do not capture the initial point of the disease etiology to differentiate whether abnormal A $\beta$  or neuroinflammation starts first. Considering the existing literature supporting the earliest A $\beta$  toxic events due to the soluble A $\beta$ , which cannot be

quantified using PET at this time, may trigger the neuron-derived inflammatory signalling or precede tau tangles accumulation, we hypothesized the  $A\beta \rightarrow$  activated microglia  $\rightarrow$  tau model would be appropriate to test in this study [232, 263]. Although it becomes a circular argument akin to the chicken or the egg question invalidating model assumptions,  $A\beta/\tau \rightarrow$  activated microglia  $\rightarrow$   $A\beta/\tau \rightarrow$  activated microglia  $\rightarrow$  tau provided the best model. Capturing the early window of the  $A\beta$  and activated microglia pathology would be paramount in future studies.

Previous *in vivo* PET studies have described the trajectory of activated microglia as biphasic where the first peak during the prodromal AD stage reflects the protective role of microglia, whereas the second peak during the AD stage reflects the detrimental role of microglia [235, 236]. Here, we report a progressive increase and decrease in activated microglia in the AD continuum compared to the  $A\beta^-$  that depended on the region. While the [ $^{11}\text{C}$ ]PBR28 data are cross-sectional, hypothesizing that the AD pathophysiology follows the progression from  $A\beta^-$  (lack of pathology) to AD continuum (presence of pathology), our data support the biphasic trajectory of activated microglia in AD overall as well: first peak in conjunction with the first AD hallmark,  $A\beta$ , and the second peak in conjunction with the second hallmark tau. Notably, activated microglia demonstrated a protective effect on CDRSOB in the  $A\beta^-$ , however, tau demonstrated deleterious effects in the AD continuum. While previous studies have provided an insightful dynamic profile of activated microglia following the clinical manifestation of AD, to the best of our knowledge, the present study is the first to investigate activated microglia using *in vivo* PET imaging based on the pathological definition of AD following the new NIA-AA A/T/(N) classification research framework [67].

In conclusion, this study highlights the *in vivo* evidence of AD-related activated microglia effects that are intimately entangled with  $A\beta$  and tau pathology. While activated

microglia in A $\beta$ - protect against pathologic debris, activated microglia interact with A $\beta$  to drive tau propagation and subsequent cognitive decline in AD. These findings support the growing body of evidence that activated microglia are imperative in AD pathology, and targeting the AD pathological aggregates (A $\beta$  and tau) together with tightly maintaining the homeostatic condition of activated microglia would be imperative to achieve successful therapeutic strategies and efficacy.

## **Materials and Methods:**

### **Study design and participants.**

The primary objective of this study was to investigate whether activated microglia drive tau seeding and propagation in the presence of A $\beta$  in living individuals defined by the A/T/(N) classification. Data used in this study were part of the Translational Biomarkers in Aging and Dementia (TRIAD) cohort, which is an ongoing longitudinal cohort study to describe longitudinal biomarker trajectories in AD as part of the McGill University Research Centre for Studies in Aging. We included 120 individuals who received all 3 PET ([<sup>18</sup>F]AZD4694, [<sup>11</sup>C]PBR28, and [<sup>18</sup>F]MK6240) imaging at baseline with [<sup>18</sup>F]AZD4694 and [<sup>18</sup>F]MK6240 imaging being less than one year apart from [<sup>11</sup>C]PBR28 imaging date. In addition, they all underwent structural magnetic resonance imaging (MRI), APOE $\epsilon$ 4, and translocator protein (TSPO) genotyping. Due to the single nucleotide polymorphism in TSPO leading to a varying degree of [<sup>11</sup>C]PBR28 binding affinity, we have only included high-affinity binding individuals in this study [157]. A subset of individuals had completed detailed neuropsychological examinations including MMSE, CDRSOB, and MOCA at baseline, and underwent a one-year

follow-up [ $^{18}\text{F}$ ]MK6240 imaging. Cognitively normal individuals had no objective cognitive impairment and MMSE score  $> 26$  and/or CDR score of 0. Mild cognitive impairment individuals had subjective and objective cognitive impairments and/or an MMSE score  $> 24$ , CDR score of 0.5 but maintained the autonomy of daily living. Mild-to-moderate sporadic AD patients had an MMSE score  $< 24$  and/or CDR score between 0.5 and 2. History of alcohol abuse, clinical depression, major neuropsychiatric or neurological disorders, early-onset presenilin-1 mutation carriers, or diagnosis with early-onset AD were our exclusion criteria for the study. To define the presence of pathological A $\beta$  and tau in each subject, we used global meta ROI and Braak region 3 and 4, respectively. In particular, Braak region 3 and 4 ROI was chosen based on extensive histopathological staining of 95 post-mortem tissues that showed A $\beta$ <sup>+</sup> when reaching Braak stage 4 [264]. The detailed demographic descriptions are outlined in Table 6. The McGill University research ethical board and all participants had approved all the procedures and informed consents.

### **MRI acquisition and processing.**

All MRI acquisitions were performed at Montreal Neurological Institute (MNI) using a 3T system (Siemens Magnetom) with T1-weighted volumetric magnetization prepared rapid gradient echo (MPRAGE) sequence (TR: 2300 ms, TE: 2.96 ms, 9° flip angle) resulting in 1x1x1mm<sup>3</sup> resolution. Each subject's MRI was corrected for non-uniformity, field distortion, and brain masking. Then, the subject MRI was transformed into Alzheimer's disease Neuroimaging Initiative (ADNI) template using an affine and nonlinear transformation algorithm based on the ANTS toolbox.

## **PET acquisition and processing.**

All PET acquisitions were performed at MNI using a Siemens High-Resolution Research Tomography (HRRT) scanner. All the radiopharmaceuticals were produced and quality checked by the cyclotron unit at MNI. [<sup>18</sup>F]AZD4694, [<sup>11</sup>C]PBR28, and [<sup>18</sup>F]MK6240 images were acquired between 40-70 minutes, 60-90 minutes, and 90-110 minutes post-injection, respectively. Following the emission scan, a 6-minute <sup>137</sup>Co rotating point source was used to acquire a transmission scan. All images were reconstructed using an Ordered-subsets Expectation Maximization (OSEM) algorithm on a 4D volume with 300 seconds per frame for [<sup>18</sup>F]AZD4694 and [<sup>18</sup>F]MK6240, while 600 seconds per frame for [<sup>11</sup>C]PBR28. Last, all images were corrected for decay, dead time, random and scatter coincidences, and attenuation.

The PET images were first transformed to the subject MRI using rigid body transformation using the ANTS toolbox. By combining the affine and nonlinear transformation from subject MRI into ADNI template, all the PET images were transformed to ADNI space. Then, the images were blurred to the final resolution of 8mm full-width at half maximum. The semi-quantitative parametric maps resulting in SUVR were generated using cerebellar grey as a reference tissue for all PET tracers. In quantifying the PET SUVRs in different regions, we used a global meta-ROI, including the precuneus, cingulate, prefrontal, orbitofrontal, parietal, and temporal regions, Braak stages ROIs based on the anatomical regions reported from the histopathological staining and tau-PET imaging, bilaterally combined LPBA40 atlas using grey matter cortical regions ([http://www.loni.usc.edu/atlas/Atlas\\_Detail.php?atlas\\_id=12](http://www.loni.usc.edu/atlas/Atlas_Detail.php?atlas_id=12)), and ROI based on our voxel-based interaction between [<sup>18</sup>F]AZD4694 and [<sup>11</sup>C]PBR28 with a threshold t statistic > 2 [24, 230, 247].

## Statistical Analyses

No statistical methods were used to predetermine the sample size as this is an ongoing longitudinal characterization of a cohort in Montreal. However, our sample sizes are similar to previous publications performing the same statistical analysis [110, 265]. In addition, our preliminary analyses based on a subset of subjects as well as a multivariate approach to investigate the multi-dimensional data together with bootstrapping and permutation tests provide additional confidence in our findings presented in this study.

All of the continuous independent variables used in the statistical analyses below have been scaled and mean-centred at 0. A group contrast in sex and APOE $\epsilon$ 4 proportion was assessed based on a  $\chi^2$  test, while the difference in age and education was examined based on an unpaired two-tail t-test. The global [ $^{18}\text{F}$ ]AZD4694 SUVR, [ $^{18}\text{F}$ ]MK6240 SUVR in the Braak stages, and all of the cognitive test scores were statistically compared between the A $\beta$ - and AD continuum using multiple linear regression models including age, sex, education, and APOE $\epsilon$ 4 status as covariates. The regional difference in [ $^{11}\text{C}$ ]PBR28 SUVR between the A $\beta$ - and AD continuum was examined using a two-way ANCOVA including an interaction term between the group and regions and age, sex, education, and APOE $\epsilon$ 4 status as covariates. The pairwise multiple comparisons concerning the number of regions based on FDR were applied. To establish the significant association among the 3 PET imaging data, we performed a series of multiple linear regression models in each region by regressing one PET image (ie. [ $^{11}\text{C}$ ]PBR28 SUVR) with another (ie. [ $^{18}\text{F}$ ]AZD4694 SUVR) and including the remaining PET imaging (ie. [ $^{18}\text{F}$ ]MK6240 SUVR), age, sex, education, and APOE $\epsilon$ 4 status as covariates. This procedure was performed in each A $\beta$ - and AD continuum group and corrected for multiple comparisons for the number of regions based on FDR. Based on a subset of subjects who had undergone a one-year follow-up

[<sup>18</sup>F]MK6240, we tested an annual change in the [<sup>18</sup>F]MK6240 SUVR in each group in 25 regions using a linear mixed-effect model with maximum likelihood estimation, a fixed effect for the predictor in time, a random intercept for each subject, and age, sex, education, and APOEε4 status as covariates. Here, we did not include a random slope as there were only two-time points but a multiple comparisons test using FDR for the number of regions was applied.

We investigated local-to-local interactive effects between [<sup>18</sup>F]AZD4694 (Aβ) and [<sup>11</sup>C]PBR28 (activated microglia) on [<sup>18</sup>F]MK6240 (tau) based on a voxel-based linear regression model including age, sex, education, and APOEε4 status as covariates, using VoxelStats [224]. The result was corrected for multiple comparisons using RFT at  $P < 0.05$ . This identified a set of regions where the tau pathology was influenced by the local interactive effect between Aβ and activated microglia, representing the Aβ and activated microglia interaction network. As a result, the identified regions overlapped with the regions where the tau pathology is vulnerable. Following the local-to-local interaction model, we interrogate whether local-to-distal interactive effects recapitulate the regional vulnerability in tau pathology as well. We extracted the [<sup>18</sup>F]AZD4694, [<sup>11</sup>C]PBR28, and [<sup>18</sup>F]MK6240 SUVR from the 35 ROIs (Table 7) and performed 42,875 combinations (35 regions from 3 PET imaging =  $35^3 = 42,875$ ) of multiple linear regression models including the [<sup>18</sup>F]AZD4694 and [<sup>11</sup>C]PBR28 interaction term and age, sex, education, and APOEε4 status as covariates to interrogate all the possible combinations of interactive effects accounting different regional influence. The multiple comparisons correction on 42,875 combinations was performed using FDR. We have also applied the same strategy but only including the main effect of [<sup>18</sup>F]AZD4694 and [<sup>11</sup>C]PBR28, not the interactive term, to identify the local-to-distal main effect of Aβ or activated microglia on tau. We have performed this step using all cohort data. The entire cohort provided the most

robust statistics allowing us to identify important regions to develop latent variables for the subsequent PLS analyses indicated by the multiple comparisons survival rate (1,624 analyses survived using the entire cohort, 6 analyses survived using AD continuum data, and A $\beta$ - did not survive the FDR multiple comparisons test). Therefore, based on the whole cohort with greater power, we identified the regional main effect of A $\beta$  or activated microglia as well as regional interactive effects between A $\beta$  and activated microglia to be used in the subsequent PLS path analysis.

Given the multidimensionality in the data, we employed PLS and PLS path modelling multivariate statistical methods to investigate the covariance in the variable of interests and estimate different mechanistic pathway models (ie. A $\beta$   $\rightarrow$  activated microglia  $\rightarrow$  tau model vs tau  $\rightarrow$  activated microglia  $\rightarrow$  A $\beta$  model) [266, 267]. A behavioural PLS analysis was used to identify the distribution patterns of age, sex, education, APOE $\epsilon$ 4, 35 [ $^{18}$ F]AZD4694 ROIs, and 35 [ $^{11}$ C]PBR28 ROIs related to 35 regional tau burden and compare between A $\beta$ - and AD continuum. A detailed description of the behaviour PLS computational procedure can be found in the previous literature [268]. Based on the previous multiple linear regression models, we have identified a set of variables (AZD, PBR\_protect (negative effects), PBR\_adverse (positive effects), Int\_protect (negative effects), Int\_adverse (positive effects), and the covariates) for PLS path modelling to 1) test the significance of path coefficients to tau burden, 2) identify direct and indirect path coefficients to tau burden, 3) investigate the difference in the path coefficients between A $\beta$ - and AD continuum, 4) compare the variance explained in tau burden between different path model designs, and 5) compare the total variance explained by the model. An iterative process of PLS path modelling was performed to refine manifest variables to represent the homogenous latent variable (Cronbach's alpha > 0.7 and first eigenvalue > 1). We have

removed a manifest variable that represented opposing direction in its effect to the latent variable following additional quality checks based on the loadings and weights. When analyzing the “tau-first” pathway model and delta tau with baseline [<sup>18</sup>F]AZD4694 and [<sup>11</sup>C]PBR28 data, we followed the same approach as above. The age, sex, education, and APOEε4 status variables are designed as formative modes by themselves, while the AZD, PBR\_protect (negative effects), PBR\_adverse (positive effects), Int\_protect (negative effects), Int\_adverse latent variables are designed as reflective modes.

To investigate the significant contribution to predicting tau positivity in addition to Aβ from activated microglia in 35 ROIs, we conducted stepwise logistic regression analysis. The first step/model included only the covariates. Then, the second step/model included global Aβ, and the last step included activated microglia. We compared the models subsequently using the likelihood ratio test to identify whether the additional variable significantly contributed to predicting tau positivity. This procedure was repeated at 35 ROIs, therefore, we applied the multiple comparisons correction using FDR on all the activated microglia comparisons.

The effect of [<sup>18</sup>F]AZD4694, [<sup>11</sup>C]PBR28, and [<sup>18</sup>F]MK6240 SUVR on cognitive tests were investigated similarly to employing 42,875 combinations of multiple linear regression models. As a result, we derived a cumulative average coefficient from [<sup>18</sup>F]AZD4694, [<sup>11</sup>C]PBR28, or [<sup>18</sup>F]MK6240 in each region to represent the overall effect adjusting for age, sex, education, APOEε4 status, and the remaining 2 PET imaging data. All of the statistical analyses were performed using R (3.6.2 version; <https://www.r-project.org/>) or Matlab (2020a; <https://www.mathworks.com/products/matlab.html>).

### 12.2.3 Study 3: Preclinical *in vivo* longitudinal assessment of KG207-M as a disease-modifying Alzheimer's disease therapeutic.

**Authors:** Min Su Kang<sup>1,2,3</sup>, Monica Shin<sup>1,2</sup>, Julie Ottoy<sup>1</sup>, Arturo Aliaga Aliaga<sup>1,2,3</sup>, Sulantha Mathotaarachchi<sup>1,2</sup>, Kely Quispialaya<sup>1</sup>, Tharick A. Pascoal<sup>1,2</sup>, D. Louis Collins<sup>3</sup>, M. Mallar Chakravarty<sup>2</sup>, Axel Mathieu<sup>2</sup>, Åsa Sandelius<sup>5</sup>, Kaj Blennow<sup>5,6</sup>, Henrik Zetterberg<sup>5,6,7,8</sup>, Gassan Massarweh<sup>3</sup>, Jean-Paul Soucy<sup>3</sup>, A. Claudio Cuello<sup>4</sup>, Serge Gauthier<sup>1,2,3</sup>, Michael Waterston<sup>10</sup>, Nathan Yoganathan<sup>11</sup>, Etienne Lessard<sup>9</sup>, Arsalan Haqqani<sup>9</sup>, Kerry Rennie<sup>9</sup>, Danica Stanimirovic<sup>9</sup>, Balu Chakravarthy<sup>9</sup>, Pedro Rosa-Neto<sup>1,2,3</sup>

**Affiliation:** Translational Neuroimaging laboratory – McGill University Research Centre for Studying in Aging<sup>1</sup>, Douglas Mental Health University Institute<sup>2</sup>, McConnell Brain Imaging Centre – McGill University<sup>3</sup>, Department of Pharmacology and Therapeutics – McGill University<sup>4</sup>, Department of Psychiatry and Neurochemistry, the Sahlgrenska Academy at the University of Gothenburg, Mölndal, Sweden<sup>5</sup>, Clinical Neurochemistry Laboratory, Sahlgrenska University Hospital, Mölndal, Sweden<sup>6</sup>, UK Dementia Research Institute at UCL, London, United Kingdom<sup>7</sup>, Department of Molecular Neuroscience, UCL Institute of Neurology, Queen Square, London, United Kingdom<sup>8</sup>, Human Health Therapeutics, National Research Council of Canada<sup>9</sup>, Centre for Imaging Technology Commercialization<sup>10</sup>, KalGene Pharmaceuticals Inc<sup>11</sup>

This work is published: Kang MS, Shin M, Ottoy J, et al. Preclinical *in vivo* longitudinal assessment of KG207-M as a disease-modifying Alzheimer's disease therapeutic. Journal of Cerebral Blood Flow & Metabolism. August 2021. doi:10.1177/0271678X211035625

## **Abstract**

*in vivo* biomarker abnormalities provide measures to monitor therapeutic interventions targeting amyloid- $\beta$  pathology as well as its effects on downstream processes associated with Alzheimer's disease pathophysiology. Here, we applied an *in vivo* longitudinal study design combined with imaging and cerebrospinal fluid biomarkers, mirroring those used in human clinical trials to assess the efficacy of a novel brain-penetrating anti-amyloid fusion protein treatment in the McGill-R-Thy1-APP transgenic rat model. The bifunctional fusion protein consisted of a blood-brain barrier crossing single domain antibody (FC5) fused to an amyloid- $\beta$  oligomer-binding peptide (ABP) via Fc fragment of mouse IgG (FC5-mFc2a-ABP). A five-week treatment with FC5-mFc2a-ABP (loading dose of 30 mg/Kg/iv followed by 15 mg/Kg/week/iv for four weeks) substantially reduced brain amyloid- $\beta$  levels as measured by positron emission tomography and increased the cerebrospinal fluid amyloid- $\beta_{42/40}$  ratio. In addition, the 5-week treatment rectified the cerebrospinal fluid neurofilament light chain concentrations, resting-state functional connectivity, and hippocampal atrophy measured using magnetic resonance imaging. Finally, FC5-mFc2a-ABP (referred to as KG207-M) treatment did not induce amyloid-related imaging abnormalities such as microhemorrhage. Together, this study demonstrates the translational values of the designed preclinical studies for the assessment of novel therapies based on the clinical biomarkers providing tangible metrics for designing early-stage clinical trials.

## Introduction

Amyloid- $\beta$  ( $A\beta$ ) aggregates remain an attractive therapeutic target for Alzheimer's disease (AD) based on a multitude of genetic and cellular evidence supporting the central role of  $A\beta$  in AD pathophysiology [89, 199, 269-271]. Consequently, there have been great efforts to develop therapeutics that target  $A\beta$  and its clearance. One approach has been immunotherapy with anti-amyloid antibodies [155, 272, 273]. Despite promising preclinical studies demonstrating Central Nervous System (CNS)  $A\beta$  clearance and improvement in cognitive deficits in transgenic mice, several anti-amyloid immunotherapies have failed in clinical trials [272, 273]. Possible reasons for this lack of clinical translation include their low blood-brain barrier (BBB) penetrance, failure to target the appropriate  $A\beta$  species, or safety concerns, such as amyloid-related imaging abnormalities (ARIA) [76, 247, 274]. To address these concerns at the preclinical level, we have recently developed a biomarker platform that allows longitudinal assessments of the effects of an anti-amyloid therapy on imaging and cerebrospinal fluid (CSF) biomarkers using the APP transgenic rat model. The platform provides measures of  $A\beta$  load obtained with [ $^{18}\text{F}$ ]AZD4694 positron emission tomography (PET) and CSF  $A\beta_{42/40}$  ratio [177, 275]. In addition, this platform provides measures of neuronal injury via CSF neurofilament light chain (NFL), structural changes using T1 weighted MRI (sMRI), and brain connectivity estimated by resting-state functional MRI (rs-fMRI). Also, potential brain microhemorrhages (ARIA-H) are detected using susceptibility MRI. By providing the same metrics utilized in human clinical trials, this platform increases the likelihood of translation of assessed target engagement and therapeutic efficacy from preclinical studies to early-stage clinical trials in humans.

This *in vivo* longitudinal imaging and CSF biomarker platform allowed us to evaluate the effects of a novel biopharmaceutical construct, FC5-mFc-ABP (amyloid binding protein), on A $\beta$  clearance, downstream effects on the neuronal injury, and disease-modifying response using a repeated dosing prospective strategy. FC5-mFc2a-ABP is a bifunctional fusion protein consisting of the BBB-crossing camelid single-domain antibody FC5 [276] fused to the N-terminus of Fc fragment of mouse IgG2a, and amyloid binding peptide (ABP) fused to the C-terminus of Fc. Previous *in vitro* and *ex vivo* studies have shown that ABP selectively binds to A $\beta$ <sub>42</sub> oligomers and A $\beta$  deposits in the brains of AD transgenic mice and post-mortem human brains from AD patients, respectively [277, 278]. We have successfully fused ABP with FC5 via mFc and expressed the fusion protein in CHO cells. In this study, we have evaluated the *in vivo* target engagement and efficacy of FC5-mFc2a-ABP (referred to as KG207-M henceforth) using a rat model of AD A $\beta$  pathology carrying hAPP with Swedish and Indiana mutations called McGill-R-Thy1-APP (Tg) [89]. This model allows longitudinal biomarker assessments based on imaging and biochemical methods that are translational in nature. Here, we hypothesized that KG207-M would be transported across the BBB and show target engagement by A $\beta$  clearance, achieving therapeutic benefit. We report successful target engagement by demonstrating reduced A $\beta$  load, rectifying A $\beta$ -induced neuronal injury, functional improvements, and safety (no evidence of ARIA-H) after a 5-week treatment.

## Materials and Methods

### Study Design

This study was designed to characterize BBB penetrance, target engagement, and safety related to ARIA-H following five weeks of anti-amyloid treatment in the A $\beta$  Tg rat model (Figure 34). This is the first *in vivo* study to investigate the direct effect size and power of the KG207-M treatment in the BBB penetrance, target engagement, and ARIA-H in rats. Therefore, we calculated our power analysis based on the effect size ( $d_z = 3.21$ ) of A $\beta$  pathology progression in the McGill-R-Thy1-APP rat model from our previous cohort data. To be able to observe the A $\beta$  pathology progression at  $\alpha$  error = 0.05 and power ( $1 - \beta$ ) = 0.95 given the effect size of normal progression, we would need four animals. This led to including four animals in the control to reflect the natural progression, while the remaining animals were included to increase the power to capture the effects of the BBB penetrance, target engagement, and safety profile. Here, our Tg cohort started with a total of 17 animals where they underwent CSF collection from 10-19 months. However, four animals were sacrificed at 13.7, 17.4, and 18 months of age due to testicular tumours before the therapeutic intervention began. Consequently, the control group (Tg-SAL) included four (two males and two females) and the treatment group (Tg-ABP) included the remaining 9 animals (six males and three females) randomly selected while matching for the sex and body weight. To note, we have matched the sex rather than stratifying as a group as the effect of sex/gender will be investigated in subsequent studies. However, one Tg-SAL animal died at 23 months of age. Tg-SAL and Tg-ABP groups underwent baseline procedures including PET [ $^{18}\text{F}$ ]AZD4694, sMRI, and rs-fMRI at 21 months and follow-up at 24 months of age. We added susceptibility MRI to assess ARIA-H following the treatment in the follow-up time point. To be able to characterize the natural progression of the A $\beta$

pathology via PET from the pre-plaque stage, we included additional eight Tg animals from our previous cohort study that underwent the same PET [ $^{18}\text{F}$ ]AZD4694 procedure at 10 and 17 months, effectively increasing the power of the data [158]. Therefore, we characterized the population-based A $\beta$  pathology progression ([ $^{18}\text{F}$ ]AZD4694 PET BP<sub>ND</sub>) from 10, 17, 21, and 24 months in the McGill-R-Thy1-APP rat model. All [ $^{18}\text{F}$ ]AZD4694 images were processed and analyzed in the same methods described below. During the treatment, all animals were subjected to a serial collection of CSF and plasma to characterize the pharmacokinetics. Two months following the study completion, extra CSF samples were collected (at 25 and 26 months) to assess the post-treatment effect. From 744 CSF samples, 139 (18.7%) samples were excluded due to blood contamination. Moreover, two animals (one from Tg-SAL and Tg-ABP) were excluded from the analyses as they had a relatively lower level of A $\beta$  expression with only intraneuronal A $\beta$  hinting as a hemizygous [89]. For CSF NFL analysis, only the animals who had undergone the entire experimental protocol without any type of tissue abnormality (abscess or tumour) were included. However, all animals were included in the ARIA-H analysis, including the hemizygous animals. All the animal handling and procedures were blinded to the group identification.

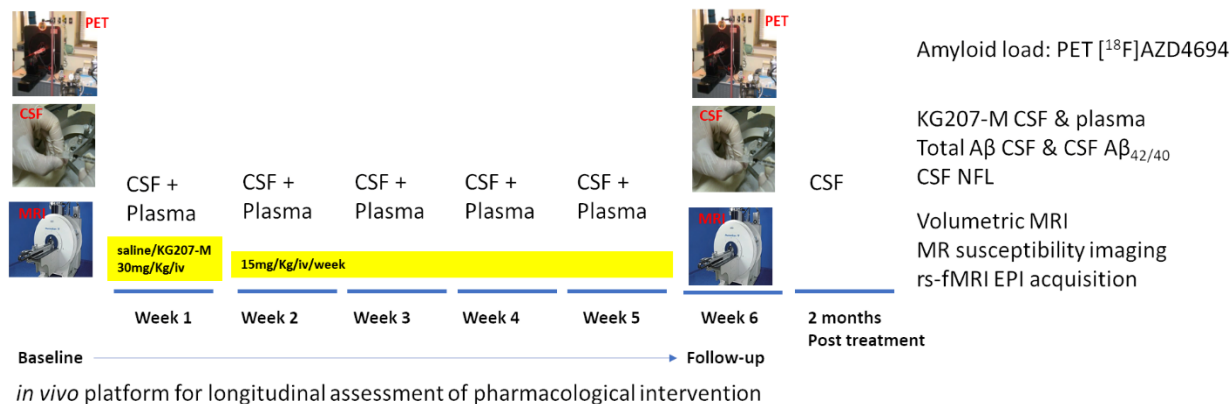


**Figure 34.** *in vivo* biomarker-based study design to evaluate KG207-M target engagement, efficacy, and safety.

Baseline measurements including PET [<sup>18</sup>F]AZD4694, sMRI, and rs-fMRI were acquired at 21 months of age. Then, weekly KG207-M injection via tail vein from 22.5-23.5 months (30 mg/Kg/iv initial dose following 15 mg/Kg/iv dose) was followed by serial CSF collection at the indicated times via cisterna magna after fixing the animals in a stereotaxic apparatus with isoflurane anesthesia. Then, serial blood was collected at the indicated times via the subclavian vein and separated into the plasma via centrifuge. On Week 6 at 24 months old, the follow-up measurements were acquired including PET [<sup>18</sup>F]AZD4694, sMRI, rs-fMRI, susceptibility MRI, and CSF.

## Animals

All procedures described here were performed in compliance with ethics protocols approved by McGill Animal Care Ethics Committee and following the Canadian Council on Animal Care guidelines. All rats were housed at the Douglas Mental Health University Institute animal facility on a 12/12 hr light/darkness cycle with *ad libidum* access to food and water. A starting sample of 17 homozygous McGill-R-Thy1-APP rats on Wistar background was used for the study.

## **KG207-M and A $\beta$ <sub>total</sub> Quantification using Selected Reaction Monitoring (SRM) in CSF and plasma**

FC5-mFc-ABP (KG207-M) fusion protein and A $\beta$  levels in the plasma and CSF were quantified using targeted multiplexed mass spectrometry in selected reaction monitoring mode (SRM) on nanoAcquity UPLC (Waters, Milford, MA) coupled to ESI LTQ XL ETD mass spectrometer (ThermoFisher, Waltham, MA) as previously described [279]. A detailed description can be found in Supplemental Materials.

## **PET imaging acquisition**

All PET images were acquired at 10, 17, 21, and 24 months using CTI Concorde R4 microPET for small animals with [<sup>18</sup>F]AZD4694 for A $\beta$  load. All rats were under 1.5% isoflurane anesthesia during the scan after the 5% anesthesia induction. The [<sup>57</sup>Co] rotating point source was used for a 9-minute transmission scan, which was followed by a simultaneous bolus tail vein injection of the radiotracer (Mean injected dose  $\pm$  standard deviation at 10 and 17 months in Tg = 13.3  $21 \pm 0.9$  MBq; at 21 and 24 months in Tg-SAL = 10.75  $\pm$  3.74 MBq and Tg-ABP = 10.72  $\pm$  4.75 MBq) with a 60-minute emission scan. The image was reconstructed using Maximum A Prior (MAP) algorithm with 27 sequential frames (8 x 30 s, 6 x 1 min, 5 x 2 min, 8 x 5 min), scatter, dead time, and attenuation corrections.

## **MRI imaging acquisition**

All MRI images were acquired using Bruker 7T BioSpec 70/30 USR dedicated for small animals. All rats were under 1.5% isoflurane anesthesia during the scan after the 5% anesthesia induction.

All structural images were obtained at 10, 17, 21, and 24 months from Bruker standard 3D-True Fast Imaging with Steady State Precession pulse sequence (FISP). A root-mean-square image with the acquisition in eight phases was performed. Each angle acquisition was acquired in FOV of 36 mm x 36 mm x 36 mm with a matrix of 180x 180x 180x of TE/TR of 2.5/5.0 ms with two flip angles of 30° and 2 NEX. The final image was an average of 16 acquisitions with 250 µm isotropic resolution from 46 minutes scan.

rs-fMRI images were acquired immediately after the structural scan at 21 and 24 months using the standard Bruker 2D-Spin Echo Planer pulse sequence (2D-SE-EPI). The FOV 25.6 mm x 25.6 mm following rostrocaudal axis with a matrix 64 x 64 at 32 slices of 1.0 mm leading to final resolution 400 µm x 400 µm x 1000 µm and 1.0 mm interslice space was acquired. TE/TR was 15/2000 ms with a flip angle of 70° and 450 repetitions for a total 15 minutes scan resulting in 3 separate runs.

Susceptibility images were acquired at 24 months with Fast Low Angle Shot (FLASH) sequence with TE/TR of 13/100 ms with 1 NEX at pulse angle 40° in FOV 33.6 mm x 20.81 mm x 14.4 mm with a matrix 208 mm x 72 mm x 335 mm resulting in a final resolution of 0.1 mm x 0.2 mm x 0.1 mm.

## **PET&MRI Imaging processes and analysis**

All images were processed using MINC toolkits ([www.bic.mni.mcgill.ca/ServicesSoftware](http://www.bic.mni.mcgill.ca/ServicesSoftware)) following the pipeline described previously [158]. In brief, all PET images received rigid body transformation to the individual anatomical MRI, which then received affine and nonlinear transformations into sample average template space [220]. Then, [<sup>18</sup>F]AZD4694 Binding Potential (BP<sub>ND</sub>) parametric maps were generated using the Simplified Reference Tissue Method (SRTM) and Logan reference method with the cerebellar grey matter as a reference region. The parametric maps were blurred using a 1 mm Full-Width at Half-Maximum (FWHM) Gaussian kernel. Since both measurements showed congruent results, we have selected to include the SRTM data following our previous publication as this study included the previous cohort data [158].

Hippocampal volume was acquired based on manual segmentation including hippocampal subiculum, dentate gyri, CA1, CA2, and CA3 according to a rat brain atlas (Paxinos and Watson 6<sup>th</sup> edition, 2007). The manual segmentation was done before and after the KG207-M treatment at 21 months and 24 months in the individual MRI.

For rs-fMRI, we used AFNI ([www.afni.nimh.nih.gov/afni/](http://www.afni.nimh.nih.gov/afni/)) for preprocessing where the dynamic functional images were corrected for motion and slice-time corrections, bandpass filtered between 0.01-0.1 Hz, and disregarded the first five frames for possible transient drift. Using anatomical-based cingulate cortex seed from our previous study, a seed-based connectivity map was generated based on FMRISTAT tools ([www.math.mcgill.ca/keith/fmristat/](http://www.math.mcgill.ca/keith/fmristat/)) in each run. Then, the individual connectivity maps were transformed via affine and nonlinear transformation into sample average template space and a 1.4 mm FWHM Gaussian blurring kernel was applied. Total 3 separate runs per subject were combined into each subject connectivity map based on

FMRISTAT tools, which produced connectivity effect size, standard deviation and t statistics maps. Then, each subject connectivity map was transformed into z distribution (z-map) by dividing the effect size by standard deviation maps.

Susceptibility MRI was first visually assessed. Then, the susceptibility contrast signals were segmented to represent the possible microhemorrhages. These images received the affine and nonlinear transformation to the template space to acquire the total volume of the susceptibility contrast signal.

### **CSF collection and analysis.**

All animals were induced with 5% isoflurane anesthesia for 5-8 minutes and placed in a stereotaxic apparatus. The CSF samples (100-150  $\mu$ L) were collected via a direct puncture through cisterna magna at 10-26 months old.

#### *Simoa CSF NFL measurements.*

Rat CSF NFL concentration was determined using the in-house Simoa NFL assay, which has been described in detail previously [280], with some modifications. Briefly, samples were diluted 100x with assay diluent and incubated for 35 minutes with paramagnetic carboxylated beads (Quanterix Corp, Boston, MA, USA) coated with a mouse anti-neurofilament light antibody (UD1, UmanDiagnostics, Umeå, Sweden) and a biotinylated mouse anti-neurofilament light antibody (UD2, UmanDiagnostics) in a Simoa HD-1 instrument (Quanterix). The bead-conjugated immunocomplex was thoroughly washed before incubation with streptavidin-

conjugated  $\beta$ -galactosidase (Quanterix). Thereafter, the bead complex was washed and resorufin  $\beta$ -D-galactopyranoside (Quanterix) was added. The immunocomplex was applied to a multiwell array designed to enable imaging of every single bead. The average number of enzymes per bead (AEB) of samples was interpolated onto the calibrator curve constructed by AEB measurements on bovine NFL (UmanDiagnostics) serially diluted in assay diluent. Samples were analyzed 'blind' and in duplicate using one batch of reagents. The average repeatability coefficient of variation of a sample with the mean concentration of 18102 pg/mL was 8.5% and intermediate precision was 8.8%, and for a sample with a mean concentration of 9460pg/mL, repeatability was 8.1% and intermediate precision was 11.5%. All samples analyzed were above the LLOQ.

*Simoa CSF  $A\beta_{42}$  and  $A\beta_{40}$  measurements.*

Rat CSF concentrations of  $A\beta_{42}$  and  $A\beta_{40}$  were measured using Quanterix kits according to kit instructions (Simoa  $A\beta_{42}$  2.0 211 and Simoa  $A\beta_{40}$  2.0 218, Quanterix) with a CSF dilution of 100x using the provided assay diluents. For  $A\beta_{42}$  CSF measurements, the average repeatability coefficient of variation of a sample with a mean concentration of 1650 pg/mL was 3.2% and intermediate precision was 9.2%, and for a sample with a mean concentration of 641 pg/mL, repeatability was 10.9% and intermediate precision was 16.6%. For  $A\beta_{40}$  CSF measurements, repeatability for a sample with a concentration of 5160 pg/mL was 17.2%, and intermediate precision 17.2%, and for a sample with a concentration of 3975 pg/mL repeatability and intermediate precision was 7.3% and 11.8%, respectively. All samples analyzed were above the LLOQ.

## **Histology**

All animals were sacrificed 2 months after the KG207-M treatment and follow-up procedures. They were anesthetized with urethane (1 g/Kg) and perfused transcardially with heparinized phosphate-buffered saline (PBS). Their brains were then collected and immersion-fixed in 4% paraformaldehyde (PFA) for 24 hours. Then, the tissues were washed with PBS three times and fixed in sucrose 30% for 48 hours and transferred to the cryoprotectant (30% sucrose and 30% ethylene glycol) to be stored at -20°C. The brains were sectioned at 40  $\mu$ m in the coronal plane with 480  $\mu$ m intervals throughout the brain using MultiBrain Technology (Neuroscience Associates).

### *Campbell-Switzer Silver Stain.*

A detailed protocol for this staining can be found on the Neuroscience Associate website (<https://www.neuroscienceassociates.com/reference/papers/alzheimers-disease-pathology-silver-stain/>). In particular, we have performed a semi-quantification of the Campbell-Switzer silver staining in the frontal, cingulate, entorhinal cortices, and hippocampus as this model develops extensive A $\beta$  pathology and/or affected significantly in these regions in this animal model [89, 158]. Considering the limited number of animals at the end of the study (Tg-SAL = 2, Tg-ABP = 8), the amount of the Campbell-Switzer silver staining was quantified across subjects in each group as the percentage of the area of Campbell-Switzer silver staining in each region per slide (each data point represents the area of the Campbell-Switzer silver staining/the total area of each slide across subjects in each group).

### *Perls/DAB stain.*

For staining of ferric iron in tissue, every twelfth section (an interval of 480  $\mu$ ) was stained free-floating. The sections were rinsed in dH<sub>2</sub>O then placed in a freshly prepared (1:1) 2% HCL and 2% Potassium Ferrocyanide solution for 30 minutes at room temperature. The sections were again rinsed, then treated with a DAB solution (0.05% diaminobenzidine and 0.011% hydrogen peroxide) to amplify Perl's reaction product. Following further rinses, the sections were mounted on gelatin-coated glass slides, then air-dried. The mounted slides were then counterstained with a light Thionine Nissl counterstain.

### *Light Thionine Nissl counterstain.*

The mounted Perl's/DAB stained slides were dehydrated through alcohols. The slides were then rehydrated and stained in a Thionine solution made in an acetate buffer: pH4.5. Following deionized water rinses, the slides were cleared in xylene and coverslipped with Permount (Fisher Scientific, Pittsburgh PA).

## **Statistical analysis**

All animals were randomly selected into Tg-SAL and Tg-ABP with age (21 months of age at baseline) and sex- and weight-matched. CSF NFL data were log-transformed to fit normality. When comparing between groups, the number of data points in each group is identified as Group1 vs Group2, while the number of data points from each sex is identified as M/F for males and females in all analyses, respectively. All statistical analyses were performed

using parametric tests except for pharmacokinetic modelling following the Shapiro-Wilk normality test.

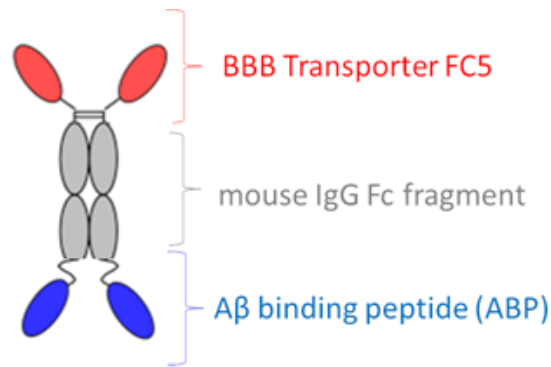
For statistical analyses, we have tested the pharmacokinetics of KG207-M in plasma and CSF based on nonlinear pharmacokinetics models (parameter estimates not shown) to evaluate the relationship between the central and peripheral compartments. To assess the longitudinal A $\beta$  progression using PET imaging, we included the animals from our previous cohort data from 9-16 months to generate a population-based longitudinal A $\beta$  progression model. We added a cohort term to adjust for its variability. We applied a linear mixed-effect model with a random intercept in the Tg-ABP group alone to evaluate the target engagement:  $[^{18}\text{F}]\text{AZD4694 BP}_{\text{ND}} \sim \text{Age} + \text{Sex} + \text{Weight} + (1|\text{subject})$ . Furthermore, we introduced an interaction term when using the whole dataset to directly assess the KG207-M effect between the groups where KG207-M was a binary variable representing 0 as animals without KG207-M treatment and 1 as Tg-ABP:  $[^{18}\text{F}]\text{AZD4694 BP}_{\text{ND}} \sim \text{Age} * \text{KG207-M} + \text{Age} + \text{KG207-M} + \text{Sex} + \text{Weight} + \text{cohort} + (1|\text{subject})$ . The same interaction model was applied at the voxel level. Furthermore, we have examined the percentage of area Campbell-Switzer silver staining in frontal, cingulate, entorhinal cortices, and hippocampus based on an ANOVA including an interaction term between the percentage of area stained and different regions. Considering the primary objective of the study, we have applied a multiple comparisons correction using False Discovery Rate based on the number of regions. Similarly, we conducted a linear mixed-effect model using CSF A $\beta_{42/40}$  and CSF NFL $_{\log}$  with a random intercept and adjusted for sex and weight:  $\text{CSF A}\beta_{42/40} \text{ ratio} \sim \text{Age} + \text{Sex} + \text{Weight} + (1|\text{subject})$  or  $\text{CSF NFL}_{\log} \sim \text{Age} + \text{Sex} + \text{Weight} + (1|\text{subject})$ . Moreover, we evaluated the change in CSF A $\beta_{42/40}$  ratio and NFL $_{\log}$  between the last sample collected before the treatment (19-month sample) and after the treatment using a linear mixed-effect model in each group. In

addition, a two-sided paired t-test was performed to compare the measured CSF  $A\beta_{42/40}$  ratio and CSF  $NFL_{log}$  concentrations to the predicted levels based on the natural progression in the population-based model in two months following the treatment. Also, the longitudinal analysis in rs-fMRI and hippocampal volume were analyzed based on the following models:  $z\text{-maps} \sim \text{Age} + \text{Sex} + \text{Weight} + (1|\text{subject})$  and  $\text{hippocampal volume} \sim \text{Age} + \text{Sex} + \text{Weight} + (1|\text{subject})$ , respectively, in each group. Last, a two-sided unpaired t-test was performed to compare the susceptibility MRI contrast signal between the groups at follow-up for any evidence of ARIA-H. All statistical analyses were performed using R 3.6.3, Prism7, and VoxelStats, while ImageJ 1.52a was used for the Campbell-Switzer silver staining [224]. All voxel-wise analyses were corrected for multiple comparisons using the Random Field Theory (RFT) method for an adjusted threshold of  $p < 0.05$ . This experiment has been conducted and reported following the ARRIVE guidelines 2.0 [281].

## Results

### **FC5-mFC2a-ABP (KG207-M) fusion protein**

The ABP fusion protein is schematically represented in Figure 35. FC5 is a single-domain camelid antibody that crosses BBB via receptor-mediated transcytosis. Fc fragment derived from mouse IgG2a increases the serum half-life. ABP is derived from human pericentriolar material 1 (PCM-1) that selectively binds to  $A\beta_{42}$  oligomers at nM concentrations [278]. This fusion protein was successfully expressed and produced in a stable pool of CHO cells and purified using Protein A affinity column.



Recombinant fusion protein (90kD MW)

**Figure 35.** A schematic representation of KG207-M.

This is a schematic representation of KG207-M. The FC5 segment is in red, ABP is in blue, and the mouse IgG Fc fragment is in grey.

### **CSF appearance of peripherally administered KG207-M**

KG207-M treatment followed the regimen as described in the Study Design in the Methods section (Figure 34). It was initiated in Tg rats at the age of 22.5 months and consisted of a total of five injections (initial loading dose of 30 mg/Kg/iv and subsequent 15 mg/Kg/iv every week for four weeks via tail vein) in the treatment group, while the control group received saline. The CSF and plasma samples were serially collected following KG207-M or saline administration at the indicated time intervals in the subsequent days (Day 1-7) to characterize serum PK and CSF exposure to the fusion protein.

As presented in Figure 36, observed (filled circles) and simulated curves (solid line) derived from a 2-compartment pharmacokinetic model (parameter estimates not shown) depict the average KG207-M plasma concentration fluctuations during the course of the study (M/F = 17/36). In addition, from an empirical pharmacokinetic model linking KG207-M plasma to CSF

concentration dynamics, approximate fluctuations of KG207-M CSF concentration (solid line) vs observed concentrations (filled circles) are represented (M/F = 15/8) (B). Based on the structure of an indirect-response PK/PD model where KG207-M stimulates the clearance of  $A\beta_{\text{total}}$ , a simulated profile of  $A\beta_{\text{total}}$  is presented in panel (C) in Figure 36 (M/F = 15/8). The model supports an inverse relation between CSF KG207-M concentrations and CSF  $A\beta_{\text{total}}$  concentrations (M/F = 15/8). Panel (D) in Figure 36 indicates that the clearance of  $A\beta_{\text{total}}$  CSF reaches an asymptote when CSF KG207-M reaches 200 ng/mL. The simulations presented in panel (B) in Figure 36 depicted the maintenance of KG207-M CSF concentration above 200 ng/ml for approximately 20% of the dosing interval.

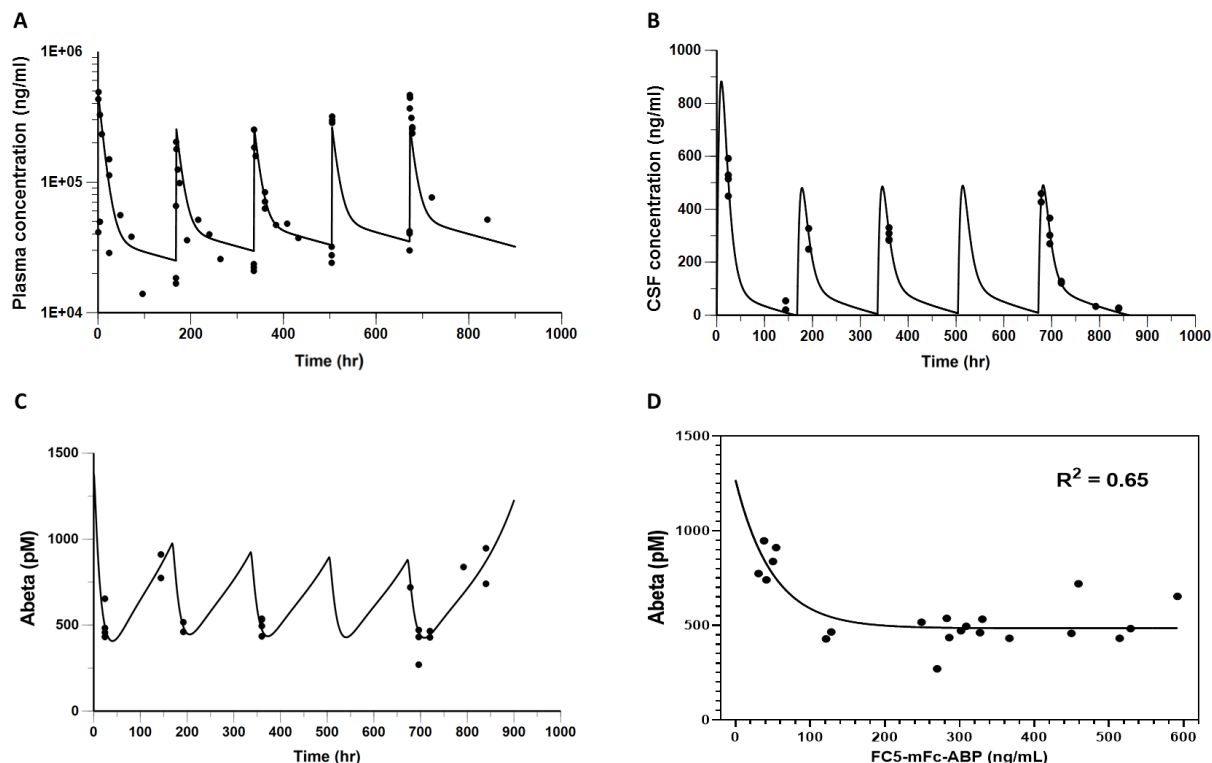


**Figure 36.** Pharmacokinetic modelling of KG207-M.

A-C): Observed (filled circles) and simulated (solid line) KG207-M (A & B) or total Aβ ( $A\beta_{\text{total}}$ ) (C). The KG207-M concentration in plasma (A) or CSF (B & C) vs time following administration of 30 mg/kg/iv bolus followed by four 15 mg/kg/iv bolus doses every 7 days for 28 days to Tg-ABP rats are shown. D)  $A\beta_{\text{total}}$  concentration vs KG207-M concentration in CSF.

### KG207-M reduces Aβ load in the brain and CSF

The natural progression of Aβ accumulation in Tg rats was demonstrated via longitudinal PET [ $^{18}\text{F}$ ]AZD4694 quantification ( $BP_{\text{ND}}$ ). The global Aβ load significantly increased in Tg rats from 9 to 24 months of age (population main effect model: M/F = 14/13,  $t(21) = 2.474$ ,  $p = 0.0349$ ) (Figure 37A). Following the KG207-M treatment initiated at 21 months of age, [ $^{18}\text{F}$ ]AZD4694  $BP_{\text{ND}}$  substantially decreased in the Tg-ABP at 24 months (main effect model: M/F = 12/4,  $t(7.4) = -2.657$ ,  $p = 0.03112$ ), showing KG207-M target engagement. When we

compare the A $\beta$  pathology progression between the Tg-SAL and Tg-ABP, we found that KG207-M significantly altered the A $\beta$  pathology progression in the Tg-ABP group adjusted for sex, weight, and cohort variability (interaction model: cohort 1 and Tg-SAL vs Tg-ABP = 21 vs 16, M/F = 16/21,  $t(17.3) = -3.321$ ,  $p = 0.00397$ ) (Figure 37A).

We also evaluated the effects of KG207-M on the CSF A $\beta_{42/40}$  ratio in Tg following the KG207-M treatment. The CSF was collected from 10 to 19 months old prior to the KG207-M treatment to characterize the natural longitudinal CSF A $\beta_{42/40}$  ratio progression model in Tg. There was a progressive and significant decline in the CSF A $\beta_{42/40}$  ratio adjusted for sex and weight (M/F = 40/84,  $t(114.4) = -2.971$ ,  $p = 0.00362$ ) (Figure 37B). However, there was a significant increase in the CSF A $\beta_{42/40}$  measurements from 0.531 at 19 months old to 0.63 following two months after the KG207-M treatment in the Tg-ABP group (main effect model: M/F = 16/6,  $t(15.34) = 2.4$ ,  $p = 0.03$ ), while the Tg-SAL group showed a significant decline from 0.50 at 19 months to mean of 0.43 at 25 and 26 months (main effect model: M/F = 4/3,  $t(7) = -6.32$ ,  $p = 0.0004$ ). To note, the Tg-ABP group seemed to carry slightly more A $\beta$  pathology, which enriched the effect of the treatment, relative to Tg-SAL, but this was not statistically different. Furthermore, when we compared the CSF A $\beta_{42/40}$  measurements following two months after the KG207-M treatment compared to the non-treated condition predicted by the longitudinal model, we found a significant increase showing rectification of the CSF A $\beta_{42/40}$  profile in the Tg-ABP (a paired t-test: M/F = 10/4,  $t(13) = 4.35$ ,  $p = 0.0008$ ) (Figure 37B). On the other hand, Tg-SAL did not show any difference compared to the predicted longitudinal model (Figure 37B). The monthly CSF A $\beta_{42}$  and A $\beta_{40}$  concentrations are summarized in Supplementary Table 17.

Then, we investigated the disease-modifying therapeutic effects of KG207-M using voxel-wise analyses and revealed up to 47% and 33% decline in [<sup>18</sup>F]AZD4694 BP<sub>ND</sub> in the prefrontal cortex and nucleus accumbens, respectively, after the KG207-M treatment (Figure 37C). Moreover, the reductions in the [<sup>18</sup>F]AZD4694 BP<sub>ND</sub> were statistically significant in the prefrontal cortex, cingulate cortex, entorhinal cortex, associative cortex, retrosplenial cortex, nucleus accumbens, and hippocampus (interaction model: cohort 1 and Tg-SAL vs Tg-ABP = 21 vs 16, M/F = 16/21, t = 2-6). (Figure 37D). It is worth noting that these brain regions play important roles in rat cognitive functions and are vulnerable to A $\beta$  pathology in this model displaying extensive A $\beta$  plaques [89, 158]. A more comprehensive view of the voxel-wise results can be found in Supplementary Figure 18.

The imaging analyses were supported by the post-mortem histology using Campbell-Switzer silver staining. We observed extensive A $\beta$  plaques in the frontal cortex (15%), cingulate cortex (13%), entorhinal cortex (18.4%), and hippocampus (24%) in Tg-SAL brains (Figure 37E). However, there was minimal to no staining in Tg-ABP brains (< 0.01% in all regions). Based on an ANOVA test, Tg-ABP showed a significantly less percentage of the Campbell-Switzer silver staining in all regions (Tg-SAL vs Tg-ABP = 2 vs 8, M/F = 7/3, t(24) > 4, p < 0.001) following a multiple comparisons correction based on the number of regions tested, supporting the clearance and prevention of A $\beta$  plaque formation (Figure 37F and Supplementary Figure 19).

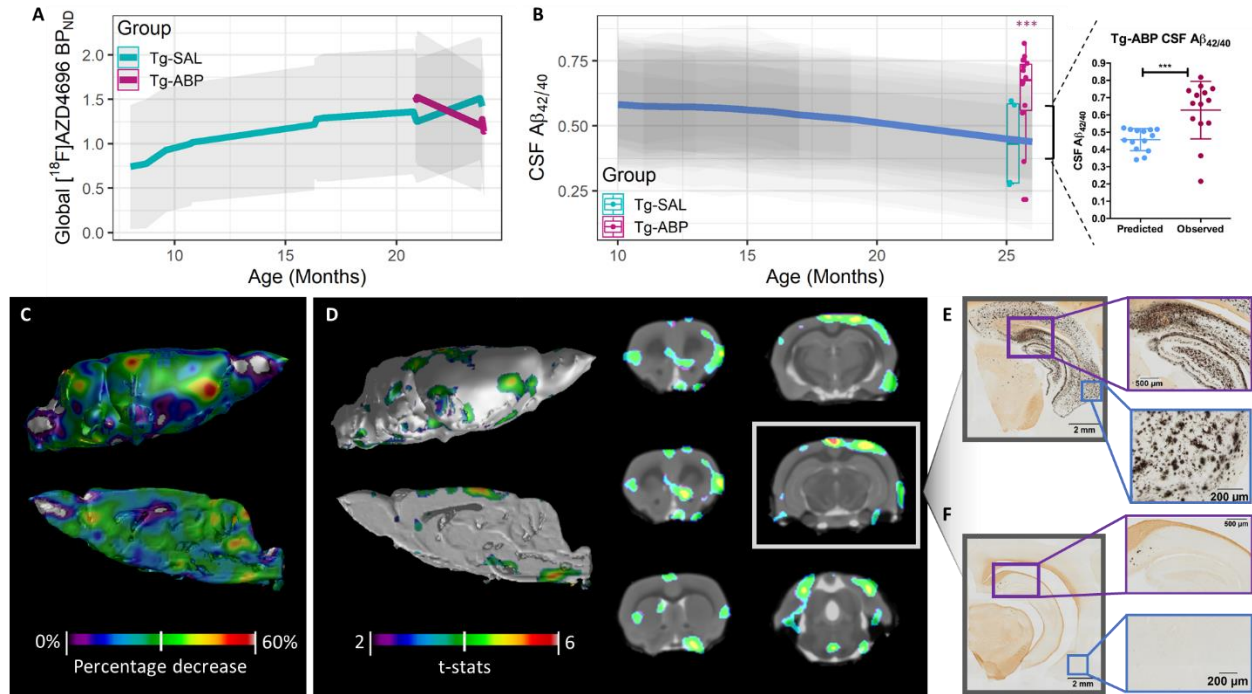


**Figure 37.** KG207-M removes brain  $A\beta$ .

The gray shadow represents the 95% confidence intervals of models in (A - B). A) The linear mixed-effect model of global  $[^{18}\text{F}]\text{AZD4694 BP}_{\text{ND}}$  showed a significant increase in Tg from 10-24 months old (solid green line;  $t(21) = 2.437$ ,  $p = 0.0238$ ) but a significant decline in Tg-ABP between 21-24 months old (solid red;  $t(7.4) = -2.657$ ,  $p = 0.03112$ ). The interaction between treatment and disease progression showed that KG207-M significantly modified global  $[^{18}\text{F}]\text{AZD4694 BP}_{\text{ND}}$  (cohort 1 and Tg-SAL vs Tg-ABP = 21 vs 16, M/F = 16/21,  $t(17.3) = -3.321$ ,  $p = 0.00397$ ). B) The linear mixed-effect model showed a significant decline in CSF  $A\beta_{42/40}$  ratio in Tg rat model from 10-19 months old (solid blue;  $t(114.4) = -2.971$ ,  $p = 0.00362$ ). A box whisker plot based on Tukey method represented a paired t-test, which revealed that CSF  $A\beta_{42/40}$  ratio increased (solid red;  $t(13) = 4.373$ ,  $p = 0.0008$ ) in Tg-ABP animals as compared with a population-based prediction by the model while no differences were found in Tg-SAL ( $t(3) = 0.4869$ ,  $p = 0.6597$ ). C) A voxel-wise effect size map showed up to 47% decline in  $[^{18}\text{F}]\text{AZD4694 BP}_{\text{ND}}$  prefrontal region (baseline-follow-up/baseline). D) A voxel-wise linear mixed-effect model analysis showed a significant  $[^{18}\text{F}]\text{AZD4694 BP}_{\text{ND}}$  clearance in Tg-ABP compared to Tg-SAL (cohort 1 and Tg-SAL vs Tg-ABP = 21 vs 16, M/F = 16/21). E-F) Campbell-Switzer silver staining displayed widespread  $A\beta$  plaques throughout the cortical regions in Tg-SAL animals while relatively few plaques were seen in Tg-ABP brains collected at 26.7 months old (Tg-SAL vs Tg-ABP = 2 vs 8, M/F = 7/5,  $t(24) > 4$ ,  $p < 0.001$ ). Here, one brain image from each group was included but comparable results were seen in all animals from each group.

## **KG207-M rescues neuronal injury biomarkers**

In addition to the longitudinal CSF  $A\beta_{42/40}$  ratio progression, CSF NFL<sub>log</sub> concentrations were analyzed as a biomarker of neuronal injury over 10-19 months of age in the McGill-R-Thy1-APP rat model prior to administration of KG207-M. Recent reports showed increased concentrations of CSF NFL in AD and other neurodegenerative diseases and reduced CSF NFL concentrations following beta-secretase 1 (BACE-1) inhibitor treatment in APPPS1 mice, suggesting that CSF NFL is a sensitive neuronal injury biomarker [206-208]. A progressive and significant increase in CSF NFL<sub>log</sub> concentrations was observed in Tg rats over 10-19 months of age (M/F = 54/25,  $t(67.6) = 4.65$ ,  $p < 0.0001$ ; adjusted for sex and weight), and it continued to increase significantly in the Tg-SAL group when we compared from the beginning of the treatment (32958 pg/mL) and the post-treatment samples (49190.5 pg/mL) (main effect model: M/F = 4/3,  $t(7) = 4.47$ ,  $p = 0.003$ ) (Figure 38A). However, the Tg-ABP group showed no significant increase in CSF NFL<sub>log</sub> concentration between the beginning of the treatment (39405 pg/mL) and the post-treatment samples (44375.5 pg/mL). Rather, there was a significant reduction in CSF NFL<sub>log</sub> concentration following two months after KG207-M treatment compared to the non-treated condition predicted by the longitudinal model suggesting a reduction in neuronal injury (paired t-test: M/F = 6/4,  $t(9) = 2.28$ ,  $p = 0.0487$ ) (Figure 38A). The monthly CSF NFL concentrations are summarized in Supplementary Table 18.

Furthermore, using the same Tg model and techniques, our group has recently reported a decline in cingulate resting-state connectivity (Figure 38B) as well as hippocampal volume in the McGill-R-Thy1-APP Tg model compared to wild type [158]. Here, Tg-ABP cingulate to brain connectivity was increased after 5 weeks of KG207-M treatment while Tg-SAL showed no change. Tg-ABP showed greater cingulate connectivity with the orbitofrontal cortex,

somatosensory cortex, parietal association cortex, basal medial amygdaloid nucleus, left posterior ventral hippocampus, striatum, and thalamus (main effect model: M/F = 12/4,  $t = 2-5$ ) (Figure 38C). A more comprehensive view of the voxel-wise results can be found in Supplementary Figure 20. In addition, Tg-ABP showed a substantial increase in hippocampal volume after the treatment while Tg-SAL did not change in their hippocampal volume adjusted for sex and weight (Tg-ABP paired t-test; M/F = 12/4,  $t(7) = 3.554$ ,  $p = 0.00397$ ) (Figure 38D).

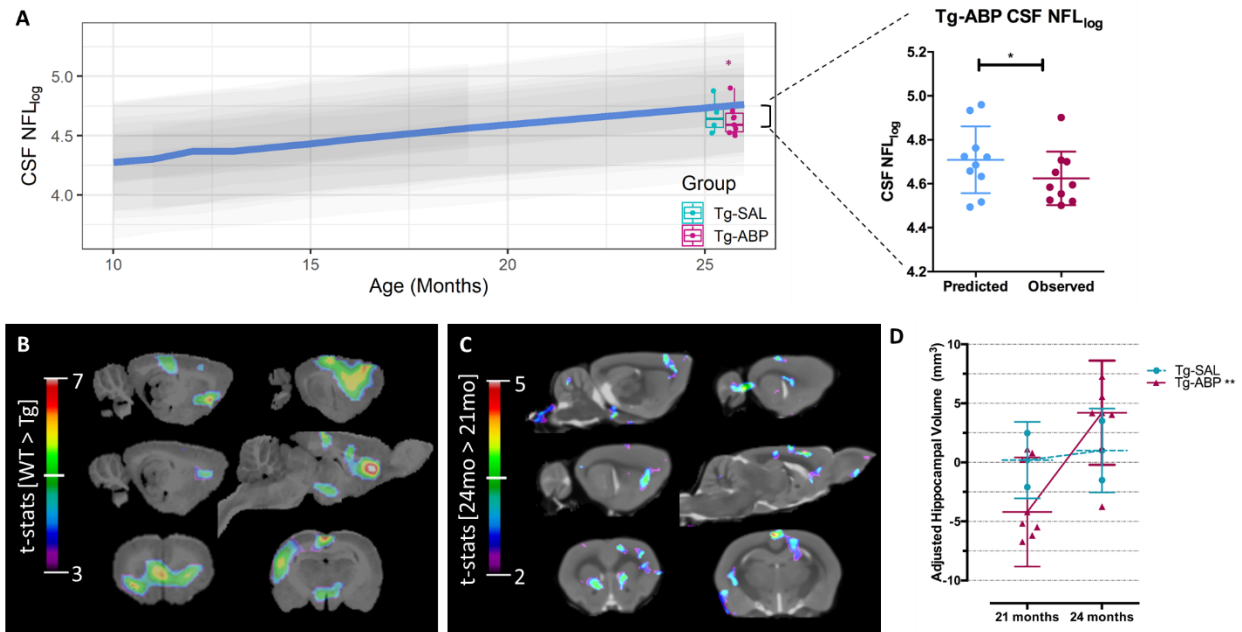


**Figure 38.** *KG207-M ameliorates A $\beta$ -induced in vivo biomarker abnormalities.*

A) The gray shadow represents the 95% confidence intervals of the model per subject. The linear mixed-effect model showed a significant increase in CSF NFL<sub>log</sub> concentrations in the Tg rat model from 10-19 months old (solid blue;  $t(67.6) = 4.819$ ,  $p < 0.0001$ ). A box whisker plot based on Tukey method represented a paired t-test, which revealed that CSF NFL<sub>log</sub> concentrations decreased (solid red;  $t(9) = 2.6286$ ,  $p = 0.0481$ ) in Tg-ABP as compared to a population-based prediction by the model while Tg-SAL showed no difference ( $t(3) = 1.208$ ,  $p = 0.3137$ ). B) The figure represents a significant group contrast in resting-state BOLD signal from cingulate to the rest of the brain between WT ( $n = 8$ ) and McGill-R-Thy1-APP ( $n = 8$ ) at 16-19 months. The voxel-wise linear mixed-effect analysis showed a significant reduction in resting-state cingulate connectivity in Tg (reproduced from Parent et al., 2017 []). The result images were adjusted for multiple comparisons based on RFT at  $p < 0.05$ . C) The figure represents a significant contrast in the resting-state BOLD signal from cingulate to the brain in Tg-ABP ( $n = 9$ ) following KG207-M treatment compared to baseline at 21 months of age. The voxel-wise linear mixed-effect analysis showed a significant increase in resting-state cingulate connectivity when the network is compared before and after the KG207-M treatment. The result images were adjusted for multiple comparisons based on RFT at  $p < 0.05$ . D) The adjusted hippocampal volume in Tg-SAL and Tg-ABP before and after KG207-M treatment are displayed as mean  $\pm$  standard deviation. The linear mixed-effect analysis revealed a significant increase in hippocampal volume in Tg-ABP ( $t(7) = 3.554$ ,  $p = 0.00397$ ), however, there was no significant hippocampal volume change in Tg-SAL ( $t(1) = 0.1694$ ,  $p = 0.8932$ ).

## **No evidence of microhemorrhage**

To examine any possible ARIA-H, we conducted a susceptibility MRI scan following the treatment. The images were visually assessed first to see possible ARIA-H. Asymmetric susceptibility signals were the primary interest as the vascular structures displayed symmetry (Figure 39A). In conjunction, the susceptibility signal was binarized to represent either vasculature, ventricles, or ARIA-H. There was no difference in susceptibility signal volume between Tg-SAL and Tg-ABP (unpaired t-test; Tg-SAL vs Tg-ABP = 3 vs 9, M/F = 7/5,  $t(2.59) = 0.455$ ,  $p = 0.685$ ) (Figure 39A-C). This was confirmed by post-mortem histology staining with Perls/DAB (Figure 39B).

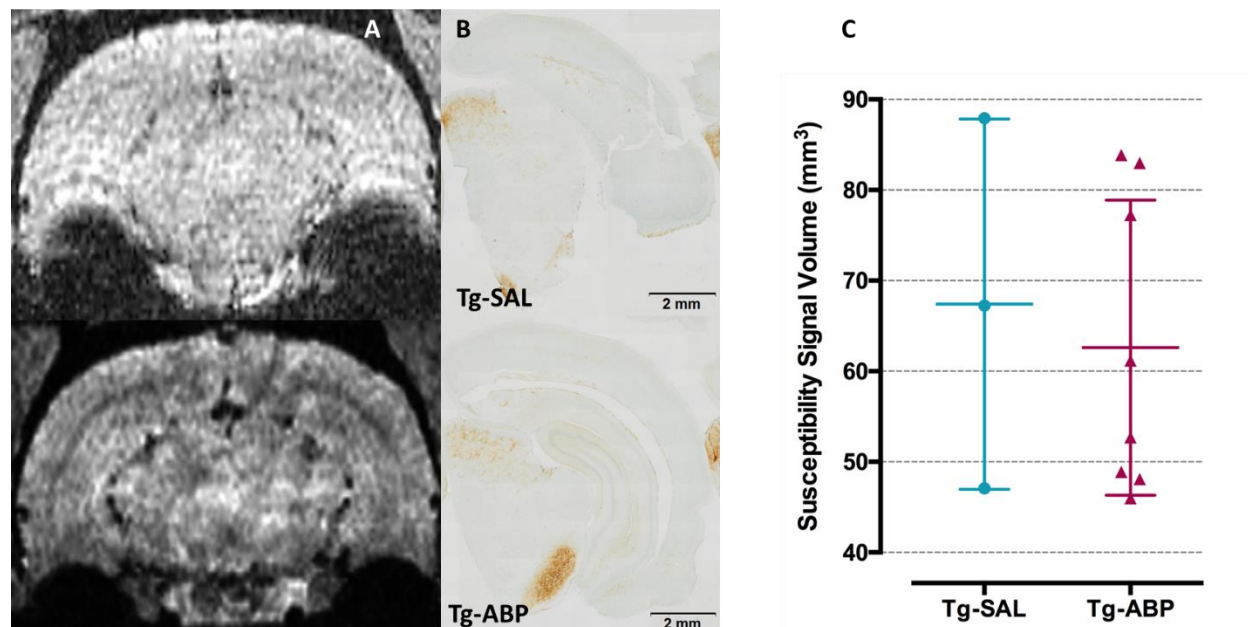


**Figure 39.** No evidence of ARIA-H.

A) The susceptibility MRI in the coronal view of Tg-SAL in the upper corner image and Tg-ABP in the lower corner. Both images do not show any evidence of ARIA-H. B) Histological staining using Perls/DAB of the same animals in the corresponding section from the susceptibility images are shown. These sections were taken adjacent to the previous Campbell-Switzer silver staining section. In both Tg-SAL and Tg-ABP, there is no evidence of ARIA-H. C) Susceptibility signal contrast was converted into volume and displayed in mean  $\pm$  standard deviation in Tg-SAL (n = 3) and Tg-ABP (n = 9). The contrast signal implies that there is a deposit of iron (ARIA-H), vasculatures, or ventricles. There was no significant difference in susceptibility signal contrast volume between Tg-SAL and Tg-ABP after 5 weeks of KG207-M treatment (unpaired t-test; Tg-SAL vs Tg-ABP = 3 vs 9, M/F = 7/5,  $t(2.59) = 0.455$ ,  $p = 0.685$ ).

## Discussion

In summary, our study demonstrated the pharmacokinetics, safety, and disease-modifying effects of KG207-M that incorporates a BBB transporter and an A $\beta_{42}$  oligomer targeting peptide. Effectively, KG207-M showed sufficient brain penetration to reduce A $\beta_{42}$  aggregates. This was demonstrated by the acute decline in CSF A $\beta_{\text{total}}$  concentration when KG207-M was at its

maximum concentration in CSF and by the subsequent reduction of PET [<sup>18</sup>F]AZD4694 uptake. The *in vivo* results were validated by the semi-quantitative observation conducted in the post-mortem tissues of the Tg-ABP animals using Campbell Switzer silver staining. In addition, KG207-M therapeutic efficacy in reducing downstream effects of A $\beta$  accumulation was demonstrated by the substantial post-therapeutic recovery of CSF A $\beta_{42/40}$  ratios and CSF NFL<sub>log</sub> concentrations, increased hippocampal volume, and rectification of rs-fMRI cingulate to brain connectivity. Last, the absence of ARIA-H supports a safe profile of the doses administered to these animals.

Previously FC5-Fc has been shown to reach peak CSF/serum level ( $\geq 1\%$ ) between 24 and 48 hours post tail vein injection, which is much higher than the conventional antibodies [282, 283]. Based on the results of recent anti-amyloid therapy clinical trials, one may argue that the BBB delivery could impact therapeutic efficacy [76, 155, 272]. Maintaining the CSF levels of KG207-M at an effective dose (200 ng/ml) in this prospective study sufficiently reduced the A $\beta$  loads in Tg-ABP animals. Importantly, our study supports the notion that KG207-M delivery using the humanized FC5-Fc nanobody via receptor-mediated transcytosis, which is conserved between rodents and humans, would be sufficient to transport the drug and modify A $\beta$  pathology in human clinical trials [276].

With abundant evidence suggesting soluble oligomers being the most toxic form of A $\beta$ , the preferential binding to the aggregated A $\beta$  by KG207-M suggests that it can selectively target A $\beta_{42}$  oligomers in the CNS [277, 278, 284-286]. Despite the lack of direct measures of target engagement of A $\beta_{42}$  oligomers non-invasively, the decline in [<sup>18</sup>F]AZD4694 uptake and rectification of CSF A $\beta_{42/40}$  ratio in the post-treatment measurement in Tg-ABP constitute remarkable proof of concept of the KG207-M intervention. The reduced brain A $\beta$  loads reported

here are likely to reflect A $\beta$  oligomer clearance, under the assumption of dynamic equilibrium among A $\beta$  species in these animals [286, 287]. As such, one can expect that A $\beta$ <sub>42</sub> oligomer clearance evoked by KG207-M would shift this dynamic equilibrium towards reducing the amount of A $\beta$  plaques, and consequently reducing the [<sup>18</sup>F]AZD4694 uptake. A similar observation made in the PRIME study showed a reduction of PET-AV45 uptake following Aducanumab treatment, an intervention that targets either soluble oligomers or insoluble fibrils [155]. Indeed, after the cessation of KG207-M administration, the levels of CSF A $\beta$ <sub>42/40</sub> were rectified until the animals were sacrificed for histological examination.

It has been challenging to predict the effects of therapeutic interventions on human imaging biomarkers based solely on *in vitro* histopathological observations in animals. In addition, the cross-sectional nature of *in vitro* observations limits the prediction in the post-therapy A $\beta$  levels compared to its pre-dosing levels [288]. Although solanezumab and bapineuzumab were successful in the preclinical stage of drug development, both therapeutic candidates failed to meet the clinical primary outcome as well as reducing A $\beta$  load with PET in their phase 3 studies [272, 273]. In this study, we attempted to reduce the gap between pre-clinical and clinical studies through a highly translational platform by incorporating a longitudinal study design with fluids and imaging biomarkers to monitor KG207-M therapeutic effects in the McGill-R-Thy1-APP rat model. These innovations offer unprecedented metrics regarding the true effect sizes of KG207-M on engaging the molecular targets, on rectifying neuronal injury based on structural and functional biomarkers, as well as providing a safety profile via the same biomarkers used in clinical trials.

This platform capitalizes on the properties of the McGill-R-Thy1-APP rat model, which has been previously characterized based on the *in vivo* biomarker platform [158, 195]. The

McGill-R-Thy1-APP rat model progressively develops A $\beta$  pathology, indicated by the significant increase in the [ $^{18}$ F]AZD4694 PET and decline in the CSF A $\beta_{42/40}$  ratio, at a similar rate as AD patients and recapitulates AD biomarker abnormalities [158, 195]. For example, the McGill-R-Thy1-APP rat model has an increased CSF NFL concentration, reduction in hippocampal volume, cingulate connectivity, and CSF A $\beta_{42/40}$  ratio, which have been shown to be sensitive biomarkers for AD pathological progression and disease severity, ultimately leading to memory impairment [44, 47, 48, 158, 195, 207, 275, 289-291]. In addition to the disease-modifying effect, five weeks of KG207-M treatment ameliorates the hippocampal volume, cingulate connectivity, and CSF A $\beta_{42/40}$  ratio and CSF NFL concentrations, among which CSF NFL and resting-state connectivity dysfunction were reported to be due to A $\beta$  oligomers in this Tg rat model [158, 195]. It is important to interpret the volumetric changes observed based on MRI in the animals with caution as such changes do not necessarily reflect neurogenesis. Rather, collective evidence suggests synaptic recovery through the dendritic growth and/or synaptic remodelling as the McGill-R-Thy1-APP rats have shown a decline in volumetric changes without significant cell death [158, 160, 195]. Nevertheless, to the best of our knowledge, this is the first study to show directly the therapeutic target engagement, efficacy, and safety using multi-parametric clinical biomarkers such as CSF, PET, and MRI in a preclinical *in vivo* longitudinal study.

It is imperative to recognize some limitations of the present study. There were no prior data to precisely estimate an effect size for ARIA-H as this study was the first *in vivo* characterization of KG207-M. While no increase in microhemorrhages was observed in the present study, a separate study should be conducted to more fully assess the ARIA potential of KG207-M — possibly in an animal model with known microhemorrhage susceptibility and with

a positive control microhemorrhage-inducing antibody. Moreover, currently, there is no established method to accurately quantify the changes in A $\beta$ <sub>42</sub> oligomers levels directly *in vivo*. As such, different methods of A $\beta$  quantifications were used as a surrogate for A $\beta$ <sub>42</sub> oligomers clearance. Also, the McGill-R-Thy1-APP rat model develops A $\beta$  pathology progressively at levels comparable to human patients. However, it lacks tau pathology that is present invariably in AD patients leading to a lack of substantial cell death in this model [89, 158, 160]. Previous studies have reported that neurofibrillary tangles (NFT) show a greater correlation with structure and memory declines as NFT are in closer proximity to the downstream AD pathological processes [292]. As such, our study did not evaluate cognitive changes following the treatment in the McGill-R-Thy1-APP rat model. Albeit the primary objective of the study was to characterize the target engagement, assessment of cognitive improvement will be critical to demonstrate therapeutic value, and this will be pursued in a subsequent study to address this limitation in the current study. While we report improvement in CSF NFL, cingulate connectivity, and hippocampal volume by targeting A $\beta$  pathology, one should be cautious in expecting full translation in the therapeutic efficacy on neuronal injury biomarkers in AD patients. Perhaps, the discrepancies reported insofar between preclinical and clinical trials regarding cognitive improvement may lie in this aspect.

With the evidence presented here based on our *in vivo* longitudinal translational biomarker platform, KG207-M holds great potential as disease-modifying therapy. By constructing ABP to selectively target more toxic forms of A $\beta$ <sub>42</sub>, KG207-M does not only alter A $\beta$  pathological progression but also rescues the typical biomarker changes that are reported in the McGill-R-Thy1-APP rat model. This is a unique effort to evaluate the disease-modifying

therapeutic effects and safety in a preclinical study. Consequently, we propose that this will increase the chance of translating the findings into clinical trials.

## **Acknowledgement**

The authors would like to send gratitude to Eve-Marie Charbonneau and her animal facility team for their technical support with animal care. The authors would like to acknowledge Olive Stange for assisting during A $\beta$ <sub>40</sub> and A $\beta$ <sub>42</sub> Simoa analysis, and Leslie Brown, Christie Delaney, Wen Ding Alexandra Star for their technical help in Mass Spec analysis of serum and CSF samples.

## **Author contributions**

M.S.K., M.S., N.Y., D.S., B.C., and P.R-N. designed the study. M.S.K., M.S., A.A.A., A.M., and M.M.C. collected the *in vivo* imaging data. M.S.K. and J.O. analyzed the *in vivo* imaging data. M.S.K., A.A.A, and K.Q.S. collected *in vitro* rat brain tissues. M.S.K. analyzed the *in vitro* microhemorrhage data. A.S., K.B., H.Z., A.H., and B.C. analyzed the CSF fluid data. A.H. and B.C. analyzed plasma data. M.S.K., S.M., J.O., K.R., B.C., and P.R-N. conducted statistical analyses. M.S.K., T.A.P., A.L.B., D.L.C., J-P.S., M.M.C., A.M., A.S., K.B., H.Z., G.M., A.C.C., S.G., M.W., E.L., A.H., K.R., D.S., B.C., and P.R-N., wrote and revised the manuscript.

## **Competing interests**

Dr. Blennow has served as a consultant or at advisory boards for Alzheon, BioArctic, Biogen, Eli Lilly, Fujirebio Europe, IBL International, Merck, Novartis, Pfizer, and Roche Diagnostics, all unrelated to the present study, and is a co-founder of Brain Biomarker Solutions in Gothenburg AB, a GU Venture-based platform company at the University of Gothenburg.

## **Funding**

This work was supported by the Brain-Canada CQDM grant, the Weston Brain Institute, the Canadian Institutes of Health Research (CIHR; FRN, 152985, PR-N), the Alzheimer's Association (NIRP-12-259245, PR-N), Fonds de Recherche du Québec – Santé (FRQS; Chercheur Boursier, PR-N). K.B. holds the Torsten Söderberg Professorship in Medicine at the Royal Swedish Academy of Sciences. S.G. and P.R.N. are members of the CIHR-CCNA Canadian Consortium of Neurodegeneration in Aging.

## **Supplemental Materials**

Supplementary materials for this paper can be found at <http://jcbfm.sagepub.com/content/by/supplemental-data>

## 13 A comprehensive scholarly discussion of all the findings

In this Ph.D. thesis, multimodal *in vivo* biomarker-based investigations of AD pathophysiology and drug discovery were discussed. This thesis had three aims and three contributions to the *in vivo* biomarker-based AD research framework. Study 1 validated NFL in CSF and plasma as a novel neuronal injury/neurodegeneration biomarker that is sensitive to tracking A $\beta$ -induced neurodegeneration in AD. Study 2 showed *in vivo* biomarker evidence of activated microglia driving aggregation of tau and spreading in the presence of A $\beta$  in AD. Last, Study 3 demonstrated a successful target engagement, efficacy, and safety of a novel anti-amyloid treatment based on the same *in vivo* biomarkers used in AD clinical trials. This thesis highlights the importance of *in vivo* biomarkers and three unique areas of AD research to support the *in vivo* biomarker-based research framework: 1) discovery and validation of new biomarkers, 2) *in vivo* biomarker-based evidence supporting disease mechanisms, and 3) *in vivo* biomarker-based evidence in evaluating novel therapeutic target engagement, efficacy, and safety. These constitute a significant contribution to advancing the field of AD research.

### 13.1 Validation of a new biomarker

Previous evidence on the influence of A $\beta$  pathology on NFL levels was conflicting in AD literature. Some studies suggest that NFL levels may be independent of A $\beta$  pathology as there was no statistical difference between A $\beta$ - and A $\beta$ + subjects in the clinical spectrum of sporadic AD [196, 207]. Furthermore, previous studies have only focused on the association between NFL concentrations and *a priori* ROIs volume over regions typically affected by AD [198, 207, 213]. In contrast, the empirical evidence on the NFL association with reduced grey matter density at a

voxel-based regional level in the context of A $\beta$  pathology was largely missing. Although NFL elevation is an indicator of the presence of neurodegenerative processes, this fluid biomarker lacks the topographical information present in [ $^{18}$ F]FDG-PET or MRI scans. Moreover, neurodegeneration is not specific to AD. Elevated NFL concentrations in CSF have been associated not only with axonal damage but also with normal aging, head trauma, and other neurological disorders [204-206, 293]. Collectively, these are important limitations since plasma or CSF NFL levels might reflect disease-specific grey or white matter neurodegenerative processes or the disease-independent healthy aging process. Thus, it is imperative to investigate whether an increased level of NFL in CSF and plasma is linked to the AD pathophysiology rather than reflecting the aging process or other comorbidities to interpret NFL as a novel fluid biomarker for neuronal injury or neurodegeneration in AD research and therapeutic trials. Study 1, “*Amyloid-beta modulates the association between neurofilament light chain and brain atrophy in Alzheimer’s disease*” [195], conducted a cross-species study design to show the effect of A $\beta$  on NFL and correlate NFL with a widely accepted neurodegeneration biomarker, VBM, as a novel neuronal injury or neurodegeneration biomarker and suited for the A/T/(N) classification.

To address the conflicting literature on the effect of A $\beta$  on NFL, a cross-species study was conducted using ADNI and McGill-R-Thy1-APP transgenic rat model. It is noteworthy that the McGill-R-Thy1-APP rat model is an AD-like A $\beta$  pathology model without tauopathy, which would be a confounding factor in examining the independent effect of A $\beta$  on NFL [89, 212]. Therefore, the McGill-R-Thy1-APP rat model was ideal to elucidate the effect of A $\beta$  on NFL. Using the ADNI dataset, an A $\beta$  cutoff (CSF p-tau/A $\beta$ <sub>42</sub> > 0.025) was used to differentiate A $\beta$ - and A $\beta$ + groups and tau was included as a covariate. The McGill-R-Thy1-APP rat model showed significantly increased CSF NFL concentrations compared to WT, and the CSF NFL was

inversely associated with CSF A $\beta$ <sub>42/40</sub> similar to the human AD literature. However, there was no interactive effect between the age and genotype, suggesting that the effect of A $\beta$  on NFL was stable over time. Here, the data were collected from 10 months, which would be the time when A $\beta$  plaques start to form in this animal model. This suggests the substantial effect of A $\beta$  on NFL is likely from more toxic A $\beta$  oligomers which occur rather early in AD pathophysiology. This notion is supported by the observation of elevated NFL concentrations decades before the symptom onsets in a familial AD cohort [198]. The effect of age on the NFL was also very significant confirming the nonspecificity of neurodegeneration biomarkers. Together, this could explain why AD literature often reported no significant difference in the NFL levels between A $\beta$ - compared to A $\beta$ + in the clinical spectrum of sporadic AD [196, 207]. The early event of the A $\beta$  oligomer toxicity would be diluted over time with other processes affecting the NFL concentrations such as aging, NFTs, inflammation, and other comorbidities, which is likely observed in an aging population.

Owing to the large-scale network analyses, a growing body of evidence suggests a disease-specific vulnerability in neurodegenerative processes to an ensemble of regions [185, 214]. Assessing the association between NFL concentrations and grey matter changes over the brain provided new insights into whether the levels of NFL are driven by AD-vulnerable regional neuronal injury or age-related neurodegeneration. Based on the empirical evidence from the McGill-R-Thy1-APP rat model, the elevated NFL levels and reduced grey matter density were associated in the neocortex and hippocampus, which are the regions with high A $\beta$  pathology in this model. Congruently, in A $\beta$ + MCI and AD, NFL in CSF and plasma were significantly associated with VBM in the temporal cortex, frontal cortex, precuneus, and hippocampus, which are the regions known to have extensive neurodegeneration. Recent evidence based on the

association between NFL levels and VBM measurements was in agreement with other studies using *a priori* defined ROIs in frontotemporal lobar degeneration and Huntington's disease, showing that increased NFL concentration was associated with reduced frontal cortex and striatum VBM measurements, respectively [206, 209]. This supports the hypothesis that indeed increased NFL concentrations in those diseases follow neuronal injury in their specific network.

Together, these findings further support the NFL as a neuronal injury biomarker in the research framework of AD biomarker classification and for the evaluation of therapeutic efficacy in clinical trials. Moreover, ultra-sensitive, high-throughput, minimally invasive, and widely available blood-based biomarkers would transform the clinical trial enrichment and available tools for general clinics.

### **13.2 *in vivo* biomarker-based evidence supporting disease mechanisms**

One of the greatest enigmas in AD research has been the pathophysiological link between A $\beta$  and p-tau, and this is still a very active research question in AD research today. One of the most challenging reasons to answer this question is due to a distinct and disparate spatiotemporal staging of A $\beta$  and p-tau in AD. Recently, collective evidence from genetic, molecular, and animal studies demonstrated an important role of activated microglia in driving hyperphosphorylated tau aggregation and spreading in AD [86, 111, 130]. However, *in vivo* biomarker-based evidence of activated microglia driving tauopathy is largely missing in a living human population. If activated microglia drive tau aggregation and spreading, then how would it fit with the current understanding of the Braak staging and trans-synaptic tau propagation hypothesis? Understanding how activated microglia are involved in such a process may highlight

the protective or pathologic roles of activated microglia in AD. Thus, the second study, “*The interaction between amyloid-beta and activated microglia drives tau propagation in Alzheimer’s disease*”, aimed to show the effect of activated microglia on tau aggregates using *in vivo* PET imaging biomarkers in AD.

Having multiple PET tracers provided a unique opportunity to investigate three molecular targets of AD: [<sup>18</sup>F]AZD4694 for A $\beta$ , [<sup>18</sup>F]MK6240 for tau, and [<sup>11</sup>C]PBR28 for activated glial cells. Based on the PET imaging biomarkers, Study 2 showed significant interactive effects between A $\beta$  and activated microglia predicting tau burden. This observation was particularly striking when A $\beta$  was divided by A $\beta$ - and A $\beta$ + because this effect was mainly driven by the A $\beta$ + group. This suggests that the A $\beta$  modulates the effect of activated microglia in AD and may reflect the disease-associated microglial phenotypes found in GWAS reports [129, 130, 132, 135]. An increased amount of pro-inflammatory processes from activated microglia could lead to increased aggregation of tau and toxic insults in AD. Another intriguing observation from Study 2 was the differential regional effect of activated microglia on AD pathophysiology. The positive or negative interactive effect between activated microglia and A $\beta$  depended on the region. Notably, regions that are thought to be the hub of DMN (ie. Precuneous) or vulnerable to early tau deposition (ie. Medial temporal region) seem to have a positive interactive effect with A $\beta$  on tau aggregation. In contrast, regions that are thought to be in the later Braak stages such as the associative parietal region and visual cortex regions seem to have a negative interactive effect with A $\beta$  on tau aggregation. This may reflect the regional vulnerability of AD pathology akin to the progression of Braak Staging. Here, microglia may play a direct role as well. At the synapse, microglia are shown to release pathologic tau via exosome and inhibiting the exosome significantly reduced the tau propagation [252]. Additionally, the regional heterogeneity of

microglia may play a role in regional vulnerability. Recent studies have reported a profound influence of microenvironment and origin of microglia to alter the transcriptomic that can be switched to the pro-inflammatory profile [87, 253, 254]. In addition to the transcriptomic profile, microglial epigenetic alteration based on the regional demand determines the microglial clearance activity [255]. For example, having a higher neuronal attrition rate in the cerebellum compared to the striatum, the PRC2 in microglia controlled the gene expressions supporting the clearance activity via epigenetic alterations. However, the aberrant activation of clearance in PRC2-deficient microglia displayed altered neuronal spines that resembled the AD pathology induced by microglial activation in the AD mouse model [255]. As the regions that show early tau deposition are intimately related to the neurogenic region such as in the dentate gyrus, microglial function during the neurogenesis may contribute to promoting tau propagation by spilling exosomes [252, 256]. Taking the advantage of three PET biomarkers, Study 2 highlights the spatiotemporal dynamics in glial neuroinflammation that lead to differential effects in AD. Therefore, the spatiotemporal dynamics in the microglial phenotypes are evident and may contribute to the regional tau predisposition. Understanding the underlying mechanisms leading to the vulnerability would bring new insights to AD drug discovery. Importantly, the convergence of regional vulnerability in AD from the *in vivo* biomarkers investigating glial activation supports the crucial role of glial activation in AD pathophysiology.

One major challenge in AD research is the complex multifactorial processes of AD pathophysiology leading to neurodegeneration and cognitive decline. This challenge could significantly hinder applying simple statistical methodologies and making an unbiased inference of rich but complex data. To circumvent the challenge, a holistic approach using *in vivo* biomarkers from multiple modalities is gaining a lot of support. As evident in cancer or genetic

research integrating vast arrays of data as multi-omics, several multi-center studies curating multimodal data banks from different parts of the world have enabled the integration of multiple biomarkers from different modalities such as the ADNI, Dominantly Inherited Alzheimer Network (DIAN), Australian Imaging, Biomarkers and Lifestyle (AIBL), and Swedish Biomarkers for Identifying Neurodegenerative Disorders Early and Reliably (BIOFINDER) studies. Multimodal biomarkers are ideal to provide rich information regarding the various molecular targets, the topography of distribution, and the quantification of interests. Furthermore, more holistic methodologies such as multivariate analysis could bring unique insights and provide a more complete interpretation of data. In Study 2, multivariate analyses revealed activated microglia in the medial inferior temporal cortex and global A $\beta$  predicted tau propagation throughout Braak stages 1-4, leading to cognitive decline in the AD continuum group. In contrast, activated microglia showed relatively balanced and neuroprotective effects on tau and cognition, respectively, in individuals without clear A $\beta$  pathological evidence. By utilizing a multivariate statistical approach based on neuroimaging data, this study highlights the multidimensional roles of activated microglia that are modulated by A $\beta$ , leading to tau propagation and cognitive decline.

### **13.3 *in vivo* biomarker-based evaluation of therapeutic target engagement, efficacy, and safety**

In June 2021, Aducanumab has been conditionally approved under the accelerated approval pathway by the FDA [3]. Since its first promising clinical trial phase 1b report in 2016, Aducanumab has galvanized AD drug discovery [155]. As it is the first clinical trial to utilize AD biomarkers to enrich the clinical trial population, it is the first drug to target underlying AD

pathophysiology, particularly one of the hallmarks of AD pathologic protein, A $\beta$  [154]. However, the praise also has come with heavy criticisms and controversies [153, 154]; most importantly, Aducanumab has yet to show a clear clinical benefit accompanied by the clearance of A $\beta$  in a prodromal and early-stage AD study sample. This has sparked the field to critically think: is A $\beta$  still a good therapeutic target? Is there enough anti-amyloid immunotherapy crossing the BBB into the brain? Is the current framework, in which the preclinical AD drug discovery pipeline to answer the primary endpoint in a human clinical trial, optimized? To address these questions, the third study, “*Preclinical in vivo longitudinal assessment of KG207-M as a disease-modifying Alzheimer’s disease therapeutic*”, aimed to evaluate the ability to cross the BBB, target engagement, therapeutic efficacy, and safety of a novel anti-amyloid therapeutic.

The novel anti-amyloid treatment, KG207-M, is uniquely designed and may potentially have a greater application than immunotherapy. The KG207-M is a bifunctional fusion protein consisting of the BBB-crossing camelid single-domain antibody FC5 fused to the N-terminus of Fc fragment of mouse IgG2a, and ABP fused to the C-terminus of Fc [276]. Previous *in vitro* and *ex vivo* studies have shown that ABP selectively binds to A $\beta$ <sub>42</sub> oligomers and A $\beta$  deposits in the brains of AD transgenic mice and post-mortem human brains from AD patients, respectively [277, 278]. Study 3 showed successful brain penetrance and significant A $\beta$  target engagement indicated by A $\beta$  PET and CSF biomarkers. This was the first *in vivo* experiment demonstrating the bifunctionality of KG207-M. Such fusion engineering is a great strategy to improve drug delivery for therapeutic molecules that have poor brain penetrance.

The main objective of Study 3 was to show the A $\beta$  target engagement, therapeutic efficacy, and safety profile of the KG207-M treatment. Following the KG207-M treatment, a significant reduction of A $\beta$  PET and an increase in the CSF A $\beta$ <sub>42/40</sub> suggested substantial

removal of A $\beta$  from the brain. This was confirmed by the histopathological Campbell-Switzer silver staining. In addition, the KG207-M treatment rectified the CSF NFL concentrations, resting-state functional connectivity, and hippocampal atrophy measured using MRI. Finally, the KG207-M treatment did not induce any evidence of ARIA-H. Using the same *in vivo* biomarker metrics used in human clinical trials in an AD-like A $\beta$  pathology transgenic rat model, the KG207-M demonstrated a successful target engagement, therapeutic efficacy, and safety profile. This is an unprecedented effort to investigate a novel therapeutic based on *in vivo* biomarkers from the preclinical stage of AD drug discovery and development. Effectively, Study 3 provides direct evidence of the pre-treatment and post-treatment conditions and related effect sizes in removing A $\beta$  and recovery of neurodegenerative biomarkers.

Together, Study 3 demonstrates the translational values of *in vivo* biomarker-based evaluation of preclinical drug discovery and development. The assessment of novel therapies based on the clinical biomarkers can provide tangible metrics for designing early-stage clinical trials. Furthermore, the rectification of CSF NFL and hippocampal volume by removing A $\beta$  is a great proof of concept that the KG207-M is a candidate for a disease-modifying therapeutic for AD.

### **13.4 Limitations**

It is imperative to recognize some limitations. Each biomarker has methodological limits on its sensitivity and specificity, therefore, it is crucial to be aware of the limitations. For example, both A $\beta$  PET and CSF A $\beta$  are biomarkers of A $\beta$ . However, A $\beta$  PET detects the amount of fibrillar form of A $\beta$  as the A $\beta$  tracers interact with the  $\beta$ -sheet structure [294]. In contrast, CSF

A $\beta$  detects A $\beta$  species that are specific to the antibody used in the assay. Therefore, A $\beta$  PET is thought to represent the cumulative A $\beta$  pathology over time while CSF A $\beta$  is considered to represent pathologic state that is associated with A $\beta$  plaque formation [67]. This was an important limitation for evaluating the effect of KG207-M in removing A $\beta$  oligomers as there is no established method to accurately quantify the changes in A $\beta$  oligomers levels directly *in vivo*. Still, using different methods of A $\beta$  quantifications as a surrogate for A $\beta$  oligomers clearance, the decline in A $\beta$  PET and rectification of CSF A $\beta_{42/40}$  ratio in the post-treatment measurement constitute a remarkable proof of concept of the KG207-M intervention. The reduced brain A $\beta$  loads likely reflect A $\beta$  oligomer clearance, under the assumption of dynamic equilibrium among A $\beta$  species in these animals. Similarly, [ $^{11}\text{C}$ ]PBR28 is not specific to activated microglia alone as it targets the TSPO expression [179]. The consensus from TSPO literature supports the binding of [ $^{11}\text{C}$ ]PBR28 to be related to glial activation representing neuroinflammation, while some off-target binding sites are also recognized [179]. However, the degree of TSPO expression from various sources may depend on the disease itself and disease stage. Some autopsy studies, though not all, suggest the TSPO expression is predominantly attributed to microglia in AD [295-297]. In addition, the binding of [ $^{11}\text{C}$ ]PBR28 PET tracer was associated with a common variant influencing the morphology of activated microglia in AD [134]. Though other sources of TSPO expression from astrocytes or vessels contribute to [ $^{11}\text{C}$ ]PBR28 signals, the interpretation of [ $^{11}\text{C}$ ]PBR28 PET tracer as activated microglia in AD could be explored cautiously.

## 14 A final conclusion and summary

In this Ph.D. thesis, the three integral aspects of AD biomarker-based research have been discussed: 1) a process of discovery and validation of a new *in vivo* biomarker, 2) *in vivo* biomarker-based evidence supporting a disease mechanism, and 3) evaluating therapeutic target engagement, efficacy, and safety. These aspects are empirical and depend on one another. To achieve preventative or disease-modifying therapeutics for AD, one must identify a potential therapeutic target that is a biologic and pathologic entity. This target must be accurately measurable as a biomarker. Furthermore, this target must be an early pathogenetic event upstream of complex AD pathophysiology and crucial in the disease progression. Such mechanisms must be demonstrated based on *in vivo* biomarkers, which then can be used to evaluate therapeutic target engagement, efficacy, and safety. While this Ph.D. thesis contributed original research findings in each aspect, it is important to emphasize that this Ph.D. thesis alone cannot *validate* a new biomarker, *prove* a disease mechanism, or *discover* a new therapeutic for AD. Rather, the three studies contributed to the greater body of the AD research field in working together towards the replication and validation process across a multitude of AD research disciplines. Therefore, the *in vivo* biomarker-based research framework was only possible with global efforts across multiple disciplines in AD research. It took more than 100 years of discovery and characterization in AD genetic, pathological proteins, and complex molecular and cellular networks that are interconnected through time and space to form AD pathophysiology.

With the foundation of AD neuropathological studies and development in technology, *in vivo* biomarkers have been validated to track and visualize A $\beta$ , NFTs, and neurodegeneration as the basis of the A/T/(N) classification system. Continuous development in biomarkers has

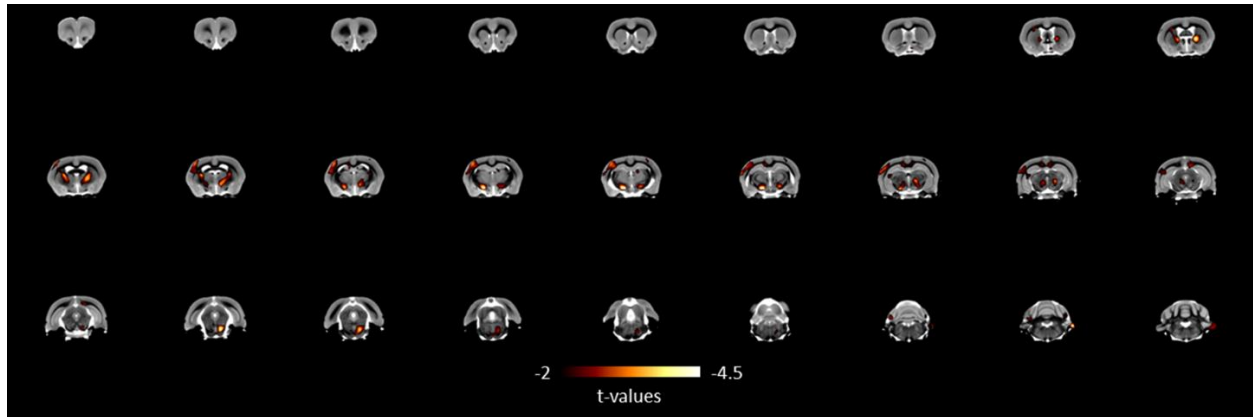
always paralleled with a deeper understanding of the disease mechanisms and the discovery of new therapeutic candidates and strategies.

Integrating multimodal biomarkers has encouraged a more open science community to not only share a large data bank but also inspire innovations and create interdisciplinary synergy across the different research fields such as genomics, proteomics, connectomics, and computer science. Consequently, this is leading to the emergence of more intelligent tools such as various machine learning algorithms to integrate multidimensional data to predict future cognitive or pathologic changes. Soon, a new era of personalized or precision medicine will enable true appreciation of the organ, body, and organism as a whole in near future.

This Ph.D. thesis highlights three important aspects of *in vivo* biomarker-based investigations to advance the knowledge and utility of the biomarkers in AD research: 1) discovery and validation of a novel *in vivo* biomarker, 2) *in vivo* biomarker-based evidence supporting disease mechanisms, and 3) *in vivo* biomarker-based evaluation of a novel therapeutic target engagement, efficacy, and safety. These findings constitute important contributions to a growing body of biomarkers, a greater understanding of disease mechanisms, and a proof of concept in disease-modifying therapeutic and drug discovery.

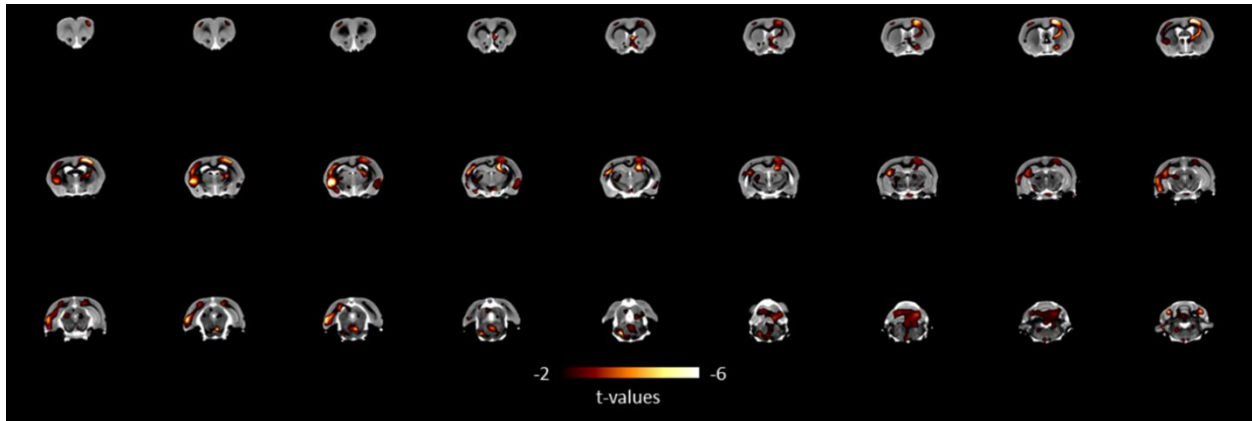
## 15 Supplementary Materials

### 15.1 Supplementary Figures



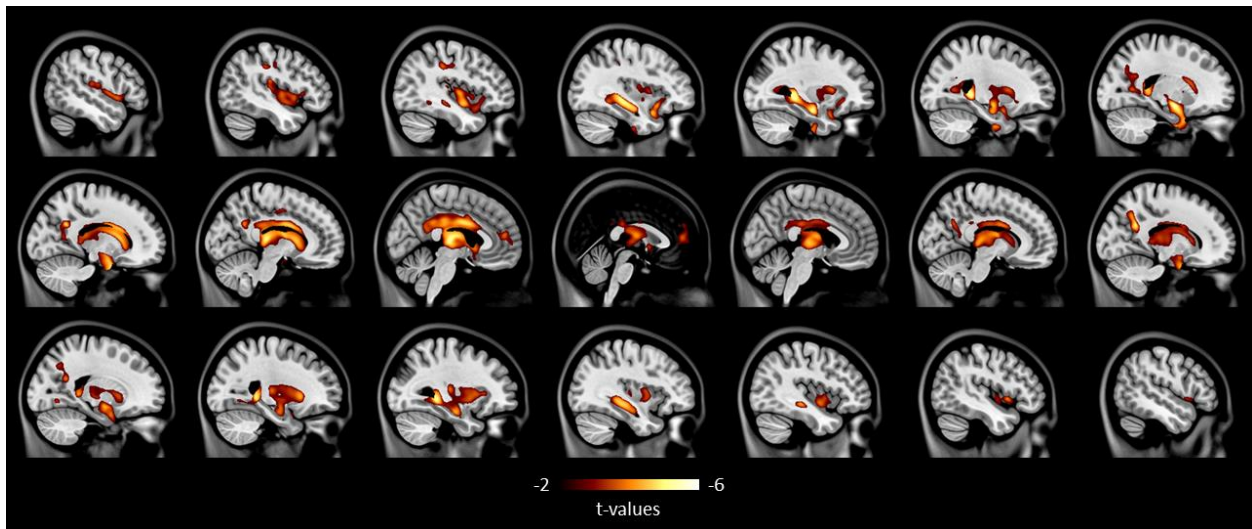
*Supplementary Figure 1. DBM comparison between WT and the McGill-R-Thy1-APP Tg rat model.*

A voxel-based group contrast between WT vs Tg at 15 months with RFT correction. The standardized stereotaxic coordinates of each peak voxel ( $> 3$  t-value) with a minimum 2 mm distance apart are reported in Supplementary Table 1.



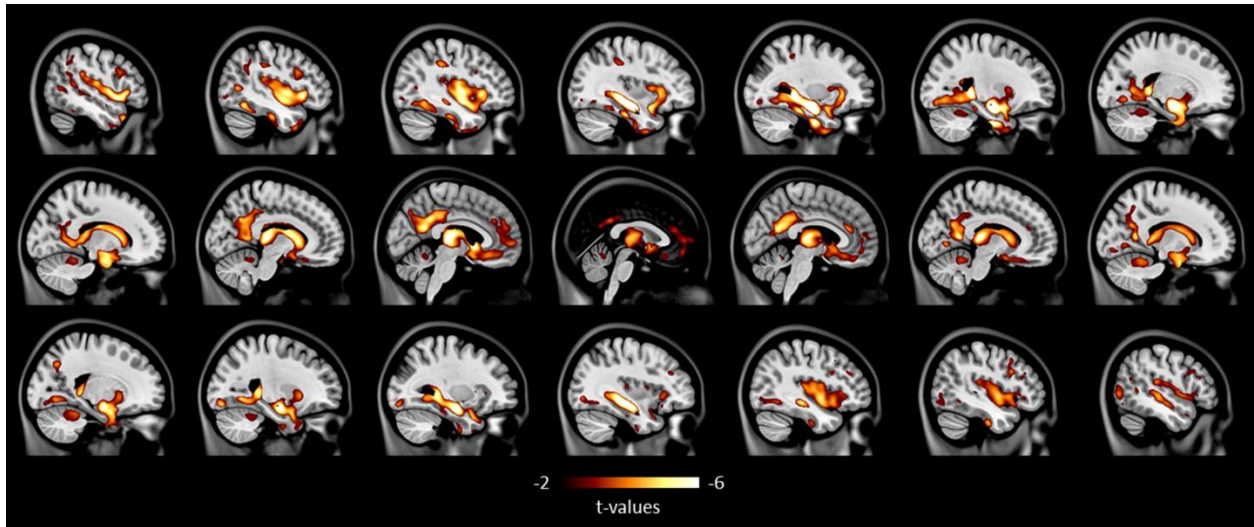
*Supplementary Figure 2. Associations between CSF NFL and DBM in the McGill-R-Thy1-APP rat model.*

A voxel-based association between CSF NFL concentrations and DBM in Tg at 15 months with RFT correction. The standardized stereotaxic coordinates of each peak voxel ( $> 3$  t-value) with a minimum 2 mm distance apart are reported in Supplementary Table 2.



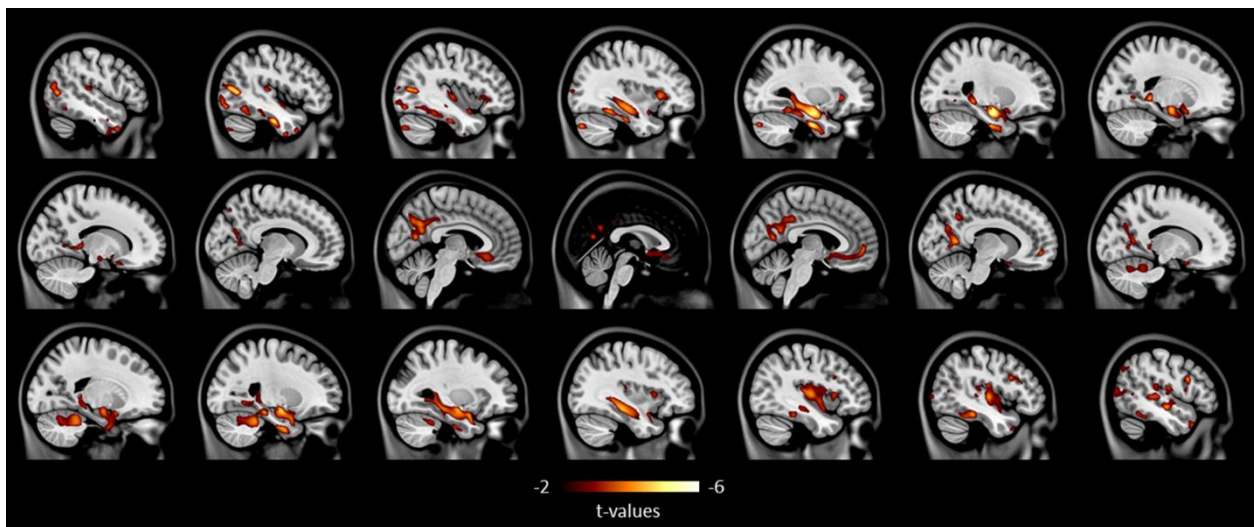
*Supplementary Figure 3. VBM comparison between CN and MCI.*

A voxel-based group contrast between CN and MCI with RFT correction. The standardized stereotaxic coordinates of each peak voxel ( $> 3.5$  t-value) with a minimum 8 mm distance apart are reported in Supplementary Table 3.



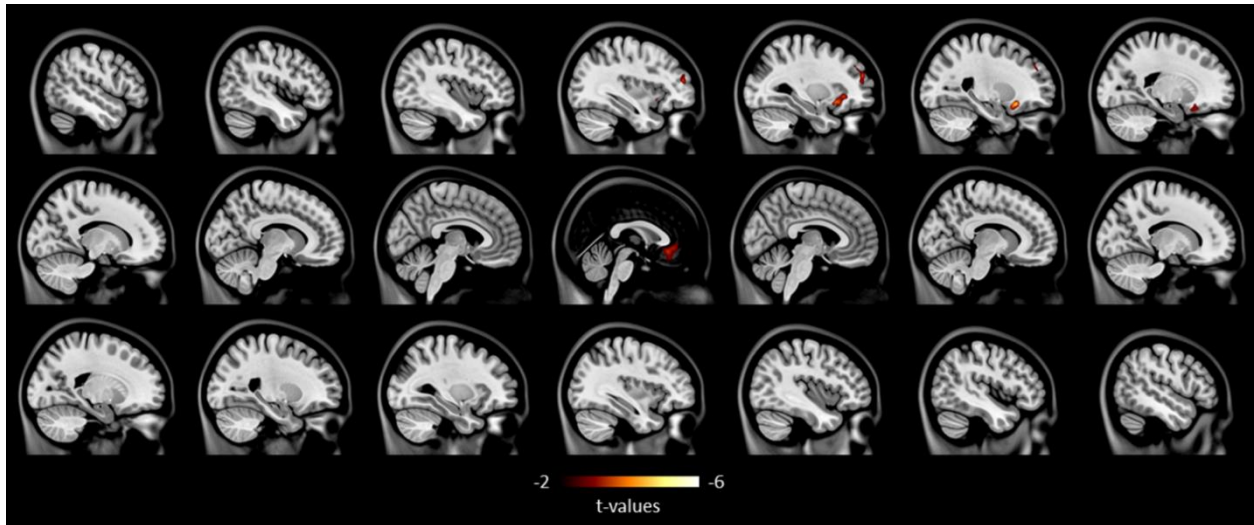
*Supplementary Figure 4. VBM comparison between CN and AD.*

A voxel-based group contrast between CN and AD with RFT correction. The standardized stereotaxic coordinates of each peak voxel ( $> 3.5$  t-value) with a minimum 8 mm distance apart are reported in Supplementary Table 4.



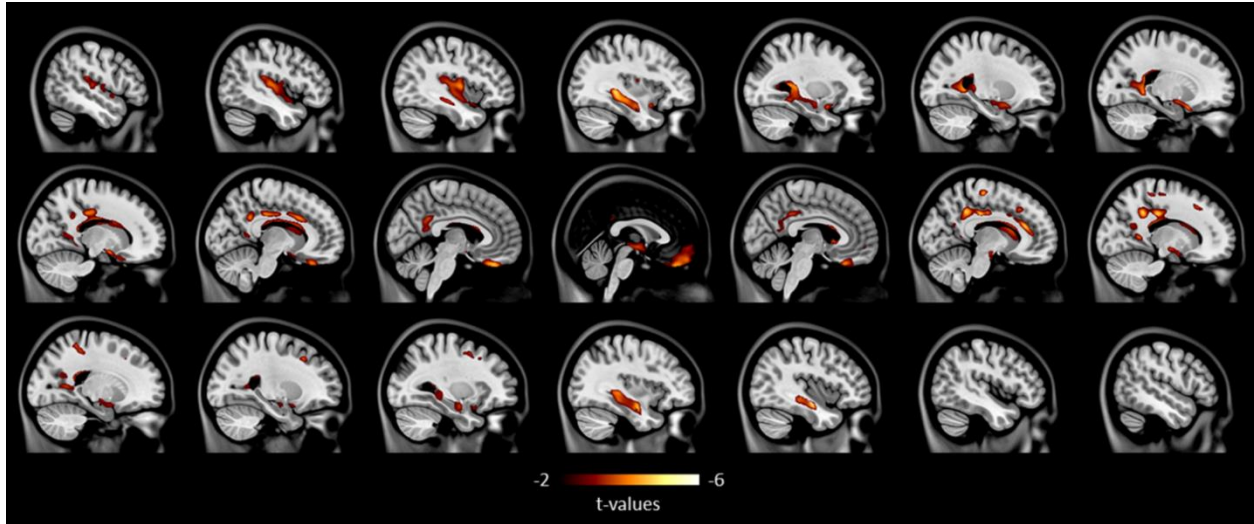
*Supplementary Figure 5. VBM comparison between MCI and AD.*

A voxel-based group contrast between MCI and AD with RFT correction. The standardized stereotaxic coordinates of each peak voxel ( $> 3.5$  t-value) with a minimum 8 mm distance apart are reported in Supplementary Table 5.



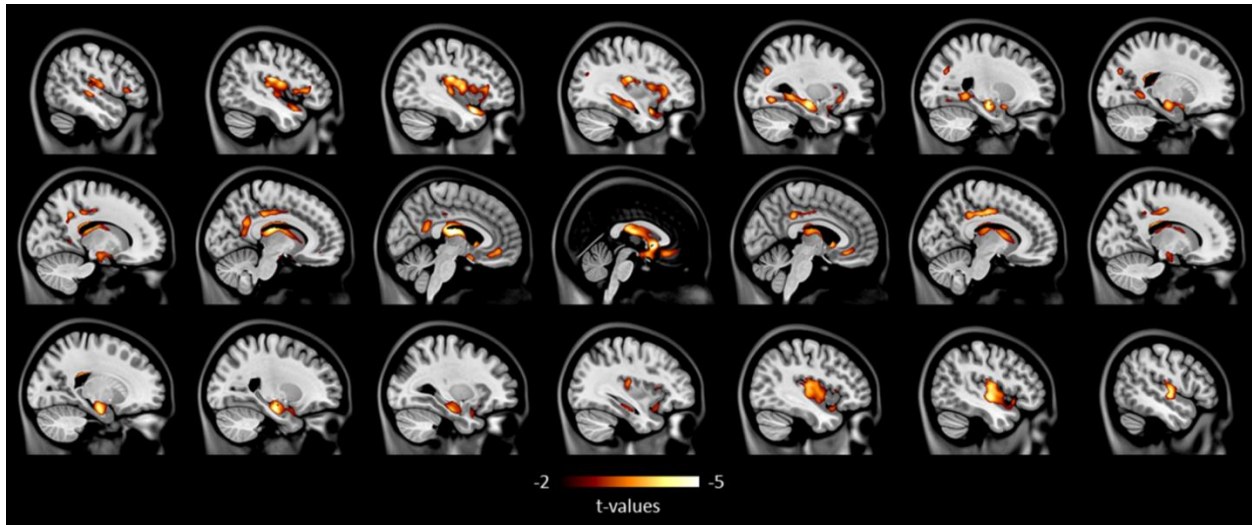
*Supplementary Figure 6. VBM comparison between CN A $\beta$ - and A $\beta$ +*.

A voxel-based group contrast between CN A $\beta$ - and A $\beta$ + with RFT correction. The standardized stereotaxic coordinates of each peak voxel ( $> 3.5$  t-value) with a minimum 8 mm distance apart are reported in Supplementary Table 6.



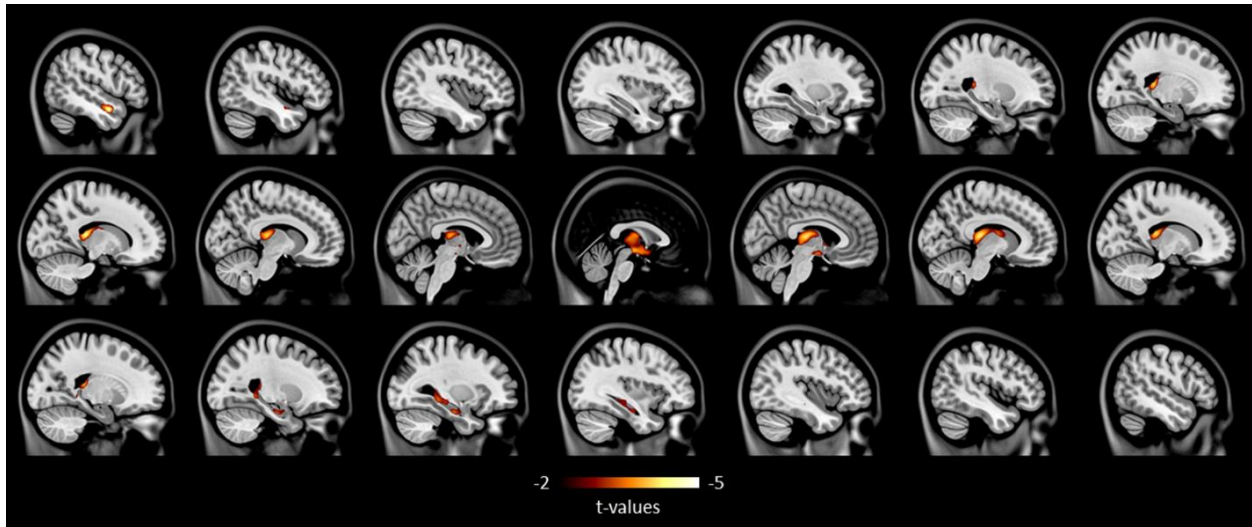
*Supplementary Figure 7. VBM comparison between MCI  $A\beta^-$  and  $A\beta^+$ .*

A voxel-based group contrast between MCI  $A\beta^-$  and  $A\beta^+$  with RFT correction. The standardized stereotaxic coordinates of each peak voxel ( $> 3.5$  t-value) with a minimum 8 mm distance apart are reported in Supplementary Table 7.



**Supplementary Figure 8.** *The association between CSF NFL and VBM in MCI A $\beta$ <sup>+</sup>.*

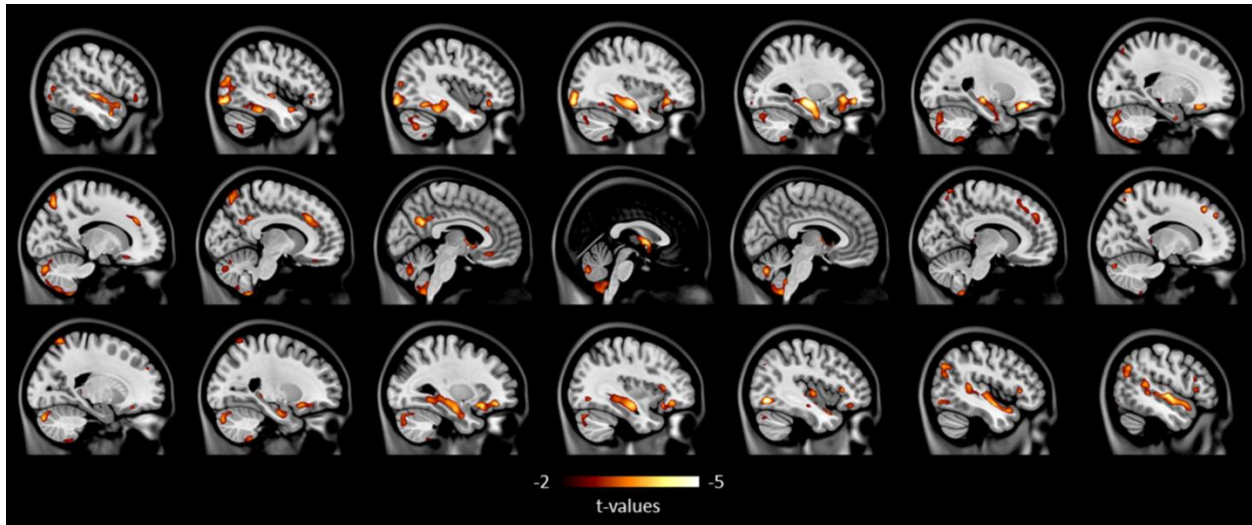
A voxel-based association between CSF NFL concentrations and VBM in MCI A $\beta$ <sup>+</sup> with RFT correction. The standardized stereotaxic coordinates of each peak voxel (> 3.5 t-value) with a minimum 8 mm distance apart are reported in Supplementary Table 8.



*Supplementary Figure 9. The association between plasma NFL and VBM in MCI A $\beta$ +*

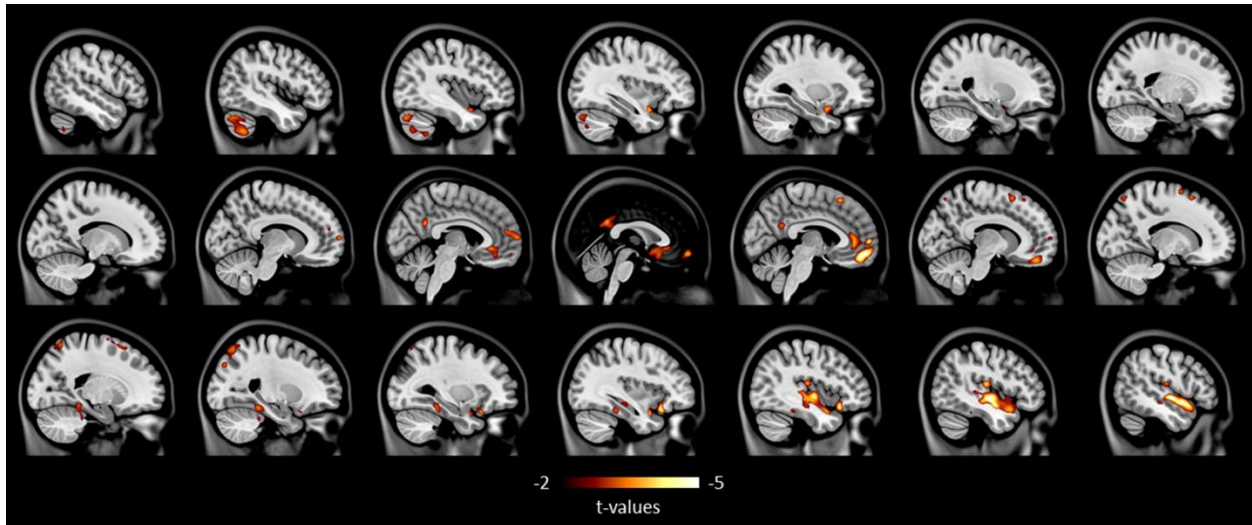
A voxel-based association between plasma NFL concentrations and VBM in MCI A $\beta$ +

 with RFT correction. The standardized stereotaxic coordinates of each peak voxel ( $> 3.5$  t-value) with a minimum 8 mm distance apart are reported in Supplementary Table 9.



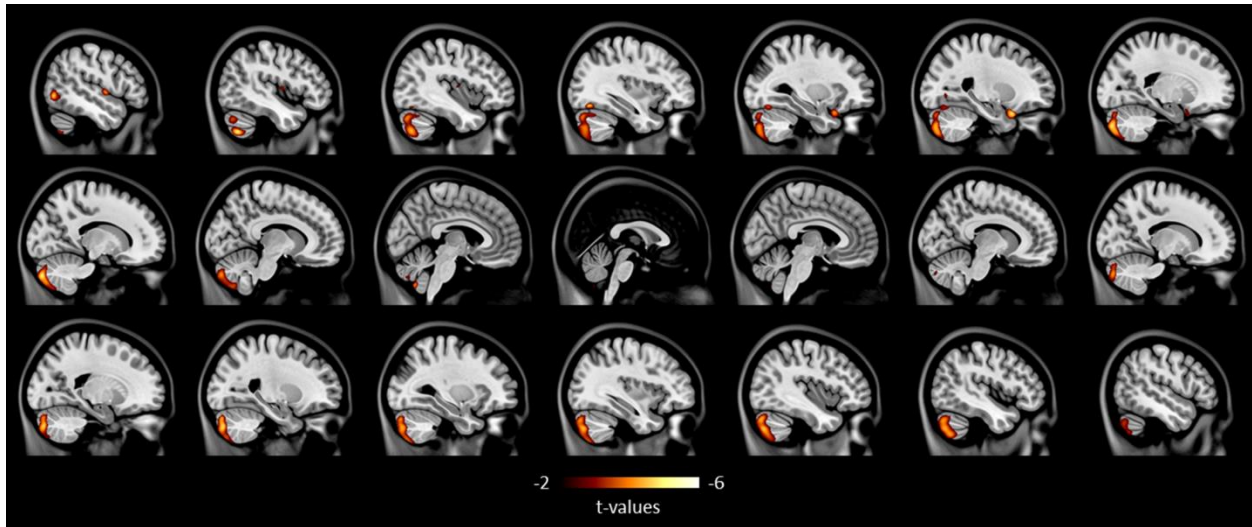
**Supplementary Figure 10.** *The association between CSF NFL and VBM in AD A $\beta$ <sup>+</sup>.*

A voxel-based association between CSF NFL concentrations and VBM in AD A $\beta$ <sup>+</sup> with RFT correction. The standardized stereotaxic coordinates of each peak voxel (> 3.5 t-value) with a minimum 8 mm distance apart are reported in Supplementary Table 10.



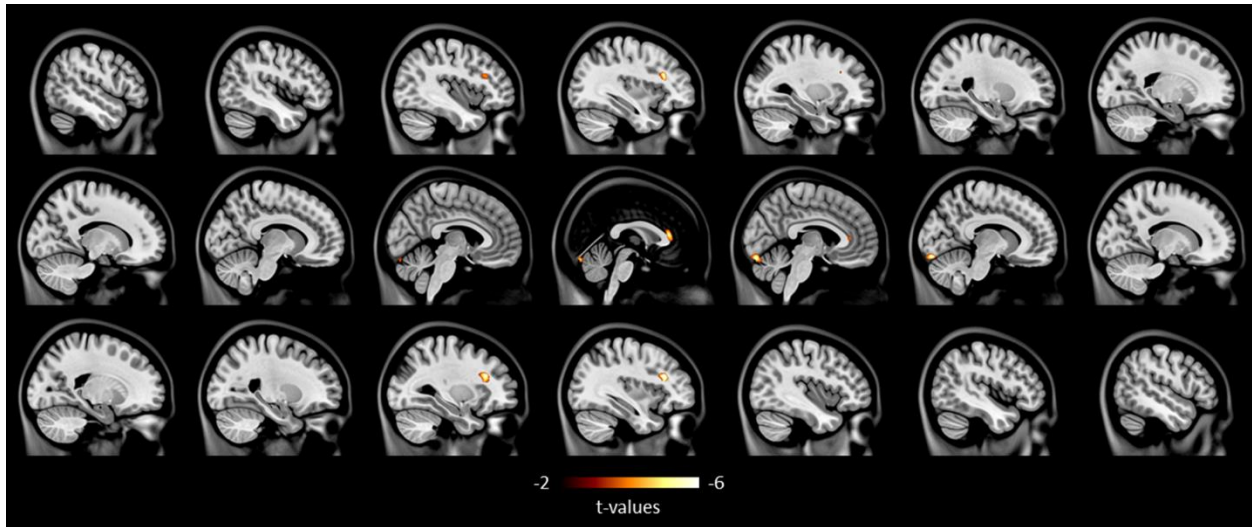
**Supplementary Figure 11.** *The association between plasma NFL and VBM in AD A $\beta$ <sup>+</sup>.*

A voxel-based association between plasma NFL concentrations and VBM in AD A $\beta$ <sup>+</sup> with RFT correction. The standardized stereotaxic coordinates of each peak voxel (> 3.5 t-value) with a minimum 8 mm distance apart are reported in Supplementary Table 11.



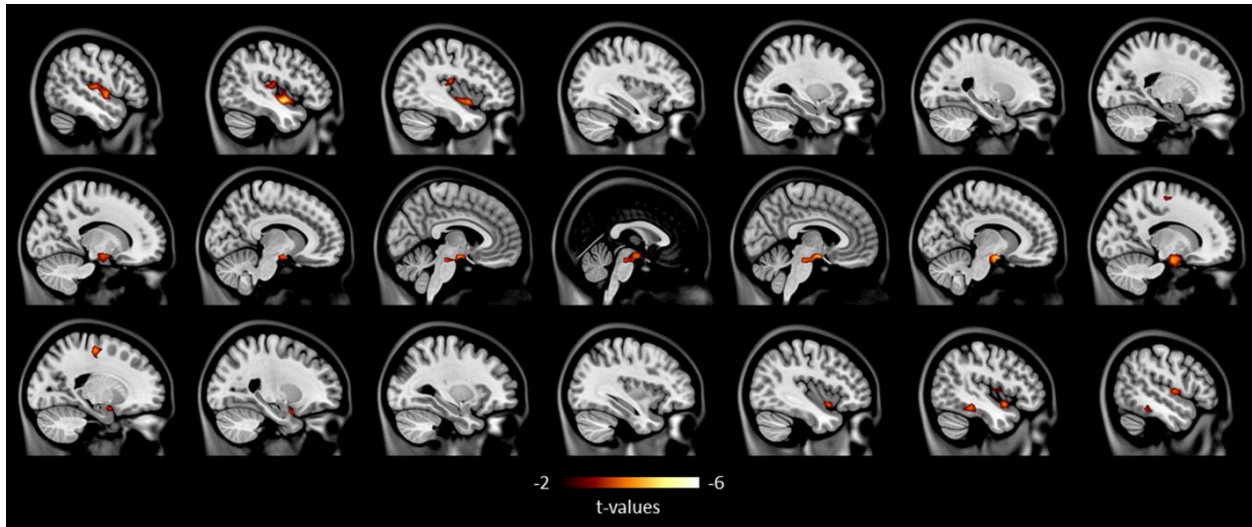
**Supplementary Figure 12.** *The association between CSF NFL and VBM in CN A $\beta$ -.*

A voxel-based association between CSF NFL concentrations and VBM in CN A $\beta$ - with RFT correction. The standardized stereotaxic coordinates of each peak voxel (> 3.5 t-value) with a minimum 8mm distance apart are reported in Supplementary Table 12.



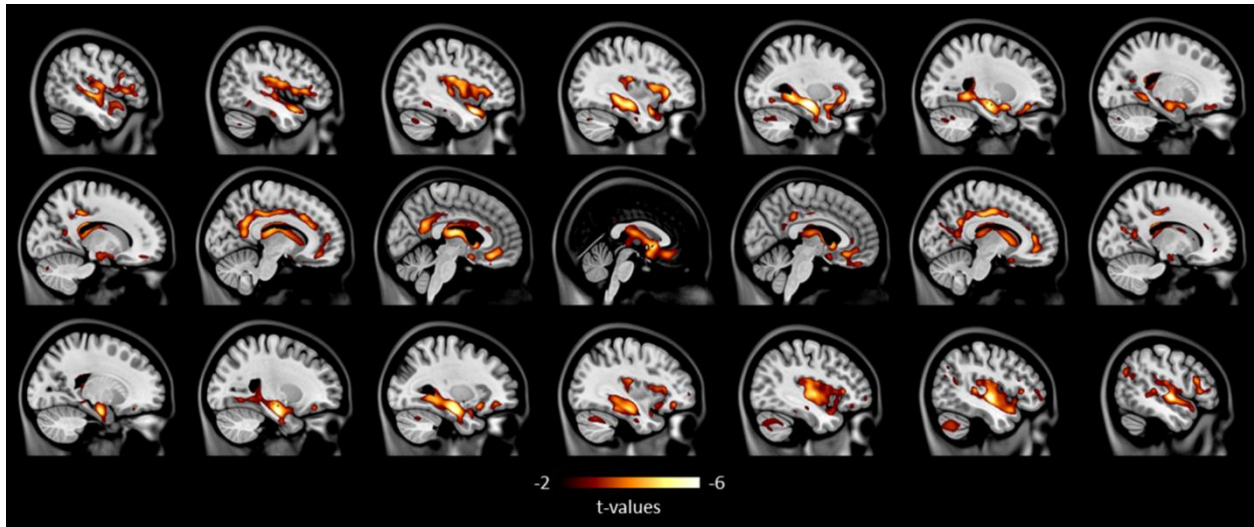
*Supplementary Figure 13. The association between CSF NFL and VBM in CN A $\beta$ +*.

A voxel-based association between CSF NFL concentrations and VBM in CN A $\beta$ + with RFT correction. The standardized stereotaxic coordinates of each peak voxel (> 3.5 t-value) with a minimum 8 mm distance apart are reported in Supplementary Table 13.



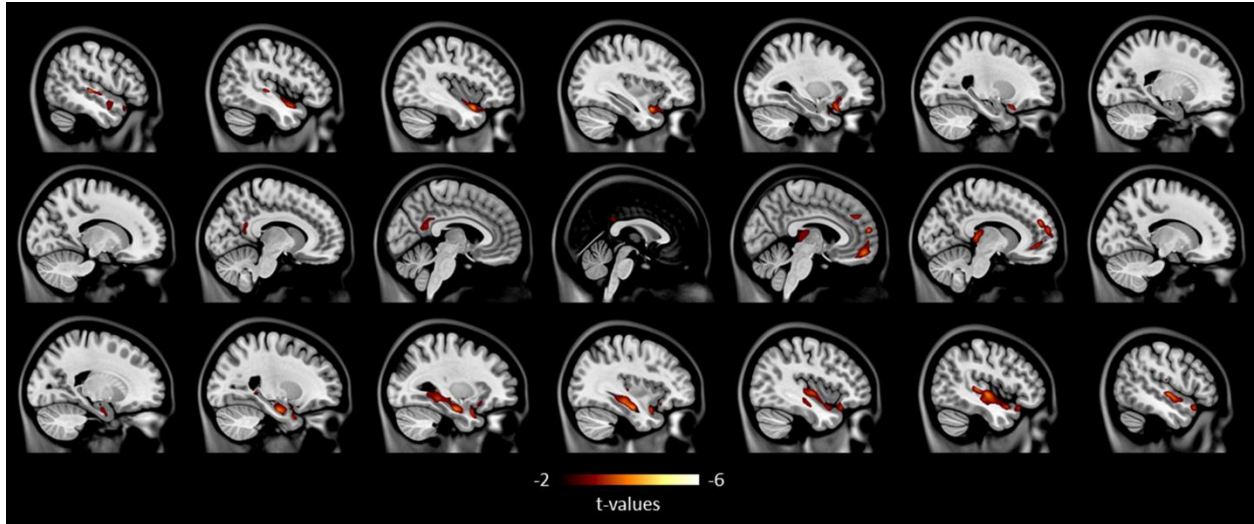
**Supplementary Figure 14.** *The association between plasma NFL and VBM in MCI A $\beta$ -.*

A voxel-based association between plasma NFL concentrations and VBM in MCI A $\beta$ - with RFT correction. The standardized stereotaxic coordinates of each peak voxel (> 3.5 t-value) with a minimum 8 mm distance apart are reported in Supplementary Table 14.



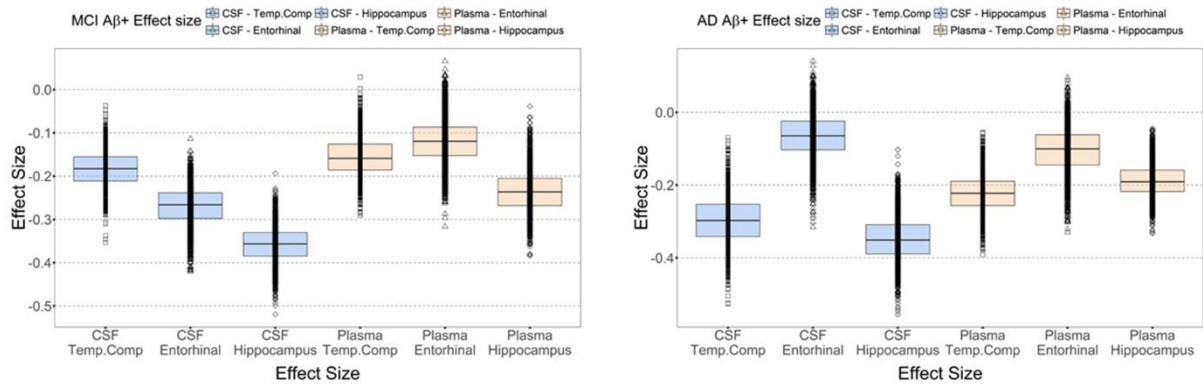
*Supplementary Figure 15. The association between CSF NFL and VBM in  $A\beta+$  groups combined.*

A voxel-based association between CSF NFL concentrations and VBM in all  $A\beta+$  combined with RFT correction. The standardized stereotaxic coordinates of each peak voxel ( $> 3.5$  t-value) with a minimum 8 mm distance apart are reported in Supplementary Table 15.



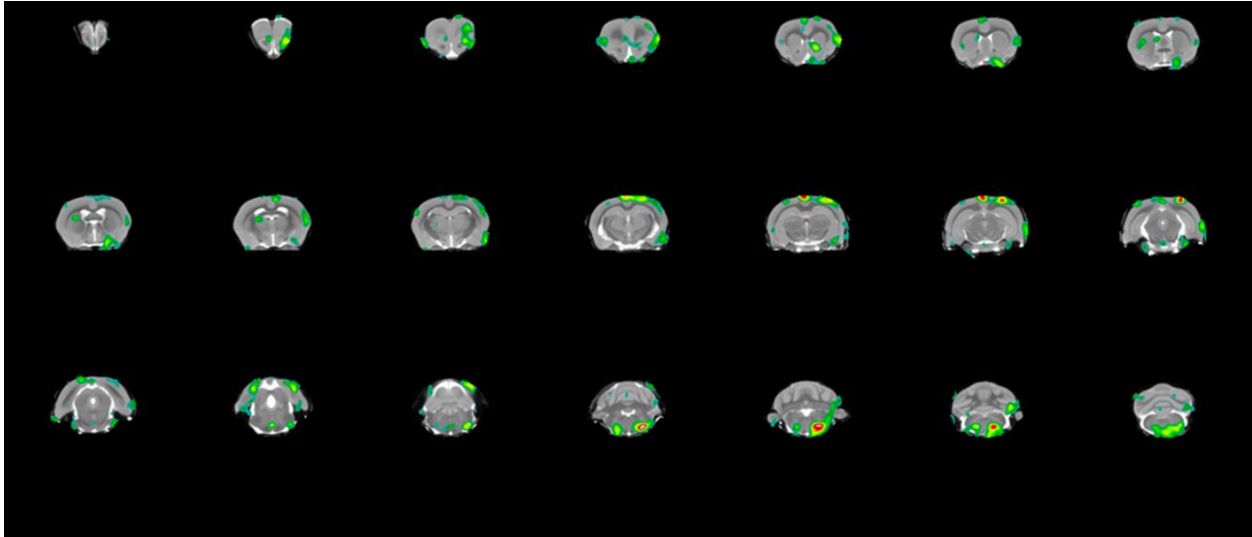
*Supplementary Figure 16. The association between plasma NFL and VBM in  $A\beta+$  groups combined.*

A voxel-based association between CSF NFL concentrations and VBM in all  $A\beta+$  combined with RFT correction. The standardized stereotaxic coordinates of each peak voxel ( $> 3.5$  t-value) with a minimum 8 mm distance apart are reported in Supplementary Table 16.



**Supplementary Figure 17.** Various effect sizes in the associations between NFL and VBM in different regions.

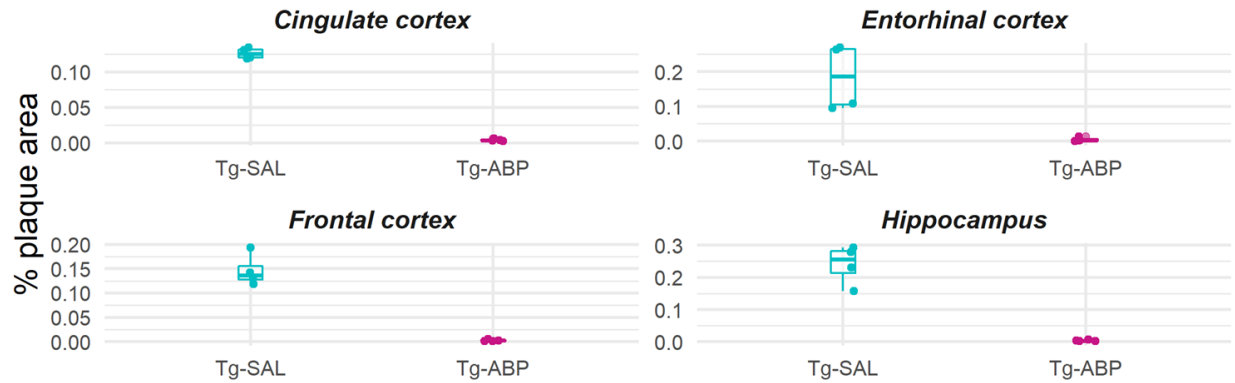
2000 bootstrapped standardized effect sizes comparison in MCI Aβ+ or AD Aβ+. Following Bonferroni multiple comparison correction, all the contrasts were significantly different ( $p < 0.0001$ ) from each other in MCI Aβ+ or AD Aβ+.



**Supplementary Figure 18.** *KG207-M reduces  $A\beta$  load in the brain.*

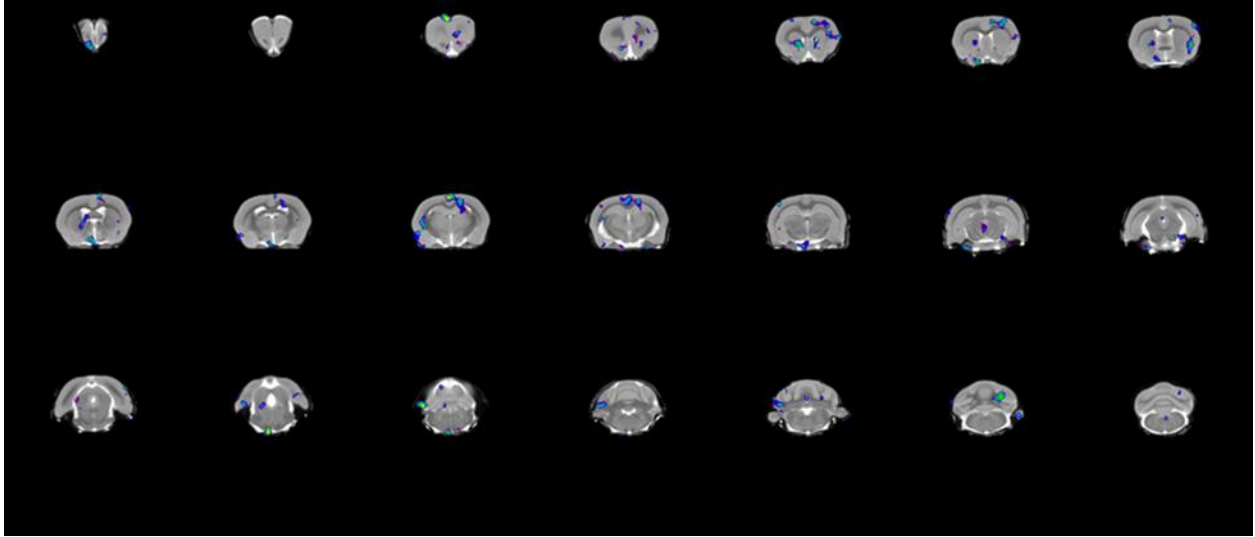
The voxel-wise linear mixed-effect model analysis showed a significant [ $^{18}\text{F}$ ]AZD4694 BP<sub>ND</sub> clearance in the prefrontal cortex, cingulate cortex, entorhinal cortex, hippocampus, and basal forebrain in Tg-ABP compared to Tg-SAL (n = 19, adjusted for sex, weight, and cohort variability). The interaction term was corrected for multiple comparisons based on RFT at  $p < 0.05$ .

## The Campbell-Switzer silver staining analysis



**Supplementary Figure 19.** *KG207-M reduces the Campbell-Switzer silver staining.*

We measured the amount of Campbell-Switzer silver staining as a percentage of the area in the frontal, cingulate, entorhinal cortices, and hippocampus regions across the subjects in each group per tissue slide. There was a significant difference in the percentage of the Campbell-Switzer silver staining in frontal, cingulate, entorhinal cortices, and hippocampus such that there was essentially minimal staining in the Tg-ABP group compared to Tg-SAL ( $p < 0.001$ ).



**Supplementary Figure 20.** *KG207-M rescues resting-state cingulate connectivity.*

The figure represents a significant contrast in the resting-state BOLD signal from cingulate to the brain in Tg-ABP ( $n = 9$ ) following KG207-M treatment compared to baseline at 21 months of age. The voxel-wise linear mixed-effect analysis showed a significant increase in resting-state cingulate connectivity in the basal forebrain, parietal associative cortex, and hippocampus when the network is compared before and after KG207-M treatment. The result images were adjusted for multiple comparisons based on RFT at  $p < 0.05$ .

## 15.2 Supplementary Tables

*Supplementary Table 1.*

x	y	z	t-values	Regions	L/R
1.904124	1.187106	5.585437	8.18	Frontal cortex	right
1.165348	-3.43619	-7.02465	4.479	Pons	right
-3.44943	1.553856	-1.62733	3.671	Striatum	left
1.919853	-0.88328	-5.0571	3.449	Thalamus	right
-4.93576	4.522994	-3.58051	3.423	Parietotemporal cortex	left
-7.33832	2.010593	-4.58955	3.095	Parietotemporal cortex	left

The standardized stereotaxic coordinates of each peak voxel ( $> 3$  t-value) with a minimum 2 mm distance apart are displayed with the corresponding t-value and region name from Supplementary Figure 1. All coordinates are in Anterior Commissure origin stereotaxic space.

*Supplementary Table 2.*

x	y	z	t-values	Regions	L/R
2.288319	5.160035	-0.84611	13.08	Parietotemporal cortex	right
2.205505	3.090039	-3.4493	7.904	Hippocampus	right
-7.20392	-0.13745	-7.78222	6.439	Entorhinal cortex	left
3.159625	1.505142	-0.24537	6.041	Striatum	right
0.69624	1.671377	-15.0027	5.881	Cerebellum	right
-2.66543	-4.06561	-8.66698	5.746	Pons	left
2.147044	1.805813	5.929955	5.553	Frontal cortex	right
4.50739	0.44114	-11.7616	5.529	Cerebellum	right
4.464944	4.274171	-1.70373	5.516	Parietotemporal cortex	right
-5.72325	2.351092	-3.7788	5.428	Parietotemporal cortex	left
0.600743	-2.98772	-7.08551	5.148	Pons	right

-4.09508	1.41938	-11.6825	4.726	Cerebellum	left
1.159431	2.989946	-13.5184	4.588	Cerebellum	right
3.452243	4.574751	4.471624	4.523	Frontal cortex	right
-6.8468	-2.20965	-5.95076	4.363	Entorhinal cortex	left
7.305979	-0.48841	-2.34516	4.228	Parietotemporal cortex	right
-4.57095	-2.48829	-2.64647	3.991	Entorhinal cortex	left
2.241364	-1.7763	0.471666	3.817	Frontal cortex	right
-5.06695	1.837376	-6.32246	3.811	Hippocampus	left
-5.65103	-2.46668	-11.5227	3.674	Cerebellum	left
0.032244	-1.03192	-14.3387	3.604	Cerebellum	right
2.606088	0.162798	-10.1736	3.542	Cerebellum	right
-4.04702	5.102023	1.006788	3.49	Frontal cortex	left
2.208129	5.010554	-4.45162	3.473	Parietotemporal cortex	right
4.073254	-1.42051	-12.5859	3.305	Cerebellum	right
-1.93241	1.372266	-10.2145	3.227	Cerebellum	left
0.016682	-1.85438	-10.4343	3.06	Cerebellum	right

The standardized stereotaxic coordinates of each peak voxel (> 3 t-value) with a minimum 2 mm distance apart are displayed with the corresponding t-value and region name from Supplementary Figure 2. All coordinates are in Anterior Commissure origin stereotaxic space.

**Supplementary Table 3.**

<b>x</b>	<b>y</b>	<b>z</b>	<b>t-values</b>	<b>Regions</b>	<b>L/R</b>
-20	-6	-13	5.542	uncus	left
-27	-39	1	5.424	hippocampal formation	left
28	-39	-3	5.348	hippocampal formation	right
-6	-21	8	5.328	thalamus	left
-34	-28	-7	5.148	hippocampal formation	left

---

-30	-12	-20	5.119	hippocampal formation	left
-6	-3	30	4.975	cingulate region	left
36	-27	-10	4.688	hippocampal formation	right
-9	-3	12	4.669	thalamus	left
-12	11	9	4.65	caudate nucleus	left
-40	-3	-10	4.553	insula	left
-18	10	19	4.532	caudate nucleus	left
5	-17	4	4.515	thalamus	right
7	-6	13	4.39	thalamus	right
20	-5	-14	4.363	uncus	right
26	17	1	4.347	putamen	right
-5	-27	29	4.293	cingulate region	left
-40	-8	3	4.278	insula	left
10	-27	6	4.271	thalamus	right
31	-13	-19	4.269	hippocampal formation	right
-3	50	12	4.166	cingulate region	left
-36	16	-14	4.114	insula	left
-4	-42	30	4.046	cingulate region	left
46	9	-3	4.012	inferior frontal gyrus	right
-32	-12	-43	3.96	inferior temporal gyrus	left
-6	3	3	3.956	thalamus	left
-4	10	-4	3.901	caudate nucleus	left
41	-2	-9	3.899	insula	right
-48	2	1	3.851	precentral gyrus	left
-46	-22	18	3.818	postcentral gyrus	left
32	5	-2	3.814	putamen	right
4	-27	28	3.66	cingulate region	right
-21	-60	7	3.623	parahippocampal gyrus	left

---

36	2	6	3.568	insula	right
-53	-14	13	3.514	postcentral gyrus	left
22	-65	-6	3.513	medial occipitotemporal gyrus	right

The standardized stereotaxic coordinates of each peak voxel (> 3.5 t-value) with a minimum 8 mm distance apart are displayed with the corresponding t-value and region name from Supplementary Figure 3. All coordinates are in MNI template space.

**Supplementary Table 4.**

<b>x</b>	<b>y</b>	<b>z</b>	<b>t-values</b>	<b>Regions</b>	<b>L/R</b>
-29	-11	-18	8.831	hippocampal formation	left
-7	-23	8	7.271	thalamus	left
-28	-9	-38	6.863	inferior temporal gyrus	left
-35	-27	-9	6.836	hippocampal formation	left
29	-10	-17	6.589	hippocampal formation	right
9	-25	8	6.425	thalamus	right
36	-28	-11	6.388	hippocampal formation	right
-41	-6	2	6.023	insula	left
-41	-5	-10	5.953	insula	left
12	-54	9	5.859	parahippocampal gyrus	right
-4	11	-5	5.76	caudate nucleus	left
-32	-28	-24	5.719	lateral occipitotemporal gyrus	left
-10	11	7	5.537	caudate nucleus	left
-5	-54	20	5.446	precuneus	left
-10	2	13	5.413	caudate nucleus	left
5	-56	20	5.399	precuneus	right
-8	-59	31	5.386	precuneus	left
-62	-22	-6	5.28	superior temporal gyrus	left

42	-2	-3	5.262	insula	right
-5	-46	32	5.246	cingulate region	left
-44	-55	-16	5.242	lateral occipitotemporal gyrus	left
-56	-45	11	5.181	superior temporal gyrus	left
57	3	4	5.139	precentral gyrus	right
19	1	-23	5.098	uncus	right
-31	25	-2	4.957	insula	left
-27	-50	-7	4.881	medial occipitotemporal gyrus	left
4	-44	30	4.842	cingulate region	right
26	-56.5	-6	4.823	medial occipitotemporal gyrus	right
12	13	8	4.81	caudate nucleus	right
-4	-34	36	4.804	cingulate region	left
-14	-12	22	4.794	caudate nucleus	left
27	7	-27	4.773	uncus	right
11	-61	24	4.754	precuneus	right
-57	-3	-15	4.754	superior temporal gyrus	left
68	-23	-5	4.709	middle temporal gyrus	right
-9	-51	8	4.709	medial occipitotemporal gyrus	left
-50	-16	13	4.678	postcentral gyrus	left
-57	-11	-32	4.667	inferior temporal gyrus	left
-53	-35	25	4.603	supramarginal gyrus	left
-43	-20	-30	4.603	lateral occipitotemporal gyrus	left
14	2	17	4.517	caudate nucleus	right
4	16	-8	4.516	cingulate region	right
61	-30	19	4.494	supramarginal gyrus	right
56	6	-22	4.486	superior temporal gyrus	right
-62	-35	17	4.427	supramarginal gyrus	left
44	-15	-37	4.42	middle temporal gyrus	right

-44	-64	6	4.397	middle temporal gyrus	left
-63	-23	-19	4.381	middle temporal gyrus	left
-5	8	-14	4.371	lateral front-orbital gyrus	left
-19	-59	4	4.369	parahippocampal gyrus	left
-25	-72.5	-9	4.362	medial occipitotemporal gyrus	left
50	-26	-3	4.356	superior temporal gyrus	right
60	-25	-22	4.355	inferior temporal gyrus	right
-15	-48	0	4.348	parahippocampal gyrus	left
41	14	-10	4.291	insula	right
-34	11	6	4.23	insula	left
-40	-32	38	4.204	postcentral gyrus	left
60	-16	-30	4.192	middle temporal gyrus	right
-61	-22	11	4.185	superior temporal gyrus	left
-26	-82	-12	4.169	lingual gyrus	left
44	11	-3	4.167	insula	right
20	-68	-7	4.149	medial occipitotemporal gyrus	right
5	33	20	4.128	cingulate region	right
39	-21	8	4.121	superior temporal gyrus	right
23	15	-2	4.096	putamen	right
-28	-61	-11	4.081	medial occipitotemporal gyrus	left
-31	3	-49	4.072	middle temporal gyrus	left
-4	28	-14	4.06	medial front-orbital gyrus	left
-57	-27	19	4.054	supramarginal gyrus	left
39	-2	11	4.033	insula	right
-49	-28	19	4.018	supramarginal gyrus	left
64	-42	3	3.985	middle temporal gyrus	right
44	14	29	3.954	middle frontal gyrus	right
-47	13	27	3.951	middle frontal gyrus	left

50	-28	17	3.903	supramarginal gyrus	right
50	-77	1	3.898	inferior occipital gyrus	right
15	-49	-22	3.892	cerebellum	right
50	-16	-12	3.871	superior temporal gyrus	right
-54	-37	0	3.858	middle temporal gyrus	left
-45	10	-44	3.847	middle temporal gyrus	left
33	25	0	3.805	insula	right
-5	58	0	3.795	medial frontal gyrus	left
-60	-40	-18	3.771	middle temporal gyrus	left
-55	-54	0	3.746	middle temporal gyrus	left
-38	-65	-12	3.708	lateral occipitotemporal gyrus	left
-6	39	-14	3.707	medial front-orbital gyrus	left
-38	-11	-42	3.699	inferior temporal gyrus	left
5	29	-16	3.665	medial front-orbital gyrus	right
-6	36	29	3.663	cingulate region	left
58	-62	11	3.635	middle temporal gyrus	right
-65	-9	-21	3.633	middle temporal gyrus	left
60	-60	-3	3.577	middle temporal gyrus	right
40	-58	-10	3.546	lateral occipitotemporal gyrus	right
-3	46	6	3.524	cingulate region	left
-2	41	17	3.522	cingulate region	left
41	24	2	3.508	inferior frontal gyrus	right

The standardized stereotaxic coordinates of each peak voxel ( $> 3.5$  t-value) with a minimum 8 mm distance apart are displayed with the corresponding t-value and region name from Supplementary Figure 4. All coordinates are in MNI template space.

*Supplementary Table 5.*

<b>x</b>	<b>y</b>	<b>z</b>	<b>t-values</b>	<b>Regions</b>	<b>L/R</b>
-26	-10	-19	5.399	hippocampal formation	left
-29	-13	-35	5.381	lateral occipitotemporal gyrus	left
-46	-66	7	4.886	middle temporal gyrus	left
-45	-18	-30	4.869	inferior temporal gyrus	left
25	-8	-16	4.765	uncus	right
35	-28	-13	4.541	hippocampal formation	right
-58	-11	-30	4.534	inferior temporal gyrus	left
-61	-19	-21	4.408	middle temporal gyrus	left
43	-37	-20	4.34	lateral occipitotemporal gyrus	right
61	-28	19	4.34	supramarginal gyrus	right
11	-58	9	4.251	parahippocampal gyrus	right
-61	-31	-3	4.231	superior temporal gyrus	left
25	-4	-40	4.227	inferior temporal gyrus	right
7	52	-4	4.221	cingulate region	right
52	-16	-12	4.221	middle temporal gyrus	right
-20	-37	-1	4.21	hippocampal formation	left
-34	-45	-18	4.204	lateral occipitotemporal gyrus	left
42	-15	4	4.19	superior temporal gyrus	right
-30	-29	-12	4.179	hippocampal formation	left
58	4	-22	4.176	superior temporal gyrus	right
-33	22	2	4.142	insula	left
23	-42	-29	4.101	cerebellum	right
30	5	-23	4.092	uncus	right
-33	-81	-36	4.04	cerebellum	left
-6	-59	32	4.024	precuneus	left
49	12	25	4.014	inferior frontal gyrus	right

---

-59	-58	18	4.009	middle temporal gyrus	left
54	-39	2	3.986	superior temporal gyrus	right
27	-12	-37	3.982	parahippocampal gyrus	right
-62	-6	-11	3.977	superior temporal gyrus	left
54	9	9	3.929	precentral gyrus	right
-4	-56	23	3.915	precuneus	left
60	-38	-20	3.893	inferior temporal gyrus	right
-34	-24	-28	3.892	lateral occipitotemporal gyrus	left
-4	-65	14	3.892	precuneus	left
67	-31	34	3.88	supramarginal gyrus	right
-44	-79	-12	3.8	lateral occipitotemporal gyrus	left
-47	-56	-15	3.784	lateral occipitotemporal gyrus	left
65	-50	15	3.738	middle temporal gyrus	right
4	-55	24	3.729	precuneus	right
57	-65	14	3.72	middle temporal gyrus	right
68	-25	27	3.714	supramarginal gyrus	right
-48	11	-41	3.699	middle temporal gyrus	left
-62	-14	-10	3.691	superior temporal gyrus	left
-5	-67	34	3.689	precuneus	left
46	-45	-23	3.687	lateral occipitotemporal gyrus	right
4	-64	14	3.649	cuneus	right
56	-63	35	3.624	angular gyrus	right
-3	18	-8	3.618	cingulate region	left
41	-3	-3	3.599	insula	right
62	-21	-10	3.591	middle temporal gyrus	right
20	9	-19	3.588	lateral front-orbital gyrus	right
46	-16	17	3.584	supramarginal gyrus	right
-38	5	-19	3.579	superior temporal gyrus	left

---

-22	9	-18	3.546	lateral front-orbital gyrus	left
-46	-2	-47	3.527	inferior temporal gyrus	left
52	-12	13	3.517	postcentral gyrus	right
39	15	5	3.509	inferior frontal gyrus	right
-59	-5	6	3.509	superior temporal gyrus	left
-40	-17	0	3.506	insula	left

The standardized stereotaxic coordinates of each peak voxel (> 3.5 t-value) with a minimum 8 mm distance apart are displayed with the corresponding t-value and region name from Supplementary Figure 5. All coordinates are in MNI template space.

**Supplementary Table 6.**

<b>x</b>	<b>y</b>	<b>z</b>	<b>t-values</b>	<b>Regions</b>	<b>L/R</b>
-27	19	-13	4.644	lateral front-orbital gyrus	left
-31	52	22	3.694	middle frontal gyrus	left
-2	31	-10	3.54	cingulate region	left

The standardized stereotaxic coordinates of each peak voxel (> 3.5 t-value) with a minimum 8mm distance apart are displayed with the corresponding t-value and region name from Supplementary Figure 6. All coordinates are in MNI template space.

**Supplementary Table 7.**

<b>x</b>	<b>y</b>	<b>z</b>	<b>t-values</b>	<b>Regions</b>	<b>L/R</b>
14	-46	37	4.807	superior parietal lobule	right
-6	34	-29	4.605	lateral front-orbital gyrus	left
-25	-47	3	4.224	parahippocampal gyrus	left
-39	-7	7	4.118	insula	left
-20	11	-21	4.054	lateral front-orbital gyrus	left

5	29	-28	4.002	lateral front-orbital gyrus	right
-43	-19	8	3.97	superior temporal gyrus	left
38	-32	-11	3.965	hippocampal formation	right
-10	-48	31	3.916	cingulate region	left
-37	-12	-19	3.902	hippocampal formation	left
15	-51	5	3.766	parahippocampal gyrus	right
27	20	43	3.68	middle frontal gyrus	right
5	15	1	3.54	caudate nucleus	right

The standardized stereotaxic coordinates of each peak voxel (> 3.5 t-value) with a minimum 8 mm distance apart are displayed with the corresponding t-value and region name from Supplementary Figure 7. All coordinates are in MNI template space.

**Supplementary Table 8.**

<b>x</b>	<b>y</b>	<b>z</b>	<b>t-values</b>	<b>Regions</b>	<b>L/R</b>
-40	10	-23	5.58	superior temporal gyrus	left
-4	-16	15	5.452	thalamus	left
48	-13	-2	5.186	superior temporal gyrus	right
-42	-20	19	4.856	postcentral gyrus	left
23	-14	-21	4.811	hippocampal formation	right
-28	-16	-13	4.61	hippocampal formation	left
7	-38	35	4.372	cingulate region	right
13	-17	43	4.338	precentral gyrus	right
-44	-8	14	4.295	precentral gyrus	left
-40	-4	8	4.223	insula	left
-29	-66	-9	4.201	medial occipitotemporal gyrus	left
-31	-40	-5	4.015	parahippocampal gyrus	left
40	-17	11	4.01	insula	right

9	-25	38	3.997	cingulate region	right
42	-6	3	3.973	insula	right
4	29	-12	3.951	cingulate region	right
-10	-30	38	3.911	cingulate region	left
61	-11	7	3.9	superior temporal gyrus	right
-39	-20	3	3.846	superior temporal gyrus	left
8	3	9	3.803	thalamus	right
-44	24	4	3.771	inferior frontal gyrus	left
-36	26	7	3.747	inferior frontal gyrus	left
-63	-18	-5	3.746	superior temporal gyrus	left
-51	-24	-1	3.729	superior temporal gyrus	left
-5	42	-11	3.719	cingulate region	left
-32	26	-1	3.698	insula	left
-46	-25	10	3.676	superior temporal gyrus	left
-15	-50	37	3.667	superior parietal lobule	left
-6	-49	24	3.658	cingulate region	left
-6	10	1	3.641	caudate nucleus	left
60	-23	11	3.628	superior temporal gyrus	right
-32	-71	29	3.6	angular gyrus	left
-12	-18	41	3.567	medial frontal gyrus	left
-35	9	8	3.517	insula	left

The standardized stereotaxic coordinates of each peak voxel ( $> 3.5$  t-value) with a minimum 8 mm distance apart are displayed with the corresponding t-value and region name from Supplementary Figure 8. All coordinates are in MNI template space.

**Supplementary Table 9.**

<b>x</b>	<b>y</b>	<b>z</b>	<b>t-values</b>	<b>Regions</b>	<b>L/R</b>
-50	0	-21	4.551	superior temporal gyrus	left
-14	-29	12	4.331	thalamus	left
11	-27	11	4.218	thalamus	right
4	-20	9	4.118	thalamus	right

The standardized stereotaxic coordinates of each peak voxel (> 3.5 t-value) with a minimum 8 mm distance apart are displayed with the corresponding t-value and region name from Supplementary Figure 9. All coordinates are in MNI template space.

**Supplementary Table 10.**

<b>x</b>	<b>y</b>	<b>z</b>	<b>t-values</b>	<b>Regions</b>	<b>L/R</b>
28	17	-15	4.925	lateral front-orbital gyrus	right
-28	-23	-11	4.923	hippocampal formation	left
59	-39	31	4.824	angular gyrus	right
-37	-91	-11	4.808	inferior occipital gyrus	left
-23	25	-18	4.794	lateral front-orbital gyrus	left
62	-30	35	4.57	supramarginal gyrus	right
-6	-57	28	4.498	precuneus	left
-45	-79	-9	4.493	lateral occipitotemporal gyrus	left
-29	41	-11	4.416	lateral front-orbital gyrus	left
60	-18	-2	4.392	superior temporal gyrus	right
1	2	2	4.355	fornix	left
31	39	-13	4.26	lateral front-orbital gyrus	right
-43	-36	-22	4.225	lateral occipitotemporal gyrus	left
-30	27	-8	4.207	insula	left
34	-16	-16	4.099	hippocampal formation	right

-16	-71	51	4.096	superior parietal lobule	left
-11	26	33	4.05	medial frontal gyrus	left
20	-84	-31	4.005	cerebellum	right
5	-72	-35	3.989	cerebellum	right
-38	-28	-12	3.977	hippocampal formation	left
-30	-9	-26	3.974	hippocampal formation	left
-43	-82	12	3.868	inferior occipital gyrus	left
-17	-82	-34	3.833	cerebellum	left
-49	2	-27	3.822	middle temporal gyrus	left
38	26	6	3.806	inferior frontal gyrus	right
-48	-45	-22	3.794	lateral occipitotemporal gyrus	left
61	-32	18	3.787	supramarginal gyrus	right
-45	-76	19	3.787	inferior occipital gyrus	left
48	-42	11	3.783	middle temporal gyrus	right
50	-64	33	3.781	angular gyrus	right
46	-73	34	3.688	middle occipital gyrus	right
15	-65	69	3.658	superior parietal lobule	right
46	11	-21	3.635	superior temporal gyrus	right
-52	11	-14	3.631	superior temporal gyrus	left
40	-11	0	3.615	insula	right
43	1	-20	3.581	superior temporal gyrus	right
-42	-63	-43	3.576	cerebellum	left
47	-70	24	3.538	middle occipital gyrus	right
-48	-71	5	3.515	inferior occipital gyrus	left

The standardized stereotaxic coordinates of each peak voxel (> 3.5 t-value) with a minimum 8 mm distance apart are displayed with the corresponding t-value and region name from Supplementary Figure 10. All coordinates are in MNI template space.

**Supplementary Table 11.**

<b>x</b>	<b>y</b>	<b>z</b>	<b>t-values</b>	<b>Regions</b>	<b>L/R</b>
58	0	-6	5.435	superior temporal gyrus	right
49	-10	-4	5.323	superior temporal gyrus	right
4	54	-14	5.288	medial front-orbital gyrus	right
44	-8	-14	4.957	superior temporal gyrus	right
37	22	-17	4.791	insula	right
41	-10	-2	4.445	insula	right
6	60	3	4.413	medial frontal gyrus	right
44	-18	14	4.085	supramarginal gyrus	right
-8	54	17	3.93	medial frontal gyrus	left
12	15	59	3.925	superior frontal gyrus	right
37	7	-23	3.908	superior temporal gyrus	right
-34	6	-21	3.869	superior temporal gyrus	left
-3	-50	27	3.801	cingulate region	left
5	23	56	3.758	medial frontal gyrus	right
-7	39	-12	3.749	cingulate region	left
5	42	1	3.72	cingulate region	right
3	15	-9	3.698	cingulate region	right
60	-27	12	3.638	superior temporal gyrus	right
-46	-57	-48	3.595	cerebellum	left
3	-55	23	3.58	precuneus	right
-4	31	-6	3.526	cingulate region	left
-42	-75	-31	3.514	cerebellum	left

The standardized stereotaxic coordinates of each peak voxel (> 3.5 t-value) with a minimum 8 mm distance apart are displayed with the corresponding t-value and region name from Supplementary Figure 11. All coordinates are in MNI template space.

**Supplementary Table 12.**

<b>x</b>	<b>y</b>	<b>z</b>	<b>t-values</b>	<b>Regions</b>	<b>L/R</b>
-17	-86	-41	5.023	cerebellum	left
-45	-64	-49	5.001	cerebellum	left
-26	15	-26	4.919	lateral front-orbital gyrus	left
24	-83	-41	4.765	cerebellum	right
-34	-70	-16	4.682	lateral occipitotemporal gyrus	left
-50	-71	-3	4.606	inferior occipital gyrus	left
38	-76	-44	4.605	cerebellum	right
39	-79	-32	4.374	cerebellum	right
26	-84	-31	4.32	cerebellum	right
44	-66	-51	4.219	cerebellum	right
-60	-57	-4	4.093	middle temporal gyrus	left
-38	-77	-31	4.057	cerebellum	left
-50	-5	2	3.971	superior temporal gyrus	left
-23	-83	-27	3.676	cerebellum	left

The standardized stereotaxic coordinates of each peak voxel (> 3.5 t-value) with a minimum 8 mm distance apart are displayed with the corresponding t-value and region name from Supplementary Figure 12. All coordinates are in MNI template space.

**Supplementary Table 13.**

<b>x</b>	<b>y</b>	<b>z</b>	<b>t-values</b>	<b>Regions</b>	<b>L/R</b>
2	32	10	7.357	cingulate region	right
9	-87	-16	6.862	lingual gyrus	right

The standardized stereotaxic coordinates of each peak voxel (> 3.5 t-value) with a minimum 8 mm distance apart are displayed with the corresponding t-value and region name from Supplementary Figure 13. All coordinates are in MNI template space.

**Supplementary Table 14.**

<b>x</b>	<b>y</b>	<b>z</b>	<b>t-values</b>	<b>Regions</b>	<b>L/R</b>
47	-42	-18	4.077	inferior temporal gyrus	right
-50	-4	-1	3.965	superior temporal gyrus	left
50	-5	4	3.756	precentral gyrus	right
-51	-19	9	3.749	postcentral gyrus	left
-41	-19	16	3.656	postcentral gyrus	left
-15	-7	-16	3.619	uncus	left
47	-33	-21	3.531	lateral occipitotemporal gyrus	right

The standardized stereotaxic coordinates of each peak voxel (> 3.5 t-value) with a minimum 8 mm distance apart are displayed with the corresponding t-value and region name from Supplementary Figure 14. All coordinates are in MNI template space.

**Supplementary Table 15.**

<b>x</b>	<b>y</b>	<b>z</b>	<b>t-values</b>	<b>Regions</b>	<b>L/R</b>
48	-13	-3	6.768	superior temporal gyrus	right
-29	-19	-16	6.473	hippocampal formation	left
-41	10	-23	6.349	superior temporal gyrus	left
25	-13	-23	6.26	hippocampal formation	right
-4	-15	14	5.481	thalamus	left
-2	11	-3	5.4	cingulate region	left
-33	-37	-7	5.307	parahippocampal gyrus	left
-40	-19	20	5.262	postcentral gyrus	left
-34	29	2	5.049	inferior frontal gyrus	left
41	-12	1	5.045	insula	right
-7	-54	27	4.874	precuneus	left
-25	6	-17	4.854	lateral front-orbital gyrus	left

-5	33	-15	4.831	medial front-orbital gyrus	left
10	-23	38	4.797	cingulate region	right
-43	-8	14	4.792	precentral gyrus	left
9	-11	41	4.705	medial frontal gyrus	right
-33	15	8	4.704	insula	left
6	10	0	4.695	caudate nucleus	right
-11	21	34	4.618	cingulate region	left
-13	-36	40	4.608	cingulate region	left
-23	34	-18	4.581	lateral front-orbital gyrus	left
31	-39	-8	4.575	parahippocampal gyrus	right
-30	24	-7	4.563	insula	left
-43	22	4	4.534	inferior frontal gyrus	left
52	21	17	4.522	inferior frontal gyrus	right
-8	-56	14	4.521	precuneus	left
41	-17	9	4.503	insula	right
-40	-4	6	4.484	insula	left
10	42	8	4.414	cingulate region	right
-45.5	9.5	4	4.41	inferior frontal gyrus	left
-7	7	2	4.389	caudate nucleus	left
3	2	4	4.376	thalamus	right
4	29	-13	4.362	medial front-orbital gyrus	right
59	-47	23	4.352	angular gyrus	right
45	11	-20	4.299	superior temporal gyrus	right
62	-12	7	4.289	superior temporal gyrus	right
30	17	-15	4.282	insula	right
10	-53	28	4.241	precuneus	right
-9	29	24	4.222	cingulate region	left
9	43	-8	4.205	medial front-orbital gyrus	right

62	-32	34	4.205	angular gyrus	right
-39	-21	3	4.193	superior temporal gyrus	left
-51	-11	10	4.192	postcentral gyrus	left
-64	-18	-5	4.103	superior temporal gyrus	left
35	-35	-18	4.025	lateral occipitotemporal gyrus	right
4	-14	14	4.004	thalamus	right
50	26	4	4.001	inferior frontal gyrus	right
40	26	4	3.999	inferior frontal gyrus	right
6	-38	36	3.998	cingulate region	right
35	38	-13	3.981	lateral front-orbital gyrus	right
61	-17	-2	3.968	superior temporal gyrus	right
-53	14	-15	3.956	superior temporal gyrus	left
-52	-38	8	3.942	superior temporal gyrus	left
13	-57	12	3.924	parahippocampal gyrus	right
-9	-11	41	3.909	medial frontal gyrus	left
49	-17	16	3.907	supramarginal gyrus	right
42	-8	14	3.797	precentral gyrus	right
-62	-48	-20	3.792	inferior temporal gyrus	left
-42	-31	20	3.766	supramarginal gyrus	left
68	-40	18	3.757	superior temporal gyrus	right
-33	-26	15	3.75	insula	left
33	20	8	3.73	insula	right
24	33	-17	3.719	lateral front-orbital gyrus	right
28	4	-21	3.679	uncus	right
13	34	22	3.678	cingulate region	right
37	6	10	3.666	precentral gyrus	right
57	-29	22	3.653	supramarginal gyrus	right
13	27	30	3.633	medial frontal gyrus	right

-18	-5	-12	3.625	uncus	left
27	-59	-5	3.579	medial occipitotemporal gyrus	right
49	-70	29	3.579	middle occipital gyrus	right
-47	-24	10	3.572	superior temporal gyrus	left
6	45	-26	3.566	lateral front-orbital gyrus	right
24	-8	-35	3.542	parahippocampal gyrus	right
46	-63	-41	3.531	cerebellum	right
45	-28	15	3.51	superior temporal gyrus	right
55	13	9	3.505	inferior frontal gyrus	right

The standardized stereotaxic coordinates of each peak voxel ( $> 3.5$  t-value) with a minimum 8 mm distance apart are displayed with the corresponding t-value and region name from Supplementary Figure 15. All coordinates are in MNI template space.

**Supplementary Table 16.**

<b>x</b>	<b>y</b>	<b>z</b>	<b>t-values</b>	<b>Regions</b>	<b>L/R</b>
7	60	15	4.481	medial frontal gyrus	right
7	44	31	4.201	medial frontal gyrus	right
64	-11	15	4.199	postcentral gyrus	right
-38	10	-22	4.166	superior temporal gyrus	left
47	-15	-3	4.123	superior temporal gyrus	right
35	-15	-20	4.022	hippocampal formation	right
9	52	23	3.993	medial frontal gyrus	right
-28	16	-20	3.959	lateral front-orbital gyrus	left
54	-5	-7	3.955	superior temporal gyrus	right
24	-10	-24	3.912	hippocampal formation	right
5	54	-14	3.816	medial front-orbital gyrus	right
34	-25	-13	3.758	hippocampal formation	right

33	9	-25	3.634	uncus	right
39	-14	-1	3.566	insula	right
32	-33	-10	3.537	hippocampal formation	right
-55	16	-16	3.53	superior temporal gyrus	left
10	-31	5	3.507	thalamus	right

The standardized stereotaxic coordinates of each peak voxel (> 3.5 t-value) with a minimum 8 mm distance apart are displayed with the corresponding t-value and region name from Supplementary Figure 16. All coordinates are in MNI template space.

**Supplementary Table 17.**

Age (months)	Group	A $\beta$ <sub>42</sub> (pg/mL)		A $\beta$ <sub>40</sub> (pg/mL)	
		mean	sd	mean	sd
10	Tg-SAL	2007.91	1604.06	3694.01	3390.68
11	Tg-SAL	1626.53	1009.57	3110.75	2079.15
12	Tg-SAL	1547.62	1369.49	2726.22	2462.63
13	Tg-SAL	1549.64	922.35	2968.53	2104.45
14	Tg-SAL	1493.29	1079.45	2964.35	2513.11
15	Tg-SAL	1471.63	941.10	2826.78	2275.09
16	Tg-SAL	1453.35	840.58	2935.90	2289.67
17	Tg-SAL	1464.05	863.34	2852.41	2410.94
19	Tg-SAL	1957.80	935.79	4363.93	3134.55
25	Tg-SAL	2358.07	28.46	6227.55	3104.13
26	Tg-SAL	2346.80	44.55	6231.98	3184.07
10	Tg-ABP	1482.72	1093.97	2410.77	1703.11
11	Tg-ABP	1128.95	745.70	2299.61	2106.24
12	Tg-ABP	1392.86	908.60	2726.06	1833.96
13	Tg-ABP	1479.48	1084.25	2687.95	2421.99
14	Tg-ABP	1294.85	692.94	2276.29	1458.56

15	Tg-ABP	1346.36	960.47	2472.63	1965.95
16	Tg-ABP	1412.14	1042.99	2405.04	1694.13
17	Tg-ABP	1260.62	619.74	2735.71	1776.78
19	Tg-ABP	1319.98	282.57	2853.73	1630.13
25	Tg-ABP	1366.17	284.76	2411.50	1234.57
26	Tg-ABP	1438.41	234.38	2774.23	2013.51

*Supplementary Table 18.*

Age (months)	Group	NFL (pg/mL)	
		mean	sd
10	Tg-SAL	34513.39	17064.23
11	Tg-SAL	28063.77	12482.05
12	Tg-SAL	37606.93	5060.17
13	Tg-SAL	45356.79	23332.12
14	Tg-SAL	42714.13	10155.53
15	Tg-SAL	30026.07	15837.76
16	Tg-SAL	39286.95	24087.07
17	Tg-SAL	50301.44	25946.46
19	Tg-SAL	32957.60	6114.41
25	Tg-SAL	44135.12	7829.70
26	Tg-SAL	54245.70	29622.63
10	Tg-ABP	21531.18	26478.27
11	Tg-ABP	20218.10	11508.13
12	Tg-ABP	20224.84	9943.31
13	Tg-ABP	20917.45	5904.87
14	Tg-ABP	19980.29	5085.04
15	Tg-ABP	22543.87	6659.42
16	Tg-ABP	31293.78	15529.65
17	Tg-ABP	34190.98	18769.73
19	Tg-ABP	39405.37	19178.53

---

25	Tg-ABP	45645.13	20495.15
26	Tg-ABP	43106.31	5807.46

---

## **16 Collaborations (Ongoing)**

### **16.1 International**

1. Developing a Bolus and Constant Infusion protocol using [<sup>18</sup>F]AV45 for Alzheimer's disease
  - a. Collaboration with Dr. Steven Staelens and Dr. Julie Ottoy from the MICA at Antwerpen University
2. Human PET motion tracking
  - a. Collaboration with Dr. Jeroen Vergaeghe and Dr. Alan Menchaca from the MICA at Antwerpen University
3. Effect of Kotho on brain metabolism
  - a. Collaboration with Dr. Dena Dubal from UCSF
4. Effect of AD pathophysiology on MBI
  - a. Collaboration with Dr. Kok Pin Ng from Singapore University

### **16.2 McGill University**

1. Anti-inflammation intervention on a transgenic rat model of AD
  - a. Collaboration with Dr. Alexey Kostikov
2. Head-to-head comparison of [<sup>11</sup>C]PBR28 and [<sup>18</sup>F]DPA714 in a transgenic rat model of AD
  - a. Collaboration with Dr. Alexey Kostikov
3. Tracer development
  - a. Collaboration with Dr. Gassan Massarweh and Dr. Alexey Kostikov
4. Effect of maternal care on early brain development in functional connectivity

- a. Collaboration with Dr. Dominique Walker
5. Effect of RHBDL4 mutation on glucose metabolism
  - a. Collaboration with Dr. Lisa Munter
6. Investigation of stress-induced glutamate changes
  - a. Collaboration with Dr. Marco Leyton
7. Stereotaxic robotic injection in the common marmoset putamen
  - a. Collaboration with Dr. Phillip Huot and Cynthia Kwan
8. Parkinson's marmoset animal model development
  - a. Collaboration with Dr. Phillip Huot and Cynthia Kwan
9. *in vivo* evaluation of [<sup>11</sup>C]-JNJ-42491239 with the mGlu2 PAM AZD-8529 in the marmoset: a positron emission tomography study
  - a. Collaboration with Dr. Phillip Huot and Dr. Adjia Hamadjida
10. Sex-dependent maternal care on functional connectivity
  - a. Collaboration with Dr. Michael Meaney and Dr. Derek Lupinsky

## 17 Publications

### 17.1 First Author

1. Kang, M. S., Shin, M., Ottoy, J., Aliaga, A. A., Mathotaarachchi, S., Quispialaya, K., ... & Rosa-Neto, P. (2021). Preclinical *in vivo* longitudinal assessment of KG207-M as a disease-modifying Alzheimer's disease therapeutic. *Journal of Cerebral Blood Flow & Metabolism*, 0271678X211035625. (Published).
2. Kang, M. S., Aliaga, A. A., Shin, M., Mathotaarachchi, S., Benedet, A. L., Pascoal, T. A., ... & Rosa-Neto, P. (2020). Amyloid-beta modulates the association between neurofilament light chain and brain atrophy in Alzheimer's disease. *Molecular Psychiatry*, 1-13. (Published).
3. Study 2: The interaction between amyloid-beta and activated microglia drives tau propagation in Alzheimer's disease. (Under review).
4. Preclinical Longitudinal *in vivo* Biomarker Platform for Alzheimer's Disease Drug Discovery (Press as a book chapter in the Alzheimer's disease drug development).

### 17.2 Co-author

1. Terada, T., Therriault, J., Kang, M. S. P., Savard, M., Pascoal, T. A., Lussier, F., ... & Rosa-Neto, P. (2021). Mitochondrial complex I abnormalities is associated with tau and clinical symptoms in mild Alzheimer's disease. *Molecular Neurodegeneration*, 16(1), 1-12.
2. Therriault, J., Pascoal, T. A., Benedet, A. L., Tissot, C., Savard, M., Chamoun, M., ... & Rosa-Neto, P. (2021). Frequency of Biologically Defined Alzheimer

Disease in Relation to Age, Sex, APOE  $\epsilon$ 4, and Cognitive Impairment. *Neurology*, 96(7), e975-e985.

3. Lussier, F. Z., Benedet, A. L., Therriault, J., Pascoal, T. A., Tissot, C., Chamoun, M., ... & Alzheimer's Disease Neuroimaging Initiative. (2021). Plasma levels of phosphorylated tau 181 are associated with cerebral metabolic dysfunction in cognitively impaired and amyloid-positive individuals. *Brain Communications*, 3(2), fcab073.
4. Therriault, J., Pascoal, T. A., Savard, M., Benedet, A. L., Chamoun, M., Tissot, C., ... & Rosa-Neto, P. (2021). Topographic Distribution of Amyloid- $\beta$ , Tau, and Atrophy in Patients With Behavioral/Dysexecutive Alzheimer Disease. *Neurology*, 96(1), e81-e92.
5. Therriault, J., Benedet, A. L., Pascoal, T. A., Savard, M., Ashton, N. J., Chamoun, M., ... & Rosa-Neto, P. (2021). Determining Amyloid- $\beta$  positivity using 18F-AZD4694 PET imaging. *Journal of Nuclear Medicine*, 62(2), 247-252.
6. Karikari, T. K., Pascoal, T. A., Ashton, N. J., Janelidze, S., Benedet, A. L., Rodriguez, J. L., ... & Blennow, K. (2020). Blood phosphorylated tau 181 as a biomarker for Alzheimer's disease: a diagnostic performance and prediction modelling study using data from four prospective cohorts. *The Lancet Neurology*, 19(5), 422-433.
7. Cisneros-Franco, J. M., Voss, P., Kang, M. S., Thomas, M. E., Côté, J., Ross, K., ... & de-Villiers-Sidani, É. (2020). PET imaging of perceptual learning-induced changes in the aged rodent cholinergic system. *Frontiers in neuroscience*, 13, 1438.

8. Therriault, J., Benedet, A. L., Pascoal, T. A., Mathotaarachchi, S., Chamoun, M., Savard, M., ... & Rosa-Neto, P. (2020). Association of apolipoprotein E  $\epsilon$ 4 with medial temporal tau independent of amyloid- $\beta$ . *JAMA neurology*, 77(4), 470-479.
9. Lussier, F. Z., Pascoal, T. A., Chamoun, M., Therriault, J., Tissot, C., Savard, M., ... & Gauthier, S. (2020). Mild behavioral impairment is associated with  $\beta$ -amyloid but not tau or neurodegeneration in cognitively intact elderly individuals. *Alzheimer's & Dementia*, 16(1), 192-199.
10. Pascoal, T. A., Therriault, J., Benedet, A. L., Savard, M., Lussier, F. Z., Chamoun, M., ... & Rosa-Neto, P. (2020). 18F-MK-6240 PET for early and late detection of neurofibrillary tangles. *Brain*, 143(9), 2818-2830.
11. Pascoal, T. A., Therriault, J., Mathotaarachchi, S., Kang, M. S., Shin, M., Benedet, A. L., ... & Alzheimer's Disease Neuroimaging Initiative. (2020). Topographical distribution of A $\beta$  predicts progression to dementia in A $\beta$  positive mild cognitive impairment. *Alzheimer's & Dementia: Diagnosis, Assessment & Disease Monitoring*, 12(1), e12037.
12. Benedet, A. L., Leuzy, A., Pascoal, T. A., Ashton, N. J., Mathotaarachchi, S., Savard, M., ... & Alzheimer's Disease Neuroimaging Initiative. (2020). Stage-specific links between plasma neurofilament light and imaging biomarkers of Alzheimer's disease. *Brain*, 143(12), 3793-3804.
13. Therriault, J., Benedet, A. L., Pascoal, T. A., Mathotaarachchi, S., Savard, M., Chamoun, M., ... & Rosa-Neto, P. (2020). APOE $\epsilon$ 4 potentiates the relationship between amyloid- $\beta$  and tau pathologies. *Molecular psychiatry*, 1-12.

14. Miranda, A., Kang, M. S., Blinder, S., Bouhachi, R., Soucy, J. P., Aliaga-Aliaga, A., ... & Verhaeghe, J. (2019). PET imaging of freely moving interacting rats. *Neuroimage*, 191, 560-567.
15. Ng, K. P., Therriault, J., Kang, M. S., Struyfs, H., Pascoal, T. A., Mathotaarachchi, S., ... & Gauthier, S. (2019). Rasagiline, a monoamine oxidase B inhibitor, reduces *in vivo* [<sup>18</sup>F] THK5351 uptake in progressive supranuclear palsy. *NeuroImage: Clinical*, 24, 102091.
16. Pascoal, T. A., Mathotaarachchi, S., Kang, M. S., Mohaddes, S., Shin, M., Park, A. Y., ... & Rosa-Neto, P. (2019). Aβ-induced vulnerability propagates via the brain's default mode network. *Nature communications*, 10(1), 1-13.
17. Hopewell, R., Ross, K., Kostikov, A., Pascoal, T. A., Alberti, T., Lacatus-Samoila, M., ... & Massarweh, G. (2019). A simplified radiosynthesis of [<sup>18</sup>F] MK-6240 for tau PET imaging. *Journal of Labelled Compounds and Radiopharmaceuticals*, 62(2), 109-114.
18. Benedet, A. L., Ashton, N. J., Pascoal, T. A., Leuzy, A., Mathotaarachchi, S., Kang, M. S., ... & Alzheimer's Disease Neuroimaging Initiative. (2019). Plasma neurofilament light associates with Alzheimer's disease metabolic decline in amyloid-positive individuals. *Alzheimer's & Dementia: Diagnosis, Assessment & Disease Monitoring*, 11(1), 679-689.
19. Therriault, J., Wang, S., Mathotaarachchi, S., Pascoal, T. A., Parent, M., Beaudry, T., ... & Rosa-Neto, P. (2019). Rostral-caudal hippocampal functional convergence is reduced across the Alzheimer's disease spectrum. *Molecular neurobiology*, 56(12), 8336-8344.

20. Guadagno, A., Kang, M. S., Devenyi, G. A., Mathieu, A. P., Rosa-Neto, P., Chakravarty, M., & Walker, C. D. (2018). Reduced resting-state functional connectivity of the basolateral amygdala to the medial prefrontal cortex in preweaning rats exposed to chronic early-life stress. *Brain Structure and Function*, 223(8), 3711-3729.
21. Zhang, H., Therriault, J., Kang, M. S., Ng, K. P., Pascoal, T. A., Rosa-Neto, P., & Gauthier, S. (2018). Cerebrospinal fluid synaptosomal-associated protein 25 is a key player in synaptic degeneration in mild cognitive impairment and Alzheimer's disease. *Alzheimer's research & therapy*, 10(1), 1-11.
22. Zhang, H., Ng, K. P., Therriault, J., Kang, M. S., Pascoal, T. A., Rosa-Neto, P., & Gauthier, S. (2018). Cerebrospinal fluid phosphorylated tau, visinin-like protein-1, and chitinase-3-like protein 1 in mild cognitive impairment and Alzheimer's disease. *Translational neurodegeneration*, 7(1), 1-12.
23. Pascoal, T. A., Shin, M., Kang, M. S., Chamoun, M., Chartrand, D., Mathotaarachchi, S., ... & Rosa-Neto, P. (2018). *in vivo* quantification of neurofibrillary tangles with [<sup>18</sup>F] MK-6240. *Alzheimer's research & therapy*, 10(1), 1-14.
24. Therriault, J., Ng, K. P., Pascoal, T. A., Mathotaarachchi, S., Kang, M. S., Struyfs, H., ... & Alzheimer's Disease Neuroimaging Initiative. (2018). Anosognosia predicts default mode network hypometabolism and clinical progression to dementia. *Neurology*, 90(11), e932-e939.
25. Pascoal, T. A., Mathotaarachchi, S., Shin, M., Park, A. Y., Mohades, S., Benedet, A. L., ... & Rosa-Neto, P. (2018). Amyloid and tau signatures of brain metabolic

decline in preclinical Alzheimer's disease. *European journal of nuclear medicine and molecular imaging*, 45(6), 1021-1030.

26. Benedet, A. L., Yu, L., Labbe, A., Mathotaarachchi, S., Pascoal, T. A., Shin, M., ... & Alzheimer's Disease Neuroimaging Initiative. (2018). CYP2C19 variant mitigates Alzheimer disease pathophysiology *in vivo* and postmortem. *Neurology Genetics*, 4(1).
27. Pascoal, T. A., Mathotaarachchi, S., Shin, M., Benedet, A. L., Mohades, S., Wang, S., ... & Alzheimer's Disease Neuroimaging Initiative. (2017). Synergistic interaction between amyloid and tau predicts the progression to dementia. *Alzheimer's & Dementia*, 13(6), 644-653.
28. Ng, K. P., Pascoal, T. A., Mathotaarachchi, S., Therriault, J., Kang, M. S., Shin, M., ... & Rosa-Neto, P. (2017). Monoamine oxidase B inhibitor, selegiline, reduces 18 F-THK5351 uptake in the human brain. *Alzheimer's research & therapy*, 9(1), 1-9.
29. Pascoal, T. A., Mathotaarachchi, S., Mohades, S., Benedet, A. L., Chung, C. O., Shin, M., ... & Rosa-Neto, P. (2017). Amyloid- $\beta$  and hyperphosphorylated tau synergy drives metabolic decline in preclinical Alzheimer's disease. *Molecular psychiatry*, 22(2), 306-311.
30. Mathotaarachchi, S., Pascoal, T. A., Shin, M., Benedet, A. L., Kang, M. S., Beaudry, T., ... & Alzheimer's Disease Neuroimaging Initiative. (2017). Identifying incipient dementia individuals using machine learning and amyloid imaging. *Neurobiology of aging*, 59, 80-90.

31. Ng, K. P., Pascoal, T. A., Mathotaarachchi, S., Chung, C. O., Benedet, A. L., Shin, M., ... & Alzheimer's Disease Neuroimaging Initiative. (2017). Neuropsychiatric symptoms predict hypometabolism in preclinical Alzheimer disease. *Neurology*, 88(19), 1814-1821.
32. Parent, M. J., Zimmer, E. R., Shin, M., Kang, M. S., Fonov, V. S., Mathieu, A., ... & Rosa-Neto, P. (2017). Multimodal imaging in rat model recapitulates Alzheimer's disease biomarkers abnormalities. *Journal of Neuroscience*, 37(50), 12263-12271.
33. Mathotaarachchi, S., Wang, S., Shin, M., Pascoal, T. A., Benedet, A. L., Kang, M. S., ... & Rosa-Neto, P. (2016). VoxelStats: a MATLAB package for multi-modal voxel-wise brain image analysis. *Frontiers in neuroinformatics*, 10, 20.
34. Gibon, J., Kang, M. S., Aliaga, A., Sharif, B., Rosa-Neto, P., Séguéla, P., ... & Kostikov, A. (2016). Towards the PET radiotracer for p75 neurotrophin receptor: [<sup>11</sup>C] LM11A-24 shows biological activity *in vitro*, but unfavorable *ex vivo* and *in vivo* profile. *Bioorganic & medicinal chemistry*, 24(19), 4759-4765.

## 18 Presentations

### 18.1 Invited

1. Brazilian Congress report 2020 — *In-vivo biomarker assessment of Alzheimer's disease pathophysiology: a cross-species study*
2. CREATE-MIA 2017 — *A brief overview of PET quantification*

### 18.2 Oral

1. International Conference on Alzheimer's & Parkinson's Diseases and related neurological disorders 2021 — *Activated microglia in the medial temporal lobe imposes sex-dependent vulnerability in Alzheimer's disease*
2. Alzheimer's Association International Conference 2020 — *Synergistic underpinning of global amyloid and cingulate neuroinflammation underlies tau propagation in Alzheimer's disease*
3. Alzheimer's Association International Conference 2020 — *A novel p75-neurotrophin receptor antagonist, EVT901, reduces neuroinflammation in the TgFAD344 rat model of Alzheimer's disease (Dr. Alexey Kostikov presented on my behalf)*
4. Human Amyloid Imaging Conference 2019 — *Friend or foe? Regional dependent roles of neuroinflammation in Alzheimer's disease pathophysiology*
5. NeuroReceptor Mapping Conference 2018 — *Amyloid driven tau deposition colocalizes with Braak Stages*

6. Alzheimer's Association International Conference 2017 — *Preclinical assessment of KAL-ABP target engagement and efficacy using PET, MRI and CSF biomarkers* (Dr. Pedro Rosa-Neto presented on my behalf)
7. Alzheimer's Association International Conference 2017 — *Amyloid-beta modulates cerebral metabolic network in rats and humans*
8. International Conference on Alzheimer's & Parkinson's Diseases and related neurological disorders 2017 — *Hippocampal metabolic network serves as a translational biomarker of Alzheimer's disease: Interspecies Study* (Short oral)
9. Quebec Network for Research on Aging 2013 — *Memory and cerebral hypometabolism in a rat model of Alzheimer's Disease*

### **18.3 Poster**

1. Alzheimer's Association International Conference 2021 — *Cognitive health mediates the effect of hippocampal volume on COVID19-related knowledge or anxiety change during the COVID19 pandemic*
2. Alzheimer's Association International Conference 2020 — *Microglial sex dimorphism poses greater vulnerability to Alzheimer's disease in females: Cross-species study*
3. Alzheimer's Association International Conference Neuroscience Next 2020 — *Activated microglia in medial temporal cortex drives tau propagation in the Ab positive individuals*
4. Human Amyloid Imaging 2019 — *Activated microglia and amyloid load potentiate tau deposition leading to cognitive dysfunction in Alzheimer's disease*

5. Human Amyloid Imaging 2019 — *Tauopathy in females is more vulnerable to amyloid or neuroinflammation in Alzheimer's disease*
6. Alzheimer's Association International Conference 2019 — *Issues regarding [<sup>18</sup>F]MK6240 reference region selection based on the full kinetic modelling*
7. Brain PET 2019 — *[<sup>18</sup>F]FDG is associated with CSF neurofilament light chain in mild cognitive impairment*
8. Alzheimer's Association International Conference 2018 — *Regional patterns of tau deposition driven by local amyloid accumulation recapitulate Braak stages in AD*
9. Alzheimer's Association International Conference 2018 — *Amyloid and microglial activation synergy lead to hypometabolism in AD brain: MicroPET longitudinal study*
10. Human Amyloid Imaging Conference 2018 — *Optimal Reference region analysis for [<sup>18</sup>F]MK6240 based on full kinetic modeling*
11. NeuroReceptor Mapping 2018 — *Brain glucose uptake is modulated by the interaction between microglial activation and amyloid load: a longitudinal microPET study*
12. Alzheimer's Association International Conference 2017 — *Gray matter neurodegeneration is associated with CSF neurofilament light chain in the patients with Alzheimer's disease and Tg animal model*
13. Brain PET 2017 — *The structural atrophy is associated with CSF neurofilament light chain in a transgenic rat model of Alzheimer's disease*

14. Human Amyloid Imaging Conference 2017 — *Increased level of CSF neurofilament light chain is associated with amyloidosis in a transgenic rat model of Alzheimer's disease*
15. Alzheimer's Association International Conference 2016 — *Synergistic effect of regional hypometabolism and A $\beta$  on a decline in cognition in AD transgenic rat model*
16. Alzheimer's Association International Conference 2016 — *Decline in regional cerebral metabolism with CSF A $\beta$ <sub>1-42</sub> level has a synergistic effect on decline in cognition*
17. NeuroReceptor Mapping 2016 — *The effect of TSPO expression on brain structures in Transgenic model of amyloidosis*
18. Alzheimer's Association International Conference 2015 — *Amyloidosis induces reorganization of the hippocampal metabolic network*
19. Human Amyloid Imaging Conference 2015 — *in vivo Competition between [<sup>11</sup>C]PiB and [<sup>18</sup>F]NAV4694 in a Transgenic Rat Model of Amyloidosis*
20. Alzheimer's Association International Conference 2014 — *Amyloidosis modulates associations between hippocampal volume and brain metabolic declines*

## 19 Awards and Recognition

1. Alzheimer's Association International Conference 2021 Travel Award
  - a. Free registration
2. Human Amyloid Imaging 2020 Young Investigator Travel Award
  - a. \$1,000 (USD)
3. Human Amyloid Imaging 2019 Young Investigator Travel Award
  - a. \$1,000 (USD)
4. Early Career Investigator Travel Bursary for BRAIN & BRAIN PET 2019
  - a. \$1,450 (USD)
5. McGill IPN GREAT Award 2018
  - a. \$500 (CAD)
6. CIHR Doctoral Award 2017
  - a. \$30,000 + \$5,000 allowance for three years of support.
7. Alzheimer's Association International Conference 2017 Travel Award
  - a. Full registration, flight, and hotel
8. CIHR 2017 Travel Award
  - a. \$1,000 (CAD)
9. CIHR 2017 Travel Award
  - a. \$1,000 (CAD)
10. Early Career Investigator Travel Bursary for BRAIN & BRAIN PET 2017
  - a. €950
11. Alzheimer's Association International Conference 2016 Volunteer Leader Award
  - a. Full registration, flight, and hotel

12. James O & Maria Meadows Award – McGill Faculty of Medicine Internal Studentship Award 2016
  - a. \$12,000 (CAD)
13. McGill IPN GREAT award 2016
  - a. \$500 (CAD)
14. Alzheimer’s Association International Conference 2015 Volunteer Award
  - a. Full registration, flight, and hotel
15. McGill IPN GREAT award 2014
  - a. \$500 (CAD)

## 20 References

- [1] 2021 Alzheimer's disease facts and figures. *Alzheimers Dement.* 2021;17:327-406.
- [2] Organization WH. Global action plan on the public health response to dementia 2017-2025. 2017.
- [3] Dunn B, Stein P, Temple R, Cavazzoni P. An Appropriate Use of Accelerated Approval — Aducanumab for Alzheimer's Disease. 2021.
- [4] Engelhardt E, Gomes Mda M. Alzheimer's 100th anniversary of death and his contribution to a better understanding of Senile dementia. *Arq Neuropsiquiatr.* 2015;73:159-62.
- [5] Alzheimer A, Stelzmann RA, Schnitzlein HN, Murtagh FR. An English translation of Alzheimer's 1907 paper, "Uber eine eigenartige Erkrankung der Hirnrinde". *Clin Anat.* 1995;8:429-31.
- [6] Goedert M. Oskar Fischer and the study of dementia. *Brain.* 2009;132:1102-11.
- [7] Tomlinson BE, Blessed G, Roth M. Observations on the brains of demented old people. *Journal of the Neurological Sciences.* 1970;11:205-42.
- [8] Blessed G, Tomlinson BE, Roth M. The association between quantitative measures of dementia and of senile change in the cerebral grey matter of elderly subjects. *Br J Psychiatry.* 1968;114:797-811.
- [9] Katzman R. Editorial: The prevalence and malignancy of Alzheimer disease. A major killer. *Arch Neurol.* 1976;33:217-8.
- [10] Davies P. Selective Loss of Central Cholinergic Neurons in Alzheimer's Disease. *The Lancet.* 1976;308:1403.
- [11] Perry EK, Perry RH, Blessed G, Tomlinson BE. Necropsy Evidence of Central Cholinergic Deficits in Senile Dementia. *Lancet.* 1977;1:189-.
- [12] Crismon ML. Tacrine: first drug approved for Alzheimer's disease. *Ann Pharmacother.* 1994;28:744-51.
- [13] Glenner GG, Wong CW. Alzheimer's disease: initial report of the purification and characterization of a novel cerebrovascular amyloid protein. *Biochem Biophys Res Commun.* 1984;120:885-90.
- [14] Glenner GG, Wong CW. Alzheimer's disease and Down's syndrome: sharing of a unique cerebrovascular amyloid fibril protein. *Biochem Biophys Res Commun.* 1984;122:1131-5.
- [15] Brion J-PP, Heloisa.; Nunez, Jacques.; lamente-Durand, Jacqueline. Mise en évidence immunologique de la protéine tau au niveau des lésions de dégénérescence neurofibrillaire de la maladie d'Alzheimer. *Archives of Biology.* 1985;96:229-35.
- [16] Kosik KS, Joachim CL, Selkoe DJ. Microtubule-associated protein tau (tau) is a major antigenic component of paired helical filaments in Alzheimer disease. *Proc Natl Acad Sci U S A.* 1986;83:4044-8.
- [17] Tanzi RE, Gusella JF, Watkins PC, Bruns GA, St George-Hyslop P, Van Keuren ML, et al. Amyloid beta protein gene: cDNA, mRNA distribution, and genetic linkage near the Alzheimer locus. *Science.* 1987;235:880-4.
- [18] St George-Hyslop PH, Tanzi RE, Polinsky RJ, Haines JL, Nee L, Watkins PC, et al. The genetic defect causing familial Alzheimer's disease maps on chromosome 21. *Science.* 1987;235:885-90.
- [19] Kang J, Lemaire HG, Unterbeck A, Salbaum JM, Masters CL, Grzeschik KH, et al. The precursor of Alzheimer's disease amyloid A4 protein resembles a cell-surface receptor. *Nature.* 1987;325:733-6.

- [20] Selkoe DJ. The molecular pathology of Alzheimer's disease. *Neuron*. 1991;6:487-98.
- [21] Hardy J, Allsop D. Amyloid deposition as the central event in the aetiology of Alzheimer's disease. *Trends in Pharmacological Sciences*. 1991;12:383-8.
- [22] Quon D, Wang Y, Catalano R, Scardina JM, Murakami K, Cordell B. Formation of beta-amyloid protein deposits in brains of transgenic mice. *Nature*. 1991;352:239-41.
- [23] Braak H, Braak E. Neuropathological staging of Alzheimer-related changes. *Acta Neuropathol*. 1991;82:239-59.
- [24] Braak H, Alafuzoff I, Arzberger T, Kretschmar H, Del Tredici K. Staging of Alzheimer disease-associated neurofibrillary pathology using paraffin sections and immunocytochemistry. *Acta Neuropathol*. 2006;112:389-404.
- [25] McGeer PL, Itagaki S, McGeer EG. Expression of the histocompatibility glycoprotein HLA-DR in neurological disease. *Acta Neuropathol*. 1988;76:550-7.
- [26] Itagaki S, McGeer PL, Akiyama H, Zhu S, Selkoe D. Relationship of microglia and astrocytes to amyloid deposits of Alzheimer disease. *J Neuroimmunol*. 1989;24:173-82.
- [27] Poirier J, Bertrand P, Poirier J, Kogan S, Gauthier S, Poirier J, et al. Apolipoprotein E polymorphism and Alzheimer's disease. *The Lancet*. 1993;342:697-9.
- [28] Holtzman DM, Herz J, Bu G. Apolipoprotein E and apolipoprotein E receptors: normal biology and roles in Alzheimer disease. *Cold Spring Harb Perspect Med*. 2012;2:a006312.
- [29] Loy CT, Schofield PR, Turner AM, Kwok JBJ. Genetics of dementia. *The Lancet*. 2014;383:828-40.
- [30] Michaelson DM. APOE epsilon4: the most prevalent yet understudied risk factor for Alzheimer's disease. *Alzheimers Dement*. 2014;10:861-8.
- [31] Buee L, Hof PR, Bouras C, Delacourte A, Perl DP, Morrison JH, et al. Pathological alterations of the cerebral microvasculature in Alzheimer's disease and related dementing disorders. *Acta Neuropathol*. 1994;87:469-80.
- [32] Schneider JA, Arvanitakis Z, Bang W, Bennett DA. Mixed brain pathologies account for most dementia cases in community-dwelling older persons. *Neurology*. 2007;69:2197-204.
- [33] Barker WW, Luis CA, Kashuba A, Luis M, Harwood DG, Loewenstein D, et al. Relative frequencies of Alzheimer disease, Lewy body, vascular and frontotemporal dementia, and hippocampal sclerosis in the State of Florida Brain Bank. *Alzheimer Dis Assoc Disord*. 2002;16:203-12.
- [34] Seab JP, Jagust WJ, Wong ST, Roos MS, Reed BR, Budinger TF. Quantitative NMR measurements of hippocampal atrophy in Alzheimer's disease. *Magn Reson Med*. 1988;8:200-8.
- [35] De Leon M, George A, Stylopoulos L, Smith G, Miller D. Early Marker for Alzheimer's Disease: The Atrophic Hippocampus. *The Lancet*. 1989;334:672-3.
- [36] Ferris SH, de Leon MJ, Wolf AP, Farkas T, Christman DR, Reisberg B, et al. Positron Emission Tomography in the Study of Aging and Senile Dementia. *Neurobiology of Aging*. 1980;1:127-31.
- [37] de Leon MJ, Convit A, Wolf OT, Tarshish CY, DeSanti S, Rusinek H, et al. Prediction of cognitive decline in normal elderly subjects with 2-[(18)F]fluoro-2-deoxy-D-glucose/positron-emission tomography (FDG/PET). *Proc Natl Acad Sci U S A*. 2001;98:10966-71.
- [38] Mosconi L, Tsui WH, Herholz K, Pupi A, Drzezga A, Lucignani G, et al. Multicenter standardized 18F-FDG PET diagnosis of mild cognitive impairment, Alzheimer's disease, and other dementias. *J Nucl Med*. 2008;49:390-8.

- [39] Sorensen L, Igel C, Pai A, Balas I, Anker C, Lillholm M, et al. Differential diagnosis of mild cognitive impairment and Alzheimer's disease using structural MRI cortical thickness, hippocampal shape, hippocampal texture, and volumetry. *Neuroimage Clin.* 2017;13:470-82.
- [40] Dickerson BC, Goncharova I, Sullivan MP, Forchetti C, Wilson RS, Bennett DA, et al. MRI-derived entorhinal and hippocampal atrophy in incipient and very mild Alzheimer's disease
- ☆ ☆ This research was supported by grants P01 AG09466 and P30 AG10161 from the National Institute on Aging, National Institutes of Health. *Neurobiology of Aging.* 2001;22:747-54.
- [41] Seubert P, Vigo-Pelfrey C, Esch F, Lee M, Dovey H, Davis D, et al. Isolation and quantification of soluble Alzheimer's beta-peptide from biological fluids. *Nature.* 1992;359:325-7.
- [42] Blennow K, Wallin A, Agren H, Spenger C, Siegfried J, Vanmechelen E. Tau protein in cerebrospinal fluid: a biochemical marker for axonal degeneration in Alzheimer disease? *Mol Chem Neuropathol.* 1995;26:231-45.
- [43] Niemantsverdriet E, Ottoy J, Somers C, De Roeck E, Struyfs H, Soetewey F, et al. The Cerebrospinal Fluid Abeta1-42/Abeta1-40 Ratio Improves Concordance with Amyloid-PET for Diagnosing Alzheimer's Disease in a Clinical Setting. *J Alzheimers Dis.* 2017;60:561-76.
- [44] Blennow K. A Review of Fluid Biomarkers for Alzheimer's Disease: Moving from CSF to Blood. *Neurol Ther.* 2017;6:15-24.
- [45] Zetterberg H, Blennow K. Moving fluid biomarkers for Alzheimer's disease from research tools to routine clinical diagnostics. *Mol Neurodegener.* 2021;16:10.
- [46] Klunk WE, Engler H, Nordberg A, Wang Y, Blomqvist G, Holt DP, et al. Imaging brain amyloid in Alzheimer's disease with Pittsburgh Compound-B. *Ann Neurol.* 2004;55:306-19.
- [47] Greicius MD, Srivastava G, Reiss AL, Menon V. Default-mode network activity distinguishes Alzheimer's disease from healthy aging; evidence from functional MRI. *Proc Natl Acad Sci U S A.* 2004;101:4637-42.
- [48] Buckner RL, Snyder AZ, Shannon BJ, LaRossa G, Sachs R, Fotenos AF, et al. Molecular, structural, and functional characterization of Alzheimer's disease: evidence for a relationship between default activity, amyloid, and memory. *J Neurosci.* 2005;25:7709-17.
- [49] Sperling RA, Laviolette PS, O'Keefe K, O'Brien J, Rentz DM, Pihlajamaki M, et al. Amyloid deposition is associated with impaired default network function in older persons without dementia. *Neuron.* 2009;63:178-88.
- [50] McKhann G, Drachman D, Folstein M, Katzman R, Price D, Stadlan EM. Clinical diagnosis of Alzheimer's disease: report of the NINCDS-ADRDA Work Group under the auspices of Department of Health and Human Services Task Force on Alzheimer's Disease. *Neurology.* 1984;34:939-44.
- [51] Jack CR, Jr., Albert MS, Knopman DS, McKhann GM, Sperling RA, Carrillo MC, et al. Introduction to the recommendations from the National Institute on Aging-Alzheimer's Association workgroups on diagnostic guidelines for Alzheimer's disease. *Alzheimers Dement.* 2011;7:257-62.
- [52] McKhann GM, Knopman DS, Chertkow H, Hyman BT, Jack CR, Jr., Kawas CH, et al. The diagnosis of dementia due to Alzheimer's disease: recommendations from the National Institute on Aging-Alzheimer's Association workgroups on diagnostic guidelines for Alzheimer's disease. *Alzheimers Dement.* 2011;7:263-9.
- [53] Albert MS, DeKosky ST, Dickson D, Dubois B, Feldman HH, Fox NC, et al. The diagnosis of mild cognitive impairment due to Alzheimer's disease: recommendations from the National

Institute on Aging-Alzheimer's Association workgroups on diagnostic guidelines for Alzheimer's disease. *Alzheimers Dement.* 2011;7:270-9.

[54] Sperling RA, Aisen PS, Beckett LA, Bennett DA, Craft S, Fagan AM, et al. Toward defining the preclinical stages of Alzheimer's disease: recommendations from the National Institute on Aging-Alzheimer's Association workgroups on diagnostic guidelines for Alzheimer's disease. *Alzheimers Dement.* 2011;7:280-92.

[55] Jack CR, Knopman DS, Jagust WJ, Shaw LM, Aisen PS, Weiner MW, et al. Hypothetical model of dynamic biomarkers of the Alzheimer's pathological cascade. *The Lancet Neurology.* 2010;9:119-28.

[56] Jack CR, Knopman DS, Jagust WJ, Petersen RC, Weiner MW, Aisen PS, et al. Tracking pathophysiological processes in Alzheimer's disease: an updated hypothetical model of dynamic biomarkers. *The Lancet Neurology.* 2013;12:207-16.

[57] Gomez-Isla T, Hollister R, West H, Mui S, Growdon JH, Petersen RC, et al. Neuronal loss correlates with but exceeds neurofibrillary tangles in Alzheimer's disease. *Ann Neurol.* 1997;41:17-24.

[58] Bennett DA, Schneider JA, Wilson RS, Bienias JL, Arnold SE. Neurofibrillary tangles mediate the association of amyloid load with clinical Alzheimer disease and level of cognitive function. *Arch Neurol.* 2004;61:378-84.

[59] DeKosky ST, Scheff SW. Synapse loss in frontal cortex biopsies in Alzheimer's disease: correlation with cognitive severity. *Ann Neurol.* 1990;27:457-64.

[60] Savva GM, Wharton SB, Ince PG, Forster G, Matthews FE, Brayne C, et al. Age, neuropathology, and dementia. *N Engl J Med.* 2009;360:2302-9.

[61] Villemagne VL, Burnham S, Bourgeat P, Brown B, Ellis KA, Salvado O, et al. Amyloid  $\beta$  deposition, neurodegeneration, and cognitive decline in sporadic Alzheimer's disease: a prospective cohort study. *The Lancet Neurology.* 2013;12:357-67.

[62] Aizenstein HJ, Nebes RD, Saxton JA, Price JC, Mathis CA, Tsopelas ND, et al. Frequent amyloid deposition without significant cognitive impairment among the elderly. *Arch Neurol.* 2008;65:1509-17.

[63] Fagan AM, Mintun MA, Mach RH, Lee SY, Dence CS, Shah AR, et al. Inverse relation between in vivo amyloid imaging load and cerebrospinal fluid Abeta42 in humans. *Ann Neurol.* 2006;59:512-9.

[64] Shaw LM, Vanderstichele H, Knapik-Czajka M, Clark CM, Aisen PS, Petersen RC, et al. Cerebrospinal fluid biomarker signature in Alzheimer's disease neuroimaging initiative subjects. *Ann Neurol.* 2009;65:403-13.

[65] Janelidze S, Stomrud E, Smith R, Palmqvist S, Mattsson N, Airey DC, et al. Cerebrospinal fluid p-tau217 performs better than p-tau181 as a biomarker of Alzheimer's disease. *Nat Commun.* 2020;11:1683.

[66] Janelidze S, Mattsson N, Palmqvist S, Smith R, Beach TG, Serrano GE, et al. Plasma P-tau181 in Alzheimer's disease: relationship to other biomarkers, differential diagnosis, neuropathology and longitudinal progression to Alzheimer's dementia. *Nat Med.* 2020;26:379-86.

[67] Jack CR, Jr., Bennett DA, Blennow K, Carrillo MC, Dunn B, Haeberlein SB, et al. NIA-AA Research Framework: Toward a biological definition of Alzheimer's disease. *Alzheimers Dement.* 2018;14:535-62.

[68] Hampel H, Cummings J, Blennow K, Gao P, Jack CR, Jr., Vergallo A. Developing the ATX(N) classification for use across the Alzheimer disease continuum. *Nat Rev Neurol.* 2021.

- [69] Ikonomic MD, Klunk WE, Abrahamson EE, Mathis CA, Price JC, Tsopelas ND, et al. Post-mortem correlates of in vivo PiB-PET amyloid imaging in a typical case of Alzheimer's disease. *Brain*. 2008;131:1630-45.
- [70] Clark CM, Pontecorvo MJ, Beach TG, Bedell BJ, Coleman RE, Doraiswamy PM, et al. Cerebral PET with florbetapir compared with neuropathology at autopsy for detection of neuritic amyloid- $\beta$  plaques: a prospective cohort study. *The Lancet Neurology*. 2012;11:669-78.
- [71] Villemagne VL, Fodero-Tavoletti MT, Masters CL, Rowe CC. Tau imaging: early progress and future directions. *The Lancet Neurology*. 2015;14:114-24.
- [72] Buerger K, Ewers M, Pirttila T, Zinkowski R, Alafuzoff I, Teipel SJ, et al. CSF phosphorylated tau protein correlates with neocortical neurofibrillary pathology in Alzheimer's disease. *Brain*. 2006;129:3035-41.
- [73] Jagust W. Imaging the evolution and pathophysiology of Alzheimer disease. *Nat Rev Neurosci*. 2018;19:687-700.
- [74] Kovacs GG, Milenkovic I, Wohrer A, Hoftberger R, Gelpi E, Haberler C, et al. Non-Alzheimer neurodegenerative pathologies and their combinations are more frequent than commonly believed in the elderly brain: a community-based autopsy series. *Acta Neuropathol*. 2013;126:365-84.
- [75] Jack CR, Jr., Knopman DS, Weigand SD, Wiste HJ, Vemuri P, Lowe V, et al. An operational approach to National Institute on Aging-Alzheimer's Association criteria for preclinical Alzheimer disease. *Ann Neurol*. 2012;71:765-75.
- [76] Selkoe DJ, Hardy J. The amyloid hypothesis of Alzheimer's disease at 25 years. *EMBO Mol Med*. 2016;8:595-608.
- [77] Liu PP, Xie Y, Meng XY, Kang JS. History and progress of hypotheses and clinical trials for Alzheimer's disease. *Signal Transduct Target Ther*. 2019;4:29.
- [78] Chen GF, Xu TH, Yan Y, Zhou YR, Jiang Y, Melcher K, et al. Amyloid beta: structure, biology and structure-based therapeutic development. *Acta Pharmacol Sin*. 2017;38:1205-35.
- [79] Vassar R. BACE1: The  $\beta$ -Secretase Enzyme in Alzheimer's Disease. *Journal of Molecular Neuroscience*. 2004;23:105-14.
- [80] Kagan BL, Jang H, Capone R, Teran Arce F, Ramachandran S, Lal R, et al. Antimicrobial properties of amyloid peptides. *Mol Pharm*. 2012;9:708-17.
- [81] Maloney B, Lahiri DK. The Alzheimer's amyloid beta-peptide (A $\beta$ ) binds a specific DNA A $\beta$ -interacting domain (A $\beta$ IID) in the APP, BACE1, and APOE promoters in a sequence-specific manner: characterizing a new regulatory motif. *Gene*. 2011;488:1-12.
- [82] Tabaton M, Zhu X, Perry G, Smith MA, Giliberto L. Signaling effect of amyloid-beta(42) on the processing of A $\beta$ PP. *Exp Neurol*. 2010;221:18-25.
- [83] Jarrett JT, Berger EP, Lansbury PT, Jr. The carboxy terminus of the beta amyloid protein is critical for the seeding of amyloid formation: implications for the pathogenesis of Alzheimer's disease. *Biochemistry*. 1993;32:4693-7.
- [84] Esparza TJ, Zhao H, Cirrito JR, Cairns NJ, Bateman RJ, Holtzman DM, et al. Amyloid-beta oligomerization in Alzheimer dementia versus high-pathology controls. *Ann Neurol*. 2013;73:104-19.
- [85] Zott B, Simon MM, Hong W, Unger F, Chen-Engerer HJ, Frosch MP, et al. A vicious cycle of beta amyloid-dependent neuronal hyperactivation. *Science*. 2019;365:559-65.
- [86] Park J, Wetzel I, Marriott I, Dreau D, D'Avanzo C, Kim DY, et al. A 3D human triculture system modeling neurodegeneration and neuroinflammation in Alzheimer's disease. *Nat Neurosci*. 2018;21:941-51.

- [87] Heneka MT, Carson MJ, Khoury JE, Landreth GE, Brosseron F, Feinstein DL, et al. Neuroinflammation in Alzheimer's disease. *The Lancet Neurology*. 2015;14:388-405.
- [88] Hickman S, Izzy S, Sen P, Morsett L, El Khoury J. Microglia in neurodegeneration. *Nat Neurosci*. 2018;21:1359-69.
- [89] Leon WC, Canneva F, Partridge V, Allard S, Ferretti MT, DeWilde A, et al. A novel transgenic rat model with a full Alzheimer's-like amyloid pathology displays pre-plaque intracellular amyloid-beta-associated cognitive impairment. *J Alzheimers Dis*. 2010;20:113-26.
- [90] Bekris LM, Yu CE, Bird TD, Tsuang DW. Genetics of Alzheimer disease. *J Geriatr Psychiatry Neurol*. 2010;23:213-27.
- [91] Goedert M, Wischik CM, Crowther RA, Walker JE, Klug A. Cloning and sequencing of the cDNA encoding a core protein of the paired helical filament of Alzheimer disease: identification as the microtubule-associated protein tau. *Proc Natl Acad Sci U S A*. 1988;85:4051-5.
- [92] Papanikolopoulou K, Roussou IG, Gouzi JY, Samiotaki M, Panayotou G, Turin L, et al. Drosophila Tau Negatively Regulates Translation and Olfactory Long-Term Memory, But Facilitates Footshock Habituation and Cytoskeletal Homeostasis. *J Neurosci*. 2019;39:8315-29.
- [93] Dehmelt L, Halpain S. The MAP2/Tau family of microtubule-associated proteins. *Genome Biol*. 2005;6:204.
- [94] Leuzy A, Chiotis K, Lemoine L, Gillberg PG, Almkvist O, Rodriguez-Vieitez E, et al. Tau PET imaging in neurodegenerative tauopathies-still a challenge. *Mol Psychiatry*. 2019;24:1112-34.
- [95] Nishimura I, Yang Y, Lu B. PAR-1 Kinase Plays an Initiator Role in a Temporally Ordered Phosphorylation Process that Confers Tau Toxicity in Drosophila. *Cell*. 2004;116:671-82.
- [96] Gendreau KL, Hall GF. Tangles, Toxicity, and Tau Secretion in AD - New Approaches to a Vexing Problem. *Front Neurol*. 2013;4:160.
- [97] Takashima A. Tauopathies and tau oligomers. *J Alzheimers Dis*. 2013;37:565-8.
- [98] Buée L, Bussièrè T, Buée-Scherrer V, Delacourte A, Hof PR. Tau protein isoforms, phosphorylation and role in neurodegenerative disorders<sup>11</sup>These authors contributed equally to this work. *Brain Research Reviews*. 2000;33:95-130.
- [99] Dujardin S, Begard S, Caillierez R, Lachaud C, Carrier S, Lieger S, et al. Different tau species lead to heterogeneous tau pathology propagation and misfolding. *Acta Neuropathol Commun*. 2018;6:132.
- [100] Aguero C, Dhaynaut M, Normandin MD, Amaral AC, Guehl NJ, Neelamegam R, et al. Autoradiography validation of novel tau PET tracer [F-18]-MK-6240 on human postmortem brain tissue. *Acta Neuropathol Commun*. 2019;7:37.
- [101] Ono M, Sahara N, Kumata K, Ji B, Ni R, Koga S, et al. Distinct binding of PET ligands PBB3 and AV-1451 to tau fibril strains in neurodegenerative tauopathies. *Brain*. 2017;140:764-80.
- [102] Graff-Radford J, Yong KXX, Apostolova LG, Bouwman FH, Carrillo M, Dickerson BC, et al. New insights into atypical Alzheimer's disease in the era of biomarkers. *The Lancet Neurology*. 2021;20:222-34.
- [103] Dujardin S, Commins C, Lathuilière A, Beerepoot P, Fernandes AR, Kamath TV, et al. Tau molecular diversity contributes to clinical heterogeneity in Alzheimer's disease. *Nat Med*. 2020;26:1256-63.
- [104] Lowe VJ, Wiste HJ, Senjem ML, Weigand SD, Therneau TM, Boeve BF, et al. Widespread brain tau and its association with ageing, Braak stage and Alzheimer's dementia. *Brain*. 2018;141:271-87.

- [105] Jack CR, Jr., Wiste HJ, Schwarz CG, Lowe VJ, Senjem ML, Vemuri P, et al. Longitudinal tau PET in ageing and Alzheimer's disease. *Brain*. 2018;141:1517-28.
- [106] Hansson O, Mormino EC. Is longitudinal tau PET ready for use in Alzheimer's disease clinical trials? *Brain*. 2018;141:1241-4.
- [107] Gibbons GS, Lee VMY, Trojanowski JQ. Mechanisms of Cell-to-Cell Transmission of Pathological Tau: A Review. *JAMA Neurol*. 2019;76:101-8.
- [108] Guo JL, Narasimhan S, Changolkar L, He Z, Stieber A, Zhang B, et al. Unique pathological tau conformers from Alzheimer's brains transmit tau pathology in nontransgenic mice. *J Exp Med*. 2016;213:2635-54.
- [109] Jacobs HIL, Hedden T, Schultz AP, Sepulcre J, Perea RD, Amariglio RE, et al. Structural tract alterations predict downstream tau accumulation in amyloid-positive older individuals. *Nat Neurosci*. 2018;21:424-31.
- [110] Franzmeier N, Neitzel J, Rubinski A, Smith R, Strandberg O, Ossenkoppele R, et al. Functional brain architecture is associated with the rate of tau accumulation in Alzheimer's disease. *Nat Commun*. 2020;11:347.
- [111] Shi Y, Manis M, Long J, Wang K, Sullivan PM, Remolina Serrano J, et al. Microglia drive APOE-dependent neurodegeneration in a tauopathy mouse model. *J Exp Med*. 2019;216:2546-61.
- [112] Arnsten AFT, Datta D, Tredici KD, Braak H. Hypothesis: Tau pathology is an initiating factor in sporadic Alzheimer's disease. *Alzheimers Dement*. 2021;17:115-24.
- [113] Todd KJ, Serrano A, Lacaille JC, Robitaille R. Glial cells in synaptic plasticity. *J Physiol Paris*. 2006;99:75-83.
- [114] Morrens J, Van Den Broeck W, Kempermann G. Glial cells in adult neurogenesis. *Glia*. 2012;60:159-74.
- [115] Cope EC, Gould E. Adult Neurogenesis, Glia, and the Extracellular Matrix. *Cell Stem Cell*. 2019;24:690-705.
- [116] Araque A, Navarrete M. Glial cells in neuronal network function. *Philos Trans R Soc Lond B Biol Sci*. 2010;365:2375-81.
- [117] Butovsky O, Weiner HL. Microglial signatures and their role in health and disease. *Nat Rev Neurosci*. 2018;19:622-35.
- [118] Ahmad MH, Fatima M, Mondal AC. Influence of microglia and astrocyte activation in the neuroinflammatory pathogenesis of Alzheimer's disease: Rational insights for the therapeutic approaches. *J Clin Neurosci*. 2019;59:6-11.
- [119] Frost GR, Li YM. The role of astrocytes in amyloid production and Alzheimer's disease. *Open Biol*. 2017;7.
- [120] Li Q, Barres BA. Microglia and macrophages in brain homeostasis and disease. *Nat Rev Immunol*. 2018;18:225-42.
- [121] Hammond TR, Robinton D, Stevens B. Microglia and the Brain: Complementary Partners in Development and Disease. *Annu Rev Cell Dev Biol*. 2018;34:523-44.
- [122] Neumann H, Kotter MR, Franklin RJ. Debris clearance by microglia: an essential link between degeneration and regeneration. *Brain*. 2009;132:288-95.
- [123] Lee CYD, Daggett A, Gu X, Jiang LL, Langfelder P, Li X, et al. Elevated TREM2 Gene Dosage Reprograms Microglia Responsivity and Ameliorates Pathological Phenotypes in Alzheimer's Disease Models. *Neuron*. 2018;97:1032-48 e5.
- [124] Grubman A, Choo XY, Chew G, Ouyang JF, Sun G, Croft NP, et al. Transcriptional signature in microglia associated with Abeta plaque phagocytosis. *Nat Commun*. 2021;12:3015.

- [125] Luo W, Liu W, Hu X, Hanna M, Caravaca A, Paul SM. Microglial internalization and degradation of pathological tau is enhanced by an anti-tau monoclonal antibody. *Sci Rep*. 2015;5:11161.
- [126] Shi Y, Holtzman DM. Interplay between innate immunity and Alzheimer disease: APOE and TREM2 in the spotlight. *Nat Rev Immunol*. 2018;18:759-72.
- [127] Wang Y, Cella M, Mallinson K, Ulrich JD, Young KL, Robinette ML, et al. TREM2 lipid sensing sustains the microglial response in an Alzheimer's disease model. *Cell*. 2015;160:1061-71.
- [128] Zhou Y, Ulland TK, Colonna M. TREM2-Dependent Effects on Microglia in Alzheimer's Disease. *Front Aging Neurosci*. 2018;10:202.
- [129] Jansen IE, Savage JE, Watanabe K, Bryois J, Williams DM, Steinberg S, et al. Genome-wide meta-analysis identifies new loci and functional pathways influencing Alzheimer's disease risk. *Nat Genet*. 2019;51:404-13.
- [130] Kunkle BW, Grenier-Boley B, Sims R, Bis JC, Damotte V, Naj AC, et al. Genetic meta-analysis of diagnosed Alzheimer's disease identifies new risk loci and implicates Abeta, tau, immunity and lipid processing. *Nat Genet*. 2019;51:414-30.
- [131] Nott A, Holtman IR, Coufal NG, Schlachetzki JCM, Yu M, Hu R, et al. Brain cell type-specific enhancer-promoter interactome maps and disease-risk association. *Science*. 2019;366:1134-9.
- [132] Keren-Shaul H, Spinrad A, Weiner A, Matcovitch-Natan O, Dvir-Szternfeld R, Ulland TK, et al. A Unique Microglia Type Associated with Restricting Development of Alzheimer's Disease. *Cell*. 2017;169:1276-90 e17.
- [133] Krasemann S, Madore C, Cialic R, Baufeld C, Calcagno N, El Fatimy R, et al. The TREM2-APOE Pathway Drives the Transcriptional Phenotype of Dysfunctional Microglia in Neurodegenerative Diseases. *Immunity*. 2017;47:566-81 e9.
- [134] Felsky D, Roostaei T, Nho K, Risacher SL, Bradshaw EM, Petyuk V, et al. Neuropathological correlates and genetic architecture of microglial activation in elderly human brain. *Nat Commun*. 2019;10:409.
- [135] Srinivasan K, Friedman BA, Etxeberria A, Huntley MA, van der Brug MP, Foreman O, et al. Alzheimer's Patient Microglia Exhibit Enhanced Aging and Unique Transcriptional Activation. *Cell Rep*. 2020;31:107843.
- [136] Lewcock JW, Schlepckow K, Di Paolo G, Tahirovic S, Monroe KM, Haass C. Emerging Microglia Biology Defines Novel Therapeutic Approaches for Alzheimer's Disease. *Neuron*. 2020;108:801-21.
- [137] Wyss-Coray T, Loike JD, Brionne TC, Lu E, Anankov R, Yan F, et al. Adult mouse astrocytes degrade amyloid-beta in vitro and in situ. *Nat Med*. 2003;9:453-7.
- [138] Matejuk A, Ransohoff RM. Crosstalk Between Astrocytes and Microglia: An Overview. *Front Immunol*. 2020;11:1416.
- [139] Kirkley KS, Popichak KA, Afzali MF, Legare ME, Tjalkens RB. Microglia amplify inflammatory activation of astrocytes in manganese neurotoxicity. *J Neuroinflammation*. 2017;14:99.
- [140] Escartin C, Galea E, Lakatos A, O'Callaghan JP, Petzold GC, Serrano-Pozo A, et al. Reactive astrocyte nomenclature, definitions, and future directions. *Nat Neurosci*. 2021;24:312-25.
- [141] Liddelow SA, Guttenplan KA, Clarke LE, Bennett FC, Bohlen CJ, Schirmer L, et al. Neurotoxic reactive astrocytes are induced by activated microglia. *Nature*. 2017;541:481-7.

- [142] McAlpine CS, Park J, Griciuc A, Kim E, Choi SH, Iwamoto Y, et al. Astrocytic interleukin-3 programs microglia and limits Alzheimer's disease. *Nature*. 2021;595:701-6.
- [143] Cummings J, Lee G, Zhong K, Fonseca J, Taghva K. Alzheimer's disease drug development pipeline: 2021. *Alzheimers Dement (N Y)*. 2021;7:e12179.
- [144] Barroeta-Espar I, Weinstock LD, Perez-Nievas BG, Meltzer AC, Siao Tick Chong M, Amaral AC, et al. Distinct cytokine profiles in human brains resilient to Alzheimer's pathology. *Neurobiol Dis*. 2019;121:327-37.
- [145] Perez-Nievas BG, Stein TD, Tai HC, Dols-Icardo O, Scotton TC, Barroeta-Espar I, et al. Dissecting phenotypic traits linked to human resilience to Alzheimer's pathology. *Brain*. 2013;136:2510-26.
- [146] Moir RD, Lathe R, Tanzi RE. The antimicrobial protection hypothesis of Alzheimer's disease. *Alzheimers Dement*. 2018;14:1602-14.
- [147] Seaks CE, Wilcock DM. Infectious hypothesis of Alzheimer disease. *PLoS Pathog*. 2020;16:e1008596.
- [148] Kobayashi N, Masuda J, Kudoh J, Shimizu N, Yoshida T. Binding sites on tau proteins as components for antimicrobial peptides. *Biocontrol Sci*. 2008;13:49-56.
- [149] Wozniak MA, Shipley SJ, Combrinck M, Wilcock GK, Itzhaki RF. Productive herpes simplex virus in brain of elderly normal subjects and Alzheimer's disease patients. *J Med Virol*. 2005;75:300-6.
- [150] Jamieson GA, Maitland NJ, Wilcock GK, Craske J, Itzhaki RF. Latent herpes simplex virus type 1 in normal and Alzheimer's disease brains. *J Med Virol*. 1991;33:224-7.
- [151] Cummings J, Reiber C, Kumar P. The price of progress: Funding and financing Alzheimer's disease drug development. *Alzheimers Dement (N Y)*. 2018;4:330-43.
- [152] Association As. FDA-approved drugs for Alzheimer's. 2021.
- [153] Alexander GC, Knopman DS, Emerson SS, Ovbiagele B, Kryscio RJ, Perlmutter JS, et al. Revisiting FDA Approval of Aducanumab. *N Engl J Med*. 2021.
- [154] Rabinovici GD. Controversy and Progress in Alzheimer's Disease - FDA Approval of Aducanumab. *N Engl J Med*. 2021.
- [155] Sevigny J, Chiao P, Bussiere T, Weinreb PH, Williams L, Maier M, et al. The antibody aducanumab reduces Abeta plaques in Alzheimer's disease. *Nature*. 2016;537:50-6.
- [156] Sperling RA, Jack CR, Jr., Black SE, Frosch MP, Greenberg SM, Hyman BT, et al. Amyloid-related imaging abnormalities in amyloid-modifying therapeutic trials: recommendations from the Alzheimer's Association Research Roundtable Workgroup. *Alzheimers Dement*. 2011;7:367-85.
- [157] Owen DR, Yeo AJ, Gunn RN, Song K, Wadsworth G, Lewis A, et al. An 18-kDa translocator protein (TSPO) polymorphism explains differences in binding affinity of the PET radioligand PBR28. *J Cereb Blood Flow Metab*. 2012;32:1-5.
- [158] Parent MJ, Zimmer ER, Shin M, Kang MS, Fonov VS, Mathieu A, et al. Multimodal Imaging in Rat Model Recapitulates Alzheimer's Disease Biomarkers Abnormalities. *J Neurosci*. 2017;37:12263-71.
- [159] Yoshiyama Y, Higuchi M, Zhang B, Huang SM, Iwata N, Saido TC, et al. Synapse loss and microglial activation precede tangles in a P301S tauopathy mouse model. *Neuron*. 2007;53:337-51.
- [160] Heggland I, Storkaas IS, Soligard HT, Kobro-Flatmoen A, Witter MP. Stereological estimation of neuron number and plaque load in the hippocampal region of a transgenic rat model of Alzheimer's disease. *Eur J Neurosci*. 2015;41:1245-62.

- [161] Malcolm JC, Breuillaud L, Do Carmo S, Hall H, Welikovitch LA, Macdonald JA, et al. Neuropathological changes and cognitive deficits in rats transgenic for human mutant tau recapitulate human tauopathy. *Neurobiol Dis.* 2019;127:323-38.
- [162] Palmqvist S, Janelidze S, Quiroz YT, Zetterberg H, Lopera F, Stomrud E, et al. Discriminative Accuracy of Plasma Phospho-tau217 for Alzheimer Disease vs Other Neurodegenerative Disorders. *JAMA.* 2020;324:772-81.
- [163] Thal DR, Capetillo-Zarate E, Del Tredici K, Braak H. The development of amyloid beta protein deposits in the aged brain. *Sci Aging Knowledge Environ.* 2006;2006:re1.
- [164] Tuisku J, Plaven-Sigraay P, Gaiser EC, Airas L, Al-Abdulrasul H, Bruck A, et al. Effects of age, BMI and sex on the glial cell marker TSPO - a multicentre [(11)C]PBR28 HRRT PET study. *Eur J Nucl Med Mol Imaging.* 2019;46:2329-38.
- [165] Stephen TL, Cacciottolo M, Balu D, Morgan TE, LaDu MJ, Finch CE, et al. APOE genotype and sex affect microglial interactions with plaques in Alzheimer's disease mice. *Acta Neuropathol Commun.* 2019;7:82.
- [166] Altmann A, Tian L, Henderson VW, Greicius MD, Alzheimer's Disease Neuroimaging Initiative I. Sex modifies the APOE-related risk of developing Alzheimer disease. *Ann Neurol.* 2014;75:563-73.
- [167] Montagne A, Nation DA, Sagare AP, Barisano G, Sweeney MD, Chakhoyan A, et al. APOE4 leads to blood-brain barrier dysfunction predicting cognitive decline. *Nature.* 2020;581:71-6.
- [168] Buckley RF, Mormino EC, Rabin JS, Hohman TJ, Landau S, Hanseeuw BJ, et al. Sex Differences in the Association of Global Amyloid and Regional Tau Deposition Measured by Positron Emission Tomography in Clinically Normal Older Adults. *JAMA Neurol.* 2019;76:542-51.
- [169] Liu M, Paranjpe MD, Zhou X, Duy PQ, Goyal MS, Benzinger TLS, et al. Sex modulates the ApoE epsilon4 effect on brain tau deposition measured by (18)F-AV-1451 PET in individuals with mild cognitive impairment. *Theranostics.* 2019;9:4959-70.
- [170] Stern Y. Influence of Education and Occupation on the Incidence of Alzheimer's Disease. *JAMA: The Journal of the American Medical Association.* 1994;271.
- [171] Stern Y, Albert S, Tang MX, Tsai WY. Rate of memory decline in AD is related to education and occupation: cognitive reserve? *Neurology.* 1999;53:1942-7.
- [172] Stern Y. Cognitive reserve in ageing and Alzheimer's disease. *The Lancet Neurology.* 2012;11:1006-12.
- [173] Ottoy J, Verhaeghe J, Niemantsverdriet E, Wyffels L, Somers C, De Roeck E, et al. Validation of the Semiquantitative Static SUVR Method for (18)F-AV45 PET by Pharmacokinetic Modeling with an Arterial Input Function. *J Nucl Med.* 2017;58:1483-9.
- [174] Cselenyi Z, Jonhagen ME, Forsberg A, Halldin C, Julin P, Schou M, et al. Clinical validation of 18F-AZD4694, an amyloid-beta-specific PET radioligand. *J Nucl Med.* 2012;53:415-24.
- [175] Jureus A, Swahn BM, Sandell J, Jeppsson F, Johnson AE, Johnstrom P, et al. Characterization of AZD4694, a novel fluorinated Abeta plaque neuroimaging PET radioligand. *J Neurochem.* 2010;114:784-94.
- [176] Leuzy A, Zimmer E, Gauthier S, Rosa-Neto P. Amyloid imaging in Alzheimer's disease: a potential new era of personalized medicine? *Translational Neuroscience.* 2014;5.

- [177] Rowe CC, Pejoska S, Mulligan RS, Jones G, Chan JG, Svensson S, et al. Head-to-head comparison of <sup>11</sup>C-PiB and <sup>18</sup>F-AZD4694 (NAV4694) for beta-amyloid imaging in aging and dementia. *J Nucl Med.* 2013;54:880-6.
- [178] Pascoal TA, Shin M, Kang MS, Chamoun M, Chartrand D, Mathotaarachchi S, et al. In vivo quantification of neurofibrillary tangles with [(18)F]MK-6240. *Alzheimers Res Ther.* 2018;10:74.
- [179] Kreisl WC, Kim M-J, Coughlin JM, Henter ID, Owen DR, Innis RB. PET imaging of neuroinflammation in neurological disorders. *The Lancet Neurology.* 2020;19:940-50.
- [180] Lyoo CH, Ikawa M, Liow JS, Zoghbi SS, Morse CL, Pike VW, et al. Cerebellum Can Serve As a Pseudo-Reference Region in Alzheimer Disease to Detect Neuroinflammation Measured with PET Radioligand Binding to Translocator Protein. *J Nucl Med.* 2015;56:701-6.
- [181] Zanutti-Fregonara P, Kreisl WC, Innis RB, Lyoo CH. Automatic Extraction of a Reference Region for the Noninvasive Quantification of Translocator Protein in Brain Using (11)C-PBR28. *J Nucl Med.* 2019;60:978-84.
- [182] Plaven-Sigra P, Schain M, Zanderigo F, Karolinska PBRsg, Rabiner EA, Gunn RN, et al. Accuracy and reliability of [(11)C]PBR28 specific binding estimated without the use of a reference region. *Neuroimage.* 2019;188:102-10.
- [183] Zarow C, Vinters HV, Ellis WG, Weiner MW, Mungas D, White L, et al. Correlates of hippocampal neuron number in Alzheimer's disease and ischemic vascular dementia. *Ann Neurol.* 2005;57:896-903.
- [184] Johnson KA, Fox NC, Sperling RA, Klunk WE. Brain imaging in Alzheimer disease. *Cold Spring Harb Perspect Med.* 2012;2:a006213.
- [185] Grothe MJ, Teipel SJ. Alzheimer's Disease Neuroimaging I. Spatial patterns of atrophy, hypometabolism, and amyloid deposition in Alzheimer's disease correspond to dissociable functional brain networks. *Hum Brain Mapp.* 2016;37:35-53.
- [186] Hillman EM. Coupling mechanism and significance of the BOLD signal: a status report. *Annu Rev Neurosci.* 2014;37:161-81.
- [187] Bateman RJ, Xiong C, Benzinger TL, Fagan AM, Goate A, Fox NC, et al. Clinical and biomarker changes in dominantly inherited Alzheimer's disease. *N Engl J Med.* 2012;367:795-804.
- [188] Olsson B, Lautner R, Andreasson U, Öhrfelt A, Portelius E, Bjerke M, et al. CSF and blood biomarkers for the diagnosis of Alzheimer's disease: a systematic review and meta-analysis. *The Lancet Neurology.* 2016;15:673-84.
- [189] Hansson O, Lehmann S, Otto M, Zetterberg H, Lewczuk P. Advantages and disadvantages of the use of the CSF Amyloid beta (Aβ) 42/40 ratio in the diagnosis of Alzheimer's Disease. *Alzheimers Res Ther.* 2019;11:34.
- [190] Schindler SE, Gray JD, Gordon BA, Xiong C, Batrla-Utermann R, Quan M, et al. Cerebrospinal fluid biomarkers measured by Elecsys assays compared to amyloid imaging. *Alzheimers Dement.* 2018;14:1460-9.
- [191] Lewczuk P, Lukaszewicz-Zajac M, Mroczko P, Kornhuber J. Clinical significance of fluid biomarkers in Alzheimer's Disease. *Pharmacol Rep.* 2020;72:528-42.
- [192] Mattsson N, Palmqvist S, Stomrud E, Vogel J, Hansson O. Staging beta-Amyloid Pathology With Amyloid Positron Emission Tomography. *JAMA Neurol.* 2019;76:1319-29.
- [193] Spiegel J, Pirraglia E, Osorio RS, Glodzik L, Li Y, Tsui W, et al. Greater specificity for cerebrospinal fluid P-tau231 over P-tau181 in the differentiation of healthy controls from Alzheimer's disease. *J Alzheimers Dis.* 2016;49:93-100.

- [194] Palmqvist S, Tideman P, Cullen N, Zetterberg H, Blennow K, Alzheimer's Disease Neuroimaging I, et al. Prediction of future Alzheimer's disease dementia using plasma phospho-tau combined with other accessible measures. *Nat Med*. 2021;27:1034-42.
- [195] Kang MS, Aliaga AA, Shin M, Mathotaarachchi S, Benedet AL, Pascoal TA, et al. Amyloid-beta modulates the association between neurofilament light chain and brain atrophy in Alzheimer's disease. *Mol Psychiatry*. 2020.
- [196] Mattsson N, Insel PS, Palmqvist S, Portelius E, Zetterberg H, Weiner M, et al. Cerebrospinal fluid tau, neurogranin, and neurofilament light in Alzheimer's disease. *EMBO Mol Med*. 2016;8:1184-96.
- [197] Mattsson N, Cullen NC, Andreasson U, Zetterberg H, Blennow K. Association Between Longitudinal Plasma Neurofilament Light and Neurodegeneration in Patients With Alzheimer Disease. *JAMA Neurol*. 2019.
- [198] Preische O, Schultz SA, Apel A, Kuhle J, Kaeser SA, Barro C, et al. Serum neurofilament dynamics predicts neurodegeneration and clinical progression in presymptomatic Alzheimer's disease. *Nat Med*. 2019;25:277-83.
- [199] Hardy J, Selkoe DJ. The amyloid hypothesis of Alzheimer's disease; progress and problems on the road to therapeutics. *Science*. 2002;297:353-6.
- [200] Guillozet AL, Weintraub S, Mash DC, Mesulam MM. Neurofibrillary tangles, amyloid, and memory in aging and mild cognitive impairment. *Arch Neurol*. 2003;60:729-36.
- [201] Ottoy J, Niemantsverdriet E, Verhaeghe J, De Roeck E, Struyfs H, Somers C, et al. Association of short-term cognitive decline and MCI-to-AD dementia conversion with CSF, MRI, amyloid- and (18)F-FDG-PET imaging. *Neuroimage Clin*. 2019;22:101771.
- [202] Petzold A. Neurofilament phosphoforms: surrogate markers for axonal injury, degeneration and loss. *J Neurol Sci*. 2005;233:183-98.
- [203] Trojanowski JQ, Walkenstein N, Lee VMY. Expression of Neurofilament Subunits in Neurons of the Central and Peripheral Nervous-System - an Immunohistochemical Study with Monoclonal-Antibodies. *Journal of Neuroscience*. 1986;6:650-60.
- [204] Lycke JN, Karlsson JE, Andersen O, Rosengren LE. Neurofilament protein in cerebrospinal fluid: a potential marker of activity in multiple sclerosis. *J Neurol Neurosur Ps*. 1998;64:402-4.
- [205] Rosengren LE, Karlsson JE, Karlsson JO, Persson LI, Wikkelso C. Patients with amyotrophic lateral sclerosis and other neurodegenerative diseases have increased levels of neurofilament protein in CSF. *Journal of Neurochemistry*. 1996;67:2013-8.
- [206] Scherling CS, Hall T, Berisha F, Klepac K, Karydas A, Coppola G, et al. Cerebrospinal fluid neurofilament concentration reflects disease severity in frontotemporal degeneration. *Ann Neurol*. 2014;75:116-26.
- [207] Zetterberg H, Skillback T, Mattsson N, Trojanowski JQ, Portelius E, Shaw LM, et al. Association of Cerebrospinal Fluid Neurofilament Light Concentration With Alzheimer Disease Progression. *JAMA Neurol*. 2016;73:60-7.
- [208] Bacioglu M, Maia LF, Preische O, Schelle J, Apel A, Kaeser SA, et al. Neurofilament Light Chain in Blood and CSF as Marker of Disease Progression in Mouse Models and in Neurodegenerative Diseases. *Neuron*. 2016;91:56-66.
- [209] Johnson EB, Byrne LM, Gregory S, Rodrigues FB, Blennow K, Durr A, et al. Neurofilament light protein in blood predicts regional atrophy in Huntington disease. *Neurology*. 2018;90:e717-e23.

- [210] Soylyu-Kucharz R, Sandelius A, Sjogren M, Blennow K, Wild EJ, Zetterberg H, et al. Neurofilament light protein in CSF and blood is associated with neurodegeneration and disease severity in Huntington's disease R6/2 mice. *Sci Rep.* 2017;7:14114.
- [211] Brureau A, Blanchard-Bregeon V, Pech C, Hamon S, Chaillou P, Guillemot JC, et al. NF-L in cerebrospinal fluid and serum is a biomarker of neuronal damage in an inducible mouse model of neurodegeneration. *Neurobiol Dis.* 2017;104:73-84.
- [212] Rohrer JD, Woollacott IOC, Dick KM, Brotherhood E, Gordon E, Fellows A, et al. Serum neurofilament light chain protein is a measure of disease intensity in frontotemporal dementia. *Neurology.* 2016;87:1329-36.
- [213] Mattsson N, Andreasson U, Zetterberg H, Blennow K, Alzheimer's Disease Neuroimaging I. Association of Plasma Neurofilament Light With Neurodegeneration in Patients With Alzheimer Disease. *JAMA Neurol.* 2017;74:557-66.
- [214] Seeley WW, Crawford RK, Zhou J, Miller BL, Greicius MD. Neurodegenerative diseases target large-scale human brain networks. *Neuron.* 2009;62:42-52.
- [215] Smith CD, Chebrolu H, Wekstein DR, Schmitt FA, Markesbery WR. Age and gender effects on human brain anatomy: a voxel-based morphometric study in healthy elderly. *Neurobiol Aging.* 2007;28:1075-87.
- [216] Sled JG, Zijdenbos AP, Evans AC. A nonparametric method for automatic correction of intensity nonuniformity in MRI data. *IEEE Trans Med Imaging.* 1998;17:87-97.
- [217] Smith SM. Fast robust automated brain extraction. *Hum Brain Mapp.* 2002;17:143-55.
- [218] Mazziotta JC, Toga AW, Evans A, Fox P, Lancaster J. A probabilistic atlas of the human brain: theory and rationale for its development. The International Consortium for Brain Mapping (ICBM). *Neuroimage.* 1995;2:89-101.
- [219] V. Fonov AE, R. McKinstry, C. Almlil, D. Collins. Unbiased nonlinear average age-appropriate brain templates from birth to adulthood. *Neuroimage.* 2009;47:p. S102.
- [220] Friedel M, van Eede MC, Pipitone J, Chakravarty MM, Lerch JP. Pydpipe: a flexible toolkit for constructing novel registration pipelines. *Front Neuroinform.* 2014;8:67.
- [221] Bittner T, Zetterberg H, Teunissen CE, Ostlund RE, Jr., Militello M, Andreasson U, et al. Technical performance of a novel, fully automated electrochemiluminescence immunoassay for the quantitation of beta-amyloid (1-42) in human cerebrospinal fluid. *Alzheimers Dement.* 2016;12:517-26.
- [222] Hansson O, Seibyl J, Stomrud E, Zetterberg H, Trojanowski JQ, Bittner T, et al. CSF biomarkers of Alzheimer's disease concord with amyloid-beta PET and predict clinical progression: A study of fully automated immunoassays in BioFINDER and ADNI cohorts. *Alzheimers Dement.* 2018;14:1470-81.
- [223] Gisslen M, Price RW, Andreasson U, Norgren N, Nilsson S, Hagberg L, et al. Plasma Concentration of the Neurofilament Light Protein (NFL) is a Biomarker of CNS Injury in HIV Infection: A Cross-Sectional Study. *EBioMedicine.* 2016;3:135-40.
- [224] Mathotaarachchi S, Wang S, Shin M, Pascoal TA, Benedet AL, Kang MS, et al. VoxelStats: A MATLAB Package for Multi-Modal Voxel-Wise Brain Image Analysis. *Frontiers in Neuroinformatics.* 2016;10.
- [225] Modvig S, Degen M, Horwitz H, Cramer SP, Larsson HB, Wanscher B, et al. Relationship between cerebrospinal fluid biomarkers for inflammation, demyelination and neurodegeneration in acute optic neuritis. *PLoS One.* 2013;8:e77163.

- [226] Iulita MF, Allard S, Richter L, Munter LM, Ducatenzeiler A, Weise C, et al. Intracellular Abeta pathology and early cognitive impairments in a transgenic rat overexpressing human amyloid precursor protein: a multidimensional study. *Acta Neuropathol Commun.* 2014;2:61.
- [227] Sutphen CL, McCue L, Herries EM, Xiong C, Ladenson JH, Holtzman DM, et al. Longitudinal decreases in multiple cerebrospinal fluid biomarkers of neuronal injury in symptomatic late onset Alzheimer's disease. *Alzheimers Dement.* 2018;14:869-79.
- [228] Rojas JC, Karydas A, Bang J, Tsai RM, Blennow K, Liman V, et al. Plasma neurofilament light chain predicts progression in progressive supranuclear palsy. *Ann Clin Transl Neurol.* 2016;3:216-25.
- [229] Steinacker P, Blennow K, Halbgebauer S, Shi S, Ruf V, Oeckl P, et al. Neurofilaments in blood and CSF for diagnosis and prediction of onset in Creutzfeldt-Jakob disease. *Sci Rep.* 2016;6:38737.
- [230] Jack CR, Jr., Lowe VJ, Senjem ML, Weigand SD, Kemp BJ, Shiung MM, et al. 11C PiB and structural MRI provide complementary information in imaging of Alzheimer's disease and amnesic mild cognitive impairment. *Brain.* 2008;131:665-80.
- [231] Palmqvist S, Scholl M, Strandberg O, Mattsson N, Stomrud E, Zetterberg H, et al. Earliest accumulation of beta-amyloid occurs within the default-mode network and concurrently affects brain connectivity. *Nat Commun.* 2017;8:1214.
- [232] Welikovitsh LA, Do Carmo S, Magloczky Z, Szocsics P, Loke J, Freund T, et al. Evidence of intraneuronal Abeta accumulation preceding tau pathology in the entorhinal cortex. *Acta Neuropathol.* 2018;136:901-17.
- [233] Lawson LJ, Perry VH, Gordon S. Turnover of resident microglia in the normal adult mouse brain. *Neuroscience.* 1992;48:405-15.
- [234] Salter MW, Stevens B. Microglia emerge as central players in brain disease. *Nat Med.* 2017;23:1018-27.
- [235] Hamelin L, Lagarde J, Dorothee G, Leroy C, Labit M, Comley RA, et al. Early and protective microglial activation in Alzheimer's disease: a prospective study using 18F-DPA-714 PET imaging. *Brain.* 2016;139:1252-64.
- [236] Fan Z, Brooks DJ, Okello A, Edison P. An early and late peak in microglial activation in Alzheimer's disease trajectory. *Brain.* 2017;140:792-803.
- [237] Shi Y, Yamada K, Liddelow SA, Smith ST, Zhao L, Luo W, et al. ApoE4 markedly exacerbates tau-mediated neurodegeneration in a mouse model of tauopathy. *Nature.* 2017;549:523-7.
- [238] Dani M, Wood M, Mizoguchi R, Fan Z, Walker Z, Morgan R, et al. Microglial activation correlates in vivo with both tau and amyloid in Alzheimer's disease. *Brain.* 2018;141:2740-54.
- [239] Frackowiak J, Wisniewski HM, Wegiel J, Merz GS, Iqbal K, Wang KC. Ultrastructure of the microglia that phagocytose amyloid and the microglia that produce beta-amyloid fibrils. *Acta Neuropathol.* 1992;84:225-33.
- [240] Stalder M, Phinney A, Probst A, Sommer B, Staufenbiel M, Jucker M. Association of Microglia with Amyloid Plaques in Brains of APP23 Transgenic Mice. *The American Journal of Pathology.* 1999;154:1673-84.
- [241] Brelstaff J, Tolkovsky AM, Ghetti B, Goedert M, Spillantini MG. Living Neurons with Tau Filaments Aberrantly Expose Phosphatidylserine and Are Phagocytosed by Microglia. *Cell Rep.* 2018;24:1939-48 e4.
- [242] Tzioras M, Daniels MJD, King D, Popovic K, Holloway RK, Stevenson AJ, et al. Altered synaptic ingestion by human microglia in Alzheimer's disease. *BioRxiv.* 2019.

- [243] Srinivasan K, Friedman BA, Etxeberria A, Huntley MA, van der Brug MP, Foreman O, et al. Alzheimer's patient brain myeloid cells exhibit enhanced aging and unique transcriptional activation. *BioRxiv*. 2019.
- [244] Mathys H, Davila-Velderrain J, Peng Z, Gao F, Mohammadi S, Young JZ, et al. Single-cell transcriptomic analysis of Alzheimer's disease. *Nature*. 2019;570:332-7.
- [245] Zhao Y, Wu X, Li X, Jiang LL, Gui X, Liu Y, et al. TREM2 Is a Receptor for beta-Amyloid that Mediates Microglial Function. *Neuron*. 2018;97:1023-31 e7.
- [246] Cserep C, Posfai B, Lenart N, Fekete R, Laszlo ZI, Lele Z, et al. Microglia monitor and protect neuronal function through specialized somatic purinergic junctions. *Science*. 2020;367:528-37.
- [247] Scholl M, Lockhart SN, Schonhaut DR, O'Neil JP, Janabi M, Ossenkoppele R, et al. PET Imaging of Tau Deposition in the Aging Human Brain. *Neuron*. 2016;89:971-82.
- [248] Iba M, Guo JL, McBride JD, Zhang B, Trojanowski JQ, Lee VM. Synthetic tau fibrils mediate transmission of neurofibrillary tangles in a transgenic mouse model of Alzheimer's-like tauopathy. *J Neurosci*. 2013;33:1024-37.
- [249] Uemura N, Uemura MT, Luk KC, Lee VM, Trojanowski JQ. Cell-to-Cell Transmission of Tau and alpha-Synuclein. *Trends Mol Med*. 2020.
- [250] Peng C, Trojanowski JQ, Lee VM. Protein transmission in neurodegenerative disease. *Nat Rev Neurol*. 2020;16:199-212.
- [251] Yamada K, Holth JK, Liao F, Stewart FR, Mahan TE, Jiang H, et al. Neuronal activity regulates extracellular tau in vivo. *J Exp Med*. 2014;211:387-93.
- [252] Asai H, Ikezu S, Tsunoda S, Medalla M, Luebke J, Haydar T, et al. Depletion of microglia and inhibition of exosome synthesis halt tau propagation. *Nat Neurosci*. 2015;18:1584-93.
- [253] Bennett ML, Bennett FC. The influence of environment and origin on brain resident macrophages and implications for therapy. *Nat Neurosci*. 2020;23:157-66.
- [254] Deczkowska A, Keren-Shaul H, Weiner A, Colonna M, Schwartz M, Amit I. Disease-Associated Microglia: A Universal Immune Sensor of Neurodegeneration. *Cell*. 2018;173:1073-81.
- [255] Ayata P, Badimon A, Strasburger HJ, Duff MK, Montgomery SE, Loh YE, et al. Epigenetic regulation of brain region-specific microglia clearance activity. *Nat Neurosci*. 2018;21:1049-60.
- [256] Polanco JC, Hand GR, Briner A, Li C, Gotz J. Exosomes induce endolysosomal permeabilization as a gateway by which exosomal tau seeds escape into the cytosol. *Acta Neuropathol*. 2021.
- [257] Ising C, Venegas C, Zhang S, Scheiblich H, Schmidt SV, Vieira-Saecker A, et al. NLRP3 inflammasome activation drives tau pathology. *Nature*. 2019;575:669-73.
- [258] Wood H. Alzheimer disease: ApoE4 implicated in tau-mediated neurodegeneration. *Nat Rev Neurol*. 2017;13:706-7.
- [259] Leyns CEG, Ulrich JD, Finn MB, Stewart FR, Koscal LJ, Remolina Serrano J, et al. TREM2 deficiency attenuates neuroinflammation and protects against neurodegeneration in a mouse model of tauopathy. *Proc Natl Acad Sci U S A*. 2017;114:11524-9.
- [260] Rangaraju S, Dammer EB, Raza SA, Rathakrishnan P, Xiao H, Gao T, et al. Identification and therapeutic modulation of a pro-inflammatory subset of disease-associated-microglia in Alzheimer's disease. *Mol Neurodegener*. 2018;13:24.
- [261] Venegas C, Kumar S, Franklin BS, Dierkes T, Brinkschulte R, Tejera D, et al. Microglia-derived ASC specks cross-seed amyloid-beta in Alzheimer's disease. *Nature*. 2017;552:355-61.

- [262] Yamazaki Y, Zhao N, Caulfield TR, Liu CC, Bu G. Apolipoprotein E and Alzheimer disease: pathobiology and targeting strategies. *Nat Rev Neurol*. 2019;15:501-18.
- [263] Welikovitsh LA, Do Carmo S, Magloczky Z, Malcolm JC, Loke J, Klein WL, et al. Early intraneuronal amyloid triggers neuron-derived inflammatory signaling in APP transgenic rats and human brain. *Proc Natl Acad Sci U S A*. 2020;117:6844-54.
- [264] Braak H, Del Tredici K. From the Entorhinal Region via the Prosubiculum to the Dentate Fascia: Alzheimer Disease-Related Neurofibrillary Changes in the Temporal Allocortex. *J Neuropathol Exp Neurol*. 2020;79:163-75.
- [265] Mormino EC, Betensky RA, Hedden T, Schultz AP, Amariglio RE, Rentz DM, et al. Synergistic effect of beta-amyloid and neurodegeneration on cognitive decline in clinically normal individuals. *JAMA Neurol*. 2014;71:1379-85.
- [266] McIntosh AR, Bookstein FL, Haxby JV, Grady CL. Spatial pattern analysis of functional brain images using partial least squares. *Neuroimage*. 1996;3:143-57.
- [267] Sanchez G. *PLS Path Modeling with R*. 2013.
- [268] McIntosh AR, Lobaugh NJ. Partial least squares analysis of neuroimaging data: applications and advances. *Neuroimage*. 2004;23 Suppl 1:S250-63.
- [269] O'Brien RJ, Wong PC. Amyloid precursor protein processing and Alzheimer's disease. *Annu Rev Neurosci*. 2011;34:185-204.
- [270] Kadowaki H, Nishitoh H, Urano F, Sadamitsu C, Matsuzawa A, Takeda K, et al. Amyloid beta induces neuronal cell death through ROS-mediated ASK1 activation. *Cell Death Differ*. 2005;12:19-24.
- [271] Choi SH, Kim YH, Hebisch M, Sliwinski C, Lee S, D'Avanzo C, et al. A three-dimensional human neural cell culture model of Alzheimer's disease. *Nature*. 2014;515:274-8.
- [272] Doody RS, Thomas RG, Farlow M, Iwatsubo T, Vellas B, Joffe S, et al. Phase 3 trials of solanezumab for mild-to-moderate Alzheimer's disease. *N Engl J Med*. 2014;370:311-21.
- [273] Salloway S, Sperling R, Fox NC, Blennow K, Klunk W, Raskind M, et al. Two phase 3 trials of bapineuzumab in mild-to-moderate Alzheimer's disease. *N Engl J Med*. 2014;370:322-33.
- [274] Hardy J, De Strooper B. Alzheimer's disease: where next for anti-amyloid therapies? *Brain*. 2017;140:853-5.
- [275] Janelidze S, Zetterberg H, Mattsson N, Palmqvist S, Vanderstichele H, Lindberg O, et al. CSF A $\beta$ <sub>42</sub>/A $\beta$ <sub>40</sub> and A $\beta$ <sub>42</sub>/A $\beta$ <sub>38</sub> ratios: better diagnostic markers of Alzheimer disease. *Ann Clin Transl Neurol*. 2016;3:154-65.
- [276] Abulrob A, Zhang J, Tanha J, MacKenzie R, Stanimirovic D. Single domain antibodies as blood-brain barrier delivery vectors. *International Congress Series*. 2005;1277:212-23.
- [277] Chakravarthy B, Menard M, Brown L, Hewitt M, Atkinson T, Whitfield J. A synthetic peptide corresponding to a region of the human pericentriolar material 1 (PCM-1) protein binds beta-amyloid (A $\beta$ <sub>1-42</sub>) oligomers. *J Neurochem*. 2013;126:415-24.
- [278] Chakravarthy B, Ito S, Atkinson T, Gaudet C, Menard M, Brown L, et al. Evidence that a synthetic amyloid-ss oligomer-binding peptide (ABP) targets amyloid-ss deposits in transgenic mouse brain and human Alzheimer's disease brain. *Biochem Biophys Res Commun*. 2014;445:656-60.
- [279] Haqqani AS, Caram-Salas N, Ding W, Brunette E, Delaney CE, Baumann E, et al. Multiplexed evaluation of serum and CSF pharmacokinetics of brain-targeting single-domain antibodies using a NanoLC-SRM-ILIS method. *Mol Pharm*. 2013;10:1542-56.

- [280] Jonathan D. Rohrer IOCW, Katrina M. Dick, Emilie Brotherhood, Elizabeth Gordon, Alexander Fellows, Jamie Toombs, Ronald Druyeh, M. Jorge Cardoso, Sebastien Ourselin, Jennifer M. Nicholas, Niklas Norgren, Simon Mead, Ulf Anderasson, Kaj Blennow, Jonathan M. Schott, Nick C. Fox, Jason D. Warren, Henrik Zetterberg. Serum neurofilament light chain protein is a measure of disease intensity in frontotemporal dementia. *American Academy of Neurology*. 2016.
- [281] Percie du Sert N, Hurst V, Ahluwalia A, Alam S, Avey MT, Baker M, et al. The ARRIVE guidelines 2.0: Updated guidelines for reporting animal research. *J Cereb Blood Flow Metab*. 2020;40:1769-77.
- [282] Banks WA, Terrell B, Farr SA, Robinson SM, Nonaka N, Morley JE. Passage of amyloid beta protein antibody across the blood-brain barrier in a mouse model of Alzheimer's disease. *Peptides*. 2002;23:2223-6.
- [283] Farrington GK, Caram-Salas N, Haqqani AS, Brunette E, Eldredge J, Pepinsky B, et al. A novel platform for engineering blood-brain barrier-crossing bispecific biologics. *FASEB J*. 2014;28:4764-78.
- [284] Ahmed M, Davis J, Aucoin D, Sato T, Ahuja S, Aimoto S, et al. Structural conversion of neurotoxic amyloid-beta(1-42) oligomers to fibrils. *Nat Struct Mol Biol*. 2010;17:561-7.
- [285] Yang T, Li S, Xu H, Walsh DM, Selkoe DJ. Large Soluble Oligomers of Amyloid beta-Protein from Alzheimer Brain Are Far Less Neuroactive Than the Smaller Oligomers to Which They Dissociate. *J Neurosci*. 2017;37:152-63.
- [286] Mucke L, Selkoe DJ. Neurotoxicity of amyloid beta-protein: synaptic and network dysfunction. *Cold Spring Harb Perspect Med*. 2012;2:a006338.
- [287] DeMattos RB, Bales KR, Parsadanian M, O'Dell MA, Foss EM, Paul SM, et al. Plaque-associated disruption of CSF and plasma amyloid-beta (A $\beta$ ) equilibrium in a mouse model of Alzheimer's disease. *Journal of Neurochemistry*. 2002;81:229-36.
- [288] Karran E, Hardy J. A critique of the drug discovery and phase 3 clinical programs targeting the amyloid hypothesis for Alzheimer disease. *Ann Neurol*. 2014;76:185-205.
- [289] Dickerson BC, Wolk DA, Alzheimer's Disease Neuroimaging I. Biomarker-based prediction of progression in MCI: Comparison of AD signature and hippocampal volume with spinal fluid amyloid-beta and tau. *Front Aging Neurosci*. 2013;5:55.
- [290] Schuff N, Woerner N, Boreta L, Kornfield T, Shaw LM, Trojanowski JQ, et al. MRI of hippocampal volume loss in early Alzheimer's disease in relation to ApoE genotype and biomarkers. *Brain*. 2009;132:1067-77.
- [291] Sheline YI, Raichle ME. Resting state functional connectivity in preclinical Alzheimer's disease. *Biol Psychiatry*. 2013;74:340-7.
- [292] Brier MR, Gordon B, Friedrichsen K, McCarthy J, Stern A, Christensen J, et al. Tau and Ab imaging, CSF measures, and cognition in Alzheimer's disease. *Sci Transl Med*. 2016;8.
- [293] Shahim P, Politis A, van der Merwe A, Moore B, Chou YY, Pham DL, et al. Neurofilament light as a biomarker in traumatic brain injury. *Neurology*. 2020;95:e610-e22.
- [294] Niu Z, Sarkar R, Aichler M, Wester HJ, Yousefi BH, Reif B. Mapping the Binding Interface of PET Tracer Molecules and Alzheimer Disease A $\beta$  Fibrils by Using MAS Solid-State NMR Spectroscopy. *Chembiochem*. 2020;21:2495-502.
- [295] Maeda J, Zhang MR, Okauchi T, Ji B, Ono M, Hattori S, et al. In vivo positron emission tomographic imaging of glial responses to amyloid-beta and tau pathologies in mouse models of Alzheimer's disease and related disorders. *J Neurosci*. 2011;31:4720-30.

[296] Cosenza-Nashat M, Zhao ML, Suh HS, Morgan J, Natividad R, Morgello S, et al. Expression of the translocator protein of 18 kDa by microglia, macrophages and astrocytes based on immunohistochemical localization in abnormal human brain. *Neuropathol Appl Neurobiol.* 2009;35:306-28.

[297] Gui Y, Marks JD, Das S, Hyman BT, Serrano-Pozo A. Characterization of the 18 kDa translocator protein (TSPO) expression in post-mortem normal and Alzheimer's disease brains. *Brain Pathol.* 2020;30:151-64.